

AD\_\_\_\_\_

**Award Number:**

W81XWH-08-1-0148

**TITLE**

ACUTE LUNG INJURY: MAKING THE INJURED LUNG PERFORM BETTER  
AND REBUILDING HEALTHY LUNGS

**PRINCIPAL INVESTIGATOR:** Alan Fine, MD

**CONTRACTING ORGANIZATION:** Boston University Medical Center  
Boston, MA 02118

**REPORT DATE:** April 2014

**TYPE OF REPORT:** Final

**PREPARED FOR:**

U.S. Army Medical Research and Materiel Command  
Fort Detrick, Maryland 21702-5012

**DISTRIBUTION STATEMENT:**

xx Approved for public release; distribution unlimited

The views, opinions and/or findings contained in this report are those of the author(s) and should not be construed as an official Department of the Army position, policy or decision unless so designated by other documentation.

| REPORT DOCUMENTATION PAGE   |                      |                         |                                      | Form Approved<br>OMB No. 0704-0188                   |   |
|---|----------------------|-------------------------|--------------------------------------|--|---|
| Public reporting burden for this collection of information is estimated to average 1 hour per response, including the time for reviewing instructions, searching existing data sources, gathering and maintaining the data needed, and completing and reviewing this collection of information. Send comments regarding this burden estimate or any other aspect of this collection of information, including suggestions for reducing this burden to Department of Defense, Washington Headquarters Services, Directorate for Information Operations and Reports (0704-0188), 1215 Jefferson Davis Highway, Suite 1204, Arlington, VA 22202-4302. Respondents should be aware that notwithstanding any other provision of law, no person shall be subject to any penalty for failing to comply with a collection of information if it does not display a currently valid OMB control number. <b>PLEASE DO NOT RETURN YOUR FORM TO THE ABOVE ADDRESS.</b>   |                      |                         |                                      |  |   |
| 1. REPORT DATE (DD-MM-YYYY)<br>April 2014   |                      | 2. REPORT TYPE<br>Final |                                      | 3. DATES COVERED (From - To)<br>1Jul2008 - 31Dec2013 |   |
| 4. TITLE AND SUBTITLE<br><br>ACUTE LUNG INJURY: MAKING THE INJURED LUNG PERFORM BETTER AND REBUILDING HEALTHY LUNGS   |                      |                         |                                      | 5a. CONTRACT NUMBER                                  |   |
|   |                      |                         |                                      | 5b. GRANT NUMBER<br>W81XWH-08-1-0148                 |   |
|   |                      |                         |                                      | 5c. PROGRAM ELEMENT NUMBER                           |   |
| 6. AUTHOR(S)<br>Alan Fine, MD<br><br>email: afine@bu.edu  |                      |                         |                                      | 5d. PROJECT NUMBER                                   |   |
|   |                      |                         |                                      | 5e. TASK NUMBER                                      |   |
|   |                      |                         |                                      | 5f. WORK UNIT NUMBER                                 |   |
| 7. PERFORMING ORGANIZATION NAME(S) AND ADDRESS(ES)<br><br>Boston University Medical Center<br>715 Albany Street, R-304<br>Boston, MA 02118  |                      |                         |                                      | 8. PERFORMING ORGANIZATION REPORT NUMBER             |   |
| 9. SPONSORING / MONITORING AGENCY NAME(S) AND ADDRESS(ES)<br><br>US ARMY MEDICAL RESEARCH AND MATERIEL COMMAND<br>504 SCOTT STREET<br>FORT DETRICK, MD 21702-5012   |                      |                         |                                      | 10. SPONSOR/MONITOR'S ACRONYM(S)                     |   |
|   |                      |                         |                                      | 11. SPONSOR/MONITOR'S REPORT NUMBER(S)               |   |
| 12. DISTRIBUTION / AVAILABILITY STATEMENT<br>Approved for public release; distribution unlimited  |                      |                         |                                      |  |   |
| 13. SUPPLEMENTARY NOTES   |                      |                         |                                      |  |   |
| 14. ABSTRACT<br><br>The focus of our original proposal was to identify new strategies for treating acute lung injury (ALI. This is a complex condition associated with diffuse injury to the distal alveolar epithelial gas exchange surface, resulting in marked impairment in the ability of the lung to oxygenate the blood. While there are many causes of ALI, this condition commonly occurs in cancer patients due to the immunosuppressive and toxic effects of chemotherapy and the debilitating effects of cancer. In this grant, we proposed to develop ventilatory and cell based strategies to treat the ALI syndromes. Project 1 focused on developing a novel mode of ventilation (variable ventilation; VV) that is less injurious to the already damaged lung. Using an in vitro system, we determined parameters of how this ventilator strategy works and how it can be optimized. We obtained an IND from the FDA to initiate a first in human pilot study on VV in patients with ALI, which is now ongoing. Project 2 was focused on identifying what stem cell populations to repair the injured alveolar epithelial surface. During the course of this grant, we made considerable progress in understanding the biology of lung stem cells, how they can be generated, and have begun studies to determine which cell type may be most efficacious in lung repair. Overall, we have been able to meet the basic objectives of our initial application, developed new knowledge in this important area, and will use what we have learned for further investigation. . |                      |                         |                                      |  |   |
| 15. SUBJECT TERMS<br>Lung injury, cancer, ventilator, stem cells  |                      |                         |                                      |  |   |
| 16. SECURITY CLASSIFICATION OF:<br>unclassified   |                      |                         | 17. LIMITATION OF ABSTRACT<br><br>UU | 18. NUMBER OF PAGES<br><br>84                        | 19a. NAME OF RESPONSIBLE PERSON USAMRMC   |
| a. REPORT<br><br>U  | b. ABSTRACT<br><br>U | c. THIS PAGE<br><br>U   |                                      |  | 19b. TELEPHONE NUMBER (include area code) |

# Table of Contents

|                                    | Page                |
|------------------------------------|---------------------|
| COVER PAGE.....                    | 1                   |
| SF298.....                         | 2                   |
| TABLE OF CONTENTS.....             | 3                   |
| INTRODUCTION.....                  | 4                   |
| BODY.....                          | -5                  |
| KEY RESEARCH ACCOMPLISHMENTS ..... | 13                  |
| REPORTABLE OUTCOMES.....           | 14                  |
| CONCLUSION.....                    | 15                  |
| BIBLIOGRAPHY OF PUBLICATIONS.....  | 16                  |
| LIST OF SUPPORTED PERSONNEL.....   | 17                  |
| APPENDIX.....                      | Publications (PDFs) |

## Introduction

The over-riding goal of our original application was to develop new treatments for patients with acute lung injury syndromes (ALI). ALI is the end-result of a variety of clinical scenarios. These include: severe infections, inhaled toxins, severe trauma, multiple blood transfusions, and long bone fractures. Notably, many of these conditions afflict military personnel. In addition, patients suffering from cancer are prone to developing ALI as a result of the immunosuppressive effects of chemotherapy. While poorly understood, it is also the case that certain chemotherapeutic agents, themselves, cause a syndrome with features of ALI. The pathology and pathophysiology of ALI are very complex and include features of acute inflammation, distortion of lung cellular integrity, marked derangements in lung compliance, and significant impairment of gas exchange. Type I cells, which comprise the vast majority of the gas exchange surface are particularly susceptible to injury.

To meet our goal, we originally planned 2 Projects. In Project 1, we proposed to build upon findings from animal and *in silico* studies to determine whether we can develop a better method for mechanical ventilation of patients with ALI. This objective relates to the fact that conventional methods of ventilation, *themselves*, worsen underlying ALI by causing further damage to lung epithelial cells and also by amplifying inflammation. Specifically, we proposed to evaluate *variable ventilation* in patients with ALI relative to conventional ventilation. This project used computational models to discern how VV worked and how it could be optimized. The second element of this Project was a pilot study in humans with ALI, examining whether VV diminished expression of inflammatory surrogates and improved lung physiology. In Project 2, our goal was to develop a cell based therapy to repair the damaged alveolar gas exchange surface. A prominent feature of this Project was to clarify what are the most appropriate and scalable cell populations that can be used to treat and replace injured alveolar epithelium. Notably, we have made considerable progress in this effort. In this report, I will discuss the progress and achievements for both of these 2 Projects.



## Body of Final Report

Below is a summary of what has been achieved for the 2 Projects that comprised the original parent proposal.

### Project 1: We will determine if variable ventilation is a more effective mode of ventilation in patients with ALI.

As previously detailed, we initially had some unforeseen barriers for the initiation of the clinical study comparing variable ventilation to conventional ventilation in patients with acute lung injury. These delays included completing a legal agreement with the ventilator manufacturer (Covidien<sup>R</sup>), and in overcoming several distinct software programming issues. One vexing problem has been building a capacity to titrate inspiratory time and inspiratory flow ratio into our software control panel. A second issue has been securing approval of an IDE from the FDA for this work. All of these issues have been resolved and we are now in the midst of recruiting patients for the first in human study of VV in patients with ALI. The “Variable Ventilation in Acute Respiratory Failure” is a randomized crossover trial is currently enrolling mechanically ventilated participants. We have thus far enrolled 5/16 subjects. The Data Safety Monitoring Committee has evaluated each subject’s Case Report forms and has approved continuation of the trial. Notably, the Wallace Coulter Foundation continues to fund the trial on a no-cost extension, up to July 2014.

Part of this Project was also focused on using *in vitro* and *in silico* computational models to further establish how VV works and what effect it has on the lung. To do this, a computational model of stretch induced surfactant release in the setting of mechanical ventilation was established. This work was published with data shown below (4).

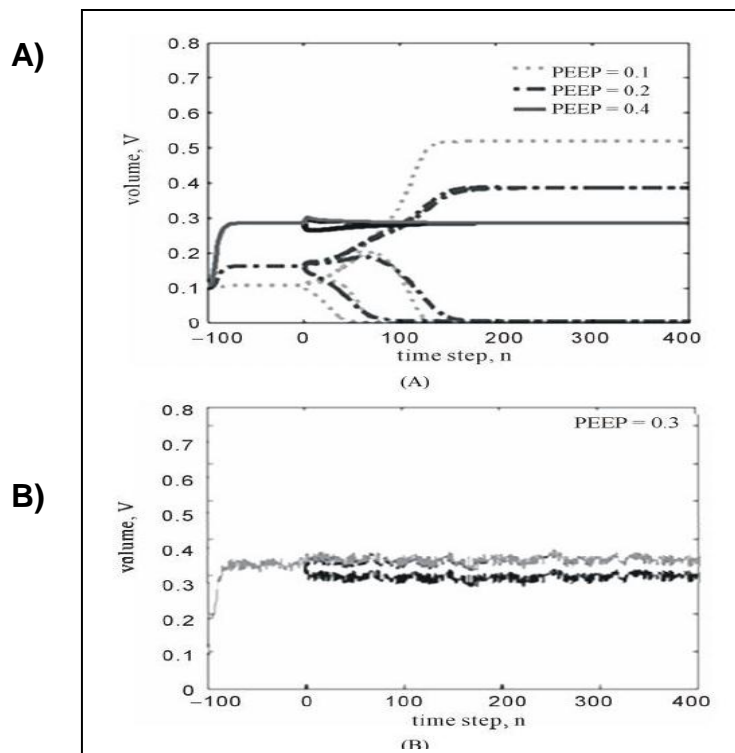


**Fig. 1:** Four unit simulations. (A) End-inspiratory volumes VEI stabilized by the application of PEEP during Conventional Ventilation. Dotted, dashed-dotted and solid lines correspond to PEEP = 0.1, 0.2 and 0.4, respectively. The four curves with each line type correspond to the four compartments. (B) Variable ventilation results in the lung reaching steady equilibrium, reducing the extent of alveolar collapse as compared to conventional ventilation. For clarity, here only the traces of the 4 units corresponding to PEEP = 0.3 are shown where all four units remain open. Notice that 3 units follow essentially the same pattern while the fourth is kept open at a slightly lower VEI. This is the same unit that collapsed during CV at PEEP < 0.4.

Figure 1 demonstrates one of the key findings of this study. We found that PEEP can increase long-term alveolar recruitment and at the same time delay collapse of unrecoverable alveolar units. In combination with VV, however, this delay can be made much longer as injured units appear to remain at non-equilibrium, fluctuating volumes. Second, during ventilation in the presence of heterogeneous surfactant release or tissue stiffness, we find that VV can maintain higher recruitment while avoiding over-distention for a wider range of PEEP and mean tidal volume (VT) values, partly through the mechanism described above.

Another important observation is shown in Figure 2. Herein we present the results for conventional ventilation (CV) with heterogeneous injury to surfactant release. On the left panel, we see alveolar collapse with  $PEEP < 0.5$  and  $VT < 0.5$ . The extent of collapse gradually decreases with increasing VT. On the other hand, there appears to be a distinct threshold around  $PEEP = 0.4$  where collapse is completely avoided regardless of VT. Over-distention defined as  $VEI = VEE + VT$  reaching 75% of maximum alveolar volume showed an opposing trend, where the highest VT which avoids over-distention decreases approximately linearly with increasing PEEP. Simultaneous collapse and over-distention can be observed at midrange values of PEEP and VT.

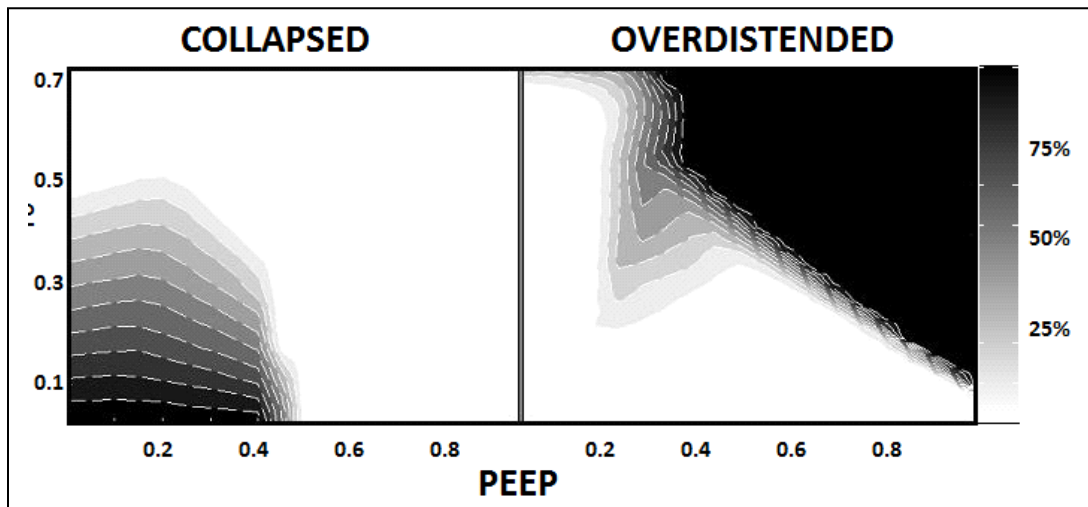


**Fig 2:** Alveolar collapse and over-distention in the presence of surfactant heterogeneity during conventional ventilation. Contour plots describe the fraction of the lung in the specified category when ventilating with a given PEEP and VT. Left: Fraction of collapsed alveoli reduces gradually with increasing VT and sharply with PEEP. Right: Fraction of over-distended alveoli increases with PEEP at high tidal volumes.

Additional simulations allowed us to compare and contrast the results for applying VV or CV for heterogeneous surfactant release as well as heterogeneous acinar stiffness (Figure 3). For a disruption of normal homogeneous surfactant release under CV (top left panel), alveolar collapse occurs at low-PEEP-low-VT settings, while over-distention occurs for high-PEEP-high-VT settings resulting in two relatively small disjoint regions (blue) whereby alveolar injury is prevented. When VV is applied (top right panel), one contiguous region of PEEP and VT allows for full recruitment without over-distention. Overall, the possible combinations of PEEP and VT during VV are much greater than

during CV. For the heterogeneous acinar stiffness case under CV (bottom left panel), again alveolar collapse occurs at low-PEEP-low- VT settings, while over-distention occurs for high-PEEP- high-VT settings. However, in this case a contiguous band of good PEEP-VT settings exist. When VV is applied (right panel), the size of this region is significantly larger.

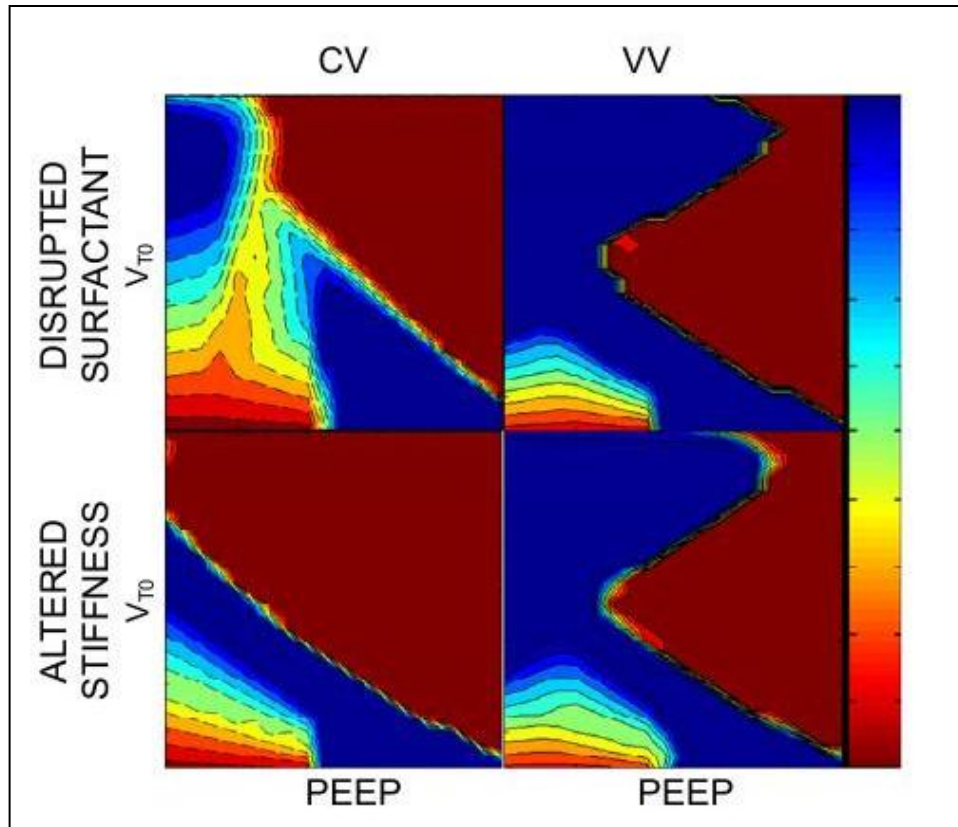


**Fig. 3:** Comparison of best PEEP-VT settings for CV vs. VV for two different pathologies. Contour plots describe the fraction of the lung which are neither collapsed nor over-distended when ventilating with a given PEEP and VT for CV and VV. For instance, the top left panel shows the superimposed view of Figure 3, presenting the PEEP and VT settings which resulted in the best outcomes (number of units recruited but not over-distended) in blue and injury due to collapse or over-distention marked by red. Top left: Heterogeneous surfactant release under CV. Top right: Heterogeneous surfactant release under VV. Bottom left: Heterogeneous alveolar stiffness under CV. Bottom right: Heterogeneous alveolar stiffness under VV.

Methods and findings are detailed in the publication. Despite technical limitations, the novel features of the model allowed us to explore patient-ventilator coupling and optimization of best PEEP-VT combination in the presence of collapse and over-distention injury. The main result was that the coupling between surfactant secretion and regional lung mechanics during ventilation has a significant impact on the outcome of patient ventilation. While this was possible only using an appropriate computational model due to the difficulties associated with the breath-by-breath experimental

assessment of surfactant pool and regional lung mechanics, the long-term predictions of the model could be tested in clinical settings...This work showed that VV can be modulated to minimize stretch injury to the ventilated lung. This important observation validates, in part, the notion that VV ventilator mode is better than conventional modes of ventilation for patients with ALI.

**Project 2: We will establish a pre-clinical program conducted in laboratory mice with the objective of developing cell-based treatments for ALI.**

The long-term goal of this project was to develop a cell-based therapy that can replace and reconstitute the injured lung epithelium. It would be preferable that such a therapy employ autologous cells so as to obviate immune issues that might arise during administration of exogenous therapeutic cells. As discussed previously, we developed a mouse that has a knockin GFP into the Nkx2-1 locus (3). We generated this mouse so that we could obtain Nkx2-1-expressing candidate lung/thyroid progenitors. This was done by inserting a GFP reporter gene to the Nkx2-1 locus using homologous recombination (Figure 5). In Nkx2-1GFP mice generated from this cell line, the GFP reporter was expressed in the developing forebrain, lung, and thyroid in the expected distribution of endogenous Nkx2-1 mRNA and protein (Figure 5). The importance of this tool is the fact that this gene is essential for lung epithelial stem cell function. By having a fluorescent marker to track, we can isolate and identify lung stem cells. It also affords us the capacity to assess whether cells assume a lung stem cell fate. Thus, this very labor intensive effort opened up a variety of possibilities for the objectives set forth in this Project.

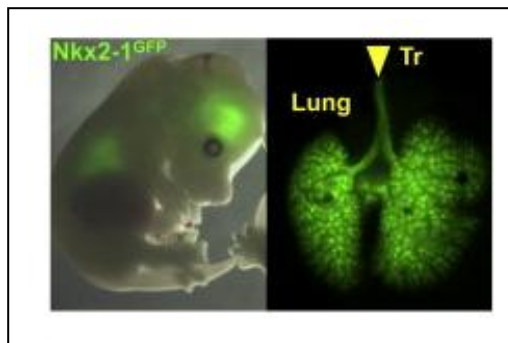


**Fig. 5:** Nkx2-1GFP knockin mouse embryo and lung whole mount (both at E14.5) with GFP fluorescence visible in the forebrain, thyroid, and lung (thyroid in Figure S2). In the lung and trachea, fluorescence appears in an epithelial pattern (Tr; arrowhead).

We generated embryonic stem cells from this mouse and used expression of GFP to assess conditions that lead to derivation of Nkx2-1+ lung progenitor cells (Figure 6). As shown in figure 6, these GFP+ progenitors under specialized conditions express markers of the distal differentiated lung epithelium (pro-SPC). Since structure and function are inextricably linked features of lung alveolar epithelial cells, we also assessed the capacity of sorted day 15 Nkx2-1GFP+ progenitors to regenerate 3D alveolar lung structure (Figures 4C–4H). To examine this, sorted day 15 Nkx2-1GFP+ ESC-derived cells, delivered by intra-tracheal instillation into decellularized murine lungs, were able to seed alveolar lung regions and adopt the morphology of lung alveolar epithelia (Figures 4C–4H). In explant cultures of lung tissue reseeded with GFP+ cells on day 15 and cultured for 10 more days, 71% ± 12% (average ± SD) of engrafted cells maintained GFP fluorescence and continued to express nuclear Nkx2-1 protein (Figure 4E). Some engrafted cells acquired a flattened morphology and lost expression of Nkx2-1 protein, a pattern reminiscent of developing AEC1 cells in vivo. Consistent with this pattern, the majority of these flattened cells expressed the AEC1 marker protein T1α (Figures 4F and 4G), but lacked expression of Nkx2-1. In contrast, day 0 undifferentiated cells did not form alveolar structures after intra-tracheal instillation, but rather gave rise to masses of cells in the distal lung (Figure 4D) with only very rare cells (<0.1%) expressing either Nkx2-1 or T1α proteins



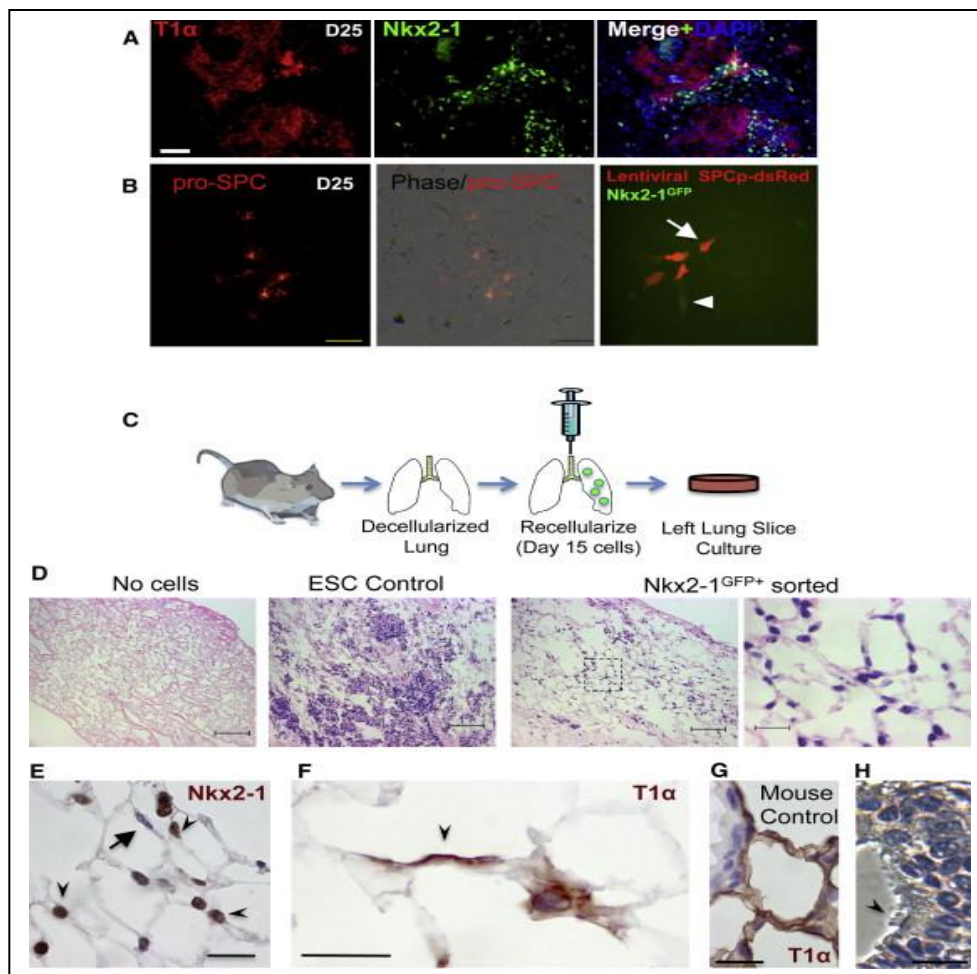


**Fig 6:** Alveolar Differentiation Repertoire of ESC-Derived Nkx2-1+ Lung Progenitors (A and B) Immunostaining for alveolar epithelial markers T1 $\alpha$ , pro-SPC, and Nkx2-1 on cells at the completion of the 25 day directed differentiation protocol. ESCs sorted on day 15 based on Nkx2-1GFP+ expression subsequently gave rise to (A) cells reminiscent of type 1 alveolar epithelial cells (AEC1) as they lost Nkx2-1 nuclear protein expression (green immunostain) while expressing T1 $\alpha$  protein. (B) Other patches of cells appeared more reminiscent of distal SPC+ alveolar epithelial cells as they expressed punctate cytoplasmic pro-SPC protein and displayed SPC promoter activation while retaining Nkx2-1GFP expression. Arrow = SPC-dsRed and Nkx2-1GFP coexpressing cell (orange). Arrowhead = cell expressing only Nkx2-1GFP. (C) Schematic summarizing the decellularization-recellularization assay. (D) H&E stains of lung sections showing lung scaffold appearance with no recellularization (left panel) versus hypercellular sheets following reseeding with undifferentiated ESCs (middle panel) versus cells of alveolar structural morphologies after seeding with Nkx2-1GFP+ purified ESC-derived progenitors (right panel). Scale bars = 100  $\mu$ m in three left panels. Zoom of the indicated boxed region is shown in far right panel with scale bar = 20  $\mu$ m. (E and F) Nkx2-1+ nuclear protein (brown; arrowheads in E) immunostaining of engrafted cuboidal epithelial cells in the corners of alveoli, derived 10 days after reseeding with Nkx2-1GFP+ sorted cells. Arrow = flattened nucleus of an Nkx2-1 negative cell (purple) lining the alveolar septum. Many of these flattened cells were T1 $\alpha$ + (F; arrowhead). Scale bars = 20  $\mu$ m. (G) Control mouse lung without decellularization showing T1 $\alpha$  apical membrane staining pattern (brown) of mature AEC1. (H) Ciliated airway epithelial cell (arrow) 10 days after reseeding with differentiated/unsorted ESC-derived cells. Scale bar = 20  $\mu$ m. All nuclei were counterstained with hematoxylin (purple).

**Table 1**

Top differentially expressed transcripts in iPS cells  
versus ES cells with  $\pm 4$  fold change

| FC<br>(iPS/ES cells) <sup>A</sup> | Transcript                  | mRNA accession | P value <sup>B</sup>   |
|-----------------------------------|-----------------------------|----------------|------------------------|
| -4.1                              | <i>Rian</i> <sup>C</sup>    | AF357355       | $2.74 \times 10^{-12}$ |
| -3.3                              | <i>Mir380</i> <sup>C</sup>  | mmu-mir-380    | $7.22 \times 10^{-6}$  |
| -2.9                              | <i>Mir410</i> <sup>C</sup>  | mmu-mir-410    | $9.67 \times 10^{-7}$  |
| -2.9                              | <i>Mir382</i> <sup>C</sup>  | mmu-mir-382    | $9.67 \times 10^{-7}$  |
| -2.8                              | <i>Mir300</i> <sup>C</sup>  | mmu-mir-300    | $5.84 \times 10^{-7}$  |
| -2.7                              | <i>Mir377</i> <sup>C</sup>  | mmu-mir-377    | $2.80 \times 10^{-5}$  |
| -2.7                              | <i>Gtl2</i> <sup>C</sup>    | NR_003633      | $1.45 \times 10^{-5}$  |
| -2.6                              | <i>Mir329</i> <sup>C</sup>  | mmu-mir-329    | $4.45 \times 10^{-7}$  |
| -2.3                              | <i>Mir381</i> <sup>C</sup>  | mmu-mir-381    | 0.00057                |
| -2.2                              | <i>Mir539</i> <sup>C</sup>  | mmu-mir-539    | 0.00032                |
| -2.2                              | <i>Mir487b</i> <sup>C</sup> | mmu-mir-487b   | $4.31 \times 10^{-5}$  |
| -2.1                              | <i>Mir411</i> <sup>C</sup>  | mmu-mir-411    | 0.001                  |
| 6.6                               | <i>Nr1h5</i>                | NM_198658      | $2.09 \times 10^{-8}$  |

Top fold change (FC) values ( $\log_2$  transformed) for iPS cells versus ES cells (subset of FDR < 0.001) are shown. <sup>A</sup>Fold change values shown are  $\log_2$  transformed and ranked in ascending order by fold change.

<sup>B</sup>Two-way ANOVA, FDR-adjusted *P* value for cell-type effect.

<sup>C</sup>Members of *Dlk1-Dio3* gene cluster.

These exciting findings provide a general strategy for treating ALI with Nkx-2-1 derived cells. This work resulted in a high profile publication (3) that is provided in the appendix. Results and important new methodologies are contained therein.

In order to begin to evaluate the optimal source of Nkx-2.1+ lung progenitors, we examined comparative gene expression profiles on mouse embryonic vs. mouse induced-pluripotent cells (iPS cells). To evaluate potential differences in the gene expression programs of ES cells versus iPS cells, we first compared cells in both the differentiated and undifferentiated states. We found that 111 transcripts (including mRNA, microRNA [miRNA], and small nucleolar RNA) were differentially expressed across the 3 cell lines regardless of differentiation state (data not shown). Clustering analysis illustrated that the majority of these transcripts distinguished the 2 iPS cell clones from their parental ES cells. Remarkably, we found 36 of these differentially expressed transcripts were encoded by the *Dlk1-Dio3*—imprinted gene cluster on mouse chromosome 12qF1 (Table 1). For example, 2 of the top 3 most differentially expressed genes between iPS and ES cells were maternally expressed 3 (*Gtl2*, also known as *Meg3*) and maternally expressed 8 (*Rian*, also known as *Meg8* or *Irm*), which appeared to have low to undetectable expression levels in both ST5 and ST8 cell lines compared with those in ES cells (qRT-PCR; Figure 6C). Both these genes are noncoding RNA members of the *Dlk1-Dio3*—imprinted cluster that are typically monoallelically expressed from only the maternally inherited allele along with 5 other noncoding RNAs. Of 11 remaining transcripts that distinguished iPS cells from ES cells

with more than 4-fold differential expression (Table 1), 10 were miRNAs encoded by the Dlk1-Dio3 gene cluster, and all 10 appeared to be silenced in both iPS cell clones. Overall, 63 members of this gene cluster had known probe IDs on our microarray platform, and 36 of these were differentially expressed between ES and iPS cell lines with FDR < 0.001 (Fisher's exact test for enrichment,  $P = 1.5 \times 10^{-63}$ ). These results suggested aberrant silencing of many maternally expressed members of this imprinted gene cluster in both iPS cell lines in both differentiation state profiles of embryonic and epigenetic properties of 2 potential lung progenitor cell populations. Whether these interesting differences may affect the ability to derive lung progenitors is a focus of our current work. This paper is in the appendix where results and pertinent methodologies are described.

We also published several papers (see appendix) on a critical and related topic related to the origin and regulation of lung stem cells in the developing lung (2, 5). Data derived from this work provide an important foundation for understanding the basic biology of lung stem cells, and in turn how they can be modulated for repair. Most interestingly, we found that the overlying lung mesothelium is a source of mesenchymal progenitor cells that give rise to bronchial and vascular smooth muscle, fibroblastic cells in the developing lung. To do this we took advantage of the selective expression of the transcription factor WT1 and thus used a tamoxifen (TAM) inducible Cre-dependent lineage tracing system that tracks the fate of mesothelial cells that are labeled with TmRed (red fluorescent protein).

Specifically, we performed detailed lineage analysis of the early fetal lung mesothelium using Wt1CreERT2/+;Rosa(tmRed) mice. TAM was administered at E10.5 and E11.5 and lungs were harvested at E18.5 and at several postnatal time points (P7, P14 and P21). At all times examined, tmRed+ cells that co-express  $\alpha$ -SMA were found circumferentially positioned around airways, indicative of a bronchial smooth muscle (BSM) fate (Figures. 7A-D). These cells comprised a distinct subset of the total BSM compartment. Among five different lungs analyzed, 14% to 60% of airways contained at least one or multiple tmRed+ BSM cells. Administration of TAM at the time of lung bud formation (E9.5 and E10.5) revealed a similar pattern of tmRed+ cell infiltration and of tmRed+ BSM mesothelial-derived cells at E18.5. In the postnatal lung only, we observed tmRed+ cells that co-express  $\alpha$ -SMA in the walls of pulmonary arteries and veins, indicative of a vascular smooth muscle (VSM) fate (Figures. 7E-G). We also found tmRed+ peri-bronchiolar cells with a fibroblastic morphology that were  $\alpha$ -SMA- and desmin+ (Figure 7H), indicating a fibroblast cell fate. How mesothelial derived cells can be harnessed and regulated in ALI is a focus of our current work.

Overall, our findings/publications represent a major advance for the field. This work met our basic objectives and has provided a substantial foundation for further work on this important topic.

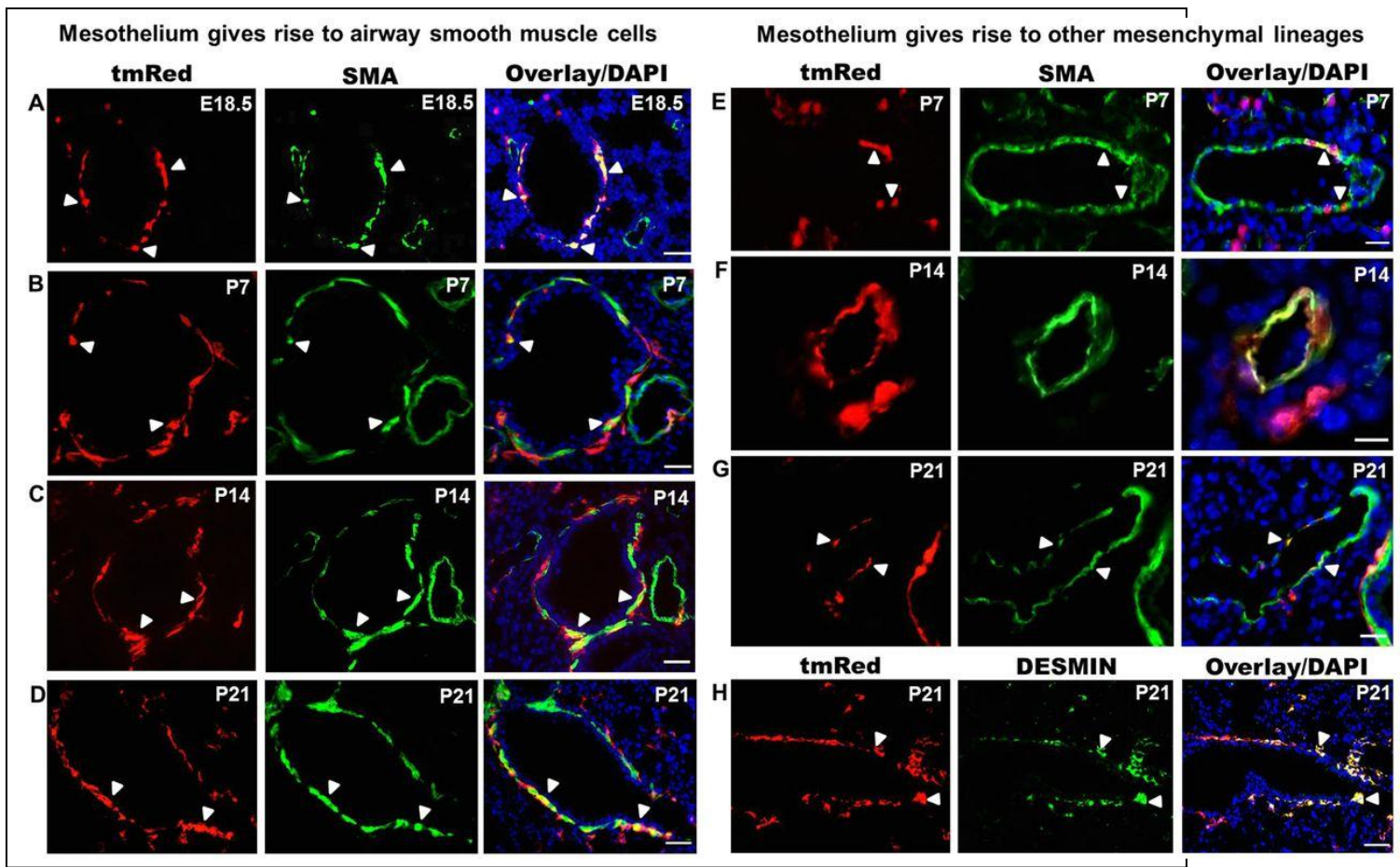


**Fig. 7:** Lineage tracing of fetal lung mesothelium using Wt1CreERT2/+;Rosa(tmRed) mice. TAM was given at E10.5 and E11.5 and the lungs examined at E18.5, P7, P14 and P21 for tmRed+ cells that co-express  $\alpha$ -SMA or desmin. (A-D) Colocalization of tmRed and  $\alpha$ -SMA in a subset of bronchial smooth muscle cells (arrowheads) from E18.5 to P21. Vascular smooth muscle cells were not labeled with tmRed at E18.5. (E-G) Colocalization of tmRed and  $\alpha$ -SMA in postnatal vascular (E,F) and venous (G) smooth muscle cells (arrowheads). (H) Colocalization of tmRed and desmin in fibroblast cells around the airway at P21 (arrowheads). Nuclei were counterstained with DAPI (blue). Scale bars: 50  $\mu$ m.



## **Key Research Accomplishments**

- Developed software for VV administration in humans.
- Successfully modeled VV in computational system and its effects on surfactant secretion. This was published.
- Secured approval of the FDA IDE application (enclosed)
- Initiated Phase I variable ventilation study in humans with ALI.
- Developed protocols with clinical and research staff to improve compliance with the control and research arms of the study.
- Obtained a supplemental grant from the Coulter foundation to support the clinical study
- Successfully developed protocols to obtain alveolar epithelial cells from mouse ESC cells and published this work
- Developed in vitro engraftment model for alveolar epithelial progenitors using decellularized rodent lung and published this work
- Published work on basic biology of lung progenitor cell populations.

\*Note all 5 papers enclosed

### **Reportable Outcomes**

- 1) Multiple publications from Projects 1 and 2
- 2) Approval of IND to initiate clinical project
- 3) Development of training protocols for clinical project.
- 4) Initiation and ongoing Phase I clinical study of VV in humans with ALI.

## **Conclusion**

We made considerable progress in both Projects of the original parent grant. Most notably, by using data generated from this grants, we were able to secure Coulter Foundation funding for our Phase I trial. This is a randomized crossover trial that is currently enrolling mechanically ventilated participants. We have thus far enrolled 5/16 subjects. The Data Safety Monitoring Committee has evaluated each subject's case report forms and has approved continuation of the trial for this year.

In Project 2, we established conditions that promote differentiation of embryonic stem cells to lung epithelium and demonstrated that these cells can reconstitute the distal epithelium in decellularized lung preparations. This is a notable achievement for the field. We have also made significant contributions in understanding the basic biology of lung stem cells. Together these data, provide a powerful foundation for future work in this important area

## Bibliography of Publications

- 1) Christodoulou C, Longmire TA, Shen SS, Bourdon A, Sommer CA, Gadue P, Spira, A, Gouon-Evans V, Murphy GJ, Mostoslavsky G, and Kotton, D. Mouse ES and iPS cells can form similar definitive endoderm despite differences in imprinted genes. *Journal of Clinical Investigation* 121:2313–2325, 2011.
- 2) Ghosh, S, Paez-Cortez, JR, Bopppidi K, Vasconelos M, Roy M, Cardoso W, Ai X, and Fine A. Activation Dynamics and Signaling Properties of Notch3 Receptor in the Developing Pulmonary Artery. *Journal of Biological Chemistry* 286:22678-22687, 2011.
- 3) Longmire TA, Laertis I, Hawkins F, Christodoulou C, Cao Y. Jeam JC, Mou H, Rajagopal J, Shen SS, Downton AA, Serra M, Weiss DJ, Green MD, Snoeck, HW, and Kotton D. Efficient Derivation of Purified Lung and Thyroid Progenitors from Embryonic Stem Cells. *Cell Stem Cell* 10:396-411, 2012.
- 4) Amin SD, Majumdar A, Alana P, Walkey AJ, O'Connor GT, and Suki B. Modeling the Effects of Stretch-Dependent surfactant Secretion on Lung Recruitment during Variable Ventilation. *Journal of Biomedical Science and Engineering* 6: 61-70, 2013.
- 5) Dixit R, Ai X, and Fine A. Derivation Lung Mesenchymal Lineages from the Fetal Mesothelium Requires Hedgehog Signaling for Mesothelial Cell Entry. *Development* 140:4398-4405.

## **List of supported Personnel**

- 1)** Anneliese Arno, BS
- 2)** Shamik Ghosh, PhD
- 3)** Bela Suki, PhD
- 4)** Alan Fine, MD
- 5)** Arnab Majumdar, PhD
- 6)** George O'Connor, MD
- 7)** Darrell Kotton, MD
- 8)** Christopher Ford, BS
- 9)** Laertis Oikonomou, PhD
- 10)** Konstantina Christodoulou, PhD

## Appendix (PDFs of pertinent publications)



cell stem cell.pdf



Development-2013-D  
ixit-4398-406.pdf



jci.pdf



Notch 3 and vascular  
stem cells1.pdf



Samir W  
modeling.pdf



## DEPARTMENT OF HEALTH &amp; HUMAN SERVICES

Public Health Service

MAR 15 2012

Food and Drug Administration  
10903 New Hampshire Avenue  
Document Control Room - WO66-G609  
Silver Spring, MD 20993-0002

Boston University School of Medicine  
George T. O'Connor, M.D., M.S.  
Professor of Medicine  
715 Albany St., Room R304  
Boston, MA 02118

Re: G110202

Variable Ventilation Using the Covidien Puritan-Bennett 840 Ventilator

Dated: February 13, 2012

Received: February 15, 2012

CMS Reimbursement Category: A1 (for procedures to request re-evaluation of  
the categorization decision, please see the  
appropriate enclosure)

Annual Report Due: One Year from the Date of This Letter.

Dear Dr. O'Connor:

The Food and Drug Administration (FDA) has reviewed your investigational device exemptions (IDE) application to conduct a feasibility study for a significant risk device. A feasibility study is a preliminary study which is not expected to provide the primary support for the safety and effectiveness evaluation of a medical device for the purposes of a marketing application. Your application to conduct a feasibility clinical investigation is approved, and you may begin your investigation at Boston Medical Center, Boston, Massachusetts you have obtained institutional review board (IRB) approval and submitted certification of IRB approval to FDA. Your investigation is limited to 2 institutions and 16 subjects.

We would like to point out that FDA approval of your IDE application to conduct a clinical investigation does not imply that this investigation will provide reasonable assurance of the safety and effectiveness of your device or assure a determination of clearance/ approval for your premarket submission.

You should also give serious consideration to the following item which is considered essential for the analysis of your data for the purposes of clearance/approval of a premarket submission:

Page 2 – Dr. O'Connor

Use of corticosteroids will diminish the inflammatory response, therefore decreasing biomarker levels. Steroid use will therefore mask biomarker levels associated with tissue injury / infection, to an extent that is unknown. If enrollment includes patients on corticosteroids, then please remove biomarkers as secondary outcome. Otherwise, if biomarkers are included, subject selection should be refined to patients not administered steroid therapy. Furthermore, please stratify patient data according to corticosteroids use.

FDA encourages sponsors to collect clinical trial data in accordance with the Guidance for Industry: Collection of Race and Ethnicity Data in Clinical Trials (<http://www.fda.gov/downloads/RegulatoryInformation/Guidances/UCM126396.pdf>) and to enroll patients that would reflect the demographics of the affected population with regard to age, sex, race and ethnicity. Reference is made to 21 CFR 812.25(c) regarding description of patient population and to 21 CFR 814.15(d)(1) with regard to the need for data, including foreign data, to be applicable to the U.S. population and U.S. medical practice. We recommend that you include a background discussion of prevalence, diagnosis and treatment patterns for the type of disease for which your device is intended. This should include sex- and race-specific prevalence, identification of proportions of women and minorities included in past trials for the target indication, and a discussion of your plan to address any factors identified or suggested, which may explain potential for under-representation of women and minorities, if applicable. We recommend that you include a summary of this information in your protocol and investigator training materials. Consideration should be given to enrollment of investigational sites where recruitment of needed populations for study can be more easily facilitated.

Future correspondence concerning this application should be identified as an IDE supplement referencing the IDE number above, and must be submitted in triplicate to:

U.S. Food and Drug Administration  
Center for Devices and Radiological Health  
IDE Document Mail Center – WO66-G609  
10903 New Hampshire Avenue  
Silver Spring, MD 20993-0002

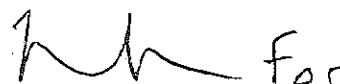
Information to help you understand the function and duties of a sponsor, titled, "Sponsor's Responsibilities for a Significant Risk Device Investigation," is available at: <http://www.fda.gov/MedicalDevices/DeviceRegulationandGuidance/HowtoMarketYourDevice/InvestigationalDeviceExemptionIDE/ucm049859.htm>. Additionally, information which you should provide to participating investigators, titled, "Investigators' Responsibilities for a Significant Risk Device Investigation," is available at: <http://www.fda.gov/MedicalDevices/DeviceRegulationandGuidance/HowtoMarketYourDevice/InvestigationalDeviceExemptionIDE/ucm049864.htm>.



Page 3 – Dr. O'Connor

If you have any questions, please contact Mr. Chan Lee at (301) 796-6267.

Sincerely yours,

A handwritten signature in black ink, appearing to read "Anthony D. Watson".

Anthony D. Watson, B.S., M.S., M.B.A.  
Director

Division of Anesthesiology, General Hospital,  
Infection Control and Dental Devices  
Office of Device Evaluation  
Center for Devices and  
Radiological Health



## FAX COVER SHEET

Voice Phone Number: 301-796-6598

U.S. Food and Drug Administration  
Center for Devices and Radiological Health  
IDE Document Mail Center – WO66-G609  
10903 New Hampshire Avenue  
Silver Spring, MD 20993-0002

TO: See addressee on next page  
FROM: IDE Document Control Center

Comments: Fax copy of the letter being mailed to you.

"This document is intended only for the use of the party to whom it is addressed and may contain information that is privileged, confidential, and protected from disclosure under applicable law. If you are not the addressee, or a person authorized to deliver the document to the addressee, you are hereby notified that any review, disclosure, dissemination, copying or other action based on the content of this communication is not authorized. If you have received this document in error, please notify us by telephone and return it to us at the above address by mail. Thank you."

# Efficient Derivation of Purified Lung and Thyroid Progenitors from Embryonic Stem Cells

Tyler A. Longmire,<sup>1,4,11</sup> Laertis Ikonou,<sup>1,4,11</sup> Finn Hawkins,<sup>1,4</sup> Constantina Christodoulou,<sup>1,4</sup> Yuxia Cao,<sup>1,4</sup> J.C. Jean,<sup>1,4</sup> Letty W. Kwok,<sup>1,4</sup> Hongmei Mou,<sup>5</sup> Jayaraj Rajagopal,<sup>5</sup> Steven S. Shen,<sup>2,3,6,7,8</sup> Anne A. Dowton,<sup>1,4</sup> Maria Serra,<sup>1,4</sup> Daniel J. Weiss,<sup>9</sup> Michael D. Green,<sup>10</sup> Hans-Willem Snoeck,<sup>10</sup> Maria I. Ramirez,<sup>1,4</sup> and Darrell N. Kotton<sup>1,4,\*</sup>

<sup>1</sup>Boston University Pulmonary Center

<sup>2</sup>Section of Computational Biomedicine

<sup>3</sup>Department of Medicine

Boston University School of Medicine, Boston, MA 02118, USA

<sup>4</sup>Center for Regenerative Medicine (CRoM), Boston University and Boston Medical Center, Boston, MA 02118, USA

<sup>5</sup>Center for Regenerative Medicine, Massachusetts General Hospital, Boston, MA 02114, USA

<sup>6</sup>Center for Health Informatics and Bioinformatics

<sup>7</sup>Department of Biochemistry

<sup>8</sup>Department of Medicine

New York University School of Medicine, New York, NY 10016

<sup>9</sup>Vermont Lung Center, University of Vermont College of Medicine, Burlington, VT 05405, USA

<sup>10</sup>Mount Sinai School of Medicine, Department of Oncological Science, New York, NY 10029, USA

<sup>11</sup>These authors contributed equally to this work

\*Correspondence: [dkotton@bu.edu](mailto:dkotton@bu.edu)

DOI 10.1016/j.stem.2012.01.019

## SUMMARY

Two populations of Nkx2-1<sup>+</sup> progenitors in the developing foregut endoderm give rise to the entire postnatal lung and thyroid epithelium, but little is known about these cells because they are difficult to isolate in a pure form. We demonstrate here the purification and directed differentiation of primordial lung and thyroid progenitors derived from mouse embryonic stem cells (ESCs). Inhibition of TGF $\beta$  and BMP signaling, followed by combinatorial stimulation of BMP and FGF signaling, can specify these cells efficiently from definitive endodermal precursors. When derived using Nkx2-1<sup>GFP</sup> knockin reporter ESCs, these progenitors can be purified for expansion in culture and have a transcriptome that overlaps with developing lung epithelium. Upon induction, they can express a broad repertoire of markers indicative of lung and thyroid lineages and can recellularize a 3D lung tissue scaffold. Thus, we have derived a pure population of progenitors able to recapitulate the developmental milestones of lung/thyroid development.

## INTRODUCTION

Early in embryonic development definitive endoderm progenitor cells of the developing foregut are specified into organ domains, such as the primordial thyroid, lung, liver, and pancreas fields (Cardoso and Kotton, 2008; Serls et al., 2005). These primordial progenitors then give rise to all the differentiated epithelial progeny of each endodermally derived tissue. Hence, those

interested in purifying thyroid, lung, liver, or pancreatic stem or progenitor cells for disease therapies are increasingly focused on using the developing embryo as a roadmap to derive these progenitors in vitro through the directed differentiation of pluripotent embryonic stem cells (ESCs) whose phenotype resembles the early embryo (Gadue et al., 2005). Based on this developmental approach, definitive endoderm progenitors have been efficiently derived from mouse and human ESCs using Activin A (hereafter Activin) to induce embryonic Nodal/Activin signaling (D'Amour et al., 2005; Gouon-Evans et al., 2006; Kubo et al., 2004). The definitive endoderm cells derived in this manner have been presumed to be broadly multipotent; however, the most anterior foregut endodermal lineages, such as thymus, thyroid, and lung epithelia, have been difficult to derive from these progenitors (Green et al., 2011), in contrast to more posterior foregut or hindgut endodermal tissues, such as hepatic and intestinal lineages (Gouon-Evans et al., 2006; Spence et al., 2011).

Although specific markers or “knockin reporter cell lines” (such as Pdx1<sup>GFP</sup> mouse ESCs) have been employed to facilitate isolation of inefficiently specified foregut progenitors, such as those of pancreatic lineage (Micallef et al., 2005), no tools have been engineered that can allow the isolation of the most primordial murine lung and thyroid progenitors. Consequently, lung and thyroid epithelia remain among the least studied lineages derived from ESCs in vitro to date. In heterogeneous cultures of differentiating ESCs, induction of late markers of developing lung (Ali et al., 2002; Ameri et al., 2010; Coraux et al., 2005; Qin et al., 2005; Rippon et al., 2004, 2006; Roszell et al., 2009; Samadikuchaksaraei et al., 2006; Van Vranken et al., 2005; Wang et al., 2007; Winkler et al., 2008) and thyroid (Arufe et al., 2006, 2009; Jiang et al., 2010; Ma et al., 2009), such as surfactant protein C (SPC) and thyroglobulin, respectively, have been reported, but their expression appears to be stochastic, and the cells expressing these markers have been difficult to expand

further in culture. It is broadly accepted that prior to differentiation, all lung or thyroid epithelia must first progress through a primordial progenitor stage defined by the onset of expression of the homeodomain-containing transcription factor, Nkx2-1 (also known as thyroid transcription factor-1; Ttf1 or Ttf1). However, lack of specificity of this marker has made it difficult to utilize for ESC differentiation studies, a hurdle common to many ESC-based model systems where differentiated lineages of diverse germ layers must first proceed through a progenitor state expressing a transcription factor that lacks complete specificity for that lineage.

Despite its lack of specificity, Nkx2-1 is known to be a key transcriptional regulator of lung, thyroid, and forebrain development, as evidenced by Nkx2-1 knockout mice, which display abnormalities in forebrain development and lung/thyroid agenesis (Kimura et al., 1996; Minoo et al., 1999). In addition, humans born with Nkx2-1 gene mutations develop pediatric lung disease, hypothyroidism, and neurological impairment (Krude et al., 2002). Inability to access the presumed very rare, multipotent primordial lung and thyroid progenitors at their moment of specification within endoderm has resulted in a lack of information about their phenotype, genetic programs, or epigenetic mechanisms that control their differentiation. In turn this has limited any rational approach to try to developmentally derive their equivalents from ESCs in culture.

Here we present an Nkx2-1 knockin ESC line and reporter mouse that has allowed us to develop serum-free culture protocols for the step-wise derivation of pure populations of Nkx2-1 progenitors that exhibit the differentiation repertoire of Nkx2-1<sup>+</sup> lung/thyroid endodermal and neuroectodermal primordia known to be present in the developing embryo. We find that definitive endoderm derived from ESCs with Activin alone resists lung or thyroid lineage specification, and we propose that stage-specific inhibition of BMP and TGF $\beta$  signaling renders these endodermal progenitors competent to specify efficiently into Nkx2-1<sup>+</sup> endodermal lung or thyroid progenitors with little if any contamination of Nkx2-1<sup>+</sup> neuroectoderm. Following BMP/TGF $\beta$  inhibition, subsequent combinatorial induction of BMP and FGF signaling promotes initial lineage specification of endodermal Nkx2-1<sup>+</sup> lung and thyroid progenitors. These primordial progenitors can be sorted to purity and thereafter expanded and differentiated in culture. In contrast, prolonged exposure to BMP/TGF $\beta$  inhibitors results in highly efficient derivation in culture of Nkx2-1<sup>+</sup> neuroectodermal progeny that do not express any endodermal, lung, or thyroid markers, revealing precise control in culture over the germ layer lineage specification of cells expressing an otherwise nonspecific transcriptional regulator.

## RESULTS

### Inhibition of TGF $\beta$ and BMP Signaling Renders ESC-Derived Endoderm Competent to Specify into Nkx2-1<sup>+</sup> Progenitors

In order to optimize culture conditions for the derivation of Nkx2-1-expressing candidate lung/thyroid progenitors, we generated an Nkx2-1 reporter ESC line (hereafter Nkx2-1<sup>GFP</sup>) by targeting a GFP reporter gene to the Nkx2-1 locus using homologous recombination (Figures S1A and S1B). In Nkx2-1<sup>GFP</sup> mice generated from this cell line, the GFP reporter was expressed in the

developing forebrain, lung, and thyroid in the expected distribution of endogenous Nkx2-1 mRNA and protein (Figure 1 and Figure S1 available online).

To test faithfulness and specificity of the Nkx2-1<sup>GFP</sup> ESC reporter line in vitro, we first derived embryoid bodies (EBs) using published serum-free culture conditions supplemented with Activin (Christodoulou et al., 2011; Gouon-Evans et al., 2006; Kubo et al., 2004), resulting in >80% efficient definitive endoderm induction in 5 days but no detectable Nkx2-1 expression (Figure S2). To induce Nkx2-1 expression, we then exposed day 5 ESC-endoderm cells to either hepatic inducing conditions, which include low levels of FGF2 (Gouon-Evans et al., 2006), or high levels of FGF2 alone, based on previous reports suggesting that FGF2 secreted by adjacent mesoderm specifies lung epithelium from endoderm (Serls et al., 2005). In either condition, we observed inefficient induction of the GFP reporter in rare cells by day 12 (~0.1% and ~1% of cells, respectively; Figure S1G). Flow-cytometry-based cell sorting of GFP<sup>+</sup> cells distinguished the entirety of Nkx2-1 mRNA-expressing cells, analyzed by RT-PCR (Figure S1G). These results confirmed that the expression of GFP faithfully and specifically reports induction of the endogenous Nkx2-1 locus in this cell line; however, Nkx2-1 induction in Activin-exposed ESCs was inefficient. Moreover, this rare GFP<sup>+</sup> population was heterogeneous, expressing markers of neuroectoderm (Pax6 and Tuj1), very low levels of the endodermal marker Foxa2 and the early thyroid marker Pax8, and expressing little to no differentiated thyroid (thyroglobulin) or differentiated lung (SPC or CC10) markers. (Figure S3). FGF1 or Wnt3a, alternative factors previously reported to induce lung lineage within developing endoderm (Goss et al., 2009; Harris-Johnson et al., 2009; Serls et al., 2005), similarly failed to efficiently induce endodermal Nkx2-1<sup>+</sup> lineages from ESC-derived endodermal progenitors (Figure S3).

Given the capacity of ESC-derived endoderm to form hepatic lineages, but its apparently limited capacity to form Nkx2-1<sup>+</sup> endodermal lineages, we considered the possibility that day 5 ESC-endoderm cells might display significant anterior-posterior (AP) patterning toward endodermal domains other than lung or thyroid. Indeed, interrogation of our microarray database detailing the transcriptome of day 5 ESC-endoderm (Christodoulou et al., 2011) suggested upregulation of Hex and Foxa3 (Figure S4), markers that indicate AP patterning in the endodermal gut tube of embryos (Martinez Barbera et al., 2000; Monaghan et al., 1993). To explore this possibility further, we employed an ESC reporter line (Figures 1A and 1B) containing Foxa2-hCD4 and Foxa3-hCD25 knockin reporters (Gadue et al., 2009). ESC-derived endoderm coexpressed Foxa3 in approximately 40% of Foxa2<sup>+</sup> cells, indicating significant AP patterning of the cells in response to Activin (Figure 1B). By FACS analysis, these double positive cells appeared to arise within the Foxa2<sup>+</sup> population between days 4 and 5 of differentiation. This Foxa2<sup>+</sup>/Foxa3<sup>+</sup> population has previously been demonstrated to rapidly specify into hepatic lineages in the presence of BMP4 (Gadue et al., 2009).

Given the role of Activin and BMP4 in the patterning and specification of endodermal Foxa2<sup>+</sup>/Foxa3<sup>+</sup> cells (Gadue et al., 2009; Gouon-Evans et al., 2006), and based on reports that precise modulation of TGF $\beta$  and BMP signaling can optimize early germ layer patterning in vivo (Tiso et al., 2002) as well as

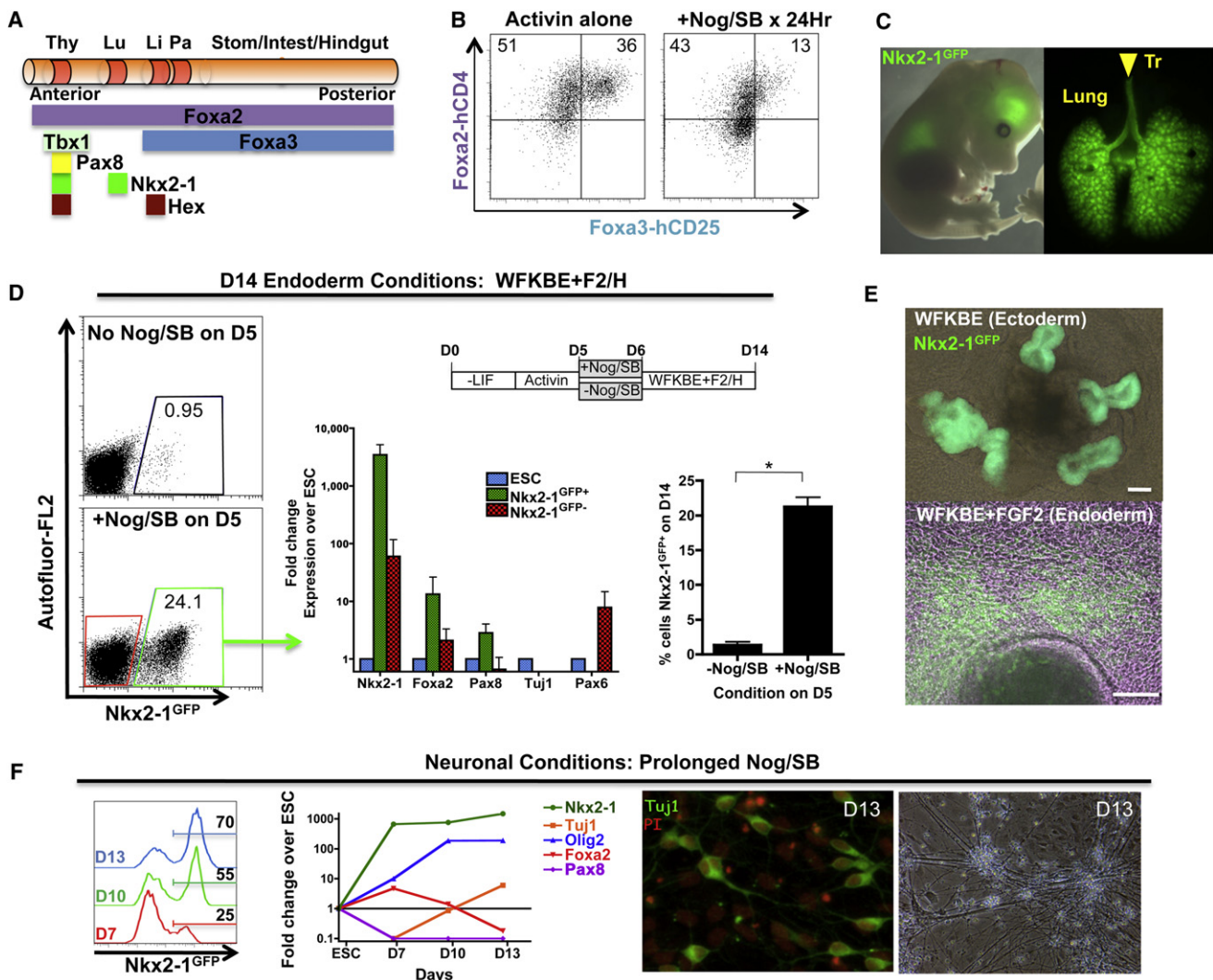


**Figure 1. Inhibition of BMP and TGF $\beta$  Signaling Alters Endodermal Patterning and Modulates Competence of ESCs to Differentiate into either Endodermal Nkx2-1<sup>+</sup> or Neuronal Nkx2-1<sup>+</sup> Cells**

(A) Schematic of AP patterning of the endodermal gut tube in the developing embryo (~E8.5–E9). Domains of expression of genes that demarcate prospective organ fields are shown.

(B) Kinetics of expression of knockin reporters, Foxa2-hCD4 and Foxa3-hCD25, indicating effect of Activin stimulation alone (left panel) compared to Activin followed by exposure to the BMP and TGF $\beta$  inhibitors Noggin and SB431542 (Nog/SB) for 24 hr.

(C) Nkx2-1<sup>GFP</sup> knockin mouse embryo and lung whole mount (both at E14.5) with GFP fluorescence visible in the forebrain, thyroid, and lung (thyroid in Figure S2). In the lung and trachea, fluorescence appears in an epithelial pattern (Tr; arrowhead).

(D) Effect of Nog/SB exposure on the competence of day 5 cells to specify to Nkx2-1<sup>+</sup> endoderm by day 14. Representative flow cytometry dot plots and summary bar graph indicate percentages of GFP<sup>+</sup> cells in each condition ( $n = 4$ ; average  $\pm$  SEM; \* $p < 0.001$ ). qRT-PCR analysis of indicated genes comparing day 14 sorted GFP<sup>+</sup> to GFP<sup>-</sup> cells (bars = average fold change in gene expression  $\pm$  SD).

(E) Effect of WFKBE with versus without FGF2 supplementation on GFP<sup>+</sup> cell morphology. GFP fluorescence and phase contrast overlay images are shown for D12 (presort) ESC-derived GFP<sup>+</sup> cells, which occur only rarely in the absence of FGF2 (top panel) and express neuroectodermal markers such as Pax6 (data not shown). In contrast, GFP<sup>+</sup> outgrowth cells in presence of FGF2 (lower panel) show a different morphology and are endodermal (see markers in D). Scale bar = 100  $\mu$ m.

(F) Prolonged Nog/SB exposure specifies Nkx2-1<sup>+</sup> neuronal cells by day 13, as indicated by flow cytometry and kinetics of induction of neuronal markers (Olig2 and Tuj1), loss of endodermal marker Foxa2, and loss of early thyroid marker Pax8.

See also Figures S1–S4.

in vitro in ESC-endodermal or ESC-mesodermal model systems (Green et al., 2011; Kattman et al., 2011), we tested stage-specific modulation of these pathways prior to Foxa3 induction in our system. Exposing day 4 or 5 cells to Noggin and

SB431542 (hereafter Nog/SB), inhibitors of BMP and Activin/TGF $\beta$  signaling, respectively, we were able to minimize Foxa3 induction while maintaining anterior endodermal markers, such as Sox2 and Tbx1 (Figure 1B and Figure S4).



Next we tested whether exposure to Nog/SB rendered ESC-derived endoderm more competent to specify into Nkx2-1<sup>+</sup> endodermal cells. Using the Nkx2-1<sup>GFP</sup> ESC line, we found that only cells exposed to 24 hr of Nog/SB were competent to induce endodermal Nkx2-1<sup>GFP</sup> in 21.3% ± 2.7% (average ± SD) of cells (Figure 1). To induce Nkx2-1 following Nog/SB treatment, we exposed the competent cells to high doses of FGF2 (500 ng/ml) combined with Wnt3a, FGF10, KGF, BMP4, EGF, and heparin; hereafter WFKBE+F2/H. We have previously reported that WFKBE possesses endodermal ventralizing capacity in human ESC-endoderm (Green et al., 2011). However, only when supplementing the WFKBE cocktail with FGF2 in mouse ESCs did we observe efficient derivation of Nkx2-1<sup>GFP+</sup> cells. The WFKBE+F2/H combination only induced efficient Nkx2-1<sup>GFP</sup> when ESC-endoderm cells were first exposed to TGFβ/BMP inhibition with Nog/SB (Figure 1D). The sorted GFP<sup>+</sup> cells derived with WFKBE+F2/H expressed an mRNA signature suggesting that they maintained an endodermal program (Foxa2<sup>+</sup>), included thyroid competent cells (evidenced by Pax8), and were depleted of neuroectodermal Nkx2-1<sup>+</sup> contaminants (evidenced by the absence of Pax6 and Tuj1). In contrast, when rare GFP<sup>+</sup> cell clusters were observed in the absence of FGF2, these clusters displayed a distinct morphology (Figure 1E), expressed Pax6 and Tuj1, and lacked any detectable expression of Pax8, suggesting that neuroectodermal rather than endodermal Nkx2-1<sup>GFP+</sup> cells were produced in the absence of FGF2 (data not shown).

#### Efficient Derivation of Neuroectodermal Nkx2-1<sup>+</sup> Cell Fate by Prolonged TGFβ/BMP Inhibition

We anticipated that the duration of TGFβ/BMP inhibition would need to be brief to prevent loss of ESC-endoderm to competing neuronal cells, based on recent publications indicating that neuroectodermal derivatives may be rapidly derived from human ESCs exposed to these inhibitors (Chambers et al., 2009; Smith et al., 2008). Indeed, induction of Nkx2-1<sup>+</sup> cells of neuroectodermal lineage (Tuj1<sup>+</sup> and Olig2<sup>+</sup>) could be achieved with 70% efficiency after extended exposure of Activin-stimulated ESCs to Nog/SB beginning on day 4 (prior to robust induction of the endodermal markers Cxcr4/ckit) and continuing for >48 hr; these conditions yielded no detectable expression of endodermal lung or thyroid differentiation (Figure 1F). We concluded that stage- and time-dependent inhibition of TGFβ and BMP signaling allows precise control over whether Nkx2-1<sup>+</sup> endoderm versus Nkx2-1<sup>+</sup> neuroectoderm lineages are derived during in vitro directed differentiation of ESCs.

#### Purified Nkx2-1<sup>+</sup> Endodermal Progenitors Differentiate into Thyroid and Lung Lineages

The expression of Foxa2 and Pax8 in purified Nkx2-1<sup>+</sup> endoderm cells suggested the presence of primordial thyroid progenitors in culture prior to induction of the specific differentiation marker thyroglobulin. In mouse endoderm development this expression pattern occurs in developing thyroid epithelial cells between E8.5–E14.5. No specific markers of lung lineage have been described in the embryo to confirm the existence of primordial Nkx2-1<sup>+</sup> lung progenitors between E9.0, their moment of identifiable lineage specification from endoderm, and E10.5, when the earliest specific lung epithelial marker, SPC, is first expressed. Two transcription factors known to be expressed nonspecifically

in early lung endoderm progenitors, Foxp2 and Id2 (Rawlins et al., 2009; Sherwood et al., 2009), were expressed in Nkx2-1<sup>GFP+</sup> cells (Figure S5); however, both markers were also expressed in GFP<sup>−</sup> cells.

We sought to test for the presence of potential primordial lung and thyroid progenitors within the purified Nkx2-1<sup>+</sup> population by assessing whether, as in the embryo, these cells uniquely displayed the capacity to undergo further differentiation into more mature lung or thyroid epithelia, expressing more specific markers of lineage differentiation. We replated purified GFP<sup>+</sup> cells to allow further expansion and differentiation (Figure 2), and we withdrew Wnt3a, KGF, BMP4, and EGF from the media, but maintained FGF2 and FGF10. FGF2 has been employed to specify lung progenitors in endoderm explant cultures (Serls et al., 2005), and FGF10 has been implicated as necessary for the maintenance and proliferation of a variety of endodermal-lineage-specified progenitors, including those of the primordial lung (Ramasamy et al., 2007). As in the developing embryo, Nkx2-1<sup>+</sup> endodermal progenitors within 1 week of further culture continued to proliferate and upregulated a constellation of specific lung epithelial markers, SPC and SPB, as well as proximal airway patterning markers, Scgb3a2 (not shown) and the Clara cell marker CC10 (CCSP; Scgb1a1) (Figure 2 and Figure S5). In addition, markers of proximal airway basal cells (p63) and ciliated cells (Foxj1) emerged as did the cystic fibrosis transmembrane regulator Cfr, which is expressed on a variety of endodermal cells, including ciliated cells of the airway. Thyroid maturation of endodermal Nkx2-1<sup>+</sup> cells was also evident during this period, based on upregulation of thyroglobulin and the receptor for thyroid stimulating hormone (TSHR; Figure 2 and Figure S5). In contrast, the sorted GFP<sup>−</sup> population did not display the capacity to express a lung or thyroid program, as SPC or thyroglobulin was not detected after replating (data not shown). In cells deriving from the GFP<sup>+</sup> sorted population, there was no evidence at any time point studied (days 15–25) of upregulation of markers of neuroectoderm (Pax6 or Tuj1), mesoderm (Myf5), or other endodermal lineages such as liver (AFP or Albumin; data not shown and Figure 2). Furthermore, <0.1% of cells derived from the GFP<sup>+</sup>-sorted cells expressed Tuj1 protein by immunostaining (Figure 3). Overall, these results suggest a step-wise sequential progression of ESC-derived Nkx2-1<sup>+</sup> endodermal progenitors through differentiation stages reminiscent of the described sequence of lung and thyroid development in vivo.

To determine whether proteins known to be expressed in endodermal and early lung epithelial cells were present in the ESC-derived Nkx2-1<sup>+</sup> population, we performed dual immunostaining for Nkx2-1 protein and Foxa2, Sox2 or Sox9 on day 14 prior to cell sorting and on day 24 after outgrowth of purified GFP<sup>+</sup> cells (Figure 3). We found that the majority of ESC-derived Nkx2-1<sup>+</sup> cells on day 14 coexpressed the endodermal marker Foxa2. Many Nkx2-1<sup>+</sup> cells were proliferating as indicated by Ki67 immunostaining (Figure 5). In addition, a subset of Nkx2-1<sup>+</sup> cells coexpressed either Sox2 or Sox9 (Figure 3), transcription factors that, in the presence of Nkx2-1 endoderm in the embryo, mark lineages of the proximal airway (Que et al., 2009) or distal lung bud epithelium (Perl et al., 2005), respectively. At the completion of the protocol shown in Figure 2, the GFP<sup>+</sup> cells sorted on day 14 or 15 and replated in culture for 9–10 more days

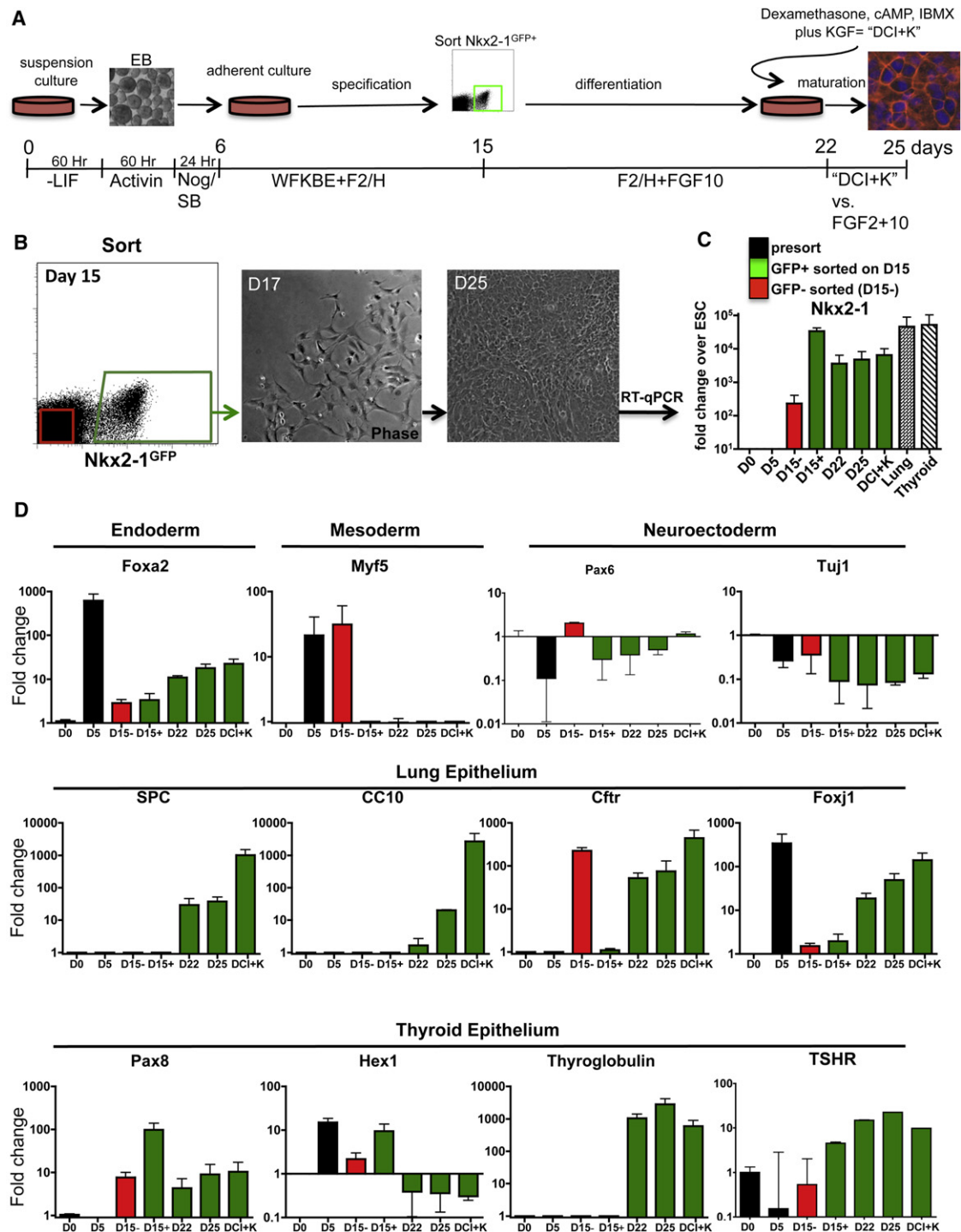


**Figure 2. Purified Endodermal Nkx2-1<sup>GFP+</sup> Progenitors Derived from ESCs Proliferate in Culture and Express a Repertoire of Lung and Thyroid Lineage Genes**

(A) Schematic of culture protocol for directed differentiation of ESCs into Nkx2-1<sup>GFP+</sup> cells. (B) Sort gate used to purify GFP<sup>+</sup> cells for replating and outgrowth. (C) Expression of Nkx2-1 mRNA and indicated marker genes (D) for each cell population, quantified by real time RT-PCR. E18.5 lung and thyroid RNA extracts served as positive controls. Bars indicate average fold change in gene expression over ESCs  $\pm$  SEM (n = 3 independent experiments). DCI+K = cells exposed to lung maturation media from day 22–25. See also Figure S5.

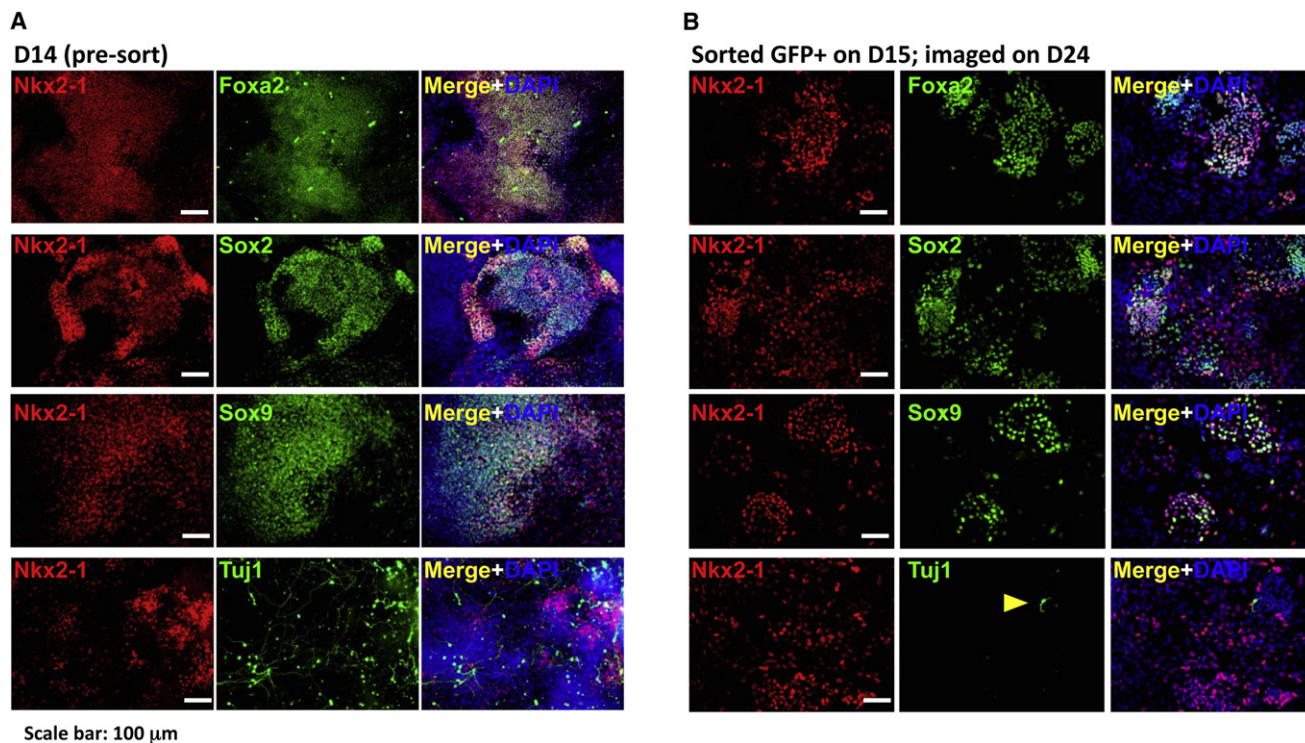


**Figure 3. Purified ESC-Derived Populations Expressing Nkx2-1 Protein Coexpress Markers of Early Developing Endoderm**

(A) Heterogeneous ESC-derived cultures on day 14 (D14; 1 day before GFP<sup>+</sup> cell sorting) immunostained for Nkx2-1, Foxa2, Sox2, Sox9, and Tuj1 proteins demonstrate coexpression of Foxa2 in the majority of Nkx2-1<sup>+</sup> cells and expression of Sox2 or Sox9 in subsets of Nkx2-1<sup>+</sup> cells and Nkx2-1<sup>-</sup> cells. In contrast, Tuj1<sup>+</sup> cells do not overlap with Nkx2-1<sup>+</sup> cells. In these wells ~16% of all cells were Nkx2-1<sup>GFP+</sup> by flow cytometry.

(B) After purification of the Nkx2-1<sup>GFP+</sup> cells shown in (A) by flow cytometry on D15, outgrowth cells stained on D24 for each indicated marker show more clearly defined morphology than before sorting in (A). Arrowhead = rare neuronal (Tuj1<sup>+</sup>) cell found after cell sorting. At this D24 time point, ~60% of cells retained Nkx2-1<sup>GFP</sup> expression by flow cytometry. Scale bar = 100 μm. Nuclei are counterstained with DAPI (blue).

still expressed Nkx2-1 protein in approximately half of the cell outgrowth, and Foxa2, Sox2, and Sox9 protein expression was still detected in subsets of Nkx2-1<sup>+</sup> cells (Figure 3). By day 25, approximately 40% of the sorted, replated GFP<sup>+</sup> population had downregulated Nkx2-1<sup>GFP</sup> expression, and a portion of these Nkx2-1<sup>-</sup> cells expressed the type 1 alveolar epithelial cell (AEC1) marker, T1α (Figure 4A and Figure 6), a gene kinetic typical of late fetal AEC1 development. In order to track SPC<sup>+</sup> cell outgrowth, we employed two independent techniques (Figure 4B): we identified patches of cells expressing pro-SPC protein by immunostaining day 25 cells, and we assayed for SPC promoter activity using a lentiviral vector (Figure S6) encoding the dsRed reporter gene expressed under regulatory control of a published 3.7 kb SPC promoter fragment (Glasser et al., 1991). We observed SPC-dsRed reporter expression only in subsets of Nkx2-1<sup>GFP+</sup> cells.

#### ESC-Derived Nkx2-1<sup>+</sup> Lung Progenitors Respond to Fetal Lung Maturation Media and Recellularize 3D Lung Tissue Scaffolds

A known feature of primary fetal lung epithelial cells late in development is their capacity to respond *in vitro* to cyclic AMP and steroid-containing media by augmenting the expression of lung epithelial-specific genes, such as surfactant proteins (Gonzales

et al., 2002). Hence, beginning on day 22 of our culture protocol, we started a 3 day treatment of the ESC-derived Nkx2-1<sup>GFP+</sup> cells with dexamethasone, cyclic AMP, IBMX, and KGF, hereafter “DCI+K,” a defined serum-free media previously shown to induce well-characterized global transcriptome changes in fetal lung epithelial cells. We found that DCI+K treatment induced ~100-fold upregulation of lung epithelial gene expression (SPC, SPB, and CC10) in the purified Nkx2-1<sup>GFP+</sup> progeny (Figure 2 and Figure S5), but did not detectably augment thyroid marker gene expression (TSHR or thyroglobulin). Epithelial-like sheets were also evident histologically at this time, as evidenced by f-actin filament orientation after phalloidin staining (Figure S5). In contrast 3 days of exposure to thyroid maturation media (TSH, IGF-1, and Nal) resulted in no increase in lung marker gene expression, but induced upregulation of the thyroid markers thyroglobulin and TSHR (Figure S5D).

Since structure and function are inextricably linked features of lung alveolar epithelial cells, we assessed the capacity of sorted day 15 Nkx2-1<sup>GFP+</sup> progenitors to regenerate 3D alveolar lung structure (Figures 4C–4H and Figure S7). The capacity of primary lung epithelial cells to seed decellularized rodent lung scaffolds is one assay recently developed to test the regenerative potential of lung epithelia (Daly et al., 2012; Ott et al., 2010; Petersen et al., 2010). Sorted day 15 Nkx2-1<sup>GFP+</sup> ESC-derived cells, delivered



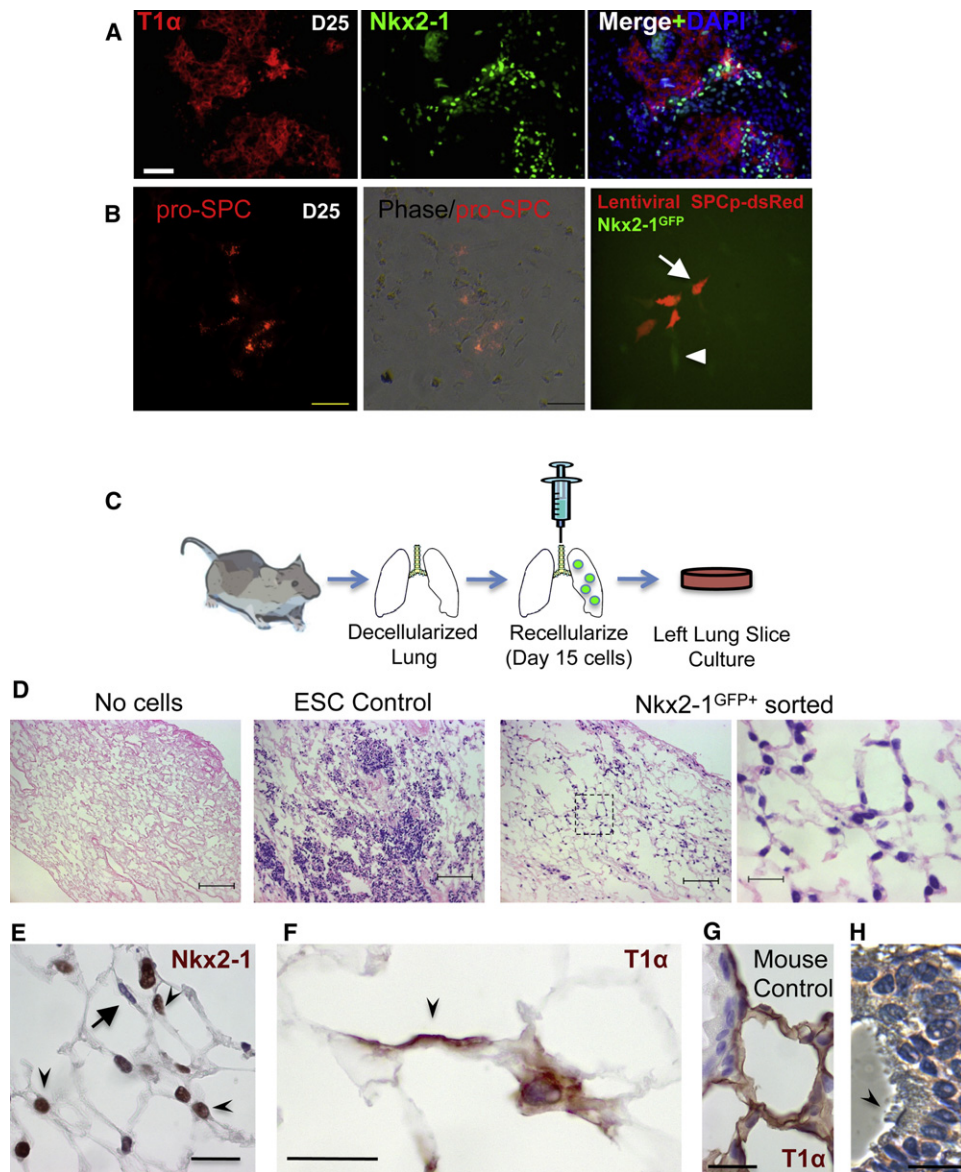


**Figure 4. Alveolar Differentiation Repertoire of ESC-Derived Nkx2-1<sup>+</sup> Lung Progenitors**

(A and B) Immunostaining for alveolar epithelial markers T1 $\alpha$ , pro-SPC, and Nkx2-1 on cells at the completion of the 25 day directed differentiation protocol. ESCs sorted on day 15 based on Nkx2-1<sup>GFP+</sup> expression subsequently gave rise to (A) cells reminiscent of type 1 alveolar epithelial cells (AEC1) as they lost Nkx2-1 nuclear protein expression (green immunostain) while expressing T1 $\alpha$  protein. (B) Other patches of cells appeared more reminiscent of distal SPC<sup>+</sup> alveolar epithelial cells as they expressed punctate cytoplasmic pro-SPC protein and displayed SPC promoter activation while retaining Nkx2-1<sup>GFP</sup> expression. Arrow = SPC-dsRed and Nkx2-1<sup>GFP</sup> coexpressing cell (orange). Arrowhead = cell expressing only Nkx2-1<sup>GFP</sup>.

(C) Schematic summarizing the decellularization-recellularization assay.

(D) H&E stains of lung sections showing lung scaffold appearance with no recellularization (left panel) versus hypercellular sheets following reseeding with undifferentiated ESCs (middle panel) versus cells of alveolar structural morphologies after seeding with Nkx2-1<sup>GFP+</sup> purified ESC-derived progenitors (right panel). Scale bars = 100  $\mu$ m in three left panels. Zoom of the indicated boxed region is shown in far right panel with scale bar = 20  $\mu$ m.

(E and F) Nkx2-1<sup>+</sup> nuclear protein (brown; arrowheads in E) immunostaining of engrafted cuboidal epithelial cells in the corners of alveoli, derived 10 days after reseeding with Nkx2-1<sup>GFP+</sup> sorted cells. Arrow = flattened nucleus of an Nkx2-1 negative cell (purple) lining the alveolar septum. Many of these flattened cells were T1 $\alpha$ <sup>+</sup> (F; arrowhead). Scale bars = 20  $\mu$ m.

(G) Control mouse lung without decellularization showing T1 $\alpha$  apical membrane staining pattern (brown) of mature AEC1. See also Figure S7.

(H) Ciliated airway epithelial cell (arrow) 10 days after reseeding with differentiated/unsorted ESC-derived cells. Scale bar = 20  $\mu$ m. All nuclei were counterstained with hematoxylin (purple).

See also Figures S6 and S7.

by intratracheal instillation into decellularized murine lungs, were able to seed alveolar lung regions and adopt the morphology of lung alveolar epithelia (Figures 4C–4H and Figure S7). In explant cultures of lung tissue reseeded with GFP<sup>+</sup> cells on day 15 and cultured for 10 more days, 71% ± 12% (average ± SD) of engrafted cells maintained GFP fluorescence and continued to express nuclear Nkx2-1 protein (Figure 4E). Some engrafted cells acquired a flattened morphology and lost expression of Nkx2-1 protein, a pattern reminiscent of developing AEC1 cells in vivo (Williams, 2003). Consistent with this pattern, the majority of these flattened cells expressed the AEC1 marker protein T1 $\alpha$  (Figures 4F and 4G), but lacked expression of Nkx2-1 protein by costaining (Figure S7G). In contrast, day 0 undifferentiated cells did not form alveolar structures after intratracheal instillation, but rather gave rise to masses of cells in the distal lung (Figure 4D) with only very rare cells (<0.1%) expressing either Nkx2-1 or T1 $\alpha$  proteins (Figure S7). Counting cell nuclei present 10 days after reseeded revealed that lung slices reseeded with undifferentiated ESCs contained more cellular outgrowth than slices reseeded with differentiated cells, but the seeded cells deriving from undifferentiated ESCs remained round, and none of these undifferentiated cells developed either the morphologic or molecular features of lung epithelia (Figure S7). Although ciliated cells were not observed after reseeded with sorted cells, day 15 unsorted, differentiated cells (containing 20% GFP<sup>+</sup> and 80% GFP<sup>−</sup> cell mixtures) were able to re-epithelialize proximal airways and gave rise to ciliated cells facing the airway lumen (Figure 4H).

#### BMP and FGF Signaling Is Required for Efficient Lineage Specification of Nkx2-1<sup>+</sup> Endodermal Progenitors

To identify factors essential for lung and thyroid lineage specification of endoderm, we tested the effects of removing each of the six growth factors from our WFKBE+F2/H cocktail. Both FGF2 and BMP4 were essential for efficient Nkx2-1<sup>+</sup> endodermal lineage specification, as removal of either factor resulted in a significant decrease in the percentage of GFP<sup>+</sup> cells (Figures 5A and 5B;  $p < 0.05$ ). In contrast, EGF, KGF, and FGF10 were each dispensable for Nkx2-1 lineage specification with no significant decrement in the percentage of GFP<sup>+</sup> cells induced in the absence of these growth factors. Removal of Wnt3a did not affect the percentage of GFP<sup>+</sup> cells induced by day 14. However, it markedly reduced proliferation of day 14 cells, as assessed by the 24 hr BrdU labeling index, which declined from 89% BrdU<sup>+</sup> in the presence of Wnt3a to 40% BrdU<sup>+</sup> in the absence of Wnt3a (Figure 5B). Removal of EGF, KGF, or FGF10 did not significantly alter the BrdU labeling index of the day 14 population. Taken together our results suggested that efficient induction of Nkx2-1 in endodermal progenitors depends on stage-specific and time-dependent inhibition of BMP and TGF $\beta$  signaling followed by reinitiation of BMP signaling together with FGF signaling.

#### Initial Lineage Commitment of Nkx2-1<sup>+</sup> versus Nkx2-1<sup>−</sup> Cells Is Associated with Definable Changes in the Genetic and Epigenetic Programs of Each Population

An attractive feature of ESC-based in vitro developmental systems is the potential to use them to learn about genetic or epigenetic programs that are otherwise difficult to study in vivo.

We found that by day 14 of differentiation, cells treated with our protocol already exhibited significant restriction of cell fates, because only sorted Nkx2-1<sup>GFP+</sup> cells at this time could go on to express lung or thyroid markers. In contrast, day 12 or day 14 sorted GFP<sup>−</sup> cells, when replated, did not express GFP, Nkx2-1, or differentiated lung/thyroid markers even after prolonged culture periods in either culture condition (WFKBE+F2/H or FGF2+10; Figures 6A and 6B). We reasoned that the epigenetic signature of the Nkx2-1 locus might also distinguish these cell populations. We extracted DNA and chromatin from ESC populations of various developmental stages (undifferentiated, definitive endodermal prior to Nkx2-1 induction, and endodermal day 12 GFP<sup>+</sup> versus GFP<sup>−</sup> sorted cells) and from primary postnatal lung cells sorted based on expression of Nkx2-1<sup>GFP+</sup> (epithelial) versus Nkx2-1<sup>GFP−</sup> (including lung mesenchyme and endothelium) (Figure 6). Regardless of developmental stage, all CpG sites in this Nkx2-1 promoter region were unmethylated. In contrast, the histone methylation signature in this promoter region in differentiated day 12 GFP<sup>−</sup> ESC-derived cells exhibited a repressive trimethylated histone modification mark (H3K27-me3), which correlated with the ESC-derived GFP<sup>−</sup> population's cell fate decision to lose endodermal lung/thyroid differentiation capacity. This same repressive mark was found in Nkx2-1<sup>GFP−</sup> sorted primary cells and contrasted with the combined active (H3K4-me3) and repressive (H3K9-me3 and H3K27-me3) marks seen in populations of undifferentiated ESCs and endoderm staged cells, and the predominantly active mark (H3K4-me3) observed in ESC-derived Nkx2-1<sup>GFP+</sup> and primary Nkx2-1<sup>GFP+</sup> cells (Figure 6C). The finding that histone modifications rather than DNA CpG methylations occur in key Nkx2-1 regulatory regions early in endoderm development is consistent with descriptions of epigenetic changes in loci encoding other key endodermal transcription factors (Zaret et al., 2008).

In contrast to Nkx2-1, the proximal promoter region of Oct4 exhibited both DNA methylation and repressive histone marks (H3K9-me3 and H3K27-me3) soon after endodermal differentiation (Figure 6D), consistent with silencing of a locus that will not be expressed in Nkx2-1<sup>+</sup> progenitors or their epithelial progeny.

Finally, we sought to apply our in vitro model system to define the global genetic program of the putative primordial Nkx2-1<sup>+</sup> endodermal progenitors. We performed microarray analysis of global transcriptomes isolated from GFP<sup>+</sup> versus GFP<sup>−</sup> day 14 ESC-derived cells. We found that 1,267 probes out of 29,000 were differentially expressed at FDR-adjusted  $p < 0.05$ . As expected, Nkx2-1 was found to be the most statistically significant differentially expressed transcript ( $p = 1.19 \times 10^{-5}$ ; Figures 7A–7C). These 1,267 differentially expressed genes provided a genetic signature that characterizes the ESC-derived Nkx2-1<sup>+</sup> endodermal progenitor population, including 83 novel candidate cell surface markers that are upregulated in the GFP<sup>+</sup> population (Table S1). In addition, this GFP<sup>+</sup> genetic signature included additional genes known to characterize early developing thyroid and lung in vivo as well as potential ligand-receptor relationships active in signaling cascades (Notch, Wnt, RA, and BMP signaling) that have been shown to play a role in early lung/thyroid development (Cardoso and Lü, 2006). Focusing on the set of 594 genes significantly upregulated in Nkx2-1<sup>GFP+</sup> cells, we performed gene ontology analysis, revealing five major biological process groupings (Figure 7B)

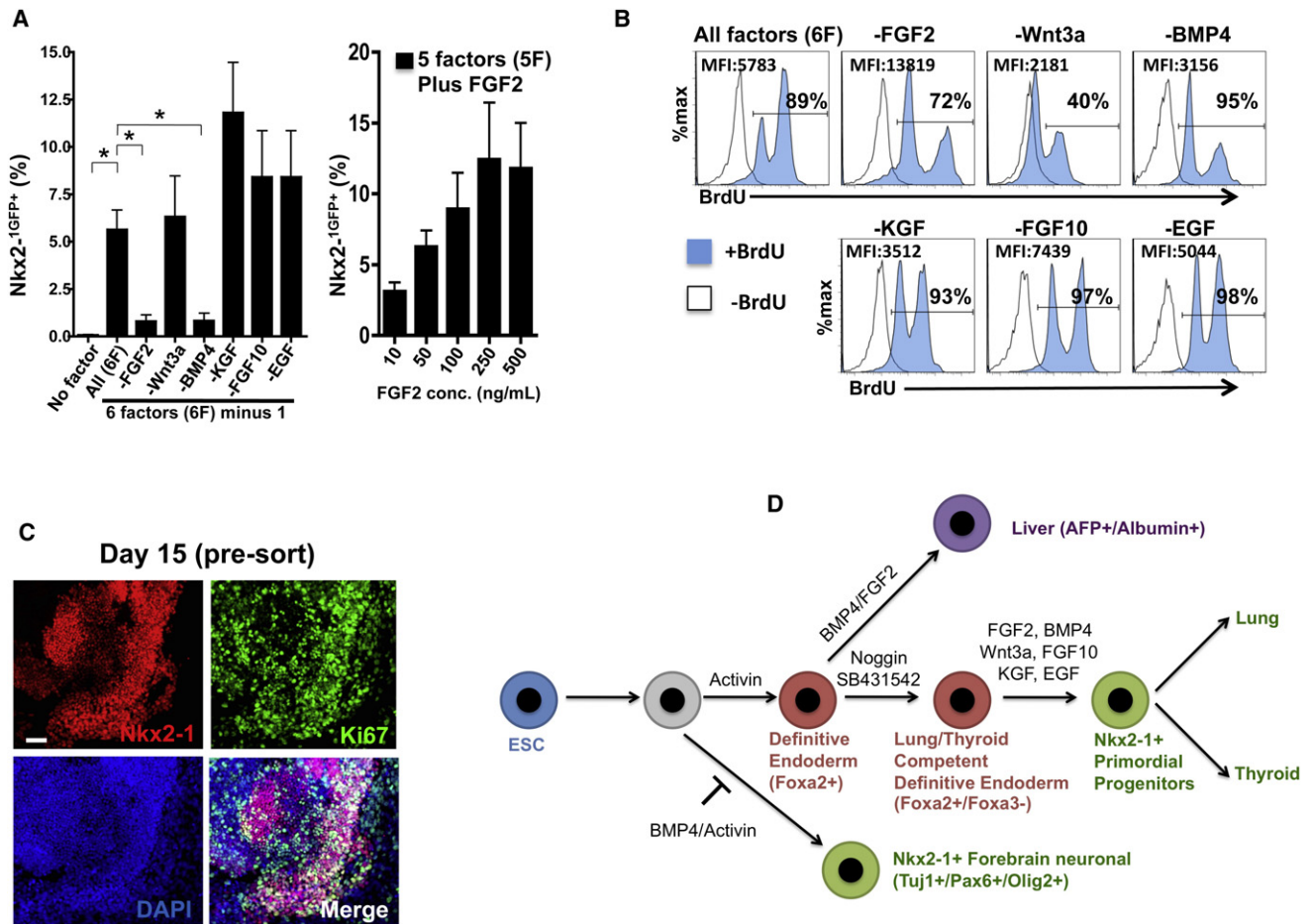


**Figure 5. Combinatorial FGF and BMP Signaling Promotes Efficient Derivation of Proliferating Nkx2-1<sup>GFP+</sup> ESC-Derived Cells**

(A) Percentage of Nkx2-1<sup>GFP+</sup> cells derived from ESCs on D14 when individual growth factors were withdrawn from the six-factor (6F) ventralizing WFKBE+FGF2 cocktail. Two-tailed t test, \*p < 0.05.

(B) BrdU labeling index (after 24 hr versus 0 hr of BrdU exposure) measured by flow cytometry in each condition from (A). Cells are scored as BrdU+ based on histogram gates set on cells that did not receive BrdU.

(C) Immunostaining for Nkx2-1 and Ki67 nuclear proteins in D15 ESC-derived cells.

(D) Model of directed differentiation of ESCs into neuroectodermal Nkx2-1<sup>+</sup> cells versus endodermal Nkx2-1<sup>+</sup> cells with lung and thyroid differentiation potential.

represented by this gene set. The two most prominent biological processes represented in this set were related to either development or regulation of cellular processes. Within the differentially expressed gene set of the GFP<sup>+</sup> population, upregulation of Col1a1, Col1a2, Twist, Gli1, Gli3, and PDGFR $\alpha$  suggested the presence of mesenchymal lineages (Figure 7B).

By comparing the transcriptome of our ESC-derived Nkx2-1<sup>+</sup> progenitors to databases established from in vivo tissues, we found that 17% of genes (100 out of 594) upregulated in Nkx2-1<sup>GFP+</sup> cells were also expressed in the E11.5 developing mouse lung epithelium (Lü et al., 2005). Finally, we determined which of the 594 upregulated genes in Nkx2-1<sup>GFP+</sup> cells overlapped with published targets of Nkx2-1 protein binding in the developing lung. Twelve percent of these genes (71 out of 594) were targets of Nkx2-1 identified previously (GEO GSE23043) (Tagne et al., 2012) by microarray analysis of chromatin ("ChIP on chip") immunoprecipitated from E11.5 lung epithelial cells using anti-Nkx2-1 antibodies (Figure 7D).

## DISCUSSION

Our results demonstrate the directed differentiation of pluripotent stem cells in serum-free culture into purified Nkx2-1<sup>+</sup> endodermal progenitors with lung and thyroid differentiation potential. We refer to the progenitors purified in 12–15 days with this approach as "primordial" because they resemble an in vivo developmental stage (approximating E8.5–E10.5 in mouse development) where Nkx2-1<sup>+</sup> endodermal progenitors have not yet expressed markers of differentiated lung or thyroid epithelium. Our protocol is the result of an approach wherein we sought to optimize the differentiation efficiency of each developmental stage prior to inducing the subsequent desired stage. We then reassessed the phenotype of the resulting cells when a stage was identified that seemed resistant to subsequent desired lineage specification. Using this approach we found definitive endoderm staged cells derived after optimization of Activin dose and timing appeared resistant to lung or thyroid lineage



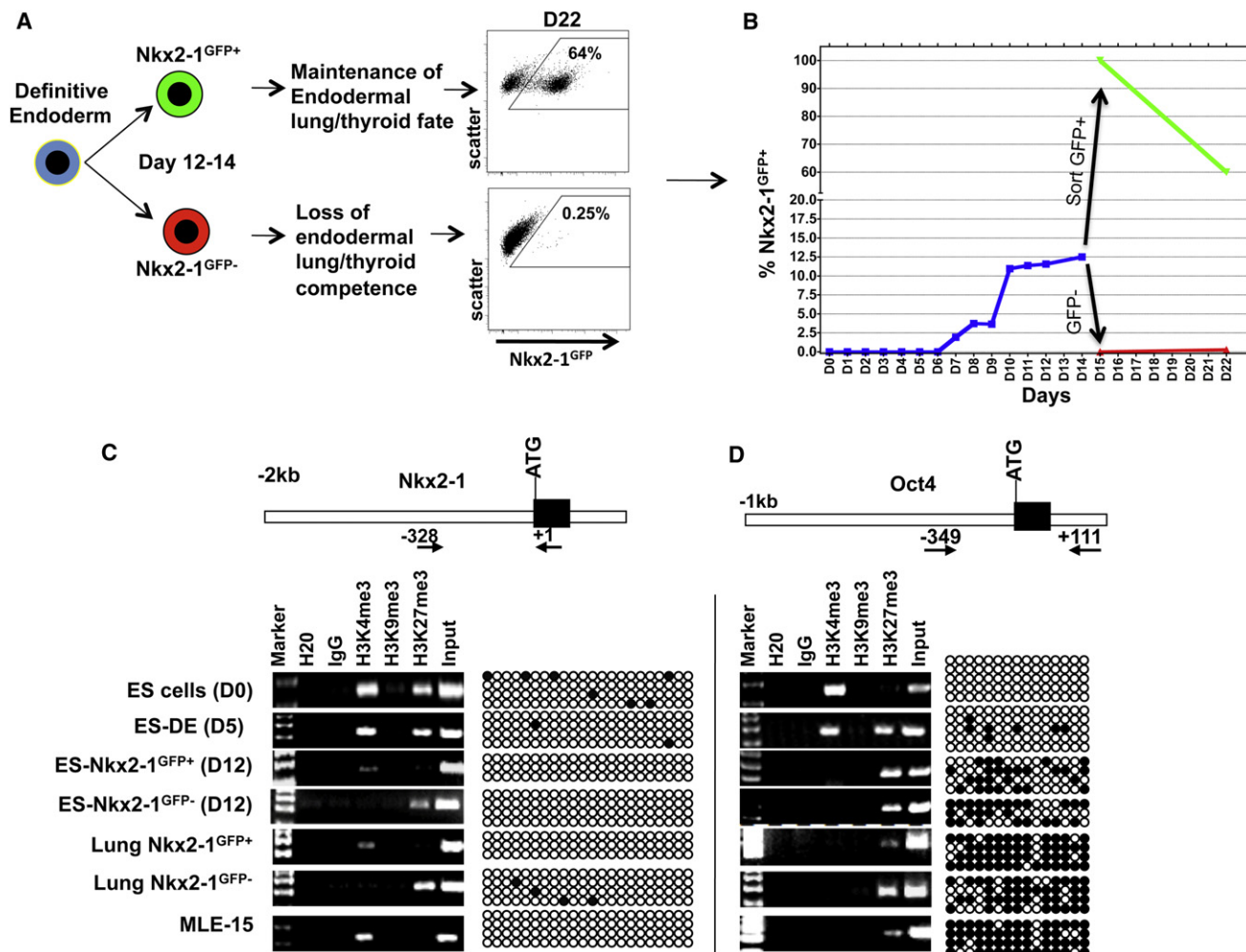


**Figure 6. Epigenetic Changes in the  $Nkx2-1$  and  $Oct4$  Proximal Promoter Regions during Directed Differentiation of ESCs**

(A) Schematic of cell fate decision in ESC-derived endodermal cells to commit to an  $Nkx2-1$  descendant lineage.

(B) Kinetics of  $Nkx2-1^{GFP}$  expression during 22 days of ESC-directed differentiation, following the protocol shown in Figure 2.

(C and D) Chromatin immunoprecipitation and bisulfite sequencing studies demonstrate the DNA methylation and histone trimethylation states of the proximal promoters of the  $Nkx2-1$  and  $Oct4$  loci in each cell population during development. Arrows and numbers indicate PCR primer binding sites relative to the ATG start site. Open circles = unmethylated DNA CpG sites; closed circles = methylated CpG sites. Lung  $Nkx2-1^{GFP+}$  versus  $Nkx2-1^{GFP-}$  samples were prepared by sorting primary lung cell digests from a 3-week-old mouse. MLE-15 = mouse lung epithelial cell line.

specification. Only after stage-specific inhibition of BMP and TGF $\beta$  signaling pathways were we able to yield these endodermal progenitors amenable to efficient lung/thyroid lineage specification. Using this strategy, the optimized protocol presented here results in approximately 160  $Nkx2-1^{GFP+}$  endodermal cells per starting input ESC within 14 days of directed differentiation.

Our studies reinforce the importance of mechanisms, such as FGF and BMP signaling, that have recently been proposed as key inducers of lung lineage within foregut endoderm (Domayan et al., 2011; Serls et al., 2005). Although these pathways have been singly manipulated in vivo using genetic mouse models, our results indicate that no single pathway alone appears to be sufficient for efficient lung or thyroid lineage specification from developing endoderm. Most importantly, our results emphasize that precise inhibition of certain pathways at defined stages is as

important as the addition of pathway stimulators at different developmental stages (model shown in Figure 5D). The combination of the two approaches, stage-specific selective inhibition combined with induction of key signals, is likely to be a common strategy that can be applied regardless of the germ layer or tissue system to be derived in vitro or in vivo (Kattman et al., 2011).

During the course of our studies we derived putative progenitors reminiscent of a developmental period (E9–E10.5) that is devoid of known specific markers for lung primordial progenitors. It was useful to develop simple marker gene signatures as indicators of passage through each sequential milestone on the way to lung/thyroid differentiation. For adequate response to Activin, we monitored for the onset of robust and efficient *Cxcr4*/*ckit* expression prior to initiating 24 hr of BMP/TGF $\beta$  inhibition. During the subsequent stage of FGF and BMP stimulation,

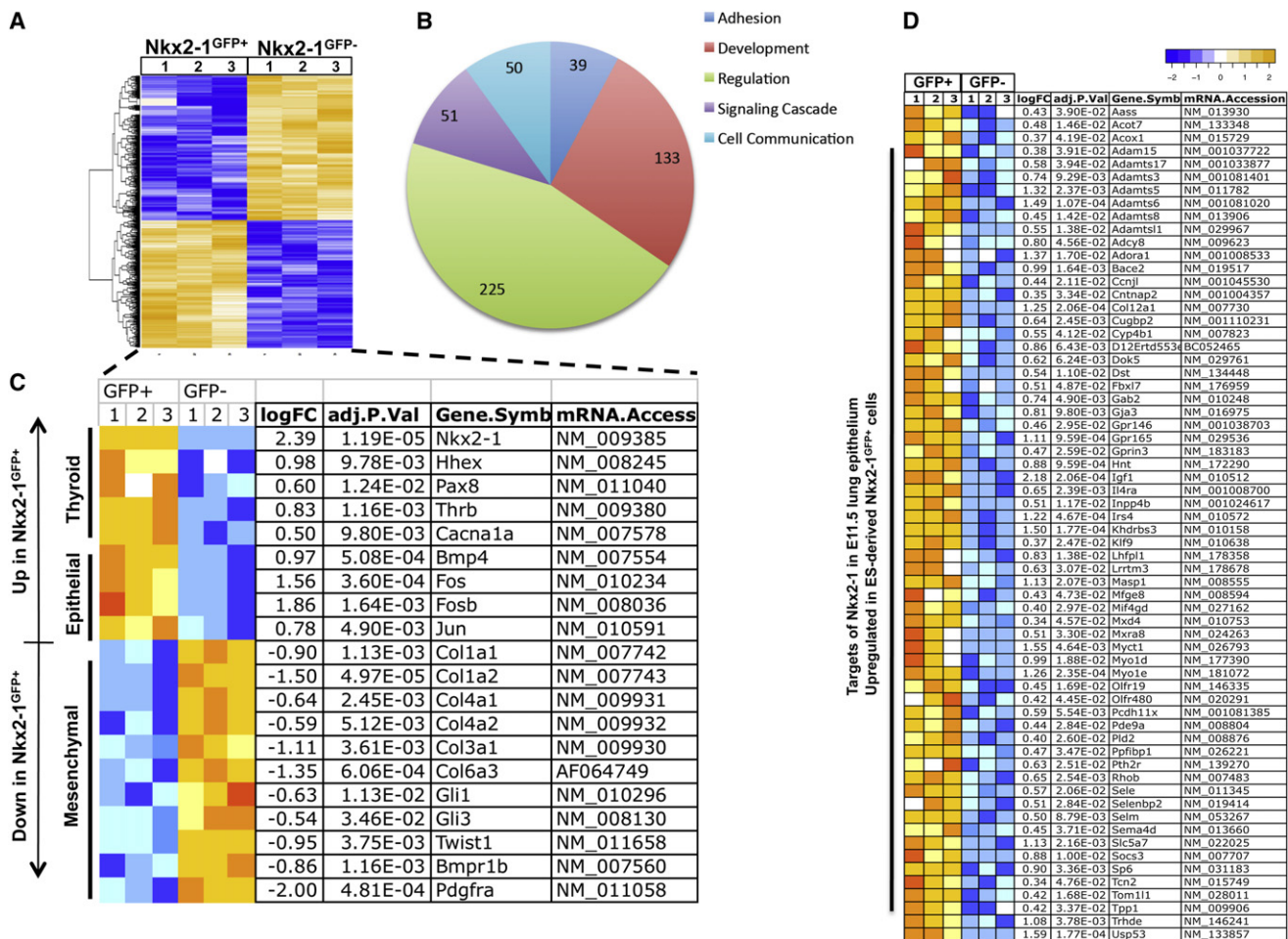


**Figure 7. Differentially Expressed Genes in ESC-Derived Nkx2-1<sup>GFP+</sup> versus Nkx2-1<sup>GFP-</sup> Cells**

(A) Heat map of 1,267 genes differentially expressed between triplicate samples of Nkx2-1<sup>GFP+</sup> versus Nkx2-1<sup>GFP-</sup> ESC-derived cells, sorted on day 14 of differentiation.

(B) Gene Ontology analysis of the 594 genes upregulated in GFP<sup>+</sup> cells (DAVID on-line analysis).

(C and D) Selections of the 1,267 differentially expressed genes (C) demonstrate differing gene programs relating to thyroid lineage, epithelial signaling, and mesenchymal programs, or (D) genes whose promoters are known targets of Nkx2-1 protein binding in E11.5 embryonic lung epithelial cells in vivo. Gene.symb = NCBI gene ID. LogFC = log<sub>2</sub> fold change in gene expression.

See also Table S1.

we checked to verify that purified candidate Nkx2-1<sup>+</sup> endodermal progenitors had confirmed expression of Foxa2 and absence of expression of Pax6 and Tuj1 in order to ensure that lung competent endoderm, rather than neuroectodermal Nkx2-1 progenitors, had been derived. The presence of Pax8 expression at this time can also be used to verify that Nkx2-1 endoderm of thyroid lineage has been derived. Since no specific markers of lung or thyroid have yet been described to prove definitively that candidate progenitors are of lung/thyroid lineage, demonstration of subsequent induction of specific differentiated lung and thyroid epithelial markers (e.g., surfactant proteins and thyroglobulin, respectively) remains the only reliable proof of the lung/thyroid competence of the putative primordial Nkx2-1<sup>+</sup> progenitors being derived.

A particularly striking and serendipitous outcome of our experiments is the development of a simple protocol for the

highly efficient derivation of Nkx2-1<sup>+</sup> neuroectodermal cells by prolonged inhibition of BMP/TGFβ signaling in ESCs. Although Nkx2-1 is expressed in three lineages across two germ layers in the developing embryo, stage-specific optimization of inhibition of BMP and TGFβ signaling pathways, as demonstrated here, can effectively direct the fate of the resulting Nkx2-1<sup>+</sup> cells preferentially to either germ layer. In the ectodermal germ layer of the developing embryo, Nkx2-1 is expressed in forebrain neuronal and oligodendrocyte progenitors. Consistent with these lineages, ESC-derived neuroectodermal Nkx2-1<sup>GFP+</sup> cells generated in our neuronal conditions expressed Tuj1, Pax6, and Olig2; however, whether they also express the full constellation of forebrain markers will require further study and in vivo correlation. It is well known that neuroectoderm differentiates easily from undifferentiated ESCs, particularly when BMP and TGFβ signaling are inhibited, and it appears that Nkx2-1<sup>+</sup>

neuroectodermal progenitors may be similarly derived from undifferentiated mouse ESCs by this approach or by recently published alternate protocols for human NKX2-1 reporter ESCs (Goulburn et al., 2011).

A useful outcome for lung and thyroid research will be the utilization of this in vitro platform for the identification of new lineage markers and the study of genetic and epigenetic programs active in early lung and thyroid development. Although the gene programs and potential markers identified in vitro will require validation in vivo in the developing embryo, we have demonstrated how this system might be applied to define the genetic program of Nkx2-1<sup>+</sup> endodermal progenitors. We found 83 cell surface markers that potentially distinguish the Nkx2-1<sup>+</sup> endodermal progenitors in our system, and we observed a definable epigenetic change in the Nkx2-1 promoter region that correlates with lineage commitment of Nkx2-1<sup>+</sup> cells away from lung or thyroid competence.

There are several issues raised by our studies. First, we acknowledge that a lack of any known genetic or epigenetic signature of authentic in vivo Nkx2-1<sup>+</sup> endodermal progenitors of similar stage limits our ability to properly compare the phenotype or the genetic signature of the in-vitro-derived Nkx2-1<sup>+</sup> endodermal population against their authentic in vivo correlates. Application of the Nkx2-1 reporter mouse introduced here for the purification of primordial Nkx2-1 endodermal thyroid and lung progenitors from developing mouse embryos will help to surmount this hurdle. Second, the relative frequency of thyroid-versus lung-committed progenitors within the Nkx2-1<sup>GFP+</sup> endodermal population needs to be more precisely quantified. This will first require the discovery of new markers specific to primordial lung epithelia prior to the E10.5 time at which the earliest known marker, SPC, is expressed in the mouse developing lung. Alternatively, we have not excluded the intriguing possibility that the Nkx2-1<sup>+</sup> progenitors derived from ESCs in vitro express bipotential features of both thyroid and lung progenitors, a differentiation repertoire that is not known to occur in vivo in endoderm development. Future work with our system, focused on testing clonogenicity and multipotency of the Nkx2-1<sup>+</sup> population, will help to address these questions. Finally, we emphasize that lung or thyroid progenitors must ultimately be defined by their capacity to give rise to functional epithelia that produce appropriate thyroid hormones or allow pulmonary gas exchange. The lack of known functional assays or reproducible in vivo engraftment models to functionally test candidate lung epithelial progenitors continues to limit progress in lung progenitor cell biology. Novel functional assays of lung epithelia, such as the recellularization of decellularized lung scaffolds employed by us and others, may provide bioartificial lungs (Ott et al., 2010) that can serve as one platform for in vitro and in vivo testing of candidate lung epithelial progenitors, such as those derived from ESCs.

In conclusion, we present here tools and protocols for the step-wise derivation, purification, and culture expansion of primordial lung and thyroid endodermal progenitors from pluripotent stem cells. Since primordial lung and thyroid progenitors are few in number in vivo and are thought to only transiently occur during early anterior foregut endodermal development, this in vitro system allows the capture of a developmental stage in culture that is otherwise difficult to study in vivo. Thus, when

partnered with in vivo studies, this in vitro system should allow high-resolution study of the mechanisms and genetic/epigenetic programs of cells that to date remain virtually unstudied in developmental biology. Derivation of a potentially unlimited supply of early Nkx2-1<sup>+</sup> lung and thyroid progenitors from ESCs should also allow the purification of progenitors for the modeling and potential treatment of the many diseases affecting lung or thyroid epithelia.

## EXPERIMENTAL PROCEDURES

### Derivation of Nkx2-1<sup>GFP</sup> ESCs and Reporter Mice

The enhanced GFP reporter gene was targeted to one allele of the endogenous Nkx2-1 locus by homologous recombination in W4/129S6 ESCs (Taconic, Hudson, NY), replacing endogenous sequences from the second ATG start site through the end of the Nkx2-1 homeobox (positions 7957–9480 in GenBank locus MMU19755), according to methods detailed in the [Supplemental Information](#). Nkx2-1<sup>GFP</sup> ESCs were injected into C57BL/6j (Jackson Laboratory) mouse blastocysts to generate knockin mice as detailed in the [Supplemental Information](#). All mouse work was approved by the Institutional Animal Care and Use Committee of Boston University.

### ESC Culture and Differentiation

The Nkx2-1<sup>GFP</sup> ESC line was maintained in the undifferentiated state in serum-free, feeder-free culture conditions using “2i” media (Ying et al., 2008). Five days of definitive endoderm induction in serum-free conditions was performed using 50 ng/ml Activin as previously published (Gouon-Evans et al., 2006) and detailed in the [Supplemental Information](#) and [Figure S2](#). On day 5 EBs were plated onto gelatin-coated plates. Media was switched to Nog/SB media: cSFDM supplemented with 100 ng/ml mNoggin (R&D) and 10  $\mu$ M SB431542 (Sigma). After 24 hr the media was switched to Nkx2-1 induction media: cSFDM supplemented with 100 ng/ml mWnt3a, 10 ng/ml mKGF, 10 ng/ml hFGF10, 10 ng/ml mBMP4, 20 ng/ml hEGF, 500 ng/ml mFGF2 (all from R&D), and 100 ng/ml Heparin Sodium Salt (Sigma). Nkx2-1<sup>GFP+</sup> cells were sorted and replated onto gelatin-coated dishes on the day indicated in the text (day 12–15). Replated cells were grown for 7 days in cSFDM supplemented with mFGF2 (500 ng/ml), hFGF10 (100 ng/ml), and 100 ng/ml Heparin Sodium Salt (Sigma). On day 22, where indicated in the text, the media was switched to lung maturation media (DCI+K): Ham's F12 media +15 mM HEPES (pH 7.4) +0.8 mM CaCl<sub>2</sub> +0.25% BSA + 5  $\mu$ g/ml insulin + 5  $\mu$ g/ml transferrin + 5 ng/ml Na selenite + 50 nM Dexamethasone + 0.1 mM 8-Br-cAMP + 0.1 mM IBMX + 10 ng/ml KGF. Detailed protocols are available in the [Supplemental Information](#).

### Immunofluorescent Staining

Cells cultured on gelatin-coated 96-well plates were fixed with fresh 4% paraformaldehyde and immunostained with the indicated antibody according to methods detailed in the [Supplemental Information](#).

### Quantitative RT-PCR

Quantitative (real time) PCR amplification of cDNA was performed using Taqman probes. Relative gene expression, normalized to 18S control, was calculated using the  $2^{(-\Delta\Delta C_T)}$  method to quantify fold change in gene expression of the indicated gene compared to baseline expression (fold change = 1) in ESCs. Undetectable genes were assigned a cycle number of 40. Detailed methods and primer sequences are available in the [Supplemental Information](#).

### Mouse Lung Recellularization and Culture

B6 mouse lungs were decellularized and recellularized according to recently described methods (Daly et al., 2012; Wallis et al., 2012). Following decellularization, the right main-stem bronchus was ligated to allow intratracheal delivery of cells only to the left lung. One million cells of each population indicated in the text were mixed with 2% low-melting temperature agarose and intratracheally injected into the decellularized left lung. Each lung was sectioned sagittally into 2 mm thick slices and cultured for 10 days (equivalent to days 15–25 of the protocol shown in [Figure 2](#)). On day 25, paraffin sections



of 4% paraformaldehyde-fixed lung slices were prepared for immunohistochemistry analyses detailed in the [Supplemental Information](#).

### Bisulfite Sequencing and ChIP

Genomic DNA was purified and bisulfite treated as published (Cao et al., 2010) prior to nested PCR of the indicated promoter region, using primers and methods detailed in the [Supplemental Information](#). ChIP of 500–2,000 bp chromatin fragments was performed using anti-H3K4me3 antibodies, H3K9me3 antibodies, H3K27me3 antibodies, or IgG isotype control as detailed in the [Supplemental Information](#).

### Statistical and Microarray Methods

Unless otherwise indicated all statistical comparisons between groups were performed by two-tailed student's *t* test, and *p* < 0.05 indicated a statistically significant difference between groups. Detailed statistical methods of analysis of Affymetrix GeneChip® Mouse Gene 1.0 ST arrays are included in the [Supplemental Information](#).

### ACCESSION NUMBERS

All raw data CEL files are available for free download from the Gene Expression Omnibus (GEO accession number GSE35063).

### SUPPLEMENTAL INFORMATION

Supplemental Information for this article includes Figures S1–S7, Table S1, and Supplemental Experimental Procedures and can be found with this article online at [doi:10.1016/j.stem.2012.01.019](https://doi.org/10.1016/j.stem.2012.01.019).

### ACKNOWLEDGMENTS

We thank Paul Gadue for supplying the TV8-Puro gene targeting vector; Raul Mostoslavsky for assistance with Southern blotting techniques; Susan Gutten-tag for DCI+K media protocols; and Mary C. Williams, Wellington V. Cardoso, Bess P. Rosen, George Murphy, Gustavo Mostoslavsky, and Jerome Brody for insightful manuscript editing. For technical support, we thank Dr. Yuriy Alekseyev, Sherry Zang, and Dr. Gang Liu for microarray processing; Dr. Jining Lu and Avrum Spira for bioinformatics analysis assistance; and John M. Wallis for lung slice culture technical support. D.N.K. is supported by NIH PO1 HL047049-16A1, 1R2HL101535-01, 1R01 HL095993-01, 1R01 HL108678, a USAMRRA Award, an Alpha-1 Foundation Award, and an ARC award from the Evans Center for Interdisciplinary Research at Boston University. T.A.L. is supported by NIH training grant T32 HL007035. L.I. is supported by R01 HL111574 and an ATS/ChILD Foundation Award. The authors have no conflicts of interest to declare.

Received: July 11, 2011

Revised: December 18, 2011

Accepted: January 25, 2012

Published: April 5, 2012

### REFERENCES

- Ali, N.N., Edgar, A.J., Samadikuchaksaraei, A., Timson, C.M., Romanska, H.M., Polak, J.M., and Bishop, A.E. (2002). Derivation of type II alveolar epithelial cells from murine embryonic stem cells. *Tissue Eng.* 8, 541–550.
- Ameri, J., Ståhlberg, A., Pedersen, J., Johansson, J.K., Johannesson, M.M., Artner, I., and Semb, H. (2010). FGF2 specifies hESC-derived definitive endoderm into foregut/midgut cell lineages in a concentration-dependent manner. *Stem Cells* 28, 45–56.
- Arufe, M.C., Lu, M., Kubo, A., Keller, G., Davies, T.F., and Lin, R.Y. (2006). Directed differentiation of mouse embryonic stem cells into thyroid follicular cells. *Endocrinology* 147, 3007–3015.
- Arufe, M.C., Lu, M., and Lin, R.Y. (2009). Differentiation of murine embryonic stem cells to thyrocytes requires insulin and insulin-like growth factor-1. *Biochem. Biophys. Res. Commun.* 381, 264–270.
- Cao, Y., Vo, T., Millien, G., Tagne, J.B., Kotton, D., Mason, R.J., Williams, M.C., and Ramirez, M.I. (2010). Epigenetic mechanisms modulate thyroid transcription factor 1-mediated transcription of the surfactant protein B gene. *J. Biol. Chem.* 285, 2152–2164.
- Cardoso, W.V., and Lü, J. (2006). Regulation of early lung morphogenesis: questions, facts and controversies. *Development* 133, 1611–1624.
- Cardoso, W.V., and Kotton, D.N. (2008). Specification and Patterning of the Respiratory System. *StemBook*. <http://www.stembook.org>. 10.3824/stembook.1.10.1.
- Chambers, S.M., Fasano, C.A., Papapetrou, E.P., Tomishima, M., Sadelain, M., and Studer, L. (2009). Highly efficient neural conversion of human ES and iPS cells by dual inhibition of SMAD signaling. *Nat. Biotechnol.* 27, 275–280.
- Christodoulou, C., Longmire, T.A., Shen, S.S., Bourdon, A., Sommer, C.A., Gadue, P., Spira, A., Gouon-Evans, V., Murphy, G.J., Mostoslavsky, G., and Kotton, D.N. (2011). Mouse ES and iPS cells can form similar definitive endoderm despite differences in imprinted genes. *J. Clin. Invest.* 121, 2313–2325.
- Coraux, C., Nawrocki-Raby, B., Hinnrasky, J., Kileztyk, C., Gaillard, D., Dani, C., and Puchelle, E. (2005). Embryonic stem cells generate airway epithelial tissue. *Am. J. Respir. Cell Mol. Biol.* 32, 87–92.
- D'Amour, K.A., Agulnick, A.D., Eliazar, S., Kelly, O.G., Kroon, E., and Baetge, E.E. (2005). Efficient differentiation of human embryonic stem cells to definitive endoderm. *Nat. Biotechnol.* 23, 1534–1541.
- Daly, A.B., Wallis, J.M., Borg, Z.D., Bonvillian, R.W., Deng, B., Ballif, B.A., Jaworski, D.M., Allen, G.B., and Weiss, D.J. (2012). Initial binding and recellularization of decellularized mouse lung scaffolds with bone marrow-derived mesenchymal stromal cells. *Tissue Eng. Part A* 18, 1–16.
- Domyan, E.T., Ferretti, E., Throckmorton, K., Mishina, Y., Nicolis, S.K., and Sun, X. (2011). Signaling through BMP receptors promotes respiratory identity in the foregut via repression of Sox2. *Development* 138, 971–981.
- Gadue, P., Huber, T.L., Nostro, M.C., Kattman, S., and Keller, G.M. (2005). Germ layer induction from embryonic stem cells. *Exp. Hematol.* 33, 955–964.
- Gadue, P., Gouon-Evans, V., Cheng, X., Wandzioch, E., Zaret, K.S., Grompe, M., Streeter, P.R., and Keller, G.M. (2009). Generation of monoclonal antibodies specific for cell surface molecules expressed on early mouse endoderm. *Stem Cells* 27, 2103–2113.
- Glasser, S.W., Korfhagen, T.R., Wert, S.E., Bruno, M.D., McWilliams, K.M., Vorbroker, D.K., and Whitsett, J.A. (1991). Genetic element from human surfactant protein SP-C gene confers bronchiolar-alveolar cell specificity in transgenic mice. *Am. J. Physiol.* 261, L349–L356.
- Gonzales, L.W., Guttentag, S.H., Wade, K.C., Postle, A.D., and Ballard, P.L. (2002). Differentiation of human pulmonary type II cells in vitro by glucocorticoid plus cAMP. *Am. J. Physiol. Lung Cell. Mol. Physiol.* 283, L940–L951.
- Goss, A.M., Tian, Y., Tsukiyama, T., Cohen, E.D., Zhou, D., Lu, M.M., Yamaguchi, T.P., and Morrissey, E.E. (2009). Wnt2/2b and beta-catenin signaling are necessary and sufficient to specify lung progenitors in the foregut. *Dev. Cell* 17, 290–298.
- Goulburn, A.L., Alden, D., Davis, R.P., Micallef, S.J., Ng, E.S., Yu, Q.C., Lim, S.M., Soh, C.L., Elliott, D.A., Hatzistavrou, T., et al. (2011). A targeted NKX2.1 human embryonic stem cell reporter line enables identification of human basal forebrain derivatives. *Stem Cells* 29, 462–473.
- Gouon-Evans, V., Boussemer, L., Gadue, P., Nierhoff, D., Koehler, C.I., Kubo, A., Shafritz, D.A., and Keller, G. (2006). BMP-4 is required for hepatic specification of mouse embryonic stem cell-derived definitive endoderm. *Nat. Biotechnol.* 24, 1402–1411.
- Green, M.D., Chen, A., Nostro, M.C., d'Souza, S.L., Schaniel, C., Lemischka, I.R., Gouon-Evans, V., Keller, G., and Snoeck, H.W. (2011). Generation of anterior foregut endoderm from human embryonic and induced pluripotent stem cells. *Nat. Biotechnol.* 29, 267–272.
- Harris-Johnson, K.S., Domyan, E.T., Vezina, C.M., and Sun, X. (2009). beta-Catenin promotes respiratory progenitor identity in mouse foregut. *Proc. Natl. Acad. Sci. USA* 106, 16287–16292.



- Jiang, N., Hu, Y., Liu, X., Wu, Y., Zhang, H., Chen, G., Liang, J., Lu, X., and Liu, S. (2010). Differentiation of E14 mouse embryonic stem cells into thyrocytes in vitro. *Thyroid* 20, 77–84.
- Kattman, S.J., Witty, A.D., Gagliardi, M., Dubois, N.C., Niapour, M., Hotta, A., Ellis, J., and Keller, G. (2011). Stage-specific optimization of activin/nodal and BMP signaling promotes cardiac differentiation of mouse and human pluripotent stem cell lines. *Cell Stem Cell* 8, 228–240.
- Kimura, S., Hara, Y., Pineau, T., Fernandez-Salguero, P., Fox, C.H., Ward, J.M., and Gonzalez, F.J. (1996). The T/ebp null mouse: thyroid-specific enhancer-binding protein is essential for the organogenesis of the thyroid, lung, ventral forebrain, and pituitary. *Genes Dev.* 10, 60–69.
- Krude, H., Schütz, B., Biebermann, H., von Moers, A., Schnabel, D., Neitzel, H., Tönnies, H., Weise, D., Lafferty, A., Schwarz, S., et al. (2002). Choreaethetosis, hypothyroidism, and pulmonary alterations due to human NKX2-1 haploinsufficiency. *J. Clin. Invest.* 109, 475–480.
- Kubo, A., Shinozaki, K., Shannon, J.M., Kouskoff, V., Kennedy, M., Woo, S., Fehling, H.J., and Keller, G. (2004). Development of definitive endoderm from embryonic stem cells in culture. *Development* 131, 1651–1662.
- Lü, J., Izvolsky, K.I., Qian, J., and Cardoso, W.V. (2005). Identification of FGF10 targets in the embryonic lung epithelium during bud morphogenesis. *J. Biol. Chem.* 280, 4834–4841.
- Ma, R., Latif, R., and Davies, T.F. (2009). Thyrotropin-independent induction of thyroid endoderm from embryonic stem cells by activin A. *Endocrinology* 150, 1970–1975.
- Martinez Barbera, J.P., Clements, M., Thomas, P., Rodriguez, T., Meloy, D., Kioussis, D., and Beddington, R.S. (2000). The homeobox gene *Hex* is required in definitive endodermal tissues for normal forebrain, liver and thyroid formation. *Development* 127, 2433–2445.
- Micallef, S.J., Janes, M.E., Knezevic, K., Davis, R.P., Elefanti, A.G., and Stanley, E.G. (2005). Retinoic acid induces Pdx1-positive endoderm in differentiating mouse embryonic stem cells. *Diabetes* 54, 301–305.
- Minoo, P., Su, G.S., Drum, H., Bringas, P., and Kimura, S. (1999). Defects in tracheoesophageal and lung morphogenesis in *Nkx2.1(-/-)* mouse embryos. *Dev. Biol.* 209, 60–71.
- Monaghan, A.P., Kaestner, K.H., Grau, E., and Schütz, G. (1993). Postimplantation expression patterns indicate a role for the mouse forkhead/HNF-3 alpha, beta and gamma genes in determination of the definitive endoderm, chordamesoderm and neuroectoderm. *Development* 119, 567–578.
- Ott, H.C., Clippinger, B., Conrad, C., Schuetz, C., Pomerantseva, I., Ikonomou, L., Kotton, D., and Vacanti, J.P. (2010). Regeneration and orthotopic transplantation of a bioartificial lung. *Nat. Med.* 16, 927–933.
- Perl, A.K., Kist, R., Shan, Z., Scherer, G., and Whitsett, J.A. (2005). Normal lung development and function after *Sox9* inactivation in the respiratory epithelium. *Genesis* 41, 23–32.
- Petersen, T.H., Calle, E.A., Zhao, L., Lee, E.J., Gui, L., Raredon, M.B., Gavrilov, K., Yi, T., Zhuang, Z.W., Breuer, C., et al. (2010). Tissue-engineered lungs for in vivo implantation. *Science* 329, 538–541.
- Qin, M., Tai, G.P., Collas, P., Polak, J.M., and Bishop, A.E. (2005). Cell extract-derived differentiation of embryonic stem cells. *Stem Cells* 23, 712–718.
- Que, J., Luo, X., Schwartz, R.J., and Hogan, B.L.M. (2009). Multiple roles for *Sox2* in the developing and adult mouse trachea. *Development* 136, 1899–1907.
- Ramasamy, S.K., Mailleux, A.A., Gupte, V.V., Mata, F., Sala, F.G., Veltmaat, J.M., Del Moral, P.M., De Langhe, S., Parsa, S., Kelly, L.K., et al. (2007). *Fgf10* dosage is critical for the amplification of epithelial cell progenitors and for the formation of multiple mesenchymal lineages during lung development. *Dev. Biol.* 307, 237–247.
- Rawlins, E.L., Clark, C.P., Xue, Y., and Hogan, B.L. (2009). The *Id2* distal tip lung epithelium contains individual multipotent embryonic progenitor cells. *Development* 136, 3741–3745.
- Rippon, H.J., Ali, N.N., Polak, J.M., and Bishop, A.E. (2004). Initial observations on the effect of medium composition on the differentiation of murine embryonic stem cells to alveolar type II cells. *Cloning Stem Cells* 6, 49–56.
- Rippon, H.J., Polak, J.M., Qin, M.D., and Bishop, A.E. (2006). Derivation of distal lung epithelial progenitors from murine embryonic stem cells using a novel three-step differentiation protocol. *Stem Cells* 24, 1389–1398.
- Roszell, B.R., Mondrinos, M.J., Seaton, A., Simons, D.M., Koutzaki, S.H., Fong, G.H., Lelkes, P.I., and Finck, C.M. (2009). Efficient derivation of alveolar type II cells from embryonic stem cells for in vivo application. *Tissue Eng. Part A* 15, 3351–3365.
- Samadikuchaksaraei, A., Cohen, S., Isaac, K., Rippon, H.J., Polak, J.M., Bielby, R.C., and Bishop, A.E. (2006). Derivation of distal airway epithelium from human embryonic stem cells. *Tissue Eng.* 12, 867–875.
- Serls, A.E., Doherty, S., Parvatiyar, P., Wells, J.M., and Deutsch, G.H. (2005). Different thresholds of fibroblast growth factors pattern the ventral foregut into liver and lung. *Development* 132, 35–47.
- Sherwood, R.I., Chen, T.Y.A., and Melton, D.A. (2009). Transcriptional dynamics of endodermal organ formation. *Dev. Dyn.* 238, 29–42.
- Smith, J.R., Vallier, L., Lupo, G., Alexander, M., Harris, W.A., and Pedersen, R.A. (2008). Inhibition of Activin/Nodal signaling promotes specification of human embryonic stem cells into neuroectoderm. *Dev. Biol.* 313, 107–117.
- Spence, J.R., Mayhew, C.N., Rankin, S.A., Kuhar, M.F., Vallance, J.E., Tolle, K., Hoskins, E.E., Kalinichenko, V.V., Wells, S.I., Zorn, A.M., et al. (2011). Directed differentiation of human pluripotent stem cells into intestinal tissue in vitro. *Nature* 470, 105–109.
- Tagne, J.B., Gupta, S., Gower, A.C., Shen, S.S., Varma, S., Lakshminarayanan, M., Cao, Y., Spira, A., Volkert, T.L., and Ramirez, M.I. (2012). Genome-wide analyses of *Nkx2-1* binding to transcriptional target genes uncover novel regulatory patterns conserved in lung development and tumors. *PLoS ONE* 7, e29907.
- Tiso, N., Filippi, A., Pauls, S., Bortolussi, M., and Argenton, F. (2002). BMP signalling regulates anteroposterior endoderm patterning in zebrafish. *Mech. Dev.* 118, 29–37.
- Van Vranken, B.E., Romanska, H.M., Polak, J.M., Rippon, H.J., Shannon, J.M., and Bishop, A.E. (2005). Coculture of embryonic stem cells with pulmonary mesenchyme: a microenvironment that promotes differentiation of pulmonary epithelium. *Tissue Eng.* 11, 1177–1187.
- Wallis, J.M., Borg, Z.D., Daly, A.B., Deng, B., Ballif, B., Allen, G.B., Jaworski, D.M., and Weiss, D. (2012). Comparative Assessment of Detergent-Based Protocols for Mouse Lung De-Cellularization and Re-Cellularization. *Tissue Eng. Part C Methods*, in press. Published online January 26, 2012. 10.1089/ten.tec.2011.0567.
- Wang, D., Haviland, D.L., Burns, A.R., Zsigmond, E., and Wetsel, R.A. (2007). A pure population of lung alveolar epithelial type II cells derived from human embryonic stem cells. *Proc. Natl. Acad. Sci. USA* 104, 4449–4454.
- Williams, M.C. (2003). Alveolar type I cells: molecular phenotype and development. *Annu. Rev. Physiol.* 65, 669–695.
- Winkler, M.E., Mauritz, C., Groos, S., Kispert, A., Menke, S., Hoffmann, A., Gruh, I., Schwanke, K., Haverich, A., and Martin, U. (2008). Serum-free differentiation of murine embryonic stem cells into alveolar type II epithelial cells. *Cloning Stem Cells* 10, 49–64.
- Ying, Q.L., Wray, J., Nichols, J., Battle-Morera, L., Doble, B., Woodgett, J., Cohen, P., and Smith, A. (2008). The ground state of embryonic stem cell self-renewal. *Nature* 453, 519–523.
- Zaret, K.S., Watts, J., Xu, J., Wandzioch, E., Smale, S.T., and Sekiya, T. (2008). Pioneer factors, genetic competence, and inductive signaling: programming liver and pancreas progenitors from the endoderm. *Cold Spring Harb. Symp. Quant. Biol.* 73, 119–126.

# Derivation of lung mesenchymal lineages from the fetal mesothelium requires hedgehog signaling for mesothelial cell entry

Radhika Dixit, Xingbin Ai\* and Alan Fine\*

## SUMMARY

Recent studies have shown that mesothelial progenitors contribute to mesenchymal lineages of developing organs. To what extent the overlying mesothelium contributes to lung development remains unknown. To rigorously address this question, we employed *Wt1<sup>CreERT2/+</sup>* mice for high-fidelity lineage tracing after confirming that Cre recombinase was mesothelial specific and faithfully recapitulated endogenous Wilms' tumor 1 (*Wt1*) gene expression. We visualized WT1<sup>+</sup> mesothelial cell entry into the lung by live imaging and identified their progenies in subpopulations of bronchial smooth muscle cells, vascular smooth muscle cells and desmin<sup>+</sup> fibroblasts by lineage tagging. Derivation of these lineages was only observed with Cre recombinase activation during early lung development. Using loss-of-function assays in organ cultures, and targeted mesothelial-restricted hedgehog loss-of-function mice, we demonstrated that mesothelial cell movement into the lung requires the direct action of hedgehog signaling. By contrast, hedgehog signaling was not required for fetal mesothelial heart entry. These findings further support a paradigm wherein the mesothelium is a source of progenitors for mesenchymal lineages during organogenesis and indicate that signals controlling mesothelial cell entry are organ specific.

**KEY WORDS:** Mesothelium, Hedgehog (Hh), Lung mesenchyme, Mouse

## INTRODUCTION

The mesothelium is a thin layer of squamous epithelium that surrounds internal organs (visceral mesothelium) and lines body wall cavities (parietal mesothelium) (Mutsaers, 2004). During development, the visceral mesothelium serves as a source of progenitors for differentiated mesenchymal cells within internal organs. Using a mouse that expresses an inducible Cre recombinase from the endogenous *Wt1* locus (Zhou et al., 2008), fetal heart mesothelial progenitors were found to undergo an epithelium-to-mesenchyme transition (EMT) before giving rise to cardiomyocytes, vascular smooth muscle (VSM) and endothelial cells. In the gut, the majority of VSM cells arise from the mesothelium (Wilm et al., 2005). In the liver, the mesothelial cells migrate inward and generate hepatic stellate cells and perivascular mesenchyme (Asahina et al., 2011).

Two independent studies using Cre-lox lineage tracing produced conflicting results regarding the contribution of WT1<sup>+</sup> fetal mesothelial progenitors to the lung (Que et al., 2008; Greif et al., 2012). One study used a non-inducible *Wt1-Cre* (WT280Cre YAC) transgenic mouse line and showed that mesothelium gives rise to intrapulmonary artery VSM cells (Que et al., 2008). These results are confounded, however, by uncertainties regarding the strength, timing and specificity of the cellular marking in this transgenic Cre line. The other study, which was focused on lineages in the main pulmonary artery, used an inducible knock-in *Wt1<sup>CreERT2/+</sup>* line and showed that the mesothelium is not a significant source of smooth muscle cells for this structure (Greif et al., 2012). The precise

contribution of the early fetal lung mesothelium to lung development thus remains an open question.

Mechanisms underlying mesothelial cell entry into the developing lung are largely unknown. The importance of the hedgehog (Hh) signaling pathway in mesenchymal differentiation and the development of bronchial smooth muscle (BSM), cell migration and EMT suggest a role of Hh signaling in lung mesothelial cell entry (Bellusci et al., 1997; Weaver et al., 2003; Polizio et al., 2011; Yoo et al., 2011). Mammals express three Hh ligands: Indian hedgehog (IHH), desert hedgehog (DHH) and sonic hedgehog (SHH) (Varjosalo and Taipale, 2008). The binding of Hh ligand to the patched family receptor releases the signaling moiety smoothened (SMO) from tonic inhibition, thereby triggering activation of downstream signaling cascades and targets such as *Gli1* and patched genes. Cellular sites of active Hh signaling can thus be identified by the expression of these targets.

In this study, we performed a detailed analysis of WT1 expression, and definitively clarified the specific contribution of WT1<sup>+</sup> mesothelial lineages to the developing lung parenchyma. Our data show that the mesothelium is a source of distinct subpopulations of BSM, VSM and peri-bronchiolar fibroblasts. We further demonstrated that mesothelial cell entry into the underlying fetal lung requires active Hh signaling whereas this pathway is not operative in the fetal heart. These findings further support a paradigm wherein the mesothelium is a source of mesenchymal progenitors in development and indicate that the signals that control mesothelial cell migration are distinct for each developing internal organ.

## MATERIALS AND METHODS

### Mice

All original mouse lines were purchased from Jackson Laboratories followed by mating to generate experimental mouse lines used in our study: *Wt1<sup>CreERT2</sup>* (Jackson Laboratories stock 010912), *Rosa-CAG<sup>tdTomato</sup>*

The Pulmonary Center, Department of Medicine, Boston University School of Medicine, 72 East Concord Street, Boston, MA 02118, USA.

\* Authors for correspondence (aix@bu.edu; afine@bu.edu)

(007909), *Rosa-lacZ* (003474), *Ptch1<sup>lacZ</sup>* (003081), *Gli1<sup>lacZ</sup>* (008211), *Gli1<sup>CreERT2</sup>* (007913), *Smo<sup>fl</sup>* (004526) and *Shh<sup>Cre</sup>* (005622). For timed pregnancy, identification of the vaginal plug was considered as embryonic day (E) 0.5. To activate CreERT2, 1 mg tamoxifen (TAM) (5 mg/ml, Sigma) was injected intraperitoneally per dose. C-sections were performed on animals that developed dystocia. The pups were fostered with CD1 timed-pregnant mothers. All mouse procedures were performed in accordance with approved protocols by LASC at Boston University School of Medicine.

#### Immunohistochemistry and detection of $\beta$ -galactosidase activity

Sections of formalin-fixed rhesus macaque lung tissues (5–6  $\mu$ m) were kindly provided by Dr Alice Tarantal, National Heart, Lung, and Blood Institute (NHLBI) Center for Fetal Monkey Gene Transfer for Heart, Lung, and Blood Diseases. Dissected mouse lungs were fixed in 4% paraformaldehyde (PFA)/PBS prior to embedding and sectioning. Tissue sections (8  $\mu$ m) were blocked in 2.5% goat serum or MOM block (Vector Laboratories). High pH antigen retrieval (Vector Laboratories) was used when staining for mesothelin and WT1. Primary antibodies used include: FITC-conjugated anti- $\alpha$ -smooth muscle actin ( $\alpha$ -SMA) (1:100, Sigma), anti-WT1 (1:200, Dako), anti-desmin (1:100, Sigma), anti-SNAI2 (SNAI2 – Mouse Genome Informatics) (1:100, Cell Signaling), anti-KI67 (1:100, BD Biosciences) and anti-mesothelin (1:1000, Abbiotec). Antigen-antibody complex was visualized by fluorescence or DAB.

Staining for  $\beta$ -gal expression ( $\beta$ -gal<sup>+</sup>) was performed as described (Hogan et al., 1994). After staining, sections were washed in PBS, postfixed with 4% PFA for 4 hours and processed for paraffin embedding. Sections (5  $\mu$ m) were deparaffinized, dehydrated, and counterstained with Nuclear Fast Red.

#### In situ hybridization

*Wt1* mRNA expression on 8  $\mu$ m frozen lung sections was assessed by *in situ* hybridization as described (Ai et al., 2007). The *Wt1* antisense probe was generated from a 1.4 kb *Wt1* cDNA (Gao et al., 2005).

#### RT-PCR

Total RNA was isolated using the RNeasy Mini Kit (Qiagen). cDNA was transcribed using the GoScript reverse transcription system (Promega). All TaqMan probes were obtained from Applied Biosystems and all SYBR primers were from Integrated DNA Technologies. Quantitative real-time PCR (qRT-PCR) was performed using a Step One Plus instrument (Applied Biosystems). Assays were performed in triplicate and normalized to 18S rRNA (*Rn18s*) or *Gapdh*. Relative gene expression was calculated by the  $2^{-\Delta\Delta CT}$  method (according to the specifications of the Applied Biosystems protocol). TaqMan primers for 18S rRNA (4319413E), *Wt1* (Mm01337048\_m1), *Gli1* (Mm00494654\_m1), *Ptch1* (Mm00436026\_m1), smoothenin (Mm00449973\_m1), *Myocd* (Mm00455051\_m1) and *Nkx2.1* (Mm00447558\_m1) were purchased from Invitrogen. Primer sequences used for SYBR-based methods were: *Acta2*, forward GTCCAGACA-TCAGGGAGTAA and reverse TCGGATACCTCAGCGTCAGGA; *Gapdh*, forward AACCAGAAGACTGTGGATGG and reverse CACATTGG-GGGTAGGAACAC.

#### Lung explant cultures and time-lapse live imaging

*Wt1<sup>CreERT2/+</sup>; Rosa(tmRed)* pregnant mice were injected with TAM at E10.5 and E11.5 and embryos were harvested at E12.5. Lungs were cultured on Transwell inserts (Corning) in the presence of cyclopamine (0.5  $\mu$ M, Calbiochem) or DMSO vehicle (Radzikinas et al., 2011). After 24 hours, lungs were processed for analysis. For live imaging, tmRed<sup>+</sup> lungs were isolated from mice that had been administered one dose of TAM at E10.5. The lungs were cultured for 24 hours on Transwell inserts and transferred to a glass-bottom culture dish, placed in a 37°C humidified chamber and imaged for 2.5 hours using a Zeiss LSM 710 Live-Duo Scan 2 photon confocal microscope with a 20 $\times$  objective. For each lung, three different locations were imaged. Transmitted light was used to visualize the edge of the lung. The data were analyzed using Zen 2011 software (Carl Zeiss). Movies were generated for each focal plane and exported to a QuickTime (Apple) format at two frames per second.

#### Cell quantification

To quantify tmRed<sup>+</sup> cells in the parenchyma of lung explants, sections from three vehicle-treated controls and three cyclopamine-treated lungs were analyzed per defined unit area. For *in vivo* mesothelial loss-of-Hh signaling studies, ten lung sections from each mouse were examined. tmRed<sup>+</sup> cells in the lung parenchyma were calculated per defined lung area and quantified using ImageJ [NIH (Schneider et al., 2012)].

#### Relative quantification of tmRed<sup>+</sup> BSM

To measure the relative percentage of the smooth muscle area around bronchi that is tmRed<sup>+</sup>, lung sections were immunostained for  $\alpha$ -smooth muscle actin ( $\alpha$ -SMA). After imaging medium-sized airways, ImageJ was used to quantify the total  $\alpha$ -SMA immunoreactive area and the area that was concomitantly tmRed<sup>+</sup>. Ten airways from five mice were examined.

#### Data analysis

Data are presented as mean  $\pm$  s.e.m. Statistical analyses were performed using Student's *t*-test with *P* < 0.05 considered significant.

## RESULTS

### Identification of WT1 as a selective fetal lung mesothelial cell marker

In order to assess whether WT1 can serve as a specific marker of the fetal lung mesothelium, we analyzed the expression of mouse *Wt1* mRNA and protein by *in situ* hybridization and immunohistochemistry. We found that WT1 is localized exclusively and uniformly in visceral mesothelial cells covering the surface of the lung and in parietal mesothelial cells lining the thoracic cavity between E10.5 and E14.5 (Fig. 1A–C,G,H). As development proceeded, expression of WT1 was shut down in an increasing number of visceral mesothelial cells and, ultimately, was not detected in any adult mesothelial cell (Fig. 1D–F,I). The dynamics of *Wt1* mRNA expression was corroborated by qRT-PCR of whole mouse lung RNA (including visceral mesothelium) (supplementary material Fig. S1A). At no time point did we find any cells in the lung parenchyma that expressed *Wt1* mRNA or protein (Fig. 1A–I). A similar temporal expression pattern for WT1 was found in rhesus macaque lungs (supplementary material Fig. S1B), indicating conserved WT1 expression across mammalian species. By contrast, mesothelin, another putative mesothelial marker, was not expressed in the early lung mesothelium, although it was detected in the heart mesothelium (supplementary material Fig. S1C).

### Validation of the *Wt1<sup>CreERT2/+</sup>* mouse for genetic labeling of fetal mesothelial cells and their lineages

The restricted expression of WT1 to the fetal lung mesothelium indicated that the TAM-inducible knock-in *Wt1<sup>CreERT2/+</sup>* mouse might be an effective tool to study fetal mesothelial cell migration and fate during lung development. To establish this, we crossed the *Wt1<sup>CreERT2/+</sup>* mouse with a *Rosa(tmRed)* reporter and administered TAM at various time points. Lungs were harvested for evaluation of Cre-dependent expression of the tmRed red fluorescent marker. No tmRed<sup>+</sup> cells were detected in *Wt1<sup>CreERT2/+</sup>; Rosa(tmRed)* mice that did not receive TAM (data not shown). In addition, tmRed<sup>+</sup> cells were not detected in E18.5 lungs from mice that received a single dose of TAM (at E5 or E8) prior to the establishment of the lung primordium. Notably, a single dose of TAM at E10.5 labeled only visceral mesothelial cells in lungs isolated 24 hours later (Fig. 2A), indicating that Cre expression in the *Wt1<sup>CreERT2/+</sup>* fetal mouse lung faithfully recapitulates endogenous *Wt1* expression. After two doses of TAM at E10.5 and E11.5, the entire visceral mesothelium was tmRed<sup>+</sup> in lungs harvested at E12.5, E14.5, E18.5 and at postnatal day (P) 21 (Fig. 2B,E), showing highly efficient Cre-mediated



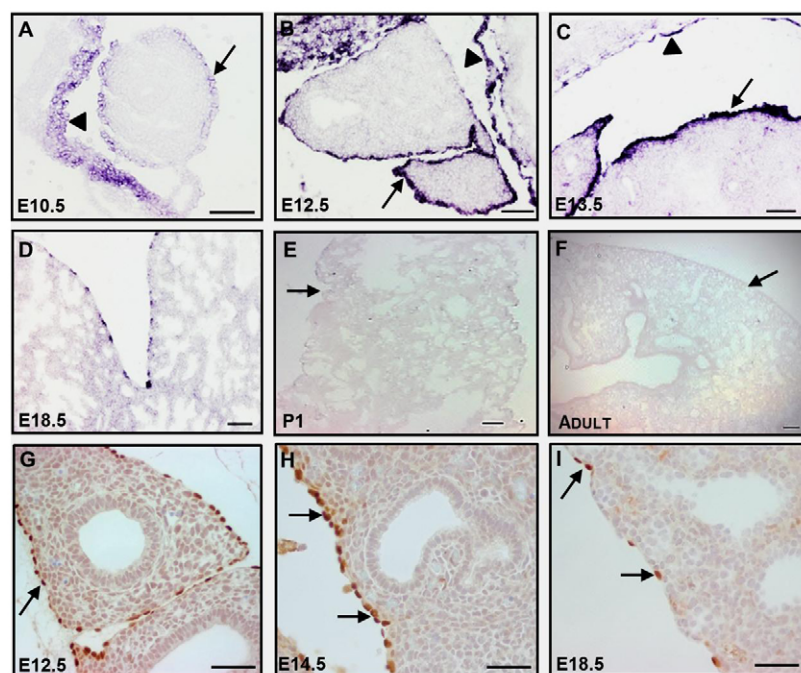


**Fig. 1. Characterization of WT1 expression in lung mesothelial cells.** (A-F) Restricted and temporal *Wt1* mRNA expression in the mouse lung mesothelium from E10.5 to adult as analyzed by *in situ* hybridization. Arrows point to the visceral mesothelium and arrowheads point to the parietal mesothelium. (G-I) WT1 immunohistochemistry in the embryonic lung. Arrows point to WT1<sup>+</sup> mesothelial cells. Scale bars: 50  $\mu$ m in A-D,G-I; 100  $\mu$ m in E,F.

recombination. In mice that received TAM injections at later gestational time points, however, there was diminished mesothelial labeling (Fig. 2F,G), consistent with the declining expression of WT1 as development advances (Fig. 1). Collectively, these findings demonstrate that WT1 is a marker of early embryonic lung mesothelium and that the *Wt1*<sup>CreERT2/+</sup> mouse is an efficient and faithful tool for characterization of mesothelial cell migration and lineage relationships during lung development.

### Migration of fetal mesothelial cells into the lung

tmRed<sup>+</sup> mesothelial cells appear thin and flat on the surface of the lung in TAM-treated *Wt1*<sup>CreERT2/+</sup>; *Rosa*(*tmRed*) mice (injection at E10.5 and E11.5) (Fig. 2A,G). However, tmRed<sup>+</sup> cells with a rounded morphology were found straddling the surface and parenchyma of the lung at E14.5 (Fig. 2H), suggesting entry into the underlying lung. Consistent with mesothelial cell migration from the surface, tmRed<sup>+</sup> cells were also found deeper within the parenchyma at E12.5, E14.5, E18.5 and P21 (Fig. 2B-E). Overall, the tmRed<sup>+</sup> mesothelium-derived cells accounted for ~5% of total lung parenchymal cells at E14.5. With later gestational TAM injections at E14.5 and E15.5, a reduced number of tmRed<sup>+</sup> parenchymal cells was observed (compare Fig. 2E with 2F). In addition, no tmRed<sup>+</sup> parenchymal cells were found in postnatal lungs after TAM injections at E17.5 and E18.5, although a few scattered visceral mesothelial cells were labeled (Fig. 2G). These observations suggest that WT1<sup>+</sup> mesothelial cells enter the fetal lung parenchyma up until ~E17.

In order to prove that WT1<sup>+</sup> mesothelial cells actively migrate into the lung parenchyma, we conducted time-lapse live imaging of lung explants. tmRed<sup>+</sup> lungs were harvested from E12.5 *Wt1*<sup>CreERT2/+</sup>; *Rosa*(*tmRed*) mice after one dose of TAM given at E10.5. The lungs were then cultured for 24 hours in an air-liquid interface prior to live imaging using a two-photon confocal microscope. Images of cells at discrete focal planes were collected every 10 minutes over 2.5 hours. During imaging, we observed thin and flat tmRed<sup>+</sup> mesothelial cells moving from the surface into parenchymal lung regions whereupon they attained a rounded morphology (Fig. 2I-L; supplementary material Movie 1). In

addition, we also observed tmRed<sup>+</sup> cells that were initially out of the focal plane but then appeared during the course of live imaging, consistent with cell movement along a vertical axis.

### Lineage analysis of fetal mesothelial cells in the lung

We performed detailed lineage analysis of the early fetal lung mesothelium using *Wt1*<sup>CreERT2/+</sup>; *Rosa*(*tmRed*) mice. TAM was administered at E10.5 and E11.5 and lungs were harvested at E18.5 and at several postnatal time points (P7, P14 and P21). At all times examined, tmRed<sup>+</sup> cells that co-express  $\alpha$ -SMA were found circumferentially positioned around airways, indicative of a BSM fate (Fig. 3A-D). These cells comprised a distinct subset of the total BSM compartment. Among five different lungs analyzed, 14% to 60% of airways contained at least one or multiple tmRed<sup>+</sup> BSM cells (supplementary material Fig. S3A). The percentage of smooth muscle surface area derived from the mesothelium ranged from 22% to 81% (supplementary material Fig. S3B). Administration of TAM at the time of lung bud formation (E9.5 and E10.5) revealed a similar pattern of tmRed<sup>+</sup> cell infiltration and of tmRed<sup>+</sup> BSM mesothelial-derived cells at E18.5 (supplementary material Fig. S2). In the postnatal lung only, we observed tmRed<sup>+</sup> cells that co-express  $\alpha$ -SMA in the walls of pulmonary arteries and veins, indicative of a VSM fate (Fig. 3E-G). We also found tmRed<sup>+</sup> peri-bronchiolar cells with a fibroblastic morphology that were  $\alpha$ -SMA<sup>-</sup> and desmin<sup>+</sup> (Fig. 3H), indicating a fibroblast cell fate.

### Active Hh signaling in WT1<sup>+</sup> fetal mesothelial cells

We next sought to identify signals that might control the entry of fetal visceral mesothelial cells into the lung parenchyma. We focused on the Hh pathway due to its specialized role in cell migration and EMT (Polizio et al., 2011; Yoo et al., 2011) and because of previous work in the fetal kidney in which it was shown that WT1 regulates the expression of Hh pathway constituents (Kreidberg et al., 1993; Hartwig et al., 2010). Using three independent reporter mouse lines, we examined whether the Hh pathway was active in the lung mesothelium between E10.5 and E16.5, a time frame that coincides

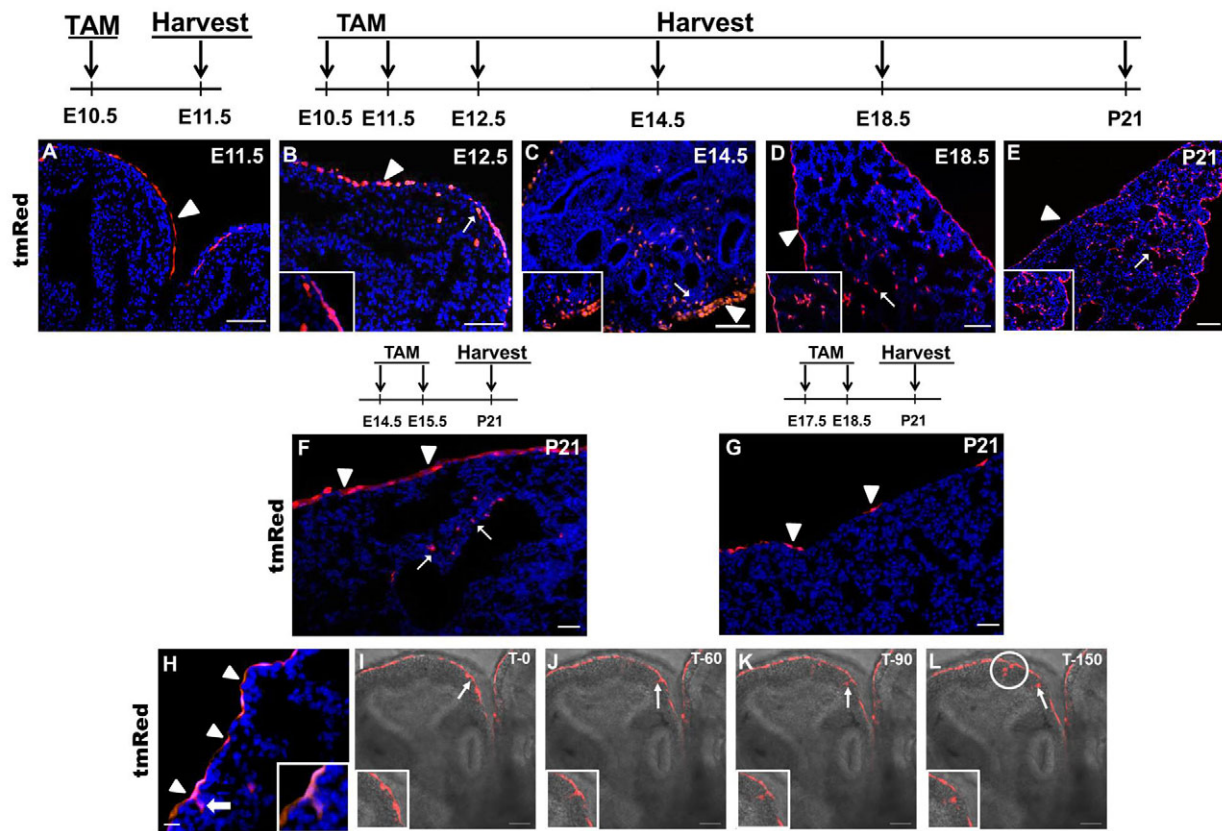


**Fig. 2. Mesothelial cell entry into the lung parenchyma.** (A–E) Examination of *tmRed*<sup>+</sup> cells in the lungs of *Wt1<sup>CreERT2/+</sup>;Rosa(tmRed)* mice at various time points after one or two doses of TAM at E10.5 and E11.5. Arrowheads point to *tmRed*<sup>+</sup> mesothelial cells and arrows point to *tmRed*<sup>+</sup> cells in the lung parenchyma, as magnified in insets. (F,G) Analysis of *tmRed*<sup>+</sup> cells in the lungs of *Wt1<sup>CreERT2/+</sup>;Rosa(tmRed)* mice at P21 after two doses of TAM at E14.5 and E15.5 (F) or at E17.5 and E18.5 (G). Arrowheads point to scattered *tmRed*<sup>+</sup> cells in the lung mesothelium. Arrows point to *tmRed*<sup>+</sup> cells in the lung parenchyma. (H) *tmRed*<sup>+</sup> mesothelial cells (arrowheads) and *tmRed*<sup>+</sup> cells that straddle the surface and the parenchyma of the lung (arrow) at E14.5 in *Wt1<sup>CreERT2/+</sup>;Rosa(tmRed)* mice that received two doses of TAM at E10.5 and E11.5. Inset is an enlargement of the straddling *tmRed*<sup>+</sup> cell. (A–H) Nuclei are counterstained with DAPI (blue). (I–L) Time-lapse series from live confocal imaging of a *tmRed*<sup>+</sup> lung explant. E12.5 lungs were isolated from TAM-treated *Wt1<sup>CreERT2/+</sup>;Rosa(tmRed)* mice and cultured on Transwell inserts for 24 hours before imaging. Sequential movie frames from a single z-focal plane show the movement of a *tmRed*<sup>+</sup> cell (arrow and magnified in inset) from the mesothelium into the lung parenchyma over 150 minutes. The appearance of three additional *tmRed*<sup>+</sup> cells in this focal plane over the 150 minutes is indicated by the white circle. The gray contours of the underlying lung are due to transmitted light. Scale bars: 50 μm.

with *Wt1* expression and mesothelial cell entry. The first reporter was a knock-in *Ptch1<sup>lacZ/+</sup>* mouse, in which *lacZ* expression parallels patched 1 (*Ptch1*) expression, a direct downstream target of Hh signaling (Bellusci et al., 1997). At E14.5 we found abundant  $\beta$ -gal<sup>+</sup> cells in the lung visceral mesothelium, indicative of active Hh signaling (Fig. 4A).

To confirm this observation, we sacrificed the *Gli1<sup>lacZ/+</sup>* reporter mouse (Bai et al., 2002) at E14.5 and similarly found  $\beta$ -gal<sup>+</sup> visceral mesothelial cells (Fig. 4B). For further validation, we employed the *Gli1<sup>CreERT2/+</sup>;R26RlacZ* reporter mouse, which carries a TAM-inducible *Cre* under the control of the Hh signaling target *Gli1* (Ahn and Joyner, 2005). This mouse was given a single dose of TAM between E10.5 and E14.5 and the lungs were analyzed at E16.5.  $\beta$ -gal<sup>+</sup> cells were found in the visceral mesothelium (Fig. 4C; supplementary material Fig. S4A) but not in the parietal mesothelium (supplementary material Fig. S4A). Consistent with published findings, active Hh signaling was also observed in other mesenchymal compartments, including the submesothelium and BSM in all three reporter mice. Notably, we did not detect any Hh-responsive cells in the heart mesothelium of TAM-treated *Gli1<sup>CreERT2/+</sup>;R26RlacZ* embryos (Fig. 4D). This latter finding is

consistent with an earlier role of Hh in heart field specification (Thomas et al., 2008). Collectively, these results demonstrate that the Hh pathway is active in the lung visceral mesothelium during a period that overlaps with WT1 expression and cell entry into the fetal lung parenchyma.

To identify the source and identity of the Hh ligand for mesothelial signaling, we assessed mRNA expression for all three Hh ligands in E14.5 lungs by qRT-PCR. *Shh* was the most abundantly expressed, whereas *Ihh* and *Dhh* were expressed at nearly undetectable levels (supplementary material Fig. S4B). We then performed *in situ* hybridization and lineage tracing using *Shh<sup>Cre/+</sup>;R26RlacZ* mice to identify SHH-producing cells. Both assays showed that *Shh* is only expressed in the lung epithelium (supplementary material Fig. S4C,D), consistent with a paracrine mode of Hh signaling to the fetal visceral mesothelium. Notably, we did not detect *Shh* expression in the visceral or parietal pleura.

### Hh signaling is required for WT1<sup>+</sup> fetal mesothelial cell entry into the lung

To further examine the role of Hh signaling in WT1<sup>+</sup> mesothelial cell entry, we isolated lungs from E12.5 *Wt1<sup>CreERT2/+</sup>;Rosa(tmRed)*



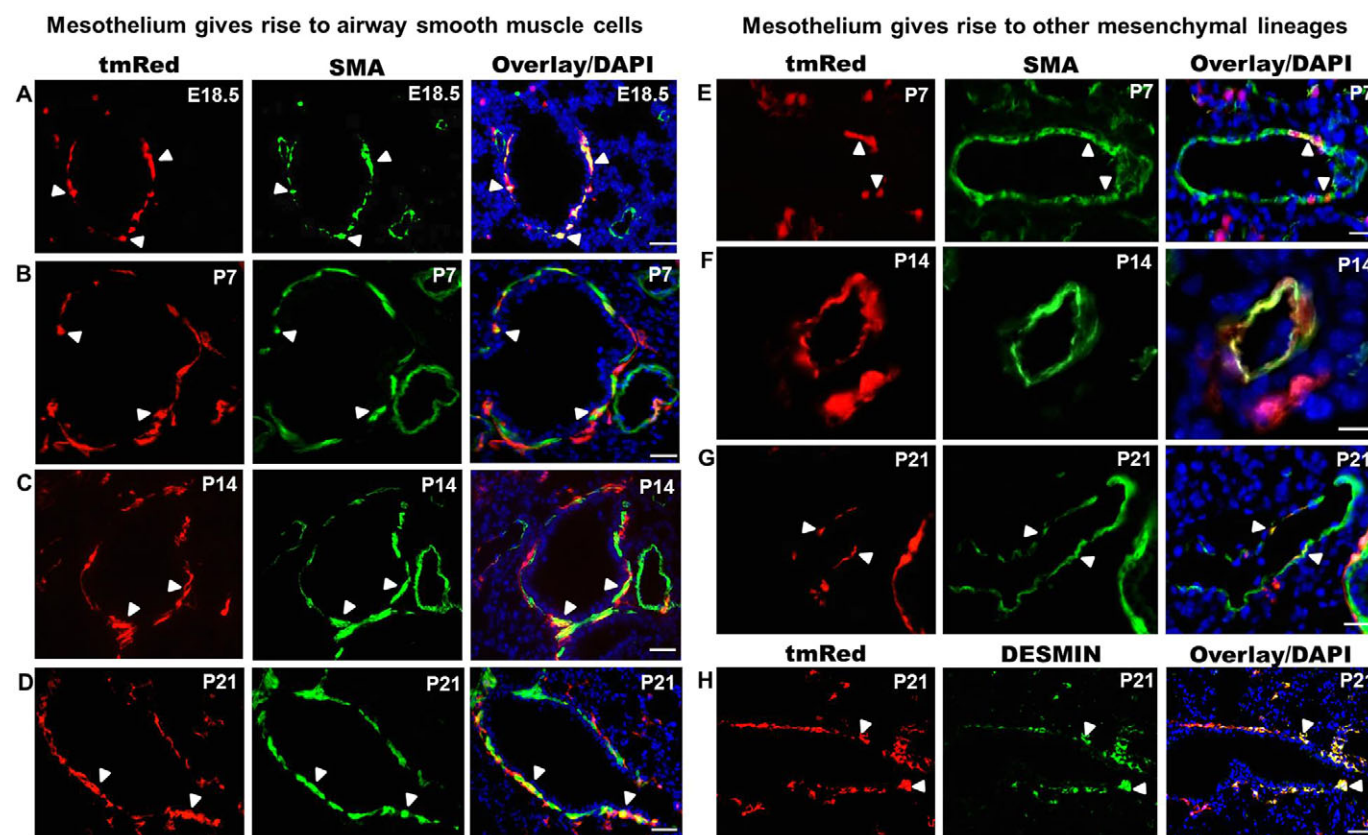


**Fig. 3. Lineage tracing of fetal lung mesothelium using *Wt1<sup>CreERT2/+</sup>;Rosa(tmRed)* mice.** TAM was given at E10.5 and E11.5 and the lungs examined at E18.5, P7, P14 and P21 for tmRed<sup>+</sup> cells that co-express  $\alpha$ -SMA or desmin. (A–D) Colocalization of tmRed and  $\alpha$ -SMA in a subset of bronchial smooth muscle cells (arrowheads) from E18.5 to P21. Vascular smooth muscle cells were not labeled with tmRed at E18.5. (E–G) Colocalization of tmRed and  $\alpha$ -SMA in postnatal vascular (E,F) and venous (G) smooth muscle cells (arrowheads). (H) Colocalization of tmRed and desmin in fibroblast cells around the airway at P21 (arrowheads). Nuclei were counterstained with DAPI (blue). Scale bars: 50  $\mu$ m.

embryos after two doses of TAM. These lungs were cultured in an air-liquid interface for 48 hours in the presence or absence of the Hh pathway inhibitor cyclopamine (Radzikinas et al., 2011). Inhibition of Hh signaling was confirmed by qRT-PCR analysis of downstream Hh targets (supplementary material Fig. S5). We assessed the number of tmRed<sup>+</sup> cells within the lung parenchyma of three DMSO vehicle-treated control lungs and three cyclopamine-treated lungs; for each lung, tmRed<sup>+</sup> parenchymal cells in eight serial sagittal sections were quantified. Cyclopamine-treated lungs

had a significant reduction ( $P < 0.05$ ) in the number of tmRed<sup>+</sup> cells ( $2.16 \pm 0.71$ /unit area compared with  $7.58 \pm 1.18$ /unit area for controls) within the lung parenchyma (Fig. 5A,B), suggesting that active Hh signaling is required for mesothelial cell entry into the lung parenchyma. Consistent with this, live imaging of cyclopamine-treated lungs revealed no migration of cells into the lung parenchyma (Fig. 5C–F; supplementary material Movie 2).

To demonstrate that Shh acts directly on fetal mesothelial cells to induce entry, we generated mesothelial loss-of-Hh signaling

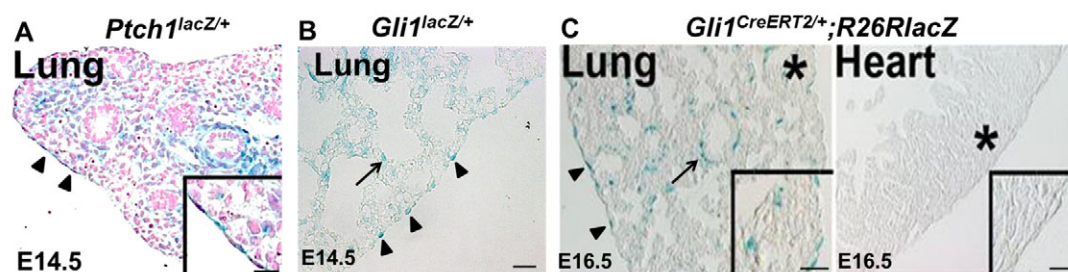


**Fig. 4. Active Hh signaling in fetal lung mesothelial cells.** (A) E14.5 *Ptch1<sup>lacZ/+</sup>* mouse lungs contained  $\beta$ -gal<sup>+</sup> visceral mesothelial cells (arrowheads and magnified in insets) and  $\beta$ -gal<sup>+</sup> submesothelial and BSM cells. Nuclei were stained with Nuclear Fast Red. (B) E14.5 *Gli1<sup>lacZ/+</sup>* reporter mice contained  $\beta$ -gal<sup>+</sup> visceral mesothelial cells (arrowheads) and  $\beta$ -gal<sup>+</sup> lung mesenchymal cells (arrow). (C) Analysis of Hh signaling in *Gli1<sup>CreERT2/+</sup>;R26RlacZ* reporter mice. TAM was injected at E12.5 and lungs were examined at E16.5.  $\beta$ -gal<sup>+</sup> cells were found in the lung mesothelium (arrowheads), BSM (arrow) and lung mesenchyme but not in the heart. Asterisk marks the area enlarged in insets. Scale bars: 50  $\mu$ m.

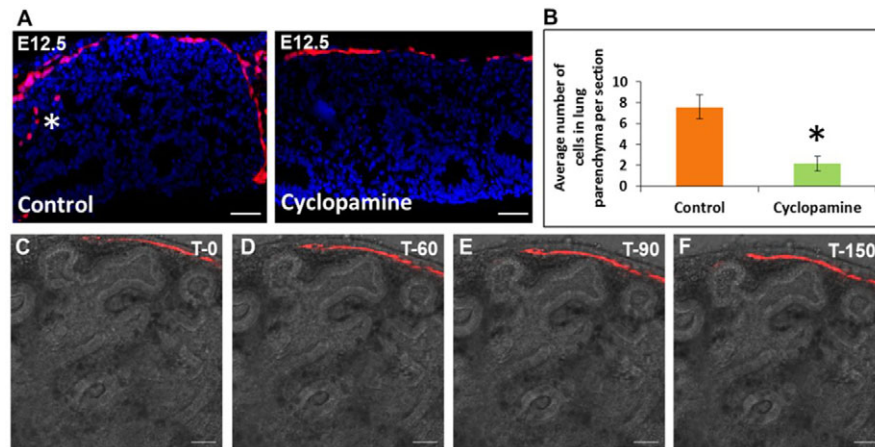


**Fig. 5. Cyclopamine blocks mesothelial cell entry into the lung parenchyma in lung explants.** (A) Effect of Hh pathway inhibition on mesothelial cell entry into cultured fetal lungs. E12.5 lungs were isolated from TAM-treated  $Wt1^{CreERT2/+};Rosa(tmRed)$  mice and cultured for 48 hours with DMSO vehicle (control) or cyclopamine (0.5  $\mu$ M). Asterisk marks mesothelium-derived  $tmRed^+$  cells in the lung parenchyma of a control lung. (B) Quantification of  $tmRed^+$  cells in the lung parenchyma of cyclopamine-treated lungs compared with controls. Data are mean  $\pm$  s.e.m. from three control and three cyclopamine-treated lungs (eight sections each). \* $P < 0.05$ . (C-F) Time-lapse series from live confocal imaging of a cyclopamine-treated lung explant. Shown are frames of a movie taken from a single z-focal plane over 150 minutes. The gray contours of the underlying lung are due to transmitted light. Scale bars: 50  $\mu$ m.

embryos by crossing  $Wt1^{CreERT2/+}$  mice with  $Smo^{fl/fl}$  mice. To allow simultaneous lineage labeling by  $tmRed$ , we took advantage of a rare recombination event that resulted in the localization of the floxed  $Smo$  gene and the  $Rosa$  locus on the same chromosome 5. Out of 74 embryos from matings between  $Wt1^{CreERT2/+};Smo^{fl/fl}$  males and  $Smo^{fl/fl};Rosa(tmRed)$  females, we identified three  $Wt1^{CreERT2/+};Smo^{fl/fl};Rosa(tmRed)$  mice. In these mutant mice, TAM administration led to mesothelial-deficient Hh signaling and concurrent activation of the lineage tag  $tmRed$ . The Hh target genes

*Gli1* and *Ptch1* were significantly downregulated in loss-of-Hh mutant lungs compared with  $Wt1^{CreERT2/+};Smo^{fl/+};Rosa(tmRed)$  littermate controls, confirming disruption of Hh signaling (Fig. 6A,B). Examination of lung sections from mutant mice revealed that the mesothelium was uniformly labeled, similar to controls (Fig. 6D). There was, however, a significant reduction ( $P < 0.05$ ) in the number of  $tmRed^+$  cells in the lung parenchyma ( $0.7 \pm 0.4$ /unit area of mutant lungs compared with  $3.91 \pm 1.0$ /unit area for littermate controls) (Fig. 6C,D). This was associated with a

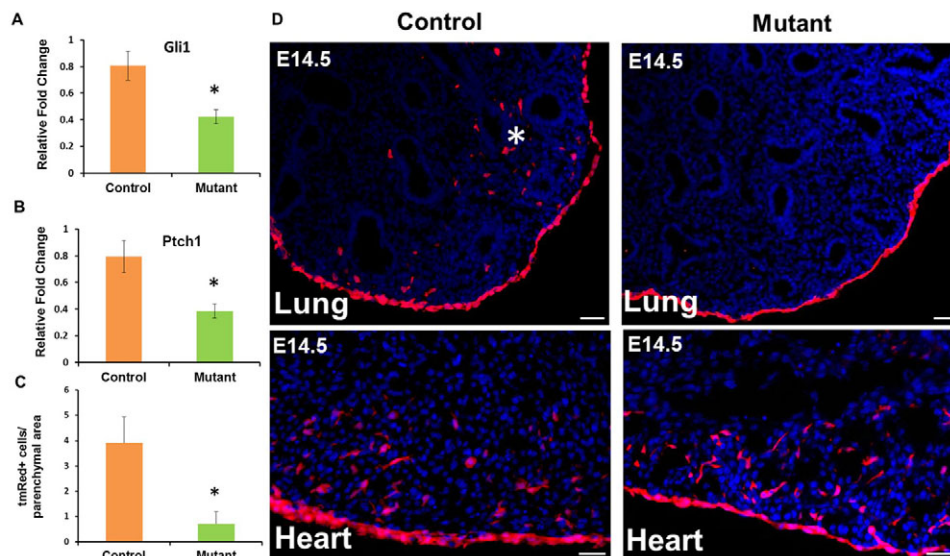


**Fig. 6. Mesothelial Hh loss-of-function prevents the appearance of mesothelium-derived cells in the lung parenchyma.** Lungs from  $Wt1^{CreERT2/+};Smo^{fl/fl};Rosa(tmRed)$  mouse embryos (mutant) and  $Wt1^{CreERT2/+};Smo^{fl/+};Rosa(tmRed)$  littermates (control) were collected at E14.5 after two doses of TAM at E10.5 and E11.5. (A,B) qRT-PCR analysis for *Gli1* and *Ptch1* mRNA expression in control and mutant lungs. Results were normalized to 18S rRNA. Data are mean  $\pm$  s.e.m. from three mice. \* $P < 0.05$ . (C) Quantification of  $tmRed^+$  cells in the lung parenchyma of mesothelial loss-of-Hh signaling mutant lungs compared with controls. The number of  $tmRed^+$  cells in the lung parenchyma was normalized by area. Data are the average ( $\pm$  s.e.m.) number of  $tmRed^+$  cells per unit area from a total of 30 lung sections, with ten sections per embryo. \* $P < 0.05$ . (D) Representative images of the lung and heart from mesothelial Hh loss-of-function mutant and control embryos at E14.5.  $tmRed^+$  cells were visualized by fluorescent microscopy. Asterisk marks  $tmRed^+$  cells in the parenchyma of a control lung. Scale bars: 50  $\mu$ m.



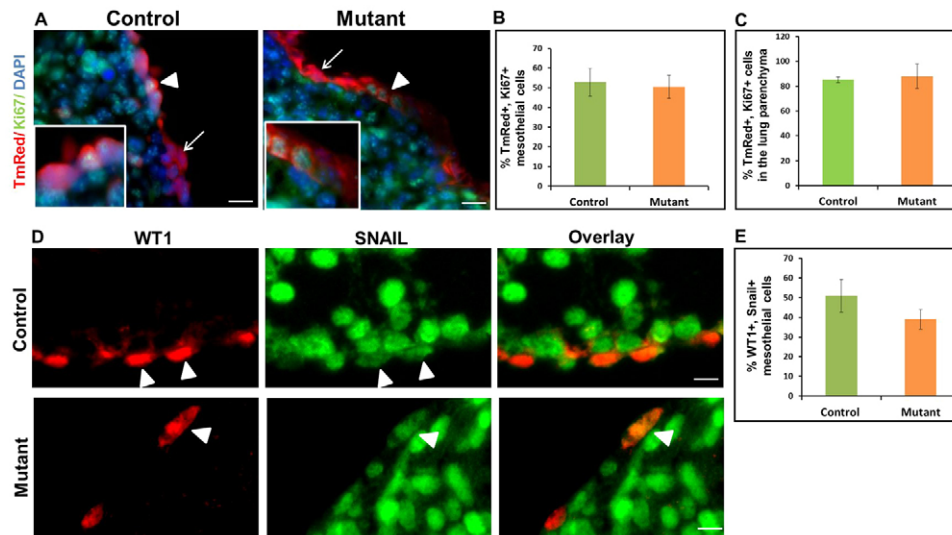


**Fig. 7. Mesothelial Hh loss-of-function has no effect on cell proliferation or SNAIL2 expression in mesothelial cells and mesothelium-derived lineages in lung parenchyma.** Lungs were dissected from E14.5 *Wt1*<sup>CreERT2/+</sup>; *Smo*<sup>f/f</sup>; *Rosa*(*tmRed*) mouse embryos (mutant) and *Wt1*<sup>CreERT2/+</sup>; *Smo*<sup>f/f</sup>; *Rosa*(*tmRed*) littermates (control) after two doses of TAM (E10.5 and E11.5). Immunohistochemistry for Ki67 and SNAIL2 was performed on lung sections from mutant and control embryos. **(A)** Ki67 immunolabeling of lung sections from mutant and control embryos. Arrowheads mark *tmRed*<sup>+</sup> mesothelial cells that were also *Ki67*<sup>+</sup>. Arrows point to *tmRed*<sup>+</sup> mesothelial cells that were *Ki67*<sup>-</sup>. **(B,C)** The percentage of *Ki67*<sup>+</sup> cells among the *tmRed*<sup>+</sup> population in the mesothelium and the lung parenchyma of control and mutant embryos. **(D)** Double staining for SNAIL2 and WT1 in the mesothelium of mutant and control lungs. Arrowheads point to SNAIL2<sup>+</sup> WT1<sup>+</sup> cells. **(E)** The percentage of SNAIL2<sup>+</sup> WT1<sup>+</sup> cells in the lung mesothelium of control and mutant embryos. Nuclei were counterstained with DAPI. Results are mean  $\pm$  s.e.m. from three mice. Scale bars: 50  $\mu$ m.

significant reduction in the expression of multiple smooth muscle-associated genes in the mutant mouse lung (supplementary material Fig. S6A). By contrast, mRNA expression of *Nkx2.1*, a key epithelium-specific transcription factor, was not affected in loss-of-Hh mutant lungs (supplementary material Fig. S6A). Grossly, mutant lungs were smaller and had a more rounded morphology at E18.5 (supplementary material Fig. S6B). Importantly, we did not detect any difference in the migration of *tmRed*<sup>+</sup> cells into mutant versus control fetal hearts (Fig. 6D).

To test whether deficient Hh signaling in mutant lungs alters the proliferation and/or apoptosis of mesothelial lineages leading to a reduced number of *tmRed*<sup>+</sup> lung parenchymal cells, we performed Ki67 and activated caspase 3 immunostaining in E14.5 mutant and control lungs. We did not detect any difference in the percentage of surface or parenchymal *tmRed*<sup>+</sup> cells that were *Ki67*<sup>+</sup> (Fig. 7A-C). In addition, we did not observe apoptosis in lungs of either genotype at this developmental stage (data not shown: fetal liver served as a positive control). Finally, to determine whether Hh loss-of-function in the visceral mesothelium affected the expression of EMT-related genes, we performed SNAIL2 immunohistochemistry and found no difference between control and mutant lungs (Fig. 7D,E).

## DISCUSSION

In this study, we employed a rigorous *Wt1*<sup>CreERT2/+</sup> lineage-tracing system whose fidelity was confirmed to identify fetal mesothelium-derived progenies. We showed that fetal WT1<sup>+</sup> mesothelial cells give rise to BSM, VSM cells and desmin<sup>+</sup> fibroblasts during embryonic and postnatal lung development. Of these cell types, only BSM was found to emerge during the embryonic period, whereas others were identified after birth, suggesting different kinetics for mesothelial progenitor differentiation between lineages. Considering that mesothelial cell entry spans several days of gestation, one possibility is that mesothelial cells that enter the lung

early give rise to BSM, whereas cells that migrate at later time points become VSM cells and fibroblast cells. Alternatively, all WT1<sup>+</sup> fetal mesothelial cells possess a similar capacity of differentiation, and their fate is determined by the environmental signals that they encounter after entering the lung.

The uniformly high efficiency of Cre recombination in our system and the fact that only subpopulations of differentiated cells were found to be *tmRed*<sup>+</sup> suggest multiple origins for the mesenchymal lineages of the lung. In this context, the primitive fetal lung mesenchyme, including Tbx<sup>+</sup> progenitors, has been shown to give rise to smooth muscle (Greif et al., 2012). Whether mesothelial and non-mesothelial progenitors have distinct and specialized roles in the development and maturation of airways, vessels and interstitium is a fundamental issue that will need to be addressed. Another key question relates to whether differentiated mesenchymal progenies with different fetal origins have discrete functional roles in homeostasis and tissue repair in postnatal life.

Using a non-inducible *Wt1-Cre* transgenic mouse, only VSM cells were found to arise from the surface mesothelium (Que et al., 2008). By contrast, we employed an inducible Cre that was knocked into the *Wt1* locus; thereby supporting rigorous lineage tracing. Furthermore, a recent lineage-tracing study using a mesothelin knock-in Cre system found that VSM cells and fibroblasts in many tissues, including lung, arise from the overlying mesothelium (Rinkevich et al., 2012). We, however, did not observe mesothelin expression in the early fetal lung mesothelium, although we did observe expression in the fetal heart mesothelium; this expression pattern is in agreement with GenePaint analysis (Visel et al., 2004). These data argue that mesothelin is not a general marker for the early lung mesothelium. Thus, mesothelin<sup>+</sup> mesothelial cells might represent a subset of progenitors whose contribution to lung development follows a timescale that is different from what we observed with WT1<sup>+</sup> progenitors.

Using complementary *in vivo* and *in vitro* assays and live imaging, we found that WT1<sup>+</sup> mesothelial cell entry into the underlying fetal lung requires the direct action of the Hh signaling pathway. Most notably, Hh signaling was not required for entry of mesothelial cells into the developing fetal heart, which is consistent with previous results showing that the canonical Wnt/ $\beta$ -catenin signaling pathway is a key signal mediating movement of heart mesothelial cells (von Gise et al., 2011). Our data suggest that lung epithelium-derived SHH ligand acts as a paracrine signal to activate Hh signaling in the overlying mesothelium. Interestingly, recent work shows that filopodia can deliver SHH ligand to targets in tissue over a long range (Sanders et al., 2013). In this context, it is important to note that the timing of SHH airway epithelial expression coincides with WT1<sup>+</sup> mesothelial cell entry (Bellusci et al., 1997). We confirmed the essential role of this pathway through the targeted disruption of mesothelial SMO function. In these mice, we demonstrated significantly reduced mesothelial cell migration into the fetal lung parenchyma without any accompanying change in the gross morphology of the overlying mesothelium, cell proliferation, expression of EMT-related genes or apoptosis. It is possible that the occurrence of tmRed<sup>+</sup> cells in the mutant lung parenchyma is due to incomplete excision of the floxed *Smo* alleles. Furthermore, we did not observe cells accumulating in the mesothelium, suggesting that Hh loss-of-function mesothelial cells are sloughed from the surface.

Based on our data, we propose two models for how Hh pathway activation controls mesothelial cell migration into the underlying fetal lung parenchyma. In the first model, SHH acts as direct chemoattractant. This model is consistent with several studies showing that SHH is a chemoattractant for multiple cell types, including neural progenitors and macrophages (Charron et al., 2003; Dunaeva et al., 2010; Polizio et al., 2011). In the second model, SHH induces a program that equips mesothelial cells with a facility for movement, which then only occurs following exposure to a second signal. In support of this second model, we did not detect any mesothelial cell movement during time-lapse imaging of cyclopamine-treated lungs. Whatever the mechanism of Hh action, WT1 expression was turned off in all cells after lung entry.

Of interest, Hh pathway activation in fetal visceral mesothelium overlaps with WT1 expression, raising the possibility of a regulatory interaction. Supporting this, WT1 binding sites have been identified within the promoter/enhancer regions of multiple Hh pathway genes, including *Smo*, *patched* and *Gli* genes (Hartwig et al., 2010). In a preliminary ChIP analysis of DNA isolated from early fetal mesothelial cells, we observed binding of WT1 to the promoters of *Smo* and *patched* genes. Together, these findings suggest that the distinct embryonic period of mesothelial migration reflects both the timing of WT1-dependent induction of Hh pathway genes and the availability of the SHH ligand.

In conclusion, our study establishes that multiple lung mesenchymal lineages arise from the fetal mesothelium during distinct developmental periods. We were also able to demonstrate that, during this process, active Hh signaling in the mesothelium is required for cells to enter the underlying parenchyma, whereupon they are likely to encounter additional signals that control their fate. The degree to which individual mesothelial cells are multipotent or hard-wired to assume a particular cell fate is an open question that requires further study.

#### Acknowledgements

We gratefully acknowledge the NHLBI Center for Fetal Monkey Gene Transfer for Heart, Lung, and Blood Diseases for providing rhesus macaque lung specimens (A. Tarantal, Principal Investigator; NIH grant #HL08574; and the

Primate Center base operating grant #OD011107). We thank Calvin Fong, Kelsi Radzikinas, Melissa Chua, Anneliese Arno and Colleen Keyes for technical assistance, and Dr Jordan Kreidberg for *Wt1* *in situ* probes.

#### Funding

This work is supported by National Institutes of Health grants [1R21HL112619 and 1R01HL116163]. Deposited in PMC for release after 12 months.

#### Competing interests statement

The authors declare no competing financial interests.

#### Author contributions

R.D. designed and performed experiments, analyzed data and wrote the manuscript. X.A. and A.F. designed the experiments and helped write the manuscript.

#### Supplementary material

Supplementary material available online at <http://dev.biologists.org/lookup/suppl/doi:10.1242/dev.098079/-/DC1>

#### References

- Ahn, S. and Joyner, A. L. (2005). In vivo analysis of quiescent adult neural stem cells responding to Sonic hedgehog. *Nature* **437**, 894-897.
- Ai, X., Do, A. T., Kusche-Gullberg, M., Lu, K., Lindahl, U. and Emerson, C. P. Jr (2006). Conserved domain structures and enzymatic activities of quail heparan sulfate 6-O endosulfatases. *J. Biol. Chem.* **281**, 4969-4976.
- Asahina, K., Zhou, B., Pu, W. T. and Tsukamoto, H. (2011). Septum transversum-derived mesothelium gives rise to hepatic stellate cells and perivascular mesenchymal cells in developing mouse liver. *Hepatology* **53**, 983-995.
- Bai, C. B., Auerbach, W., Lee, J. S., Stephen, D. and Joyner, A. L. (2002). Gli2, but not Gli1, is required for initial Shh signaling and ectopic activation of the Shh pathway. *Development* **129**, 4753-4761.
- Bellusci, S., Furuta, Y., Rush, M. G., Henderson, R., Winnier, G. and Hogan, B. L. (1997). Involvement of Sonic hedgehog (Shh) in mouse embryonic lung growth and morphogenesis. *Development* **124**, 53-63.
- Charron, F., Stein, E., Jeong, J., McMahon, A. P. and Tessier-Lavigne, M. (2003). The morphogen sonic hedgehog is an axonal chemoattractant that collaborates with netrin-1 in midline axon guidance. *Cell* **113**, 11-23.
- Dunaeva, M., Voo, S., van Oosterhoud, C. and Waltenberger, J. (2010). Sonic hedgehog is a potent chemoattractant for human monocytes: diabetes mellitus inhibits Sonic hedgehog-induced monocyte chemotaxis. *Basic Res. Cardiol.* **105**, 61-71.
- Gao, X., Chen, X., Taglienti, M., Rumballe, B., Little, M. H. and Kreidberg, J. A. (2005). Angioblast-mesenchyme induction of early kidney development is mediated by Wt1 and Vegfa. *Development* **132**, 5437-5449.
- Greif, D. M., Kumar, M., Lighthouse, J. K., Hum, J., An, A., Ding, L., Red-Horse, K., Espinoza, F. H., Olson, L., Offermanns, S. et al. (2012). Radial construction of an arterial wall. *Dev. Cell* **23**, 482-493.
- Hartwig, S., Ho, J., Pandey, P., Macisac, K., Taglienti, M., Xiang, M., Alterovitz, G., Ramoni, M., Fraenkel, E. and Kreidberg, J. A. (2010). Genomic characterization of Wilms' tumor suppressor 1 targets in nephron progenitor cells during kidney development. *Development* **137**, 1189-1203.
- Hogan, B., Beddington, R., Constantini, E. and Lacy, E. (1994). *Manipulating the Mouse Embryo*, pp. 344-351. Cold Spring Harbor, NY: Cold Spring Harbor Laboratory Press.
- Kreidberg, J. A., Sariola, H., Loring, J. M., Maeda, M., Pelletier, J., Housman, D. and Jaenisch, R. (1993). WT-1 is required for early kidney development. *Cell* **74**, 679-691.
- Mutsaers, S. E. (2004). The mesothelial cell. *Int. J. Biochem. Cell Biol.* **36**, 9-16.
- Polizio, A. H., Chinchilla, P., Chen, X., Kim, S., Manning, D. R. and Riobo, N. A. (2011). Heterotrimeric Gi proteins link Hedgehog signaling to activation of Rho small GTPases to promote fibroblast migration. *J. Biol. Chem.* **286**, 19589-19596.
- Que, J., Wilm, B., Hasegawa, H., Wang, F., Bader, D. and Hogan, B. L. (2008). Mesothelium contributes to vascular smooth muscle and mesenchyme during lung development. *Proc. Natl. Acad. Sci. USA* **105**, 16626-16630.
- Radzikinas, K., Aven, L., Jiang, Z., Tran, T., Paez-Cortez, J., Boppidi, K., Lu, J., Fine, A. and Ai, X. (2011). A Shh/miR-206/BDNF cascade coordinates innervation and formation of airway smooth muscle. *J. Neurosci.* **31**, 15407-15415.
- Rinkevich, Y., Mori, T., Sahoo, D., Xu, P. X., Bermingham, J. R., Jr and Weissman, I. L. (2012). Identification and prospective isolation of a mesothelial precursor lineage giving rise to smooth muscle cells and fibroblasts for mammalian internal organs, and their vasculature. *Nat. Cell Biol.* **14**, 1251-1260.
- Sanders, T. A., Llagostera, E. and Barna, M. (2013). Specialized filopodia direct long-range transport of SHH during vertebrate tissue patterning. *Nature* **497**, 628-632.

- Schneider, C. A., Rasband, W. S. and Eliceiri, K. W. (2012). NIH Image to ImageJ: 25 years of image analysis. *Nat. Methods* **9**, 671-675.
- Thomas, N. A., Koudijs, M., van Eeden, F. J., Joyner, A. L. and Yelon, D. (2008). Hedgehog signaling plays a cell-autonomous role in maximizing cardiac developmental potential. *Development* **135**, 3789-3799.
- Varjosalo, M. and Taipale, J. (2008). Hedgehog: functions and mechanisms. *Genes Dev.* **22**, 2454-2472.
- Visel, A., Thaller, C. and Eichele, G. (2004). GenePaint.org: an atlas of gene expression patterns in the mouse embryo. *Nucleic Acids Res.* **32**, D552-D556.
- von Gise, A., Zhou, B., Honor, L. B., Ma, Q., Petryk, A. and Pu, W. T. (2011). WT1 regulates epicardial epithelial to mesenchymal transition through  $\beta$ -catenin and retinoic acid signaling pathways. *Dev. Biol.* **356**, 421-431.
- Weaver, M., Batts, L. and Hogan, B. L. (2003). Tissue interactions pattern the mesenchyme of the embryonic mouse lung. *Dev. Biol.* **258**, 169-184.
- Wilm, B., Ipenberg, A., Hastie, N. D., Burch, J. B. and Bader, D. M. (2005). The serosal mesothelium is a major source of smooth muscle cells of the gut vasculature. *Development* **132**, 5317-5328.
- Yoo, Y. A., Kang, M. H., Lee, H. J., Kim, B. H., Park, J. K., Kim, H. K., Kim, J. S. and Oh, S. C. (2011). Sonic hedgehog pathway promotes metastasis and lymphangiogenesis via activation of Akt, EMT, and MMP-9 pathway in gastric cancer. *Cancer Res.* **71**, 7061-7070.
- Zhou, B., Ma, Q., Rajagopal, S., Wu, S. M., Domian, I., Rivera-Feliciano, J., Jiang, D., von Gise, A., Ikeda, S., Chien, K. R. et al. (2008). Epicardial progenitors contribute to the cardiomyocyte lineage in the developing heart. *Nature* **454**, 109-113.



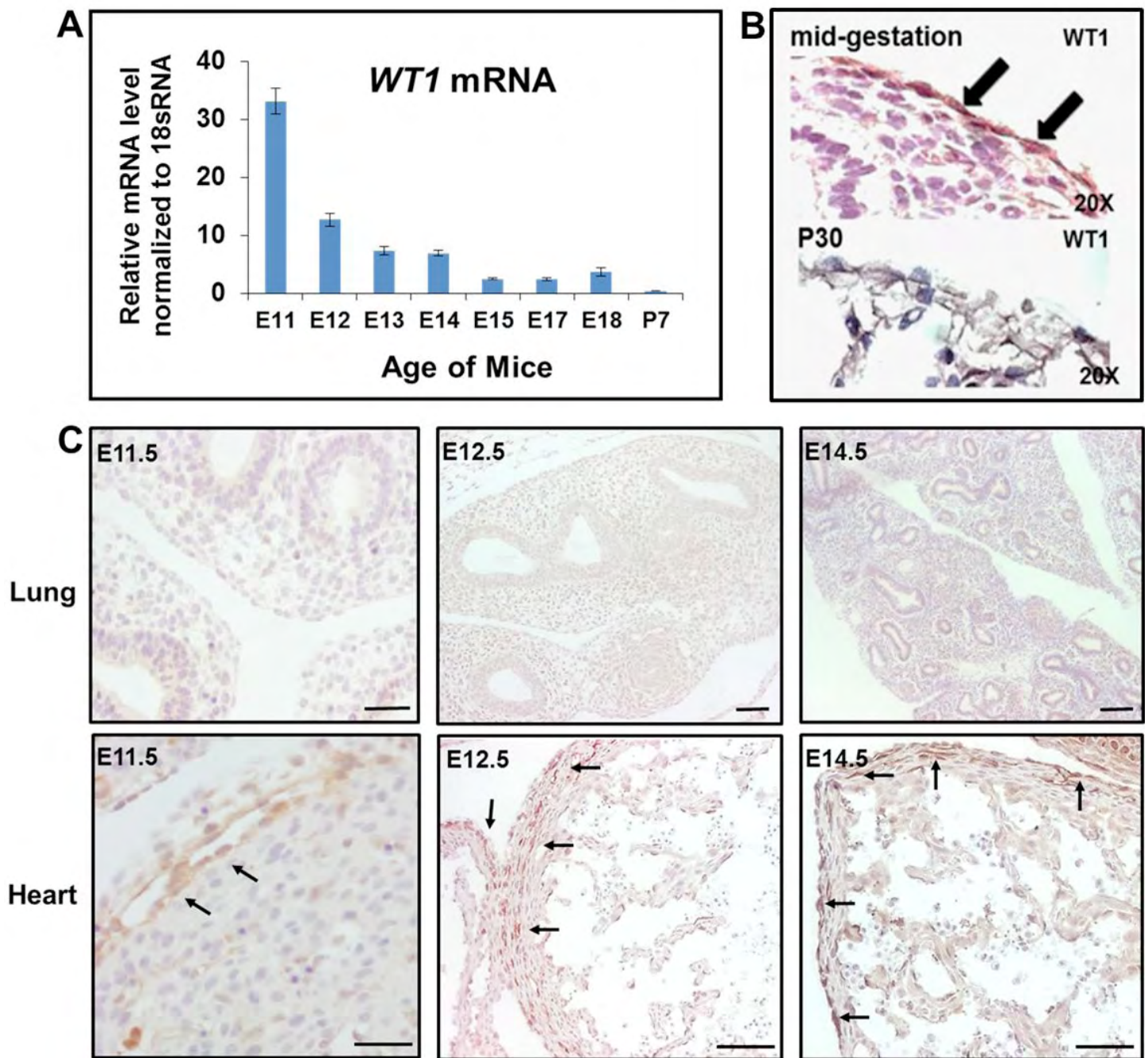


**Fig. S1. Characterization of WT1 and mesothelin expression in mesothelial cells.** (A) Temporal expression of *Wt1* mRNA in developing mouse lungs. Total RNA was extracted from whole lungs (including overlying mesothelium) of mouse embryos and postnatal day 7 (P7) pups before subjecting to qRT-PCR. Results were normalized to 18S rRNA. Data represent mean ( $\pm$  s.e.m.) from three mice for each age group. (B) Characterization of WT1 expression in *Rhesus macaque* lungs. WT1 immuno-labeling in mid-gestational (64 days) and neonatal (P30) *Rhesus macaque* lungs. WT1 protein is detected in fetal lung mesothelium (black arrow) but not in P30 lung. (C) Differential expression of mesothelin in the visceral mesothelium of the lung and the epicardium of the heart at E11.5, E12.5 and E14.5. Arrows point to mesothelin<sup>+</sup> epicardial cells. Scale bars: 50  $\mu$ m and 100  $\mu$ m.

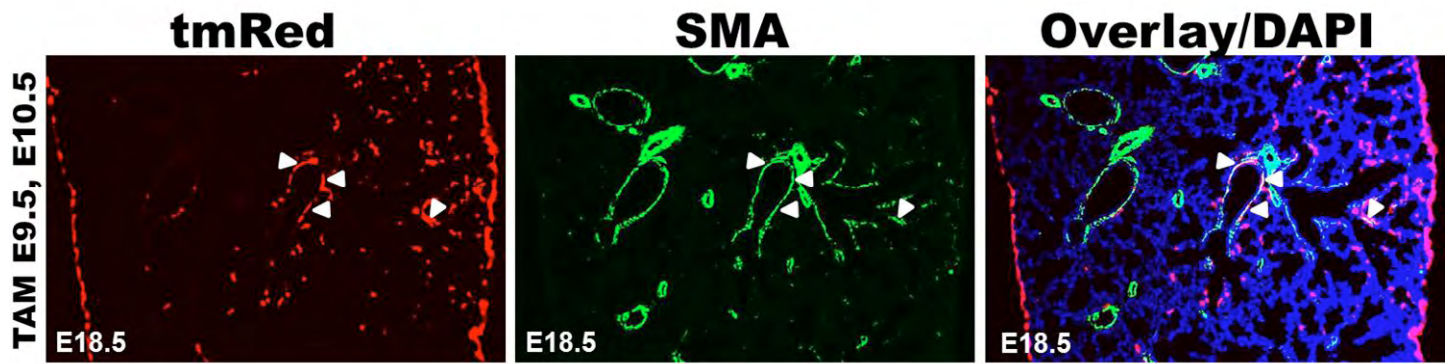


**Fig. S2. Lineage tracing of fetal mesothelium at the time of lung bud formation.** TAM was given at E9.5 and E10.5 to *Wt1<sup>CreERT2/+</sup>; Rosa(tmRed)* mice and the lungs were examined at E18.5. (A-C) Colocalization of tmRed and  $\alpha$ -SMA in a subset of BSM cells (arrowheads). Nuclei were counterstained with DAPI (Blue). Scale bars: 50  $\mu$ m.

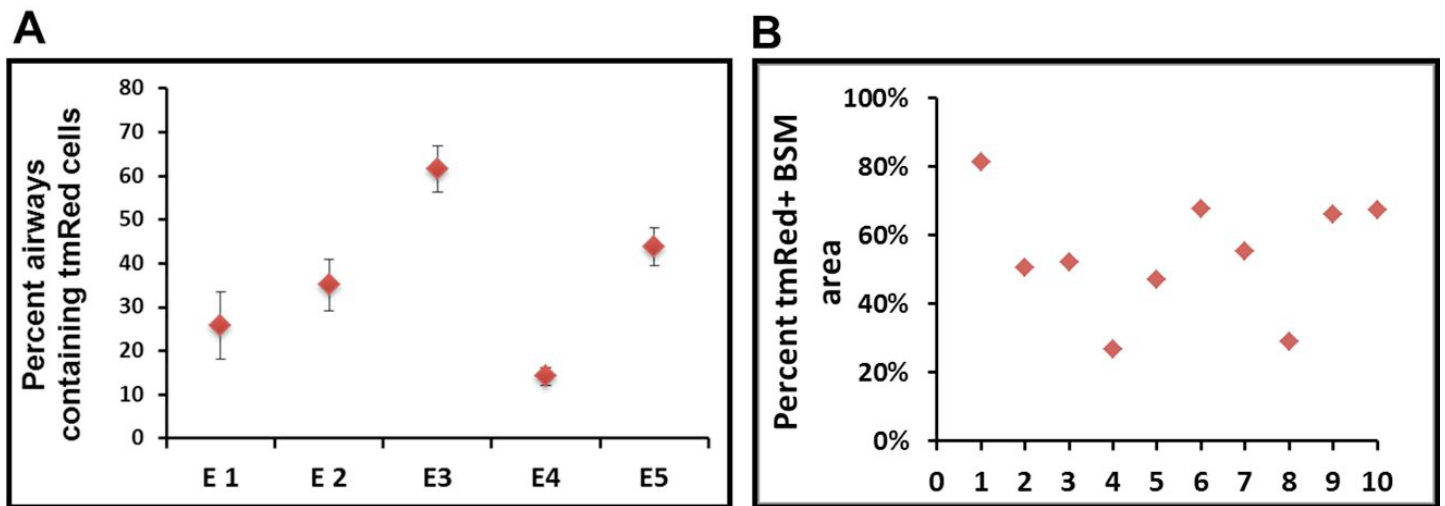


**Fig. S3. Relative contribution of fetal mesothelium-derived airway smooth muscle.** E18.5 tmRed<sup>+</sup> lungs were isolated from *Wt1<sup>CreERT2/+</sup>; Rosa(tmRed)* mice after TAM treatment at E10.5 and E11.5. Lungs were sectioned and immuno-labeled with an  $\alpha$ -SMA antibody conjugated with FITC. (A) Percent airways that contained at least one tmRed<sup>+</sup> BSM. Five embryonic lungs were analyzed with ten sections for each embryo. Data represent the average ( $\pm$  s.e.m.) for each embryo. E-Embryo. (B) Relative percent of the smooth muscle area around bronchi that is mesothelial-derived. ImageJ was used to quantify the total  $\alpha$ -SMA immune-reactive area and the area that was concomitantly tmRed<sup>+</sup>. Ten airways from five mice were examined.



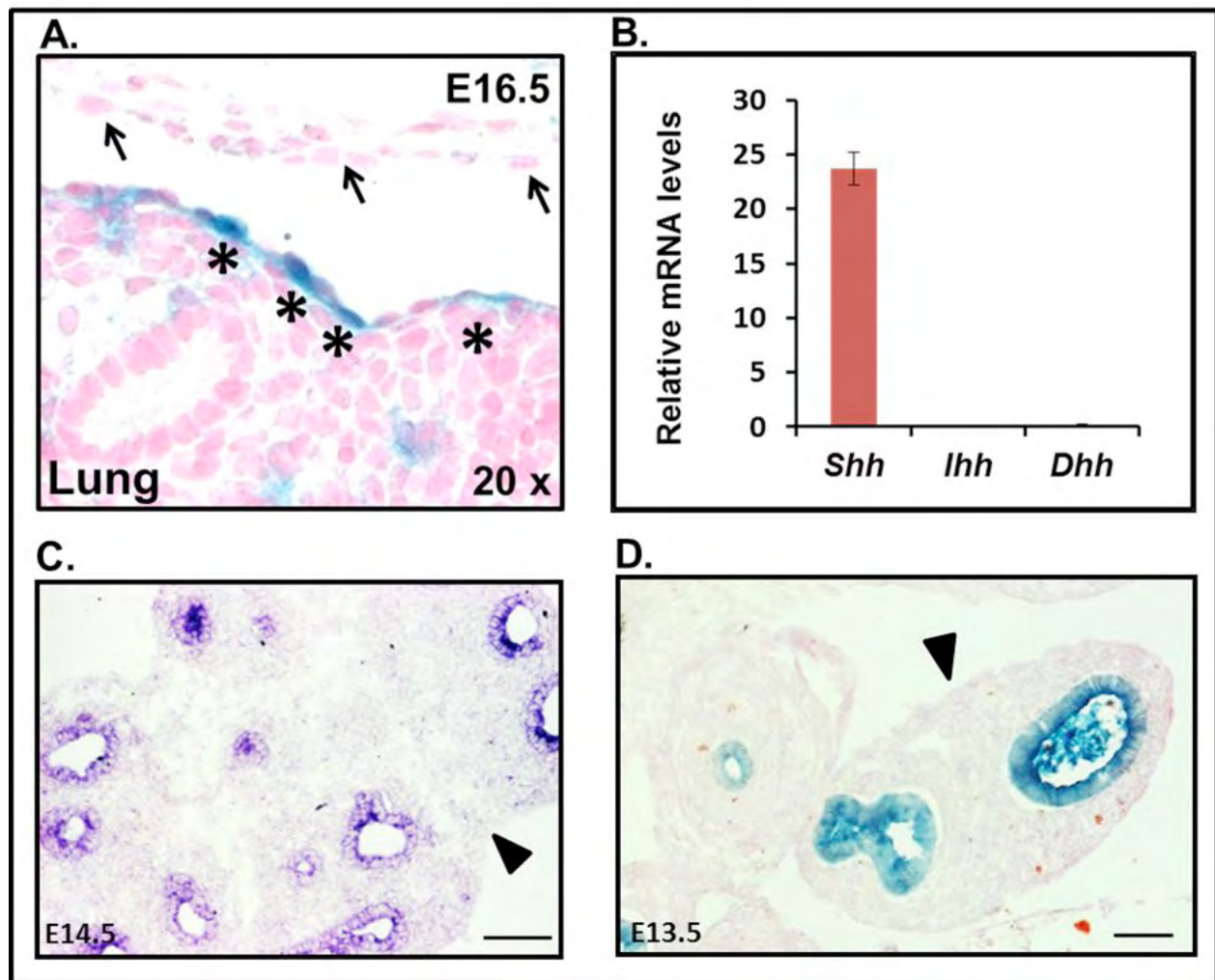


**Fig. S4. Characterization of Hh signaling and Hh ligand expression in embryonic lung.** (A) Differential Hh signaling activities in visceral and parietal mesothelium. Lungs were dissected from E16.5 *Gli1*<sup>CreERT2/+</sup>; *R26RlacZ* mice after TAM injection at E12.5. Cells in visceral mesothelium expressed  $\beta$ -galactosidase (marked by asterisk \*), indicative of active Hh signaling. In contrast, cells in parietal mesothelium (arrows) did not exhibit active Hh signaling, as indicated by a lack of  $\beta$ -galactosidase activity. Nuclei were stained with nuclear fast red. (B) Relative mRNA levels of *Shh*, *Ihh* and *Dhh* in E14.5 lungs as determined by qRT-PCR. Results were normalized to 18S rRNA. Data represent mean ( $\pm$  s.e.m.) from three different mice. (C,D) Expression of *Shh* in developing lung epithelium assayed by *in situ* hybridization at E13.5 (C) and by lineage labeling using *Shh*<sup>Cre/+</sup>; *R26RlacZ* mice at E14.5 (D). No *Shh* expression was observed in visceral mesothelium (arrowheads). Scale bars: 50  $\mu$ m.

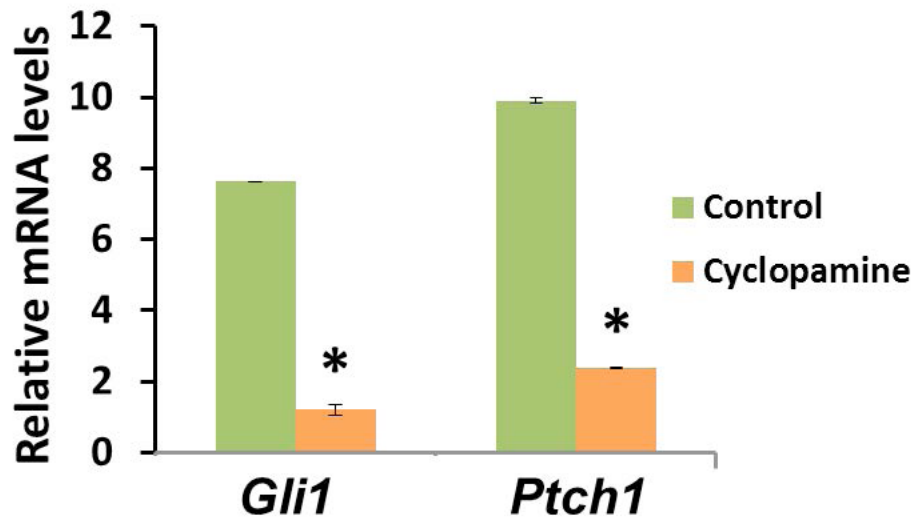


**Fig. S5. Examination of Hh activity in lung cultures.** E11.5 lungs were cultured in the presence of DMSO (vehicle) or 0.5  $\mu$ M cyclopamine (Hh pathway inhibitor) for 48 hr before gene expression analysis of Hh pathway constituents *Gli1* and *Ptch1*. Results were normalized to 18S rRNA. Data represent mean ( $\pm$  s.e.m.) from three mice. \* $p < 0.05$ .

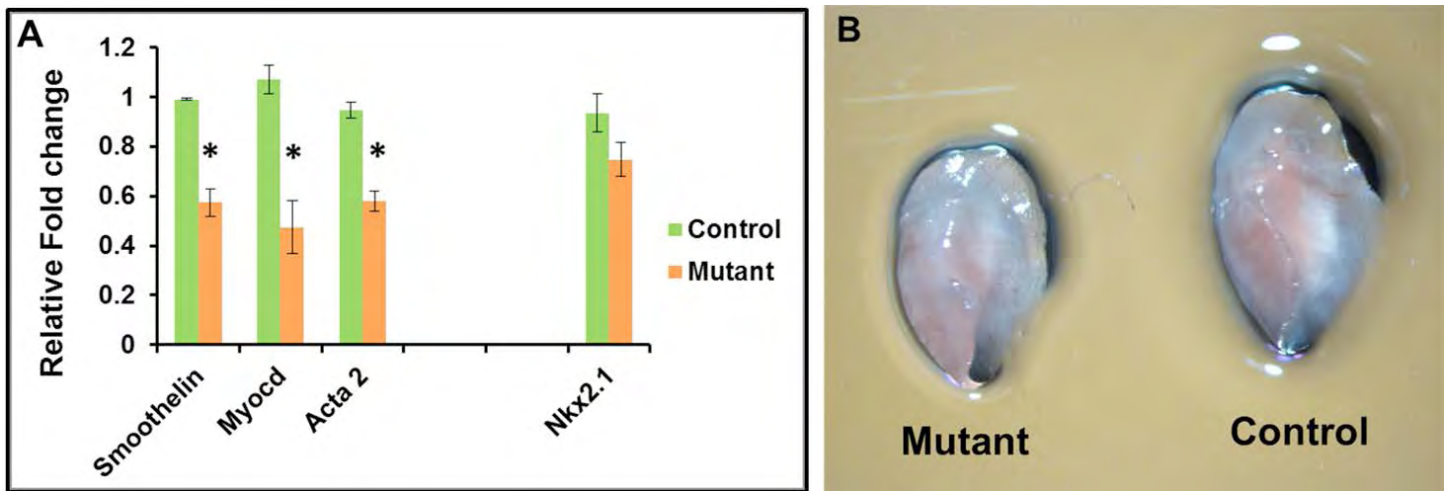
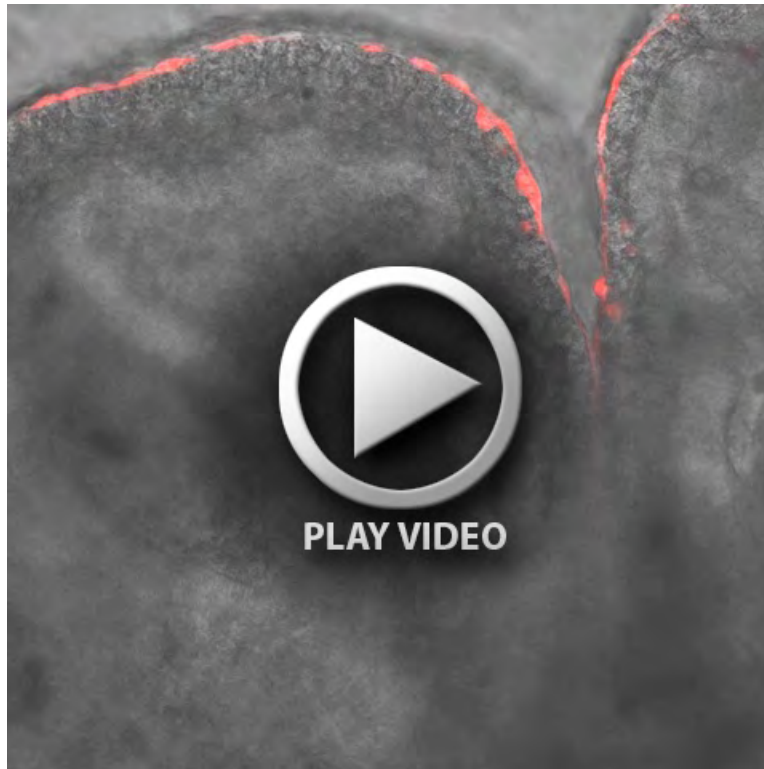


**Fig. S6. Examination of the lung phenotype in mesothelial loss-of-Hh function mutant lungs.** Lungs from *Wt1<sup>CreERT2/+</sup>;Smo<sup>flf</sup>* (mutant) and *Wt1<sup>CreERT2/+</sup>;Smo<sup>flf/+</sup>* littermate controls were analyzed at E14.5 and E18.5 after TAM administration at E10.5 and E11.5. (A) Mesothelial Hh loss-of-function mutant lungs exhibited reduced mRNA expression of smooth muscle specific genes including *Smoothelin*, *Myocd* (*myocardin*), and *Acta2* without any change in expression of the epithelium-specific transcription factor *Nkx2.1*. Results were normalized to 18S rRNA. Data represent mean ( $\pm$  s.e.m.) from three mice. \* $p < 0.05$ . (B) Mice with mesothelial Hh loss-of-function had reduced lung size at E18.5. Left lobes of mutant and control lungs were shown.



**Movie 1. Time-lapsed movie showing migration of mesothelial cells into the lung parenchyma.** E12.5 lungs were isolated from TAM-treated *Wt1<sup>CreERT2/+</sup>;Rosa(tmRed)* mice and cultured on transwell inserts for 24 hours before live imaging by confocal microscopy for 2.5 hours. Time-lapsed movie from a single Z-focal plane (corresponding to figure 2I-L) shows movement of tmRed<sup>+</sup> cells from the surface mesothelium into the lung parenchyma over 150 minutes. Note, the gray contours of the underlying lung are due to transmitted light.



**Movie 2. Time-lapsed movie showing inhibition of mesothelial cell entry by cyclopamine.** E12.5 lungs were isolated from TAM-treated *Wt1<sup>CreERT2/+</sup>;Rosa(tmRed)* mice and cultured for 24 hours in the presence of cyclopamine (Cyclo, 0.5  $\mu$ M) before imaging for 2.5 hours. Time-lapsed movie from a single Z-focal plane (corresponding to figure 5C-F) shows no mesothelial cell migration over 150 minutes. Note, the gray contours of the underlying lung are due to transmitted light.



# Mouse ES and iPS cells can form similar definitive endoderm despite differences in imprinted genes

Constantina Christodoulou,<sup>1,2</sup> Tyler A. Longmire,<sup>1</sup> Steven S. Shen,<sup>3</sup> Alice Bourdon,<sup>4</sup> Cesar A. Sommer,<sup>5</sup> Paul Gadue,<sup>6</sup> Avrum Spira,<sup>1,2,3</sup> Valerie Gouon-Evans,<sup>4</sup> George J. Murphy,<sup>7,8</sup> Gustavo Mostoslavsky,<sup>5,8</sup> and Darrell N. Kotton<sup>1,2,8</sup>

<sup>1</sup>Boston University Pulmonary Center, <sup>2</sup>Department of Genetics and Genomics, and <sup>3</sup>Section of Computational Biomedicine, Department of Medicine, Boston University School of Medicine, Boston, Massachusetts, USA. <sup>4</sup>Mount Sinai School of Medicine, Department of Gene and Cell Medicine, New York, New York, USA. <sup>5</sup>Section of Gastroenterology, Department of Medicine, Boston University School of Medicine, Boston, Massachusetts, USA. <sup>6</sup>Center for Cellular and Molecular Therapeutics, Children's Hospital of Philadelphia, Philadelphia, Pennsylvania, USA. <sup>7</sup>Section of Hematology and Medical Oncology, Department of Medicine, and <sup>8</sup>Center for Regenerative Medicine, Boston University School of Medicine, Boston, Massachusetts, USA.

**The directed differentiation of iPS and ES cells into definitive endoderm (DE) would allow the derivation of otherwise inaccessible progenitors for endodermal tissues. However, a global comparison of the relative equivalency of DE derived from iPS and ES populations has not been performed. Recent reports of molecular differences between iPS and ES cells have raised uncertainty as to whether iPS cells could generate autologous endodermal lineages in vitro. Here, we show that both mouse iPS and parental ES cells exhibited highly similar in vitro capacity to undergo directed differentiation into DE progenitors. With few exceptions, both cell types displayed similar surges in gene expression of specific master transcriptional regulators and global transcriptomes that define the developmental milestones of DE differentiation. Microarray analysis showed considerable overlap between the genetic programs of DE derived from ES/iPS cells in vitro and authentic DE from mouse embryos in vivo. Intriguingly, iPS cells exhibited aberrant silencing of imprinted genes known to participate in endoderm differentiation, yet retained a robust ability to differentiate into DE. Our results show that, despite some molecular differences, iPS cells can be efficiently differentiated into DE precursors, reinforcing their potential for development of cell-based therapies for diseased endoderm-derived tissues.**

## Introduction

It is widely accepted that early in embryonic development, broadly multipotent definitive endoderm (DE) progenitor cells of the developing foregut are specified into organ domains, such as the primordial thyroid, lung, liver, and pancreas fields (1–4). Within each domain of DE, organized along an anterior-posterior axis, these primordial progenitors rapidly give rise to all the differentiated epithelial progeny of each endodermally derived tissue. Hence, those interested in purifying thyroid, lung, liver, or pancreatic stem or progenitor cells for disease therapies are increasingly focused on using the developing embryo as a “road map” to derive these progenitors in vitro through the directed differentiation of cells whose phenotype resembles the early embryo, such as pluripotent ES cells or iPS cells (5, 6).

The recent discovery of iPS cells (7, 8) thus presents unprecedented opportunities to apply the protocols developed for the directed differentiation of ES cells in order to similarly obtain iPS cell-derived progenitor cells for tissues of all germ layers, including DE (9). Since iPS cells can be generated by reprogramming somatic cells taken from diseased adults (10, 11), we can also consider the exciting possibility of deriving autologous, disease-specific cells, such as endodermal progenitors, for potential regenerative therapies for lung, liver, or pancreatic epithelia, without fear of allogeneic rejection. Because both ES and iPS

cells resemble pluripotent cells of the early blastocyst embryo, the developmental progenitor populations derived from either population also provide novel in vitro platforms from which to evaluate the transcriptomes, epigenomes, and mechanisms that control cell fate decisions and differentiation of multipotent definitive endodermal progenitors (5, 12–14).

Several groups have recently detected differences in global gene expression profiles between ES and iPS cells, raising appropriate uncertainty as to whether iPS cells are molecularly and functionally equivalent to ES cells (15–21). If the proposed gene expression differences adversely impact the capacity of iPS cells to undergo directed differentiation into desired lineages, this would significantly dampen enthusiasm for the prospect of deriving disease-specific or patient-specific iPS cells to model and treat diseases affecting these lineages (19). With regard to endoderm, if ES or iPS cells are to be applied for the treatment of diseases affecting endoderm-derived epithelia, such as emphysema, cystic fibrosis, diabetes, and cirrhosis, it is critical to determine whether any putative difference between ES and iPS cells affects the relative endodermal potential of each cell type. Since protocols for the efficient derivation of DE from ES cells were only recently developed (6, 22), not surprisingly this germ layer has been the last to be derived from iPS cells, and only very recently have proof-of-concept studies been reported demonstrating the in vitro capacity of iPS cells to express putative endodermal markers or to form pancreatic, hepatocyte, or gut progenitors in culture (9, 11, 23, 24).

**Conflict of interest:** The authors have declared that no conflict of interest exists.

**Citation for this article:** *J Clin Invest.* 2011;121(6):2313–2325. doi:10.1172/JCI43853.





## research article

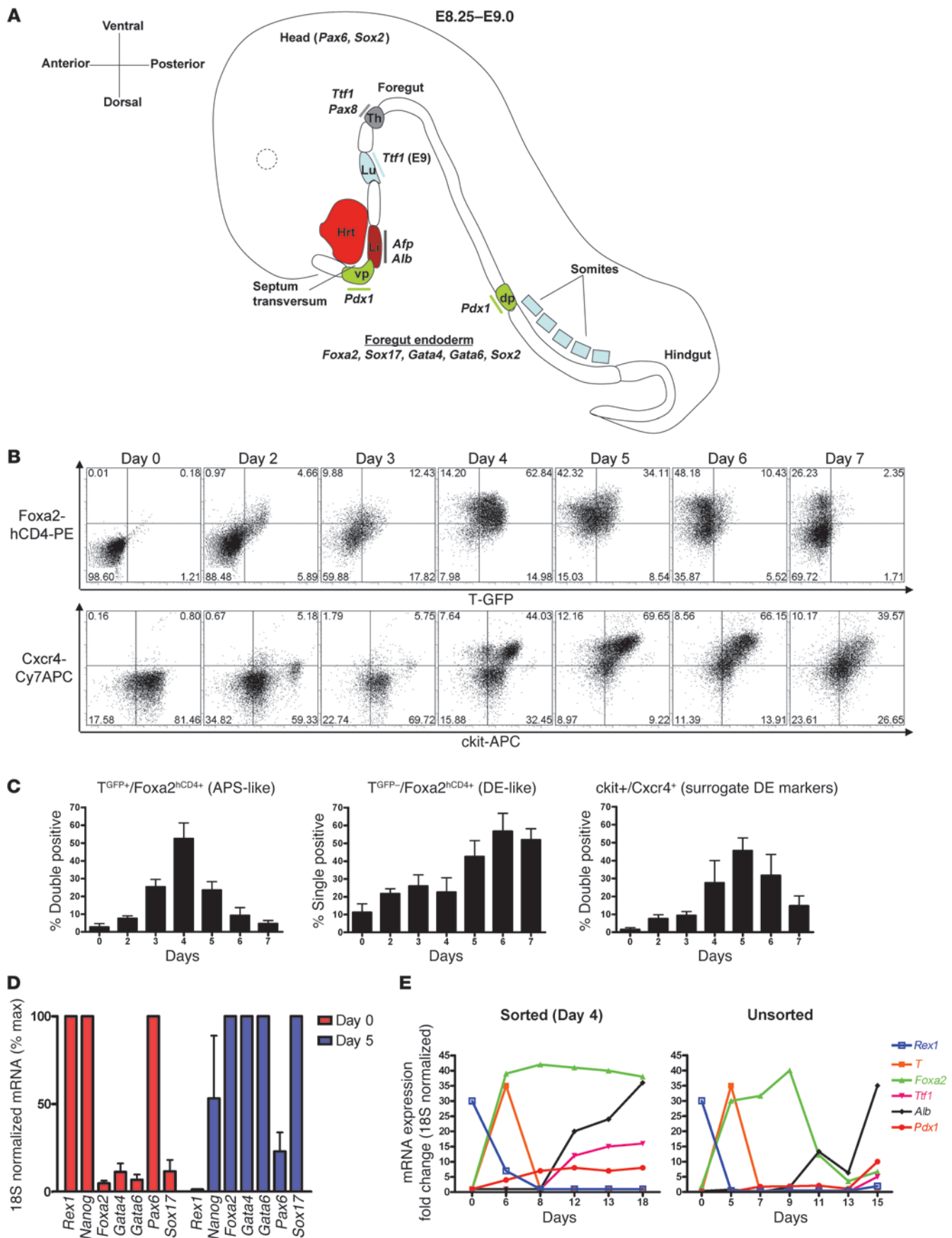






## Figure 1

Kinetics of differentiation of ES cells into DE. (A) Schematic of the mouse E8.25–E9.0 developing embryo, indicating transcription factors and marker genes induced as the foregut endoderm is patterned into prospective organ domains of thyroid, lung, liver, and dorsal/ventral pancreas. Hrt, heart; vp, ventral pancreas; Li, liver; Lu, lung; Th, Thyroid; dp, dorsal pancreas. (B) Flow cytometry quantification of the kinetics of endodermal differentiation of the 129/Ola ES cell line containing GFP and hCD4 reporters knocked-in to the brachyury (T) and *Foxa2* loci, respectively. Numbers in each quadrant indicate the percentage of cells in that quadrant. (C) Summary of endodermal differentiation kinetics of ES cells, displayed as the percentage of cells at each time point, displaying the flow cytometry profile of anterior primitive streak-like (APS-like) cells (T<sup>+</sup>/*Foxa2*<sup>+</sup>) or DE-like cells (T<sup>+</sup>/*Foxa2*<sup>+</sup>), or coexpressing *ckit*/*CXCR4*<sup>+</sup> cells, which are considered surrogate markers of endoderm differentiation. Error bars represent average  $\pm$  SEM. (D) Day 0 versus day 5 expression of transcription factors during endodermal differentiation of ES cells, as assessed by qRT-PCR. Error bars represent average  $\pm$  SEM. (E) qRT-PCR assessment of the kinetics of gene expression of ES cells in a 2-step protocol designed to accomplish DE differentiation (stage 1), followed by lineage specification (stage 2; day 6–18). T<sup>+</sup>/*Foxa2*<sup>+</sup>/*ckit*<sup>+</sup> APS-like cells were sorted on day 4 (left panel).

Here, we perform a detailed comparison of the capacity of iPS cells versus ES cells to undergo directed differentiation to definitive endodermal progenitors. Like ES cells, iPS cells respond to specified soluble ligands by proceeding through a sequence of differentiation steps that mimic the known sequence of developmental milestones encountered during authentic DE formation in the embryo. Despite these similarities, we did find notable differences in the global gene expression programs of undifferentiated iPS cells compared with those of blastocyst-derived ES cells, and some of these differences increase during endodermal differentiation, most significantly in the expression levels of maternally inherited imprinted genes localized to the delta-like 1 homolog–deiodinase, iodothyronine type III [*Dlk1-Dio3*] gene cluster on chromosome 12qF1. Although several of these imprinted genes are known to play a role in the development of endoderm-derived organs, such as the lung and liver, surprisingly, aberrantly imprinted iPS cells appear to retain robust functional capacity to undergo directed differentiation to DE progenitors and their progeny of early hepatic lineage.

## Results

In order to test the capacity of pluripotent stem cells to undergo directed differentiation to DE, we used a 2-stage serum-free culture protocol, developed by Keller and colleagues (6, 14), to recapitulate the early stages of endodermal differentiation that occur in the gastrulating embryo (Figure 1A). To establish the differentiation kinetics of pluripotent stem cells, we first used a well-characterized control 129/Ola ES cell line that features reporter transgenes, GFP and hCD4, targeted to brachyury (T) and *Foxa2* loci, respectively (13, 14). As previously published (13), this cell line demonstrated that nodal-activin signaling directed the differentiation of pluripotent stem cells into cells, reminiscent of the embryo's anterior primitive streak (defined by the phenotype T<sup>+</sup>/*Foxa2*<sup>+</sup>/*ckit*<sup>+</sup>/*CXCR4*<sup>+</sup>), followed by differentiation of these intermediates into DE (defined by the phenotype T<sup>+</sup>/*Foxa2*<sup>+</sup>/*ckit*<sup>+</sup>/*CXCR4*<sup>+</sup>; ref. 14) within 6 days in culture (Figure 1, B–D). After this first differentiation stage, the resulting DE progenitors underwent lineage specification (stage 2 hepatic-induc-

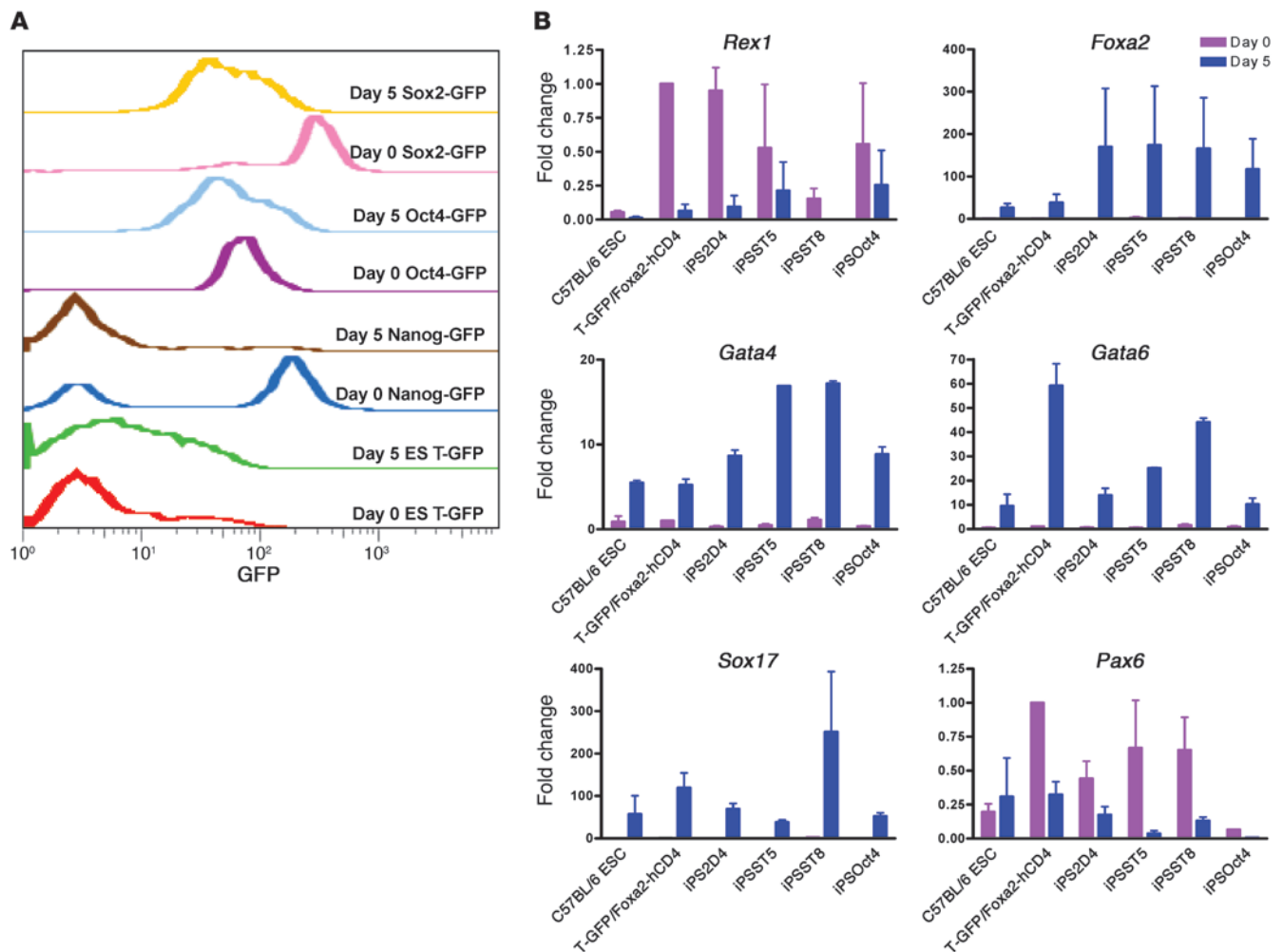
ing media; ref. 14 and Figure 1E) into cells expressing the initial transcriptional regulators or markers of primordial liver (albumin [*Alb*]) and also expressing low levels of lung or thyroid (thyroid transcription factor 1 [*Ttf1*]) and pancreatic and duodenal homeobox 1 (*Pdx1*). The waves of gene expression that define the kinetics of this differentiation sequence were evident either when assessing cells purified at intermediate stages of differentiation by flow cytometry or in unfractionated populations maintained without any cell sorting (Figure 1E). However, purification of T<sup>+</sup>/*Foxa2*<sup>+</sup>/*ckit*<sup>+</sup> anterior primitive streak-like cells on day 4 resulted in more sustained overall expression of the endodermal marker, *Foxa2*, from day 7–15 of the culture protocol, presumably due to decreased heterogeneity in the cultured progeny of sorted cells.

*Clone-to-clone variability in capacity of ES and iPS cell lines to undergo directed differentiation to DE in vitro.* Based on the differentiation kinetics of ES cells, we selected day 5 of in vitro differentiation as an optimal time when the majority of cells in each culture have differentiated into DE but have not yet undergone lineage specification to liver, thyroid, or lung. Hence, we sought to compare the capacity of iPS cells versus ES cells to undergo directed differentiation to DE over this 5-day period. We selected 4 iPS cell lines for initial testing: we previously generated the ST5 and ST8 cell lines from postnatal tail-tip fibroblasts from a Sox2-GFP knockin mouse using a doxycycline-inducible single lentiviral stem cell cassette vector (Tet-STEMCCA; ref. 25); an additional Oct4-GFP iPS cell line was generated with this vector from tail-tip fibroblasts taken from an Oct4-GFP knockin mouse (26); and a well-characterized 2D4 cell line was generated previously from Nanog-GFP knockin mice using 4 retroviral reprogramming vectors (12). Importantly, all 4 iPS cell lines tested in vivo were able to efficiently form all germ layers, including DE, in teratoma assays, in mouse chimeras after blastocyst transplantation, and (for ST8 and 2D4 lines) in second generation mice generated after germ line transmission (refs. 12, 25, and Supplemental Figure 1; supplemental material available online with this article; doi:10.1172/JCI43853DS1). Comparing these 4 iPS cell lines to 2 ES cell lines, we found that all 6 cell lines responded to the 5-day culture protocol by downregulating the expression of pluripotent transcriptional regulators (e.g., *Rex1*, *Nanog*, *Oct4*, and *Sox2*; Figure 2) and upregulating the set of essential endodermal master transcriptional regulators, such as *Foxa2*, *Sox17*, *Gata4*, and *Gata6* (Figure 2). Transcriptional regulators that are selectively active in other lineages, such as *Pax6* for neuroectoderm and *Sox7* for extraembryonic endoderm, were not upregulated over this 5-day period (Figure 2 and Supplemental Figure 2A), further suggesting that directed differentiation preferentially to the DE germ layer was accomplished in all 4 iPS cell lines. However, we noted marked clone-to-clone variability in the magnitude of this endodermal response to activin across all cell lines tested.

We considered whether the observed variability in endodermal differentiation capacity between all tested ES and iPS cell lines might be due to (a) differences in genotypes between the 2 ES lines and 3 out of the 4 iPS cell lines, (b) low levels of variable leaky expression of the integrated reprogramming transgenes in the iPS cell clones (25, 27), (c) effects of haploinsufficiency of the different loci targeted to make the different knockin reporter lines (Nanog-GFP, Sox2-GFP, or Oct4-GFP), (d) heterogeneity of cell populations produced without the use of cell sorting, or (e) inherent biological differences in the epigenetic states of each cell line. Hence, to control for genotype or knockin effects, we tested the strain-matched Sox2-GFP ES cell line used to make the mice from which the ST5 and ST8 iPS cell lines were derived



## research article

**Figure 2**

Gene expression changes in nonisogenic ES and iPS cells undergoing directed differentiation to DE over 5 days. **(A)** Flow cytometry assessment of expression of GFP reporters targeted to each indicated locus in ST8 iPS cells (Sox2-GFP), Oct4 iPS cells (Oct4-GFP), 2D4 iPS cells (Nanog-GFP), and 129/Ola ES cells (T-GFP). **(B)** qRT-PCR assessment of the levels of gene expression of each indicated marker or transcription factor on day 0 versus day 5 of directed differentiation (mean fold-change expression  $\pm$  SEM). ESC, ES cell; T-GFP/Foxa2-hCD4, 129/Ola ES cell line; iPS2D4, Nanog-GFP iPS cell line; iPSST5, Sox2-GFP clone 5 iPS cell line; iPSST8, Sox2-GFP clone 8 iPS cell line; iPSOct4, Oct4-GFP iPS cell line.

(26). We found that Sox2-GFP ES cells responded to the entire 15-day endoderm differentiation protocol with slightly slower differentiation kinetics compared with those of 129/Ola ES cells of a different genetic background (Supplemental Figure 2B). Differentiation in parallel with these strain-matched Sox2-GFP ES cells versus ST5 and ST8 iPS cell lines revealed highly similar differentiation kinetics quantified by percentages of cells expressing established surface markers, CXCR4 and klt, as well as a recently described endoderm-specific cell surface marker, ENDM1 (ref. 28 and Figure 3, A and B). Although ST8 iPS cells appeared to differentiate into endoderm slightly faster than ES or ST5 cells (Figure 3B; 2-way ANOVA,  $P = 0.04$ ), there was no statistically significant difference in the overall peak endodermal differentiation efficiency of each cell line, quantified by the percentage of cells reaching similar ENDM1 expression by day 6 (Figure 3B; ANOVA,  $P = 0.08$ ). All 3 cell lines showed the capacity to robustly proliferate in these conditions, although growth kinetics were slightly better for the parental ES cell line in 7 out of 8 repeated experiments (Figure 3B).

Next we compared the capacity of both ES and iPS cell-derived putative multipotent DE progenitors to undergo further lineage specification in response to inductive signals (stage 2 differentiation; Figure 3C). Reminiscent of the sequence of differentiation observed in developing embryos, after stimulation of the putative ES and iPS cell-derived endodermal progenitors with a defined serum-free media supplemented with lineage specifying growth factors, including BMP4, FGF2, and HGF designed to favor hepatic lineage specification, we observed sequential induction of the early liver marker genes,  $\alpha$ -fetoprotein (*Afp*) and  $\alpha$ -1 antitrypsin (*Aat*), followed by induction of *Alb* mRNA and Alb protein expression in both ES and iPS cell lines (Figure 3, C, D, and F). After 19 days of differentiation, the resulting cells also displayed glycogen storage capacity (Figure 3E). As expected for a protocol favoring directed differentiation to hepatic lineages, only low-level lineage specification to other nonhepatic endodermal lineages was detectable in all 3 cell lines, evidenced by late and transient expression of



*Ttfl*, thyroid stimulating hormone receptor (*Tshr*), intestinal fatty acid binding protein (*Ifabp*), and *Pdx1*. In this protocol, there was no induction of additional pancreatic lineage markers, such as pancreas transcription factor 1 subunit  $\alpha$  (*Ptf1a*) (Supplemental Figure 3A and data not shown). When each cell line was exposed to an established 3-stage culture protocol (29) designed to favor pancreatic lineage specification via inhibition of Shh and supplementation of FGF10 and retinoic acid, all 3 clones displayed similar early pancreatic lineage specification, indicated by induction of Hnf6, *Pdx1*, and *Ptf1a* (Supplemental Figure 3). Taken together, these waves of gene expression during differentiation to endoderm-derived lineages further supported the definitive endodermal capacity of the day 5 cells derived from each cell line in vitro. Furthermore, to demonstrate in vivo functional potential to form endoderm, unsorted day 5 iPS cell–derived putative endodermal progenitors were transplanted beneath the kidney capsules of SCID mice. These cells displayed robust capacity to form endodermal epithelia expressing nuclear Foxa2 protein (Supplemental Figure 4A), confirming the in vivo functional potential of iPS cell–derivatives following in vitro directed differentiation.

In contrast to the favorable growth kinetics we observed during differentiation of ST5 and ST8 cells, we found that additional syngeneic iPS cell lines (SEF4 and SEF11) that exhibit high-level reprogramming transgene overexpression driven by a constitutively active EF1 $\alpha$  promoter (EF1 $\alpha$ -STEMCCA; refs. 25, 27) did not robustly form endoderm in this 5-day differentiation protocol (Supplemental Figure 2C). SEF4 and SEF11 iPS cells, which showed more than 50-fold leak of reprogramming transgenes compared with that of ST5 and ST8 cells, failed to increase their cell numbers over 5 days of directed differentiation, findings in keeping with our prior work documenting the adverse effects of reprogramming transgene overexpression on the endodermal developmental capacity of iPS cells (27).

*Sox2-GFP downregulation distinguishes ES and iPS cell–derived endoderm from nonendoderm.* Although directed differentiation of the ES and iPS cell clones over 5 days into DE appeared to be efficient, heterogeneity of the cells at each time point was evident, based on (a) the residual presence of some ckit<sup>−</sup>, CXCR4<sup>−</sup>, or ENDM1<sup>−</sup> cells (Figure 3A); (b) the presence of some cells failing to express the endoderm transcriptional regulator, Foxa2, by immunostaining (Supplemental Figure 5); (c) detectable expression of mesodermal genes, *Myf5* and *Gata1* (Supplemental Figure 2A); and (d) the residual presence of cells on day 5 with nonendodermal or pluripotent potential, as reflected by the capacity of iPS cell–derived day 5 cells to form some nonendodermal lineages, such as mesodermal (smooth muscle actin<sup>+</sup>) and neuroectodermal (Tuj1<sup>+</sup>) cells in vivo after kidney capsule transplantation (Supplemental Figure 4A).

We evaluated potential strategies for distinguishing and purifying ES and iPS cell–derived DE progenitors from other cells present on day 5 of differentiation. Based on the differentiation kinetics of control ES cells (Figures 1 and 3), putative endodermal progenitors derived from ES/iPS cells by day 5 should be identifiable based on the surface phenotype ckit<sup>+</sup>/CXCR4<sup>+</sup>/ENDM1<sup>+</sup>. Analysis of the kinetics of expression of the Sox2-GFP knockin reporter also revealed residual Sox2 locus activity but at consistently lower intensity (one-half-log drop in fluorescence), as ES or iPS cells differentiated into ckit<sup>+</sup>/CXCR4<sup>+</sup>/ENDM1<sup>+</sup> cells (Figure 2A). Indeed, quantitative RT-PCR (qRT-PCR) analysis of sorted day 5 populations confirmed that putative endodermal cells could be distinguished from other cells using a Sox2-GFP<sup>dim</sup>/ckit<sup>+</sup> sort algorithm,

since endodermal marker genes were expressed preferentially in this population (Figure 4A). “Contaminating” cells expressing residual levels of Nanog and Rex1 localized to the Sox2<sup>bright</sup>/ckit<sup>−</sup> population outside this sort gate. Most importantly, decreasing the heterogeneity of the day 5 cell population by cell sorting, produced ES and iPS cell–derived endodermal cells expressing highly similar levels of endodermal master transcriptional regulators (Figure 4B). Overall, 77%  $\pm$  7.59% (average  $\pm$  SEM), 18%  $\pm$  7.32% (average  $\pm$  SEM) (2-tailed *t* test, *P* = 0.005) of cells in the sorted Sox2-GFP<sup>dim</sup>/ckit<sup>+</sup> populations expressed a putative endodermal phenotype, defined as coexpression of the endodermal markers ENDM1 and CXCR4; whereas only 18%  $\pm$  13% of Sox2-GFP<sup>bright</sup>/ckit<sup>−</sup> cells coexpressed ENDM1 and CXCR4 (*P* = 0.005).

To evaluate the in vivo differentiation potential of each sorted population derived from each ES and iPS cell clone, we performed kidney capsule transplantations in 36 SCID mice (Supplemental Figure 4). Four weeks after transplanting identical numbers of day 5 Sox2-GFP<sup>dim</sup>/ckit<sup>+</sup> cells, day 5 Sox2-GFP<sup>bright</sup>/ckit<sup>−</sup> cells, or day 18 hepatic differentiated cells (also sorted on day 5 Sox2-GFP<sup>dim</sup>/ckit<sup>+</sup> cells; data not shown), we found all transplanted cells typically gave rise to very small tumors localized to kidney capsules (0.09  $\pm$  0.21 cm<sup>2</sup>; *n* = 4 recipients per group). There was no statistically significant difference among groups in tumor size resulting from each differentiated, sorted cell population from each ES and iPS cell clone (ANOVA, *P* = 0.16). In contrast, an identical number of control undifferentiated stem cells (sorted day 0 ES Sox2-GFP<sup>bright</sup>/ckit<sup>dim</sup> cells) required recipient harvest at the 4-week end point of the study, due to abdominal distension, resulting from rapid overgrowth of the expected large 1.73 cm<sup>2</sup> teratoma (Supplemental Figure 4B), a size consistent with our prior experiments using day 0 ES cells (refs. 25, 27, and data not shown). As has been published by others (6), these findings suggest that endodermal directed differentiation of pluripotent stem cells reduces their tumorigenicity after transplantation, compared with that of undifferentiated stem cell transplants. Histological scoring of each ES and iPS cell–derived tumor revealed that endodermal epithelium was the predominant differentiated tissue type arising from each population sorted after 5 days of activation; however, no sorted population was completely depleted of mesodermal and ectodermal structures (Supplemental Figure 4D). Overall, the tumors arising from the day 5 endoderm-enriched sorted transplants were more well differentiated than the immature large teratomas that were found to arise from undifferentiated ES or iPSST5 and ST8 cell transplants, whose histology predominantly consisted of immature neural rosettes and other ectodermal keratinized derivatives in addition to endoderm and mesoderm (ref. 25 and Supplemental Figure 4B). Furthermore, in comparison with tumors arising from sorted day 5 Sox2-GFP<sup>bright</sup>/ckit<sup>−</sup> cells or from day 0 cells, the tumors arising from the sorted day 5 Sox2-GFP<sup>dim</sup>/ckit<sup>+</sup> population were relatively depleted of ectodermal skin-like keratinized epithelia (Supplemental Figure 4D). None of the 36 recipients showed any malignant features in the benign growths arising from the sorted transplants.

*Kinetics of global gene expression during endodermal differentiation of ES and iPS cells mimics that of E8.25 mouse DE in the developing embryo.* We next compared the changes in the global gene expression programs of ES cells versus iPS cells during directed differentiation into DE. Microarray analyses were performed on transcriptomes prepared from 18 samples, representing undifferentiated (day 0) ES, ST5, and ST8 iPS cells and differentiated (day 5) sorted Sox2-GFP<sup>dim</sup>/ckit<sup>+</sup> cells from each cell line. Principal components





## research article

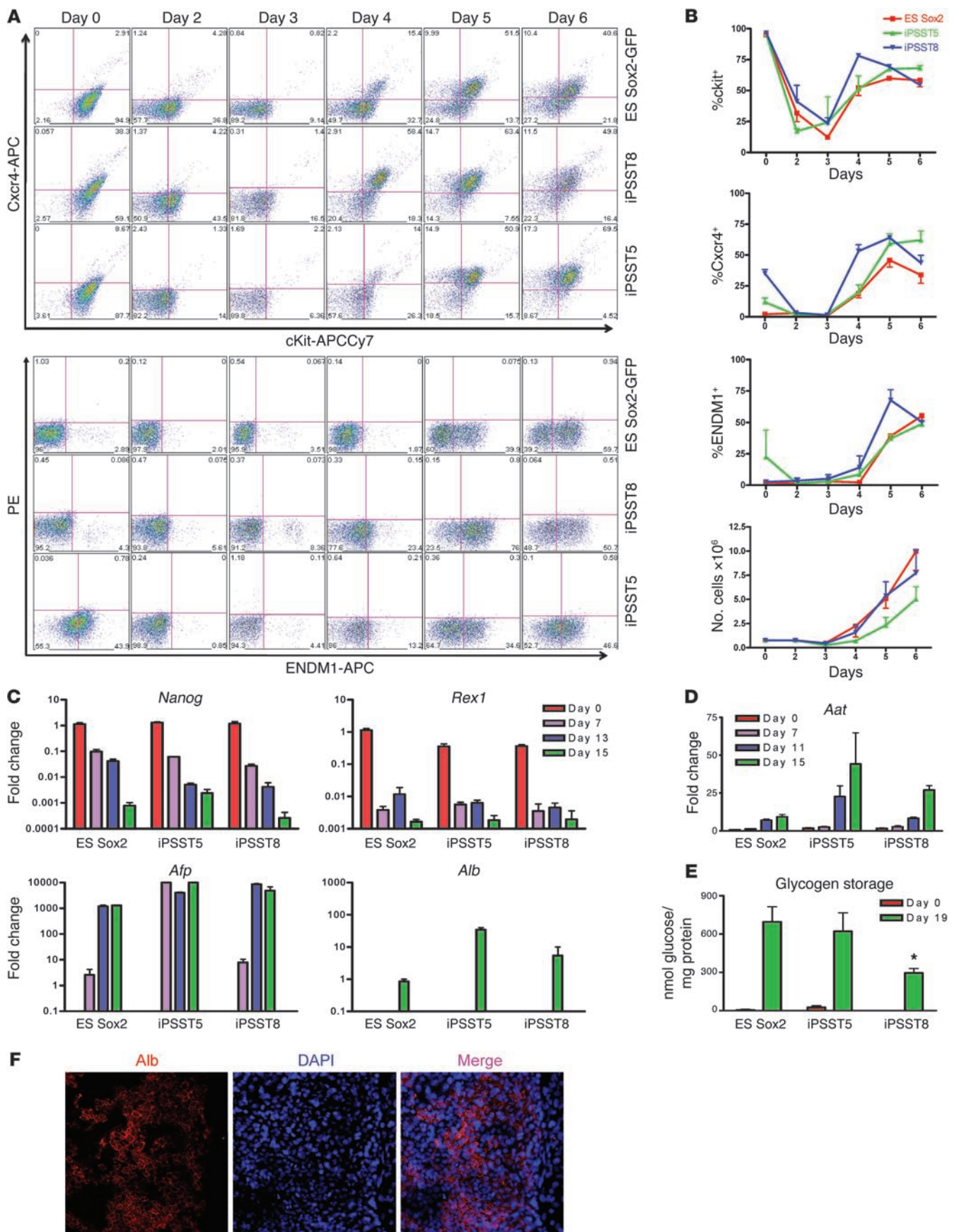




### Figure 3

Comparison of strain-matched ES and iPS cell capacity to undergo directed differentiation to DE, followed by hepatic lineage specification. (A) iPS cell clones (ST5 and ST8) and their parental syngeneic ES cells (Sox2-GFP) were differentiated in parallel to endoderm. The kinetics of expression of *ckit*, *CXCR4*, and the DE marker *ENDM1* were measured by flow cytometry. PE indicates autofluorescence. Numbers in each quadrant indicate the percentage of cells in that quadrant. (B) Summary of kinetics and cell counts from 3 repeated experiments. (C and D) Gene expression kinetics (qRT-PCR;  $n = 3$ ) during hepatic lineage specification. Note sequential decrement of pluripotent markers and induction of  $\alpha$ -fetoprotein (*Afp*), followed by  $\alpha$ -1 antitrypsin (*Aat*), followed by expression of albumin (*Alb*). (E) Glycogen storage capacity of undifferentiated (day 0) cells versus day 19 hepatocyte-like cells derived from each ES and iPS cell clone. \* $P < 0.05$ , comparing the difference in glycogen storage capacity between ST8-derived and ES-derived cells (2-tailed *t* test). (F) Albumin (red) immunostaining in day 18 iPSST5-derived hepatocytes. Nuclei were stained with DAPI (blue). Original magnification,  $\times 10$ . Graphs represent 3 biological replicates; error bars represent mean  $\pm$  SEM.

analysis across all genes measured on the array indicated that, in the undifferentiated state, the ST5 and ST8 iPS cell transcriptomes were highly similar to each other but slightly different from their parental ES cell line (Figure 5A). Differentiation over 5 days was responsible for the vast majority of the variability in gene expression across all samples (first principal component PoV = 73.3%); however, there was some variability in gene expression between different cell lines during differentiation (second principal component PoV = 10.4%; Figure 5A).

In order to interrogate the kinetics of global gene expression of each cell line during directed differentiation to endoderm, we used 2-way ANOVA of all 18 samples to identify (a) genes that are differentially expressed between day 0 and 5 of differentiation (time effect); (b) genes that are differentially expressed between ES, ST5, and ST8 cell lines (cell-type effect); and (c) gene expression differences during differentiation that are modulated by the cell line type (interaction effect of time and cell type). Endodermal differentiation from day 0 to day 5 was associated with a very large number of gene expression changes (approximately 8,000 out of approximately 29,000 probe sets were significantly associated with the time effect at false discovery rate [FDR]  $< 0.001$ ). Importantly, all master endodermal transcriptional regulators (*Foxa2*, *Gata4*, *Gata6*, *Sox17*) that were differentially expressed by qRT-PCR analysis between day 0 and day 5 (Figure 4B) were also found to be differentially expressed by this global gene expression analysis. Next, we designated the top 1,000 of these transcripts (ranked by time effect, FDR-adjusted *P* value) as a putative “1,000-gene endoderm kinetic” signature and performed cluster analysis to compare this differentiation kinetic among each cell line (Figure 5B).

When studying the directed differentiation of pluripotent stem cells, an important issue is determining how closely a putative lineage generated in vitro mimics the phenotype of its authentic counterpart that is specified during normal development in the embryo. Hence, we sought to establish whether the 1,000-gene endoderm kinetic established in our in vitro model overlapped with the authentic global gene kinetic of DE development in the mouse embryo in vivo (hereafter referred to as embryonic DE). In order to establish the global gene kinetic of embryonic DE, we prepared RNA extracts from embryonic DE cells purified by flow cytometry from E8.25 mouse embryos based on an estab-

lished ENDM1<sup>+</sup>/EpCam<sup>+</sup>/side scatter low algorithm (ref. 28 and Figure 5C). We compared the transcriptomes of these embryonic DE cells with those of undifferentiated ES cells and found 2,715 differentially expressed transcripts at the significance level of FDR  $< 0.001$ . We found this embryonic DE kinetic signature overlapped with more than 50% of the in vitro 1,000-gene endoderm kinetic (Figure 5C). These results indicate that ES and iPS cell-derived DE resembles but is not identical to E8.25 embryonic DE. Moreover, when the 2,715 genes that define embryonic DE were used to generate an unsupervised clustering dendrogram of all 18 ES and iPS cell-derived samples, ES and iPS cell-derived endoderm clearly clustered together and were distinct from the transcriptome programs of undifferentiated ES and iPS cells (Figure 5D). This cluster analysis also demonstrated that endoderm derived from the ST8 iPS cell clone appeared more similar to endoderm derived from the parental ES cells than that from the ST5 iPS cell clone.

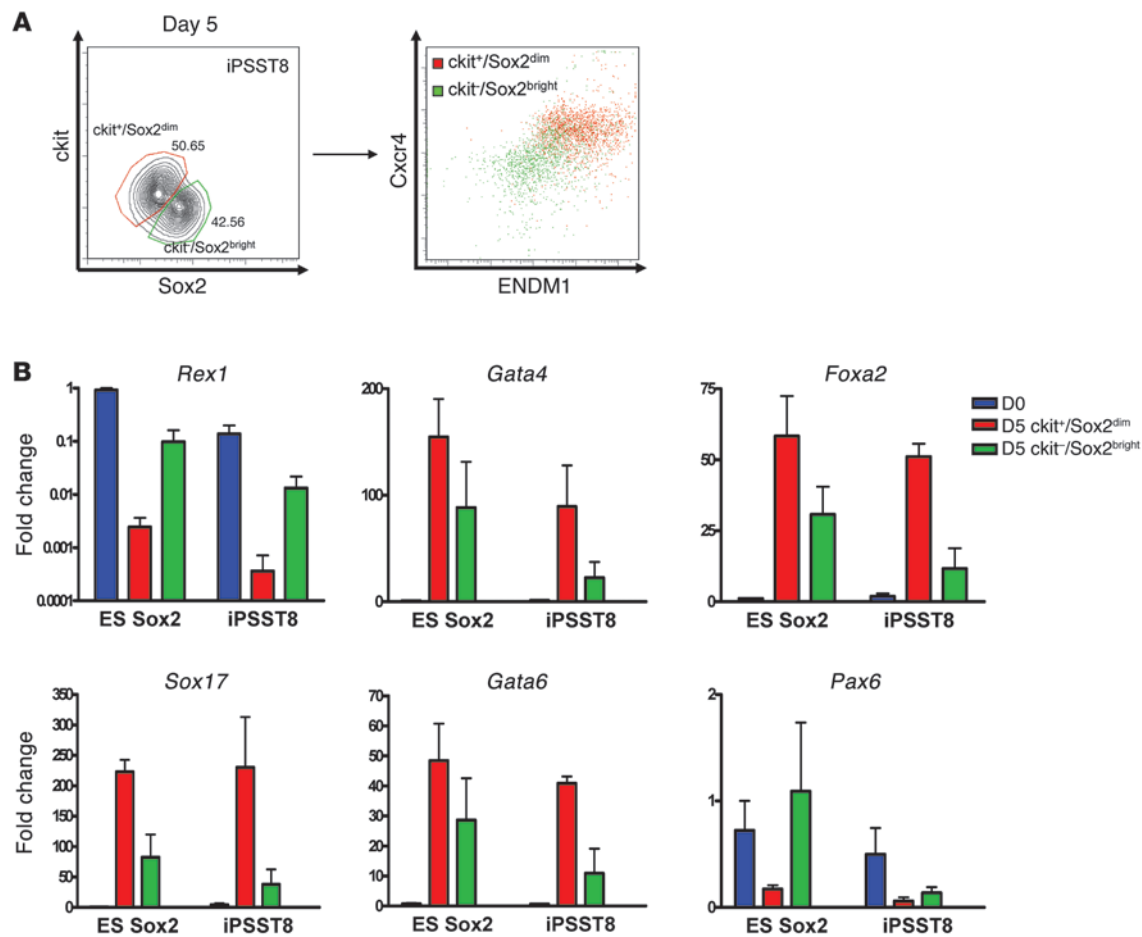
*Endodermal differentiation accentuates differences in expression levels of imprinted genes between ES and iPS cells.* To evaluate potential differences in the gene expression programs of ES cells versus iPS cells, we first compared cells in both the differentiated and undifferentiated states. We found that 111 transcripts (including mRNA, microRNA [miRNA], and small nucleolar RNA) were differentially expressed across the 3 cell lines regardless of differentiation state (cell-type effect FDR  $< 0.001$ ; Figure 6A). Clustering analysis illustrated that the majority of these transcripts distinguished the 2 iPS cell clones from their parental ES cells. Remarkably, we found 36 of these differentially expressed transcripts were encoded by the *Dlk1-Dio3*-imprinted gene cluster on mouse chromosome 12qF1 (Figure 6, A and B, and Table 1). For example, 2 of the top 3 most differentially expressed genes between iPS and ES cells were maternally expressed 3 (*Gtl2*, also known as *Meg3*) and maternally expressed 8 (*Rian*, also known as *Meg8* or *Irm*), which appeared to have low to undetectable expression levels in both ST5 and ST8 cell lines compared with those in ES cells (qRT-PCR; Figure 6C). Both these genes are noncoding RNA members of the *Dlk1-Dio3*-imprinted cluster that are typically monoallelically expressed from only the maternally inherited allele along with 5 other noncoding RNAs (30–32). Of 11 remaining transcripts that distinguished iPS cells from ES cells with more than 4-fold differential expression (fold-change cut-off set to ensure all genes met Figure 6's FDR  $< 0.001$  cutoff; Table 1), 10 were miRNAs encoded by the *Dlk1-Dio3* gene cluster, and all 10 appeared to be silenced in both iPS cell clones. Overall, 63 members of this gene cluster had known probe IDs on our microarray platform, and 36 of these were differentially expressed between ES and iPS cell lines with FDR  $< 0.001$  (Fisher's exact test for enrichment,  $P = 1.5 \times 10^{-63}$ ). These results suggested aberrant silencing of many maternally expressed members of this imprinted gene cluster in both iPS cell lines in both differentiation states.

Next we focused on gene expression differences that might distinguish ES cells from iPS cells during endodermal differentiation. Analyzing the interaction of time effect and cell type, we found that 105 transcripts were differentially expressed (FDR  $< 0.01$ ; Supplemental Figure 6), indicating that differences in expression levels of these genes emerged between the 3 cell lines during the 5 days of directed differentiation. The top-most differentially expressed of all genes was the imprinted maternally expressed gene *Gtl2* (*P* value interaction of time and cell type =  $3.59 \times 10^{-5}$ ). By qRT-PCR analysis, we confirmed that endodermal differentiation exacerbated the difference in *Gtl2* expression levels between the 3 cell lines, as *Gtl2* was upregulated in ES cells during endodermal





## research article

**Figure 4**

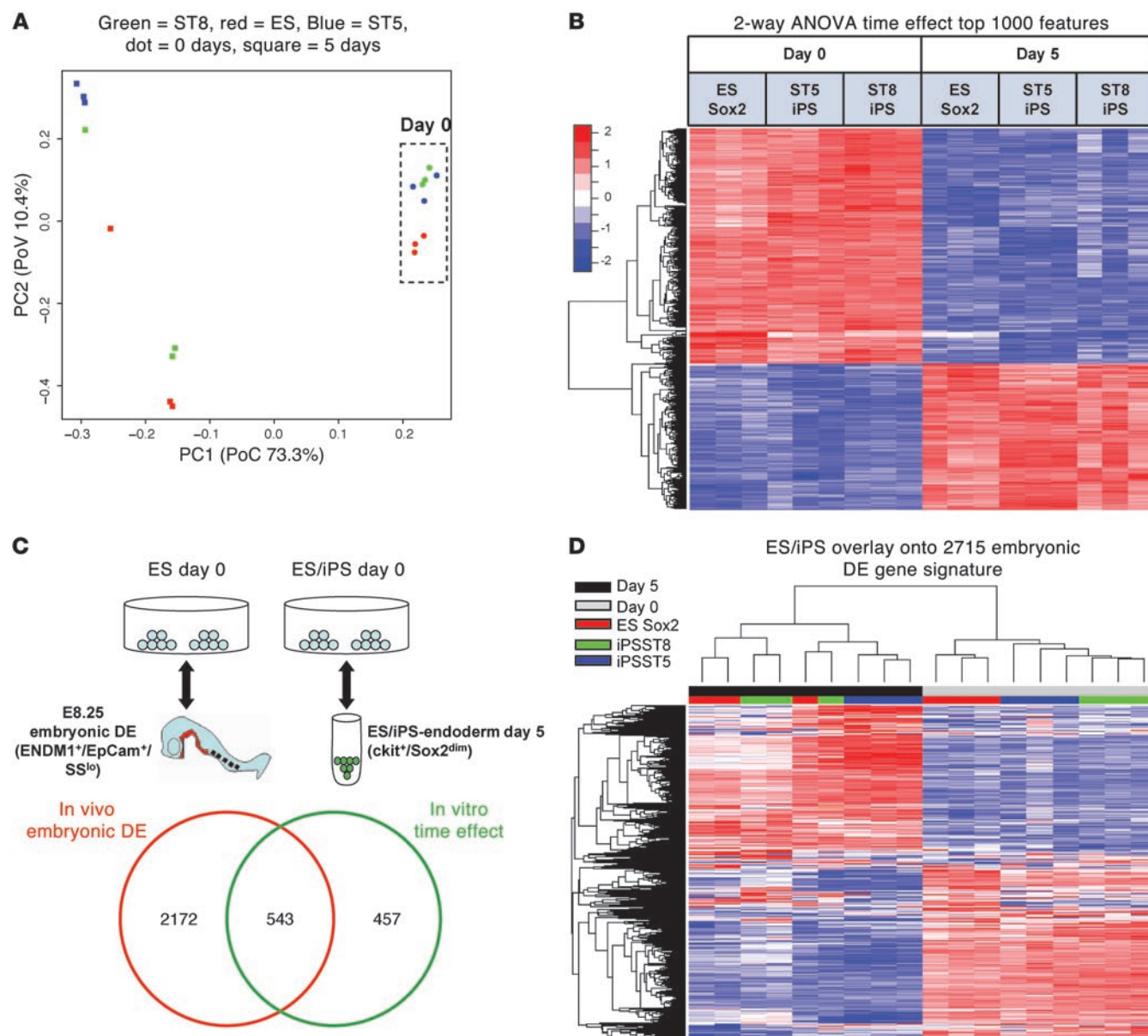
Methodology for purification of ES/iPS cell-derived endoderm. **(A)** Representative flow cytometry analysis of ckit and Sox2 expression levels in iPS cells after 5 days of directed differentiation and expression of CXCR4 and ENDM1 cell surface markers within each indicated subgate. **(B)** Comparison of gene expression profiles (qRT-PCR) of Sox2-GFP<sup>dim</sup>/ckit<sup>+</sup> and Sox2-GFP<sup>bright</sup>/ckit<sup>+</sup> sorted cell populations. Sox2-GFP<sup>dim</sup>/ckit<sup>+</sup> fractions preferentially express endodermal gene markers, while Sox2-GFP<sup>bright</sup>/ckit<sup>+</sup> fraction expresses residual *Rex1* and the neuroectodermal maker *Pax6*. D0, day 0 undifferentiated cells; D5, cells differentiated for 5 days. Error bars represent mean fold change in expression  $\pm$  SEM.

differentiation and hepatic lineage specification but remained silenced in both ST5 and ST8 iPS clones (Figure 6, C and D). In contrast, a paternally expressed gene, *Dlk1*, in this cluster was not silenced in iPS cells and was upregulated more in differentiating iPS cells than in ES cells (Figure 6C), suggesting that silencing of the maternally inherited genes was due to aberrant imprinting of the cluster rather than global silencing of both alleles of this genomic region. These findings also demonstrated that silencing of the transcripts normally expressed from the maternally inherited allele was not simply due to the differentiation state of the iPS cells.

Parental origin-specific expression of imprinted genes is typically regulated by differential DNA methylation of paternal and maternal alleles in the germline. Imprinting of the *Dlk1-Dio3* gene cluster is regulated by differentially methylated regions (DMRs), including a key intergenic region (IG-DMR) located between the *Dlk1* and *Gtl2* genes (refs. 31, 33, and Figure 6B). We found that approximately 50% of IG-DMR CpG islands were methylated in the parental ES cells or tail-tip fibroblasts prior to reprogramming, as would be expected for germ line imprinted regions (Figure 6E). In contrast, close to 100% of IG-DMR CpG islands were methylated

in ST5 and ST8 cells, both before and after endodermal differentiation. Aberrant methylation of DNA CpG islands was not evident at other loci in iPS cells, such as the Oct4 proximal promoter region, which was appropriately reprogrammed to an exclusively unmethylated state in both iPS cell lines and was amenable to developmentally appropriate initiation of CpG methylation during subsequent endodermal differentiation (Supplemental Figure 7). In addition, CpG islands around the transcriptional start site of the key endodermal master regulator, *Foxa2*, remained unmethylated in fibroblasts, ES cells, and iPS cell lines both before and after endodermal differentiation (Supplemental Figure 7), indicating that, in contrast to *Gtl2* gene regulation, epigenetic mechanisms distinct from CpG methylation are responsible for regulating expression of *Foxa2* early in development. Taken together our findings support recent reports (20) suggesting that iPS cells exhibit aberrant imprinting of the *Dlk1-Dio3* gene cluster in an exclusively paternal pattern, with resultant silencing of maternally expressed genes and overexpression of the paternally expressed imprinted gene, *Dlk1*.

We speculated that gene expression differences between ES and iPS cell lines might be particularly important if these differences

**Figure 5**

Microarray analysis of global gene expression in ES and iPS cells before (day 0) and after (day 5) endodermal differentiation. **(A)** Principal components analysis (PCA) of 18 samples reveals tight grouping of iPS cell clones in the undifferentiated state. Time effect (differentiation) is responsible for the majority of the variability in global gene expression. PC1, first principal component; PC2, second principal component. **(B)** Supervised heat map of samples across the top 1,000 genes differentially expressed with differentiation (time effect) in ES and iPS cell samples. Two-way ANOVA was used to calculate the top 1,000 probe sets, ranked by FDR-adjusted *P* value. **(C)** Venn diagram of the overlap between the genetic programs of in vivo DE from the E8.25 embryonic DE and putative DE derived from ES and iPS cells. The top 2,715 genes differentially expressed (FDR < 0.001) between undifferentiated stem cells reminiscent of the blastocyst inner cell mass and E8.25 embryonic DE are shown compared with the top 1,000 genes representing in vitro ES/iPS cell-derived DE (time effect) shown in **B**. The schematic (top) demonstrates the comparison algorithm used for each statistical analysis to calculate the 2 indicated gene kinetic signatures. **(D)** Unsupervised clustering of the 18 in vitro samples shown in **A** and **B** across the 2,715 embryonic DE gene signature list from the E8.25 embryo. Unsupervised clustering indicates similar transcriptome changes in ES and iPS cells with in vitro differentiation.

were associated with an altered capacity to undergo directed differentiation or lineage specification to desired target cell lineages, such as endoderm. Indeed deletion of maternally inherited *Gtl2* in mice is known to result in early postnatal defects in at least 2 endodermally derived epithelia, such as pulmonary alveolar hypoplasia

and hepatocellular necrosis (32). Thus, we sought to determine whether silencing of *Gtl2* due to aberrant imprinting of the *Dlk1-Dio3* gene cluster in iPS cells might be associated with altered endodermal differentiation capacity compared with ES cells. Although we had found no detectable difference among ST5 cells, ST8 iPS



## research article

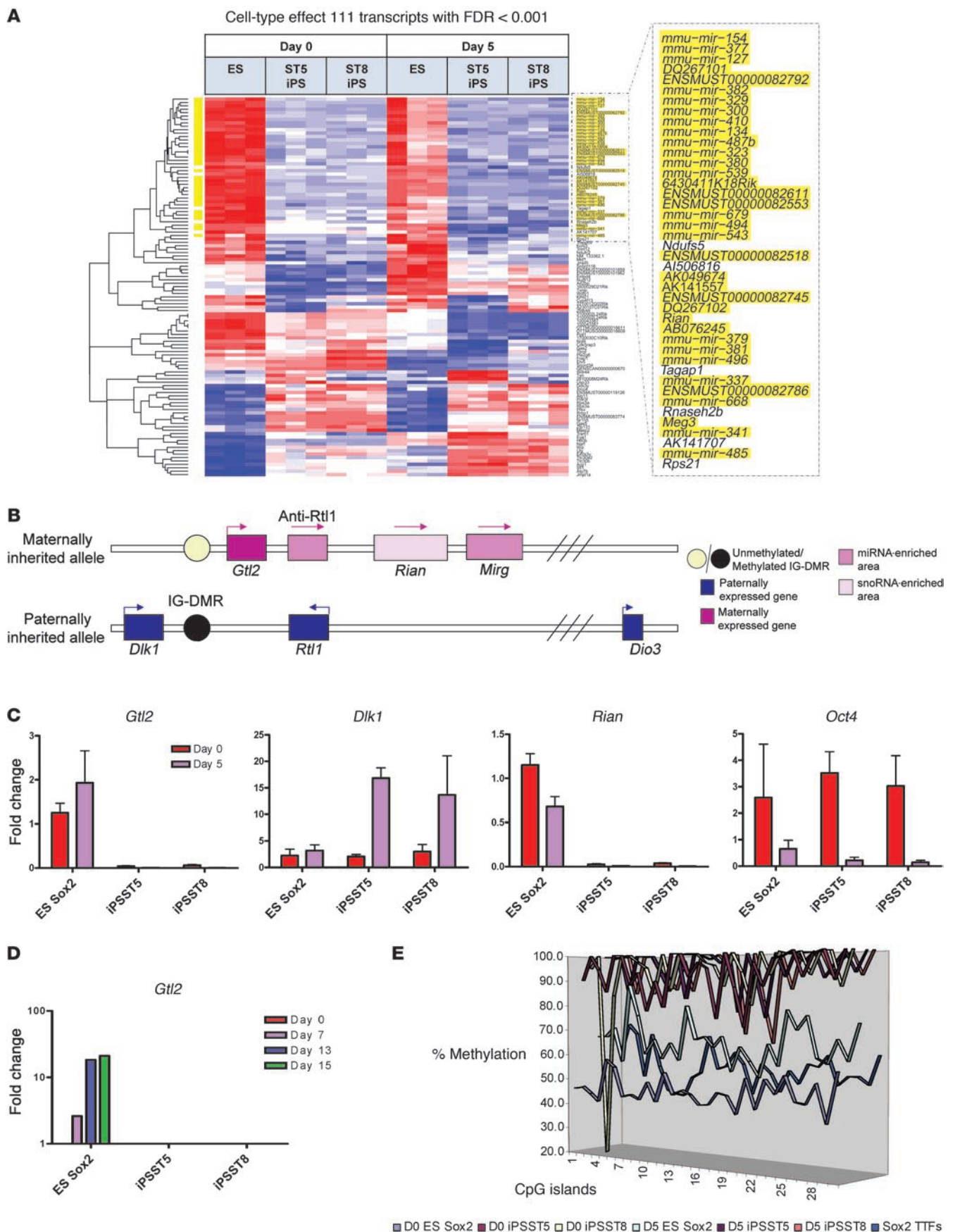






## Figure 6

Analysis of cell-type effects between ES and iPS cell samples, regardless of differentiation stage, reveals aberrant silencing of genes encoded by the *Dlk1-Dio3*-imprinted gene cluster on chromosome 12qF1. (A) Unsupervised clustering analysis of the top 111 transcripts differentially expressed due to cell-type effects, based on 2-way ANOVA with  $FDR < 0.001$ . Yellow highlighting indicates the 36 transcripts that localize to chromosome 12qF1 in the region of the *Dlk1-Dio3* gene cluster. (B) Schematic representation of the mouse *Dlk1-Dio3*-imprinted gene cluster. (C) Validation of microarray analysis through qRT-PCR quantification of each indicated gene, normalized to 18S rRNA ( $n = 3$ ; data shown as average  $\pm$  SEM). (D) qRT-PCR analysis of *Gtl2* expression kinetics during 15 days of endoderm differentiation, followed by hepatic lineage specification. During differentiation, *Gtl2* expression is upregulated in ES cells, while remaining silenced in ST5 and ST8 iPS clones. (E) Mouse *Gtl2* (AJ320506) pyrosequencing indicates aberrant DNA methylation of the *Dlk1-Dio3* gene cluster in ST5 and ST8 iPS cell clones at day 0 as well as day 5, in contrast to that of ES cells and parental tail-tip fibroblasts prior to reprogramming. The graph indicates the global percentage of methylation of each of 29 CpG islands, spanning the *Gtl2* IG-DMR region (Nt 81262-81567). TTFs, tail-tip fibroblasts.

cells, and ES cells in terms of upregulation of early endodermal markers (Figures 2 and 3), we did note that significant differential expression of BMP4 emerged during endoderm differentiation (3.5-fold higher expression in iPS cells than ES cells; interaction of time and cell type,  $P = 0.008$ ). Since BMP4 is one predicted target of miRNA-380, encoded in the *Dlk1-Dio3* cluster and aberrantly silenced in iPS cells (Table 1), differential upregulation of BMP4 between iPS and ES cells during endoderm differentiation would be expected. Since higher expression levels of BMP4 and *Dlk1* in endodermal precursors may potentially impact their capacity to undergo liver lineage specification and differentiation (14, 34, 35), we quantified hepatic lineage specification across all 3 cell lines and noted the induction of *Afp*,  $\alpha$ -1 antitrypsin, and albumin in ST5 and ST8 iPS clones to be greater than that in their parental ES cells in 4 out of 4 repeated experiments (Figure 3, C and D). Thus, the aberrant imprinting of the *Dlk1-Dio3* gene cluster in ST5 and ST8 iPS cell lines did not appear to be associated with any detectable decrement in the capacity of those lines to undergo directed differentiation to DE or early hepatic lineage specification in vitro. Only after further hepatic differentiation to day 19 did 1 out of the 2 aberrantly imprinted clones (ST8) show a statistically significant, yet subtle, functional decrement in glycogen storage capacity relative to that of ES cells ( $P = 0.03$ ; Figure 3E).

## Discussion

Our results indicate that iPS and ES cells undergo directed differentiation to DE with induction of remarkably similar global gene expression programs. The key pioneer factors and transcriptional regulators known to be important in DE development, such as *Foxa2*, *Gata4/6*, and *Sox17* (36, 37), are all similarly upregulated during endodermal directed differentiation of ES and iPS cells, and the waves of marker genes (e.g., *Afp* and *Alb*) expressed during subsequent lineage specification of ES and iPS cell-derived endoderm also follows a sequence that has been described in the developing embryo. Beyond these specific individual genes, our results indicate significant overlap in the global gene expression programs of DE precursors derived in vitro from pluripotent stem cells compared with that of embryonic DE from the developing mouse embryo.

We found ES and iPS cells do differ significantly in the expression levels of other genes encoded or targeted by transcripts normally expressed from the imprinted *Dlk1-Dio3* gene cluster. Aberrant imprinting of this gene cluster in the majority of mouse iPS cell lines in the undifferentiated state was recently described and was found to correlate with impaired functional capacity of iPS cells to form “all-iPS-derived mice” after transplantation into 4n blastocysts (20, 38). While genes in this cluster have also been reported to have functional roles in mouse development (30–33), we found a surprisingly intact capacity of aberrantly imprinted iPS cells to undergo directed differentiation into DE in vitro. This is in marked contrast to recent observations of a reduced capacity of human iPS cell lines to undergo neuronal directed differentiation, compared with ES cells (19). Since the iPS cell-derived early hepatic lineages that co-express *Afp* and albumin in our studies correlate roughly to E8.5–E10.5 in the mouse embryo, this developmental stage may be too early to detect defects in iPS cell-derived liver cells. Indeed, liver abnormalities in mice with deletions of maternally inherited *Gtl2* genes were only evident postnatally, and in mice with uniparental paternal disomy of distal chromosome 12, lethality was only evident at midgestation (30, 32, 33, 39). Although, the aberrantly imprinted iPS cells in our studies were able to contribute efficiently to E11.5 mouse chimeras after blastocyst transplantation (25), displayed germ line competence, and formed chimeric postnatal mice with high coat color chimerism (Supplemental Figure 1) and grossly normal chimeric lungs and livers (25), it remains possible that a detailed functional evaluation of mature endodermal tissues in vivo might reveal more subtle abnormalities of iPS cell-derived endodermal epithelia.

Conversely, it is also possible that increased expression levels of *Dlk1* and BMP4 in aberrantly imprinted iPS cells might result in faster or more efficient endodermal or hepatic differentiation. Although expression levels of *Afp* and albumin were higher in both our iPS cell clones than in ES cells, evaluation of many more syngeneic iPS and ES cell clones would be required to sufficiently test this hypothesis. In addition, derivation of syngeneic properly imprinted iPS cell lines would be required to definitively assess the effects of aberrant imprinting on iPS cell differentiation capacity.

Overall our results have considerable implications for those wishing to develop cell-based therapies to reconstitute diseased endoderm-derived tissues. Regardless of imprinted status, iPS cells can be differentiated efficiently into DE precursors using the same serum-free culture protocols developed to derive endoderm from ES cells. As with ES cells, flow cytometry-based sorting algorithms can be devised to both reduce heterogeneity of iPS cell-derived populations and to reduce the presence of undifferentiated cells expressing residual *Nanog* or *Rex1*. Future studies will now need to focus on the relevance of aberrant imprinting in iPS cells to in vivo functioning of iPS cell-derived endodermal lineages.

## Methods

**ES and iPS cell culture.** Undifferentiated ES and iPS cells were expanded on mitomycin C-inactivated mouse embryonic fibroblasts. Prior to differentiation, all ES and iPS cell lines were adapted to serum-free maintenance media, consisting of 50% Neurobasal medium (Gibco), 50% DMEM/F12 medium (Gibco) supplemented with N2 and B27+RA supplements (Gibco), 1% penicillin/streptomycin, 0.05% BSA, 10 ng/ml LIF, 200 mM L-glutamine, 10 ng/ml human BMP-4 (R&D Systems), and  $4.5 \times 10^{-4}$  M monothioglycerol (MTG) (Sigma-Aldrich). The following mouse ES cell





## research article

**Table 1**

Top differentially expressed transcripts in iPS cells versus ES cells with  $\pm 4$  fold change

| FC<br>(iPS/ES cells) <sup>A</sup> | Transcript                  | mRNA accession | P value <sup>B</sup>   |
|-----------------------------------|-----------------------------|----------------|------------------------|
| -4.1                              | <i>Rian</i> <sup>C</sup>    | AF357355       | $2.74 \times 10^{-12}$ |
| -3.3                              | <i>Mir380</i> <sup>C</sup>  | mmu-mir-380    | $7.22 \times 10^{-6}$  |
| -2.9                              | <i>Mir410</i> <sup>C</sup>  | mmu-mir-410    | $9.67 \times 10^{-7}$  |
| -2.9                              | <i>Mir382</i> <sup>C</sup>  | mmu-mir-382    | $9.67 \times 10^{-7}$  |
| -2.8                              | <i>Mir300</i> <sup>C</sup>  | mmu-mir-300    | $5.84 \times 10^{-7}$  |
| -2.7                              | <i>Mir377</i> <sup>C</sup>  | mmu-mir-377    | $2.80 \times 10^{-5}$  |
| -2.7                              | <i>Gtl2</i> <sup>C</sup>    | NR_003633      | $1.45 \times 10^{-5}$  |
| -2.6                              | <i>Mir329</i> <sup>C</sup>  | mmu-mir-329    | $4.45 \times 10^{-7}$  |
| -2.3                              | <i>Mir381</i> <sup>C</sup>  | mmu-mir-381    | 0.00057                |
| -2.2                              | <i>Mir539</i> <sup>C</sup>  | mmu-mir-539    | 0.00032                |
| -2.2                              | <i>Mir487b</i> <sup>C</sup> | mmu-mir-487b   | $4.31 \times 10^{-5}$  |
| -2.1                              | <i>Mir411</i> <sup>C</sup>  | mmu-mir-411    | 0.001                  |
| 6.6                               | <i>Nr1h5</i>                | NM_198658      | $2.09 \times 10^{-8}$  |

Top fold change (FC) values ( $\log_2$  transformed) for iPS cells versus ES cells (subset of FDR < 0.001) are shown. <sup>A</sup>Fold change values shown are  $\log_2$  transformed and ranked in ascending order by fold change.

<sup>B</sup>Two-way ANOVA, FDR-adjusted P value for cell-type effect.

<sup>C</sup>Members of *Dlk1-Dio3* gene cluster.

lines were used where indicated in the text: 129/Ola T-GFP/Foxa2-hCD4 cells (13) (a gift of Gordon Keller, Mount Sinai School of Medicine); ES\_W4129S6 cells (Taconic); ES-C57BL/6 (ATCC SCRC-1002); and ES Sox2-GFP Rosa26-M2RTTA cells (26) (a gift of Konrad Hochedlinger, Massachusetts General Hospital, Boston, Massachusetts, USA). The mouse iPS cell lines included iPS-2D4 (12) (gift of Konrad Hochedlinger), generated previously with 4 retroviral vectors; iPS-ST5 and ST8, generated previously with pHAGE-Tet-STEMCCA reprogramming vector (25); and SEF4 and 11, generated previously with pHAGE-EF1a-STEMCCA (25). The mouse iPS Oct4-GFP cell line was generated by infecting tail-tip fibroblasts from a postnatal Oct4-GFP Rosa26-M2RTTA knockin mouse (40) with the doxycycline-inducible pHAGE-Tet-STEMCCA lentivirus, and colonies were picked for passaging after 20 days as previously described (25).

**ES and iPS cell endoderm and hepatocyte differentiation.** DE differentiation was performed in serum-free differentiation (SFD) medium, consisting of 75% IMDM (Gibco), 25% Ham's Modified F12 (Cellgro) with N2 and B27+RA supplements, 0.05% supplemented with 200 mM L-glutamine, 0.05 mg/ml ascorbic acid (Sigma-Aldrich), and  $4.5 \times 10^{-4}$  MTG as previously described (14). Briefly, ES or iPS cells were plated under nonadherent conditions and allowed to spontaneously differentiate and form embryoid bodies (EBs) for 2 days. On day 2, EBs were trypsinized and reaggregated in complete SFD medium with 50 ng/ml Activin A (R&D Systems). On day 5, EBs were dissociated and harvested for RNA extraction, DNA extraction, or flow cytometry. For hepatocyte differentiation, day 4 EBs were trypsinized and reaggregated in SFD medium supplemented with 200 mM L-glutamine,  $4.5 \times 10^{-4}$  M MTG, 50 ng/ml Activin A, 50 ng/ml BMP-4 (R&D Systems), 10 ng/ml bFGF (R&D Systems), and 10 ng/ml VEGF (R&D Systems). On day 5, EBs were trypsinized and plated on gelatin-coated plates with SFD medium supplemented with 200 mM L-glutamine,  $4.5 \times 10^{-4}$  M MTG, 50 ng/ml BMP-4, 20 ng/ml EGF (R&D Systems), 10 ng/ml FGF2, 20 ng/ml HGF (R&D Systems), 20 ng/ml TGF- $\alpha$  (R&D Systems), 10 ng/ml VEGF, and  $10^{-7}$  M dexamethasone. For pancreatic differentiation, activin-stimulated ES and iPS cells were exposed to KAAD-cyclopamine, FGF10, and retinoic acid, according to an established differentiation protocol (29) detailed in the Supplemental Methods.

**Flow cytometry and cell sorting.** EBs were dissociated with trypsin/EDTA (1 minute, 37°C) and stained for 30 minutes on ice with the following monoclonal antibodies: APC-conjugated anti-mouse c-kit (BD Biosciences), PE-conjugated anti-human CD4 (Caltag), anti-mouse CXCR4-biotin/streptavidin-Cy7APC (BD Biosciences), or non-conjugated anti-mouse ENDM1 (28), followed by APC-conjugated donkey anti-rat IgG. Parallel aliquots of each sample were exposed to nonspecific isotype control antibodies. Cells were either analyzed using an LSRII machine (BD Biosciences) or sorted using a MoFlo High Speed Cell Sorter (DAKO). Detailed methods for characterizing sorted cell populations by assessment of glycogen storage capacity, kidney capsule transplantations, immunostainings, and CpG methylation mapping are available in the Supplemental Methods. All animal studies were approved by the Institutional Animal Care and Use Committee of Boston University School of Medicine.

**qRT-PCR.** Total RNA extraction was performed using an miRNeasy Mini Kit (Qiagen), and 1  $\mu$ g DNase-treated RNA was reverse transcribed using TaqMan Reverse Transcription Reagents (Applied Biosystems). qRT-PCR of cDNAs was performed in a StepOnePlus Real-Time PCR System (Applied Biosystems) using TaqMan inventoried primers. The SYBR Green System (Applied Biosystems) was used for *Dlk1*, *Gtl2*, *Rian*, and *Oct4*. A full inventory of all probes and primers is available in the Supplemental Methods. Reactions were performed in duplicate, using 1:20 diluted cDNA. mRNA expression levels were normalized to 18S rRNA or GAPDH, and quantification of relative gene expression, presented as fold change compared with the relevant baseline, was calculated using the  $2^{-[\Delta\Delta CT]}$  method. Biological replicates from repeat experiments were used to calculate average fold change as well as the SEM for each fold change in gene expression, represented by error bars where indicated.

**Microarrays and bioinformatics analysis of cell cultures and mouse embryos.** All ES cell- and iPS cell-derived samples were purified by flow cytometry sorting of either Sox2-GFP<sup>bright</sup> undifferentiated (day 0) cells or differentiated (day 5) cells, using the sort gate detailed in the text. Three biological replicates of each of 3 cell lines (ES, ST5, and ST8) at 2 time points were prepared (total 18 samples), and total RNA was extracted using a miRNeasy Mini Kit (Qiagen). Quality-assessed RNA samples were hybridized to Affymetrix GeneChip Mouse Gene 1.0 ST arrays, which feature probe sets for 28,853 genes and 344 microRNAs, with an average of 27 probes spread across the full length of each gene. Eighteen raw data files obtained by the Affymetrix scanner passed data quality control steps prior to RMA normalization through the Affymetrix expression console. The normalized data underwent statistical analysis as follows: 2-way ANOVA was used to determine differentially expressed genes affected by cell type, time, and the interaction between cell type and time, using FDR-adjusted P values indicated in the text.

To assess the transcriptome of embryonic DE, previously published DNase-treated RNA extracts from developing mouse E8.25 DE were used (28) (a gift of Gordon Keller). Three biological replicates of these RNA extracts (embryonic DE) were obtained from 25,000–35,000 cells, sorted from pooled E8.25 mouse embryos, based on an established EpCam<sup>+</sup>/ENDM1<sup>+</sup>/side scatter low algorithm (28). Amplified cDNAs from the 3 embryonic DE RNA extracts and 3 replicates each of extracts from day 0 and day 5 sorted ES cells (9 samples total) were prepared using the WT-OvationT Pico System (NuGEN), converted into sense-strand cDNA targets using WT-Ovation Exon Module (NuGEN), and finally labeled with the Encore Biotin Module (NuGEN) for analysis on Affymetrix GeneChip Mouse Gene 1.0 ST arrays. For statistical analysis of these 9 samples, 1-way ANOVA and follow-up post-hoc analysis was used to identify genes differentially expressed between day 0 ES cells and embryonic DE, with an FDR-adjusted P value cutoff of 0.001. All microarray data files are available for free download at the Gene Expression Omnibus (GEO accession number GSE27087; <http://www.ncbi.nlm.nih.gov/geo/>).



**Statistics.** Unless indicated otherwise in the text, the Student's *t* test (2 tailed) was used to assess differences between groups or cell lines.  $P < 0.05$  was considered statistically significant.

## Acknowledgments

The authors wish to thank members of the Kotton and Mostoslavsky laboratories for helpful discussions; Laertis Ikononou, Finn Hawkins, and Attila J. Fabian for technical support; Xingbin Ai, Jesus Paez-Cortez, and Anne Hinds for assistance with histology methods; and Carmen Sarita-Reyes of the Boston Medical Center Department of Anatomic Pathology for histopathologic review of teratoma sections. We thank Yuriy Alekseyev of the Boston University Microarray Resource and Sherry Zang and Gang Lu for technical assistance with microarray processing and Konrad Hochedlinger and Matthias Stadtfeld for helpful discussions.

D.N. Kotton and G. Mostoslavsky are supported by NIH grants PO1 HL047049-16A1, 1RC2HL101535-01, 1R01 HL095993-01, and S.S. Shen is supported by NIH grant UL1 RR025771.

Received for publication May 27, 2010, and accepted in revised form March 8, 2011.

Address correspondence to: Darrell N. Kotton, Boston University Pulmonary Center and Department of Medicine, Boston University School of Medicine, 715 Albany St., R-304, Boston, Massachusetts 02118, USA. Phone: 617.638.4860; Fax: 617.536.8063; E-mail: dkotton@bu.edu. Or to: Gustavo Mostoslavsky, Section of Gastroenterology, Department of Medicine, Boston University School of Medicine, 650 Albany Street X-513, Boston, Massachusetts 02118, USA. Phone: 617.638.6532; Fax: 617.638.7785; E-mail: gmostosl@bu.edu.

- Serls AE, Doherty S, Parvatiyar P, Wells JM, Deutsch GH. Different thresholds of fibroblast growth factors pattern the ventral foregut into liver and lung. *Development*. 2005;132(1):35–47.
- Cardoso WV, Kotton DN. Specification and patterning of the respiratory system. In: *StemBook*. Cambridge, Massachusetts, USA: Harvard Stem Cell Institute; 2008.
- Jung J, Zheng M, Goldfarb M, Zaret KS. Initiation of mammalian liver development from endoderm by fibroblast growth factors. *Science*. 1999;284(5422):1998–2003.
- Wells JM, Melton DA. Early mouse endoderm is patterned by soluble factors from adjacent germ layers. *Development*. 2000;127(8):1563–1572.
- Gadue P, Huber TL, Nostro MC, Kattman S, Keller GM. Germ layer induction from embryonic stem cells. *Exp Hematol*. 2005;33(9):955–964.
- Kubo A, et al. Development of definitive endoderm from embryonic stem cells in culture. *Development*. 2004;131(7):1651–1662.
- Takahashi K, et al. Induction of pluripotent stem cells from adult human fibroblasts by defined factors. *Cell*. 2007;131(5):861–872.
- Takahashi K, Yamanaka S. Induction of pluripotent stem cells from mouse embryonic and adult fibroblast cultures by defined factors. *Cell*. 2006;126(4):663–676.
- Si-Tayeb K, et al. Highly efficient generation of human hepatocyte-like cells from induced pluripotent stem cells. *Hepatology*. 2010;51(1):297–305.
- Park IH, et al. Disease-specific induced pluripotent stem cells. *Cell*. 2008;134(5):877–886.
- Somers A, et al. Generation of transgene-free lung disease-specific human induced pluripotent stem cells using a single excisable lentiviral stem cell cassette. *Stem Cells*. 2010;28(10):1728–1740.
- Maherali N, et al. Directly reprogrammed fibroblasts show global epigenetic remodeling and widespread tissue contribution. *Cell Stem Cell*. 2007;1(1):55–70.
- Gadue P, Huber TL, Paddison PJ, Keller GM. Wnt and TGF-beta signaling are required for the induction of an in vitro model of primitive streak formation using embryonic stem cells. *Proc Natl Acad Sci U S A*. 2006;103(45):16806–16811.
- Gouon-Evans V, et al. BMP-4 is required for hepatic specification of mouse embryonic stem cell-derived definitive endoderm. *Nat Biotechnol*. 2006;24(11):1402–1411.
- Polo JM, et al. Cell type of origin influences the molecular and functional properties of mouse induced pluripotent stem cells. *Nat Biotechnol*. 2010;28(8):848–855.
- Chin MH, et al. Induced pluripotent stem cells and embryonic stem cells are distinguished by gene expression signatures. *Cell Stem Cell*. 2009;5(1):111–123.
- Marchetto MC, Yeo GW, Kainohana O, Marsala M, Gage FH, Muotri AR. Transcriptional signature and memory retention of human-induced pluripotent stem cells. *PLoS One*. 2009;4(9):e7076.
- Wilson KD, Venkatasubrahmanyam S, Jia F, Sun N, Butte AJ, Wu JC. MicroRNA profiling of human-induced pluripotent stem cells. *Stem Cells Dev*. 2009;18(5):749–758.
- Hu BY, et al. Neural differentiation of human induced pluripotent stem cells follows developmental principles but with variable potency. *Proc Natl Acad Sci U S A*. 2010;107(9):4335–4340.
- Stadtfeld M, et al. Aberrant silencing of imprinted genes on chromosome 12qF1 in mouse induced pluripotent stem cells. *Nature*. 2010;465(7295):175–181.
- Kim K, et al. Epigenetic memory in induced pluripotent stem cells. *Nature*. 2010;467(7313):285–290.
- D'Amour KA, Agulnick AD, Eliazar S, Kelly OG, Kroon E, Baetge EE. Efficient differentiation of human embryonic stem cells to definitive endoderm. *Nat Biotechnol*. 2005;23(12):1534–1541.
- Spence JR, et al. Directed differentiation of human pluripotent stem cells into intestinal tissue in vitro. *Nature*. 2011;470(7332):105–109.
- Maehr R, et al. Generation of pluripotent stem cells from patients with type 1 diabetes. *Proc Natl Acad Sci U S A*. 2009;106(37):15768–15773.
- Sommer CA, Stadtfeld M, Murphy GJ, Hochedlinger K, Kotton DN, Mostoslavsky G. Induced pluripotent stem cell generation using a single lentiviral stem cell cassette. *Stem Cells*. 2009;27(3):543–549.
- Stadtfeld M, Maherali N, Breatult DT, Hochedlinger K. Defining molecular cornerstones during fibroblast to iPS cell reprogramming in mouse. *Cell Stem Cell*. 2008;2(3):230–240.
- Sommer CA, et al. Excision of reprogramming transgenes improves the differentiation potential of iPS cells generated with a single excisable vector. *Stem Cells*. 2010;28(1):64–74.
- Gadue P, et al. Generation of monoclonal antibodies specific for cell surface molecules expressed on early mouse endoderm. *Stem Cells*. 2009;27(9):2103–2113.
- D'Amour KA, et al. Production of pancreatic hormone-expressing endocrine cells from human embryonic stem cells. *Nat Biotechnol*. 2006;24(11):1392–1401.
- Hagan JP, O'Neill BL, Stewart CL, Kozlov SV, Croce CM. At least ten genes define the imprinted Dlk1-Dio3 cluster on mouse chromosome 12qF1. *PLoS One*. 2009;4(2):e4352.
- da Rocha ST, Edwards CA, Ito M, Ogata T, Ferguson-Smith AC. Genomic imprinting at the mammalian Dlk1-Dio3 domain. *Trends Genet*. 2008;24(6):306–316.
- Takahashi N, et al. Deletion of Gtl2, imprinted non-coding RNA, with its differentially methylated region induces lethal parent-origin-dependent defects in mice. *Hum Mol Genet*. 2009;18(10):1879–1888.
- da Rocha ST, Tevendale M, Knowles E, Takada S, Watkins M, Ferguson-Smith AC. Restricted co-expression of Dlk1 and the reciprocally imprinted non-coding RNA, Gtl2: implications for cis-acting control. *Dev Biol*. 2007;306(2):810–823.
- Tanimizu N, Nishikawa M, Saito H, Tsujimura T, Miyajima A. Isolation of hepatoblasts based on the expression of Dlk/Pref-1. *J Cell Sci*. 2003;116(pt 9):1775–1786.
- Wu Q, Kawahara M, Kono T. Synergistic role of Igf2 and Dlk1 in fetal liver development and hematopoiesis in bi-maternal mice. *J Reprod Dev*. 2008;54(3):177–182.
- Ang SL, et al. The formation and maintenance of the definitive endoderm lineage in the mouse: involvement of HNF3/forkhead proteins. *Development*. 1993;119(4):1301–1315.
- Zaret KS, Watts J, Xu J, Wandzioch E, Smale ST, Sekiya T. Pioneer factors, genetic competence, and inductive signaling: programming liver and pancreas progenitors from the endoderm. *Cold Spring Harb Symp Quant Biol*. 2008;73:119–126.
- Liu L, et al. Activation of the imprinted Dlk1-Dio3 region correlates with pluripotency levels of mouse stem cells. *J Biol Chem*. 2010;285(25):19483–19490.
- Tevendale M, Watkins M, Rasberry C, Cattanch B, Ferguson-Smith AC. Analysis of mouse conceptuses with uniparental duplication/deficiency for distal chromosome 12: comparison with chromosome 12 uniparental disomy and implications for genomic imprinting. *Cytogenet Genome Res*. 2006;113(1–4):215–222.
- Lengner CJ, et al. Oct4 expression is not required for mouse somatic stem cell self-renewal. *Cell Stem Cell*. 2007;1(4):403–415.

# Activation Dynamics and Signaling Properties of Notch3 Receptor in the Developing Pulmonary Artery<sup>\*[5]</sup>

Received for publication, March 17, 2011, and in revised form, April 20, 2011. Published, JBC Papers in Press, May 2, 2011, DOI 10.1074/jbc.M111.241224

Shamik Ghosh<sup>†1</sup>, Jesus R. Paez-Cortez<sup>†1</sup>, Karthik Boppidi<sup>‡</sup>, Michelle Vasconcelos<sup>‡</sup>, Monideepa Roy<sup>§</sup>, Wellington Cardoso<sup>‡</sup>, Xingbin Ai<sup>‡</sup>, and Alan Fine<sup>‡2</sup>

From the <sup>†</sup>Pulmonary Center, Boston University School of Medicine, Boston, Massachusetts 02118, and the <sup>§</sup>Department of Pathology, Brigham and Women's Hospital, Harvard Medical School, Boston, Massachusetts 02115

Notch3 signaling is fundamental for arterial specification of systemic vascular smooth muscle cells (VSMCs). However, the developmental role and signaling properties of the Notch3 receptor in the mouse pulmonary artery remain unknown. Here, we demonstrate that Notch3 is expressed selectively in pulmonary artery VSMCs, is activated from late fetal to early postnatal life, and is required to maintain the morphological characteristics and smooth muscle gene expression profile of the pulmonary artery after birth. Using a conditional knock-out mouse model, we show that Notch3 receptor activation in VSMCs is Jagged1-dependent. *In vitro* VSMC lentivirus-mediated Jagged1 knockdown, confocal localization analysis, and co-culture experiments revealed that Notch3 activation is cell-autonomous and occurs through the physical engagement of Notch3 and VSMC-derived Jagged1 in the interior of the same cell. Although the current models of mammalian Notch signaling involve a two-cell system composed of a signal-receiving cell that expresses a Notch receptor on its surface and a neighboring signal-sending cell that provides membrane-bound activating ligand, our data suggest that pulmonary artery VSMC Notch3 activation is cell-autonomous. This unique mechanism of Notch activation may play an important role in the maturation of the pulmonary artery during the transition to air breathing.

Lung development involves the integration of multiple signaling pathways to ensure coordinated growth and differentiation of airway and vascular structures (1). The initial event in vessel development is the formation of basic tubular structures from endothelial precursors (2). Under the influence of PDGF- $\beta$  and Wnt signaling (3, 4), formation of mature vessels occurs by the stepwise recruitment, growth, and differentiation of mesenchymal precursors into a circumferential mural cell layer composed of smooth muscle cells and pericytes (5).

It is noteworthy that the lung vascular system is subjected to a dramatic switch at birth, from a low-flow, low-pressure fetal state to a high-flow, higher pressure postnatal state (1). Although it is recognized as an essential feature of the transition

from intrauterine life, the timing and identification of signals that control how lung vascular cells adapt to this changeover remain unclear. The involvement of Notch signals in multiple aspects of vessel development led us to investigate the role of this pathway during this transition period.

The Notch signaling pathway is highly conserved across species, controlling cell fate decisions and tissue patterning during development (6). In classical Notch signaling, a cell surface Notch receptor is activated by binding with a membrane-bound ligand delivered by a neighboring signal-sending cell (7). This interaction initiates a series of proteolytic cleavages that release the Notch intracellular domain into the cytoplasm of the signal-receiving cell before translocation to the nucleus and induction of target gene transcription (8, 9).

Of the four mammalian Notch receptors, Notch3 is expressed predominantly in vascular smooth muscle cells (VSMCs)<sup>3</sup> (10, 11). Notch3 regulates arterial specification of VSMCs in fetal systemic arteries (12). In the developing retinal vasculature, Notch3 deletion impairs mural cell recruitment, resulting in progressive loss of vessel coverage (13). Its role, however, in pulmonary artery development has not yet been examined. Of note, Notch3 serves as a sensor of hemodynamic stress (14) and is involved in vascular tone regulation (15), two properties unique to this receptor. Furthermore, Notch3 has several structural features that differ from other Notch family members, including a lack of transactivation domain, a smaller number of EGF-like repeats, and a distinctive ligand-binding domain (16), thereby raising the possibility that Notch3 activation may occur through a mechanism that is distinct from classical Notch signaling. In this context, recent studies in *Drosophila* demonstrated an alternative mode of Notch activation that is cell-autonomous and occurs inside the cell (17, 18).

In this study, we show that Notch3 is expressed selectively in pulmonary artery VSMCs and is active from late fetal to early postnatal life. Our data point to a key role for Notch3 in the final stages of VSMC maturation during the adaptation to postnatal life. Most notably, we provide evidence indicating that Notch3 signaling in pulmonary artery VSMCs occurs through a unique cell-autonomous mechanism that is dependent on an interaction with Jagged1 in the interior of VSMCs.

<sup>\*</sup> This work was supported, in whole or in part, by National Institutes of Health Grant HL-089795. This work was also supported by a grant from the United States Army Medical Research Acquisition Activity.

<sup>[5]</sup> The on-line version of this article (available at <http://www.jbc.org>) contains supplemental Figs. S1–S8 and Tables 1–5.

<sup>†</sup> Both authors contributed equally to this work.

<sup>2</sup> To whom correspondence should be addressed: Pulmonary Center, R-304, Boston University School of Medicine, 80 East Concord St., Boston, MA 02118. Tel.: 617-638-4860; Fax: 617-536-8093; E-mail: [afine@bu.edu](mailto:afine@bu.edu).

<sup>3</sup> The abbreviations used are: VSMC, vascular smooth muscle cell; hrGFP, humanized *R. reniformis* GFP;  $\alpha$ -SMA,  $\alpha$ -smooth muscle actin; N3ECD, Notch3 extracellular domain; RPASMC, rat pulmonary artery smooth muscle cell; qPCR, quantitative real-time PCR; eGFP, enhanced GFP; E, embryonic day; N3ICD, Notch3 intracellular domain.



## EXPERIMENTAL PROCEDURES

**Animals**—Pregnant CD1 mice were obtained from Charles River Laboratories (Wilmington, MA). *Notch3*<sup>−/−</sup> mice were provided by Dr. Thomas Gridley (The Jackson Laboratory, Bar Harbor, ME). A transgenic mouse ( $\alpha$ -SMA-hrGFP) that expresses humanized *Renilla reniformis* GFP (hrGFP; Stratagene, Cedar Creek, TX) under the control of the rat  $\alpha$ -smooth muscle actin (*SMA*) gene promoter was generated. In brief, the rat *SMA* promoter was ligated into the multiple cloning site of the phrGFP vector (Stratagene) immediately upstream of sequences that encode hrGFP. The promoter fragment consists of 2.6 kb of sequence upstream of the transcription start site and all of intron 1 from the rat *SMA* gene. A linearized construct was microinjected into pronuclei of fertilized C57/Bl6 eggs before implantation in foster mothers. A founder line containing two copies of the transgene (as determined by quantitative Southern hybridization) was chosen. These mice selectively express hrGFP in smooth muscle cell populations *in vivo*. *Notch3*<sup>−/−</sup>  $\alpha$ -SMA-hrGFP mice were generated by crossing *Notch3*<sup>−/−</sup> and  $\alpha$ -SMA-hrGFP mice. *Jagged1*<sup>flox/flox</sup> mice were provided by Dr. Nadean Brown (Cincinnati Children's Hospital, Cincinnati, OH). To selectively delete VSMC *Jagged1*, *Jagged1*<sup>flox/flox</sup> mice were crossed with *sma22 $\alpha$ 945*, *Cre* (*Sma-22*<sup>cre/cre</sup>) mice (The Jackson Laboratory). Animal studies were approved by the Boston University Institutional Animal Care and Use Committee.

**Antibodies**—A goat polyclonal antibody directed to the mouse Notch3 extracellular domain (N3ECD; Sf21 recombinant mouse Notch3 amino acids 40–486) was purchased from R&D Systems (Minneapolis, MN). Goat anti-Notch3 polyclonal antibodies directed to the extracellular (Q-14) and intracellular (M-134) domains and goat anti-Jagged1 polyclonal antibody (C-20) were obtained from Santa Cruz Biotechnology (Santa Cruz, CA). A directly conjugated hamster anti-N3ECD monoclonal antibody (HMN3-133) was purchased from BioLegend (San Diego, CA). For Western blot analysis of rat cells, rat anti-N3ICD monoclonal antibody (8G5) from Cell Signaling Technology (Danvers, MA) was used. Antibodies directed to CD45 (30-F11) and CD31 (MEC 13.3) were obtained from Pharmingen. Biotinylated anti- $\alpha$ -SMA antibody (1A4) was purchased from Thermo Scientific (Waltham, MA). Cy2-conjugated donkey anti-rabbit IgG and Cy3-conjugated anti-goat IgG were obtained from Jackson ImmunoResearch Laboratories (West Grove, PA). Alexa Fluor 488-, 568-, and 647-conjugated anti-rabbit and anti-goat antibodies were purchased from Invitrogen. For Western blot analysis, anti-Jagged1 antibody obtained from Cell Signaling Technology was used. For all flow cytometry studies, conjugated isotype antibodies were used as controls.

**Immunohistochemistry and Immunofluorescence**—Lungs were fixed with 4% formalin, paraffin-embedded, sectioned, deparaffinized, and subjected to antigen retrieval before application of primary antibodies and incubation with HRP-conjugated or fluorescence-conjugated antibodies. Details are provided in supplemental Table 1.

**In Situ Hybridization**—*In situ* hybridization was performed on 10- $\mu$ m lung sections using digoxigenin-UTP-labeled *Hey1*

and *Hey2* riboprobes as described previously (19). See supplemental Table 2 for probe details.

**Cell Isolation**—Cell suspensions were obtained by digesting lungs with 0.1% collagenase A (Roche Diagnostics), 2.4 units/ml Dispase (Roche Diagnostics), and 6 units/ml DNase I (Qiagen, Valencia, CA) at 37 °C for 1 h. Neonatal rat pulmonary artery smooth muscle cells (RPASMCs) were isolated as described (20).

**Confocal Microscopy**—Cells were cultured for 48 h, fixed with 4% paraformaldehyde, and permeabilized with 0.25% Triton X-100 in PBS before addition of primary and fluorochrome-conjugated secondary antibodies. Images were captured using a Zeiss LSM 510 confocal laser microscope and analyzed using NIH ImageJ browser software. Further details are provided in supplemental Table 3.

**Western Blotting and Immunoprecipitation**—Lung cells were obtained as described above. CD45<sup>+</sup> and CD31<sup>+</sup> cells were depleted from lung preparations by incubation with biotinylated anti-mouse CD45 and CD31 antibodies for 30 min on ice. After washing, biotin-binding magnetic beads (Dynabeads, Invitrogen) were added before submission to a magnetic field. The non-binding cell fraction was lysed in radioimmune precipitation assay buffer in the presence of protease inhibitors (1 mM phenylmethylsulfonyl fluoride, 1  $\mu$ g/ml leupeptin, 1  $\mu$ g/ml aprotinin, and 1  $\mu$ g/ml pepstatin A) for 30 min at 4 °C. Protein concentration was measured in the supernatant using the Bradford assay. For analysis, 80  $\mu$ g of protein was separated through a 4–12% SDS-polyacrylamide gel before electrophoretic transfer to a PVDF membrane. Membranes were blocked with 2% BSA in TBS for 1 h. Blots were probed with anti-N3ICD (1:200) or anti-Jagged1 (1:200) antibody. Antigen-antibody complexes were identified with HRP-conjugated secondary antibodies. Enhanced chemiluminescence was used for detection. For immunoprecipitation, equal amounts of protein lysates were incubated with anti-N3ECD antibody for 3 h at 4 °C. Immune complexes were collected by incubation with protein A-Sepharose for 2 h before washing with PBS, separation by SDS-PAGE, and electrophoretic transfer to a PVDF membrane. Western blotting was performed with anti-Jagged1 or anti-N3ECD antibody as described above.

**Flow Cytometry and Cell Sorting**—Non-permeabilized and permeabilized cells were stained with fluorochrome-conjugated mouse-specific monoclonal antibodies prior to analysis. Permeabilization was achieved using BD Cytotfix/Cytoperm solution (BD Biosciences). Flow cytometry was performed on an LSR II cytometer (BD Biosciences), and data were analyzed using FlowJo software (Tree Star Inc., Ashland, OR). Antibody conditions are detailed in supplemental Table 4. hrGFP<sup>+</sup> cells were collected from lung cell suspensions of  $\alpha$ -SMA-hrGFP mice using a MoFlo cell sorter (Beckman Coulter, Fullerton, CA).

**Real-time PCR Analysis**—RNA was isolated using an RNeasy mini kit (Qiagen). cDNA was transcribed using the Promega reverse transcription system. Quantitative real-time PCR (qPCR) was performed in a StepOne Plus instrument (Applied Biosystems, Foster City, CA). All assays were performed in triplicate at two different cDNA concentrations to ensure that the amplification efficiencies for reference genes and genes of



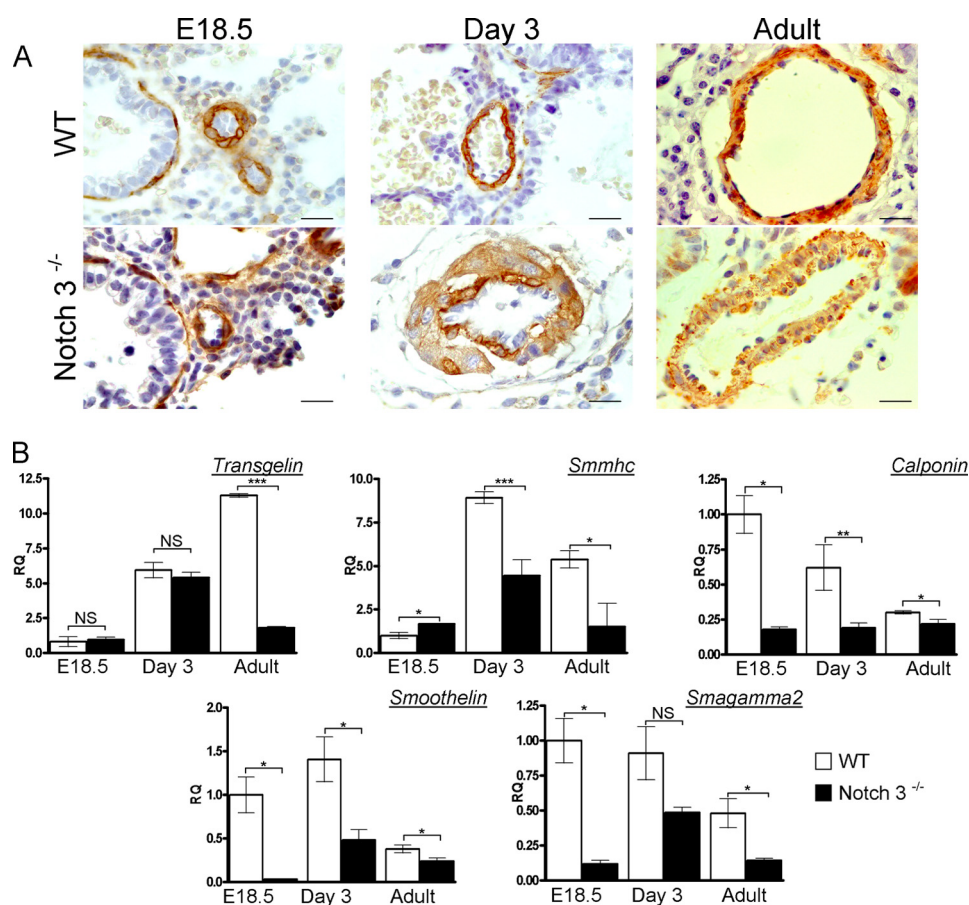


**FIGURE 1. Pulmonary artery morphology and smooth muscle marker gene expression profiles in WT and Notch3<sup>-/-</sup> mice at E18.5 and postnatal day 3 and in the adult.** A,  $\alpha$ -SMA expression pattern in WT and Notch3<sup>-/-</sup> mouse pulmonary artery segments. B, smooth muscle gene expression profiles as determined by qPCR of whole lung RNA in WT (white bars) and Notch3<sup>-/-</sup> (black bars) mice. Smmhc, smooth muscle myosin heavy chain. Data show means  $\pm$  S.D. and are representative of three independent experiments. NS, not significant; \*,  $p < 0.05$ ; \*\*,  $p < 0.01$ ; \*\*\*,  $p < 0.001$ .

interest were the same. Reactions were normalized to 18 S rRNA. All TaqMan<sup>®</sup> probes were obtained from Applied Biosystems. For contractile smooth muscle-related genes, qPCR was performed with fast SYBR reagent (Invitrogen) as described (21). GAPDH was used as an internal control. After PCR, a melting curve was constructed in the range of 60–95 °C to evaluate the specificity of the amplification. See [supplemental Table 5](#) for TaqMan primer details.

**Cell Culture**—Primary RPASMCs were cultured in DMEM supplemented with 10% FBS. The rat alveolar macrophage NR8383 cell line was purchased from American Type Culture Collection and maintained as recommended. For inhibition of  $\gamma$ -secretase activity, RPASMCs were cultured in the presence of either 10  $\mu$ M DAPT dissolved in Me<sub>2</sub>SO or only Me<sub>2</sub>SO for 72 h.

**Lentivirus-mediated Jagged1 Knockdown**—Jagged1 shRNA or scrambled shRNA (22) was cloned into the pLVTHM lentiviral vector (23), a kind gift of Dr. D. Trono (Ecole Polytechnique Fédérale, Lausanne, Switzerland). Replication-incompetent lentivirus was created using a five-plasmid transfection procedure (24). All viral supernatants were concentrated  $\sim$ 100-fold by ultracentrifugation. Titering of all vectors was performed by infection of FG293 cells. RPASMCs were transduced with a single exposure at a multiplicity of infection of 100. Infected cells were identified by enhanced GFP (eGFP) expression. Jagged1 knockdown was confirmed by qPCR and

Western blot analysis. Co-culturing of the wild type with Jagged1 or scrambled shRNA-transduced cells was performed at a 1:1 ratio for 72 h prior to collection by cell sorting.

**Cell Transfection**—Plasmids containing cDNAs encoding the mouse N3ICD or full-length Notch3 fused to GFP (25) were gifts of Dr. J. Arboleda-Velasquez (Harvard Medical School, Boston, MA). Neonatal RPASMCs and 293T cells were transiently transfected using Lipofectamine 2000 (Invitrogen). After transfection, cells were stained with anti-GFP antibody (Millipore) for microscopic analysis.

**Cell Surface Biotinylation**—To enrich for surface proteins, cell surface biotinylation of RPASMCs was performed using a cell surface protein biotinylation kit (Pierce). During the biotinylation procedure, all reagents and cultures were kept on ice. In brief, RPASMC cultures were washed with ice-cold PBS and then incubated in EZ-Link NHS-SS-biotin reagent for 30 min. Excess biotin was blocked with glycine. Cells were washed again with glycine buffer and lysed. Lysates were rocked for 1 h on a NeutrAvidin-agarose column. Non-biotinylated internal fractions were collected by washing the column with wash buffer, and biotinylated external proteins were collected by elution with 50  $\mu$ M DTT. Western blotting was performed using anti-N3ECD, anti-Jagged1, and anti-p53 antibodies in the biotinylated extracellular fraction, non-biotinylated intracellular fraction, and total cell lysates.

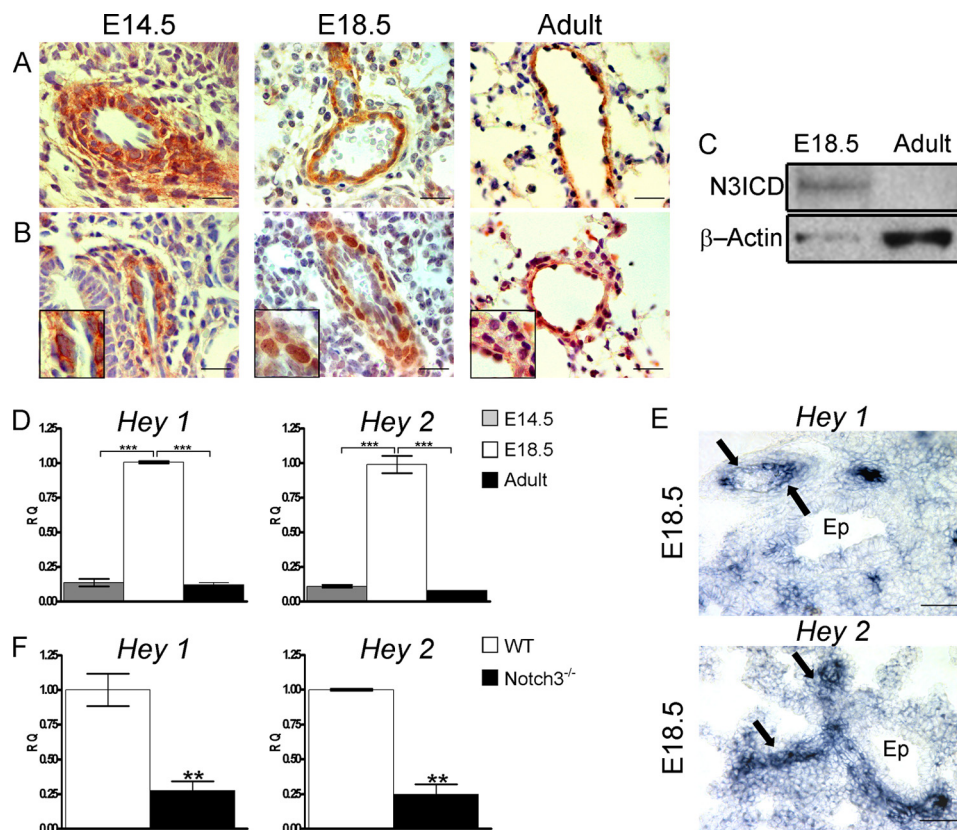


FIGURE 2. **Notch3 expression and activation in developing and adult lungs.** *A*, N3ECD expression at E14.5 and E18.5 and in the adult. *B*, N3ICD expression in developing and adult lungs. *Insets* show higher power views of perinuclear (E14.5 and adult) and nuclear (E18.5) N3ICD localization. *Scale bars* = 20  $\mu$ m. *C*, Western blot analysis for cleaved N3ICD in E18.5 and adult lung lysates.  $\beta$ -Actin was used as a loading control. *D*, relative *Hey1* and *Hey2* mRNA expression in E14.5 (gray bars), E18.5 (white bars), and adult (black bars) hrGFP<sup>+</sup> lung cells. *E*, non-isotopic *in situ* hybridization for *Hey1* and *Hey2* mRNAs showing restricted VSMC (arrows) expression in E18.5 lungs. *Ep*, airway epithelium. *F*, relative *Hey1* and *Hey2* mRNA expression in WT (white bars) and *Notch3*<sup>-/-</sup> (black bars) E18.5 hrGFP<sup>+</sup> lung cells. qPCR data show means  $\pm$  S.D. and are representative of three independent experiments. \*\*,  $p < 0.05$ ; \*\*\*,  $p < 0.001$ .

**Statistical Analysis**—Data are presented as means  $\pm$  S.D. Statistical analysis was performed using Student's *t* test. Significant differences were determined as  $p < 0.05$ ,  $p < 0.01$ , and  $p < 0.001$ .

## RESULTS

**Abnormal Pulmonary Artery Morphology and Smooth Muscle Marker Gene Expression in *Notch3*<sup>-/-</sup> Mice**—To evaluate the contribution of Notch3 receptor signaling in pulmonary artery development, we compared the morphology of vessels stained with anti- $\alpha$ -SMA antibody in WT and *Notch3*<sup>-/-</sup> mice. The pulmonary arteries in WT and *Notch3*<sup>-/-</sup> embryos at embryonic day (E) 18.5 appeared grossly similar (Fig. 1A). At postnatal day 3, however, VSMCs in *Notch3*<sup>-/-</sup> mice were dysmorphic, non-cohesive, and vacuolated and showed a disorganized distribution of SMA (Fig. 1A). Alterations in the  $\alpha$ -SMA staining pattern and the morphology of smooth muscle cells persisted into adulthood, although the changes were less pronounced than at postnatal day 3 (Fig. 1A). To determine whether these morphological abnormalities are associated with changes in expression of smooth muscle-related genes in the *Notch3*<sup>-/-</sup> mouse, we quantified mRNAs for transgelin (*Sma22*),  $\alpha$ -SMA,  $\gamma$ -SMA, smoothelin, and calponin as described (21). At all ages examined, down-regulation of these genes was observed in *Notch3*<sup>-/-</sup> mice (Fig. 1B). In contrast, the morphology of bronchial smooth

muscle was not affected in *Notch3*<sup>-/-</sup> mice (data not shown), consistent with the restricted expression of Notch3 to VSMCs (supplemental Fig. S1A).

**Temporal Expression and Activation of Notch3 in the Developing Lung**—Using an antibody directed against the N3ECD, we found that this receptor is expressed in lung arterial VSMCs from E14.5 into adulthood (Fig. 2A). To determine the kinetics of Notch3 activation, the cellular localization of the Notch3 intracellular domain (N3ICD) was determined. As discussed, the N3ICD arises from a  $\gamma$ -secretase-dependent cleavage that follows receptor activation, before translocation to the nucleus (26). For this analysis, we employed an antibody previously shown to identify the mouse N3ICD (27); the specificity of this antibody was further confirmed by the lack of positive VSMC staining in the *Notch3*<sup>-/-</sup> mouse lung (supplemental Fig. S1B). We found that the N3ICD was distributed in the cytoplasm of lung VSMCs at E14.5 (Fig. 2B) but in the nucleus at E18.5, indicating active Notch3 signaling at late gestation (Fig. 2B, inset). N3ICD nuclear localization persisted until postnatal day 5 (data not shown) before reverting to a perinuclear distribution in adult VSMCs (Fig. 2B). Consistent with the timing of nuclear localization of the N3ICD (Fig. 2B), cleaved N3ICD protein was found in E18.5 lysates but was absent in adult lysates as determined by Western blot analysis (Fig. 2C).



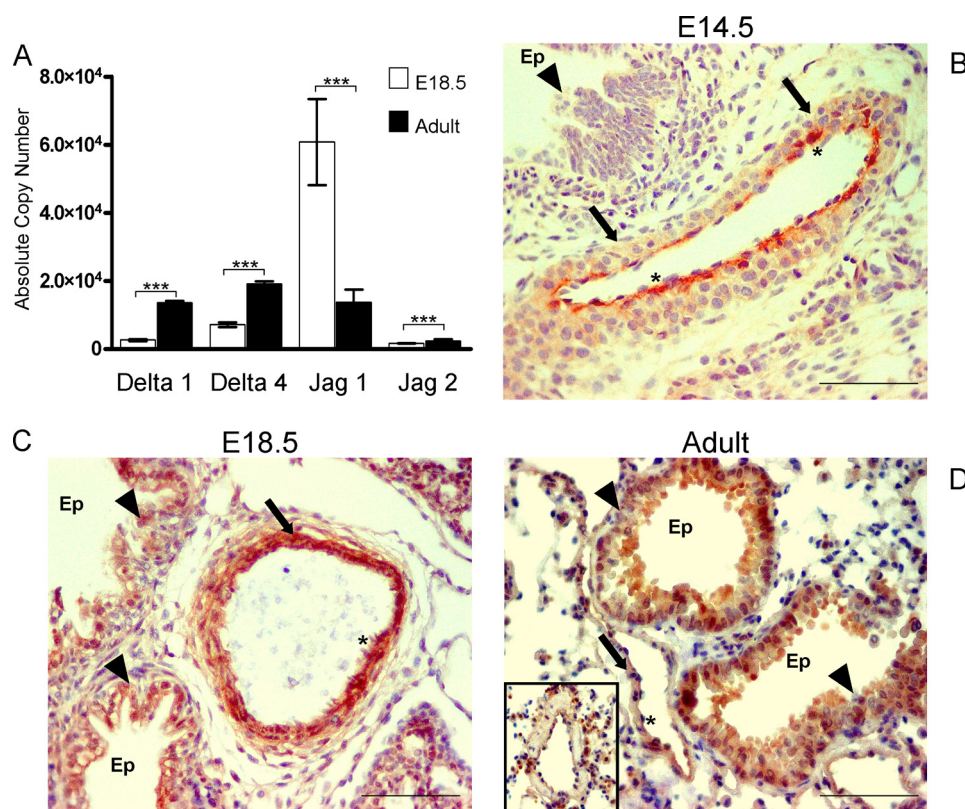


**FIGURE 3. Jagged1 expression in developing and adult lungs.** A, absolute mRNA copy number for Notch3 ligands in E18.5 (white bars) and adult (black bars) hrGFP<sup>+</sup> lung cells. Data show means ± S.D. and are representative of three independent experiments. \*\*\*,  $p < 0.001$ . B–D, Jagged1 protein expression in lung at E14.5 (B) and E18.5 (C) and in the adult (D). \*, endothelium; Ep, epithelium (arrowhead); arrows, VSMCs. The inset in D shows a high-magnification view of diminished Jagged1 expression in adult VSMCs. Scale bars = 20  $\mu$ m.

Notch3 activation has been shown to promote RBP-Jk-mediated induction of *Hey1* and *Hey2* mRNAs in VSMCs *in vitro* and *in vivo* (28). Therefore, to confirm the temporal dynamics of Notch3 signaling in the pulmonary artery, we evaluated the relative expression of *Hey1* and *Hey2* in isolated smooth muscle cells. For isolation of pulmonary artery VSMCs, a transgenic mouse that expresses hrGFP under the control of the rat  $\alpha$ -SMA promoter ( $\alpha$ -SMA-hrGFP) was generated. In the  $\alpha$ -SMA-hrGFP mouse, hrGFP co-localized exclusively with  $\alpha$ -SMA-expressing smooth muscle cells of the pulmonary artery and bronchial tubes (supplemental Fig. S2). hrGFP<sup>+</sup> cells were collected from E18.5 and adult lungs, and the levels of *Hey1* and *Hey2* were determined by qPCR. *Hey1* and *Hey2* mRNA levels were significantly higher at E18.5 compared with E14.5 or adult lungs (Fig. 2D), consistent with the timing of Notch3 activation (Fig. 2, B and C).

To further validate that the time-restricted up-regulation of *Hey1* and *Hey2* in VSMCs reflects Notch3 activation, we assessed expression of other Notch family members in E18.5 VSMCs. We found that *Notch1* and *Notch4* mRNAs were nearly undetectable, as determined by qPCR (data not shown). Although there was a low level of *Notch2* mRNA in VSMCs, Notch2 protein expression was not observed in E18.5 pulmonary artery VSMCs but was observed in adventitial cells surrounding adult pulmonary arteries (supplemental Fig. S3). Moreover, *in situ* hybridization confirmed that *Hey1* and *Hey2* were expressed only in VSMCs, but not in E18.5 bronchial smooth muscle cells (Fig. 2E).

To definitively prove that *Hey1* and *Hey2* mRNA expression in E18.5 VSMCs is reflective of Notch3 signaling, a *Notch3*<sup>−/−</sup>  $\alpha$ -SMA-hrGFP mouse was generated. In isolated E18.5 *Notch3*<sup>−/−</sup> VSMCs, *Hey1* and *Hey2* mRNA levels were decreased by ~75% relative to WT VSMCs (Fig. 2F). Taken together, these observations show that Notch3 signaling is active in VSMCs from late fetal to early postnatal life.

**Notch3 Activation Is Dependent on VSMC-derived Jagged1**—Based on *in vitro* co-culture studies, endothelium-derived Notch ligands have been proposed to engage Notch receptors expressed in VSMCs (29). However, the presence of an intervening basement membrane between the endothelium and VSMC layer raises questions regarding the feasibility of this mode of activation *in vivo*. To identify the activating Notch3 ligand in VSMCs, we assessed the relative mRNA expression of *Delta1*, *Delta4*, *Jagged1*, and *Jagged2* in sorted hrGFP<sup>+</sup> cells from E18.5 and adult lungs. We found that *Jagged1* was the most abundantly expressed ligand at E18.5 and was down-regulated in the adult (Fig. 3A).

To further assess the dynamics and pattern of Jagged1 expression, immunohistochemistry of embryonic and adult lungs was performed. At E14.5, Jagged1 was located in the endothelium (Fig. 3B). At E18.5, Jagged1 was expressed in the endothelium, airway epithelium, and, consistent with the timing of Notch3 activation, VSMCs (Fig. 3C). In the adult, Jagged1 was expressed primarily in the airway epithelium and endothelium (Fig. 3D) and was reduced in VSMCs (Fig. 3D, inset). Taken together, these findings demonstrate that lung VSMCs

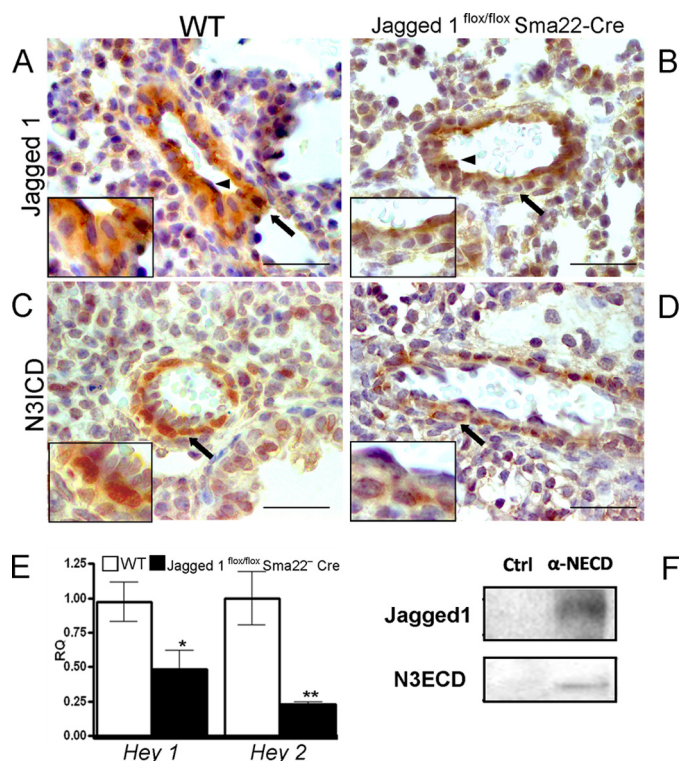


**FIGURE 4. Notch3 activation is dependent on VSMC Jagged1 expression.** A and B, immunohistochemistry for Jagged1 in E18.5 WT (A) and *Jagged1<sup>flox/flox</sup> Sma22-Cre* (B) mouse lungs. Arrows indicate the VSMC layer, and arrowheads indicate the endothelium. Insets show higher power views of WT and *Jagged1<sup>flox/flox</sup> Sma22-Cre* VSMCs. C and D, immunohistochemistry for the N3ICD in E18.5 WT (C) and *Jagged1<sup>flox/flox</sup> Sma22-Cre* (D) mouse lungs. Arrows indicate VSMC nuclei. Insets show higher power views of nuclei. Scale bars = 20 mm. E, relative *Hey1* and *Hey2* mRNA expression in the lungs of E18.5 WT (white bars) and *Jagged1<sup>flox/flox</sup> Sma22-Cre* (black bars) mice. Data show means  $\pm$  S.D. and are representative of two independent experiments. \* $p < 0.05$ ; \*\* $p < 0.01$ . F, proteins derived from CD45/CD31-depleted E18.5 lung cells immunoprecipitated with anti-Notch3 antibody ( $\alpha$ -NECD) or with nonimmune rabbit serum (Ctrl) and immunoblotted with anti-Jagged1 or anti-N3ECD antibody.

express activated Notch3 and its ligand Jagged1 in a time-coordinated manner.

To specifically evaluate the importance of VSMC-derived Jagged1 in Notch3 activation, we generated a VSMC-specific Jagged1-deficient mouse by crossing the *Jagged1<sup>flox/flox</sup>* mouse and a mouse that expresses *Cre* under the control of the smooth muscle-specific transgelin promoter (*Sma22-Cre*) (30). Lungs derived from E18.5 *Jagged1<sup>flox/flox</sup> Sma22-Cre* embryos exhibited widespread loss of Jagged1 selectively in VSMCs. In contrast, Jagged1 expression in the endothelium was intact in this mouse (Fig. 4, A and B), confirming the tissue-specific expression of the *Cre* recombinase. Jagged1 deletion in VSMCs resulted in suppression of Notch3 activation, as assessed by diminished N3ICD nuclear localization in VSMCs (Fig. 4, C and D) and diminished *Hey1* and *Hey2* expression (Fig. 4E).

In recent work, expression of contractile smooth muscle marker genes was found to be down-regulated in the ductus arteriosus of *Jagged1<sup>flox/flox</sup> Sma22-Cre* embryos (21). Interestingly, we also observed down-regulation of contractile smooth muscle marker genes in the absence of VSMC-derived Jagged1 (supplemental Fig. S4) in the embryonic lung. This pattern of smooth muscle gene expression was nearly identical to what was observed in the *Notch3<sup>-/-</sup>* mouse lung (Fig. 1B), providing

further evidence that endothelium-derived Jagged1 is not involved in VSMC Notch3 activation but rather requires the action of VSMC-derived Jagged1.

In view of these observations, we sought to demonstrate that Notch3 and Jagged1 are physically associated in the E18.5 lung. For this, immunoprecipitation of Notch3 was performed on lysates isolated from CD45/CD31-depleted E18.5 whole lung preparations, followed by Western blot analysis using anti-Jagged1 antibody. Jagged1 was detected in immunoprecipitates obtained with anti-Notch3 antibody, but not in a preimmune rabbit serum control (Fig. 4F). This finding shows that Jagged1 is engaged with Notch3 at E18.5.

**Evidence for Cell-autonomous Notch3 Cell Activation in Pulmonary Artery VSMCs**—Our observations are thus far consistent with two possible modes of Notch3 activation by Jagged1 in lung VSMCs. Notch3 may be activated through (a) a cell-autonomous pathway or (b) a homotypic interaction between two neighboring VSMCs. To help distinguish between these possibilities, we established an *in vitro* culture system with RPASMCs isolated from neonatal rats. Similar to murine VSMCs, cultured RPASMCs expressed Jagged1, Notch3, and the cleaved N3ICD (supplemental Fig. S5, A and B). Interestingly, Western blot analysis indicated that the majority of Notch3 in these cells was found in the cleaved form (supplemental Fig. S5B). Importantly, the diminished intensity of the band corresponding to the cleaved N3ICD in lysates from cells incubated with a  $\gamma$ -secretase inhibitor (DAPT) confirmed that expression of this protein fragment reflects Notch3 activation (supplemental Fig. S5C).

To evaluate whether Notch3 activation in RPASMCs is cell-autonomous, N3ICD cellular localization was determined in sparsely plated cells by confocal microscopy. As shown in Fig. 5 (A–C), individual RPASMCs exhibited a nuclear N3ICD despite a lack of contact with neighboring cells, compatible with cell-autonomous activation. It is noteworthy that the N3ICD was predominantly localized in nuclei, consistent with our assessment of Notch3 activation by Western blot analysis (supplemental Fig. S5B).

To further address whether cell-cell contact contributes to Notch3 activation, we designed a functional *in vitro* assay. We hypothesized that 1) if Jagged1 activates Notch3 independently of cell-to-cell contact, then we will observe down-regulation of target genes after knocking down *Jagged1* in RPASMCs and 2) this down-regulation will not be rescued by co-culturing *Jagged1* knockdown cells with WT RPASMCs. To evaluate this, RPASMCs were transduced with a lentivirus expressing *Jagged1* shRNA or a control scrambled shRNA coupled to the reporter gene eGFP. RPASMC transduction with the *Jagged1* shRNA lentivirus resulted in *Jagged1* knockdown (supplemental Fig. S6, A and B), as well as a significant reduction in *Hey1* and *Hey2* gene expression (supplemental Fig. S6, C and D).

To test whether WT RPASMCs could rescue *Hey1* and *Hey2* expression in knockdown cells, control scrambled shRNA or *Jagged1* knockdown RPASMCs were co-cultured with WT RPASMCs at a 1:1 ratio for 72 h. Cells were then separated by cell sorting using eGFP as a selection marker, and *Hey1* and *Hey2* expression was assessed by qPCR. Consistent with a cell-



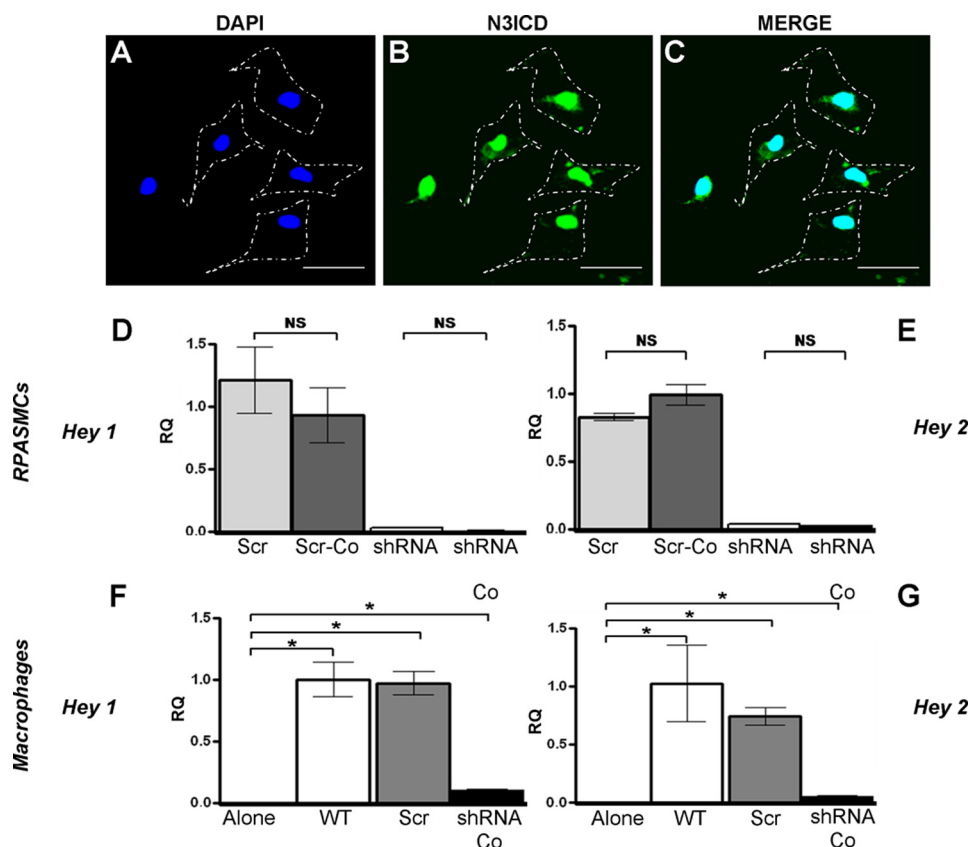


**FIGURE 5. Evidence for cell-autonomous Notch3 signaling in VSMCs.** A–C, N3ICD localization in RPASMCs by confocal microscopy. A, nuclei; B, N3ICD; C, merged signals. Dashes indicate cell outlines. Scale bars = 20 μm. D and E, relative *Hey1* and *Hey2* mRNA levels, respectively, in scrambled shRNA RPASMCs (*Scr*), scrambled shRNA RPASMCs co-cultured with WT RPASMCs (*Scr-Co*), *Jagged1* knockdown RPASMCs (*shRNA*), and *Jagged1* knockdown RPASMCs co-cultured with WT RPASMCs (*shRNA Co*). F and G, relative *Hey1* and *Hey2* mRNA levels, respectively, in rat macrophages cultured alone or co-cultured with WT, scrambled shRNA, or *Jagged1* knockdown RPASMCs. For qPCR, data show means ± S.D. and are representative of two independent experiments run in triplicates. NS, not significant; \*,  $p < 0.05$ .

autonomous signaling model, determination of *Hey1* and *Hey2* in WT, scrambled shRNA, and *Jagged1* knockdown cells showed that WT cells were unable to rescue the down-regulation of *Hey1* or *Hey2* mRNA in *Jagged1* knockdown cells (Fig. 5, D and E).

To confirm that RPASMCs are capable of activating Notch signaling in neighboring cells *in vitro*, we co-cultured RPASMCs with a rat alveolar macrophage cell line that expresses detectable cell surface Notch3 (supplemental Fig. S7), but neither *Jagged1* (data not shown) nor *Hey1* or *Hey2* mRNA (Fig. 5, F and G). We found that WT cells and RPASMCs expressing scrambled shRNA stimulated *Hey1* and *Hey2* mRNA expression in co-cultured macrophages to a greater level than *Jagged1* knockdown RPASMCs (Fig. 5, F and G). These findings confirm that RPASMC-derived *Jagged1* is competent to activate neighboring cells. These observations also raise the possibility that Notch3 may not be expressed on or activated from the surface of VSMCs.

**Evidence for Intracellular Localization of Notch3 in VSMCs—**To investigate the cellular localization of Notch3 in E18.5 mouse lung cells, flow cytometry was performed. We were unable to detect the N3ECD on the surface of E18.5 lung cells (Fig. 6A). In contrast, the N3ECD was detected in permeabilized lung cells (Fig. 6A). To more specifically evaluate N3ECD expression in VSMCs, non-permeabilized and permeabilized

E18.5 hrGFP<sup>+</sup> cells were analyzed by flow cytometry. As observed with whole lung cells, the N3ECD was detected only in permeabilized cells (Fig. 6B), consistent with an intracellular localization of Notch3 in VSMCs.

To examine this further, confocal microscopy of isolated E18.5 hrGFP<sup>+</sup> cells was performed. Analysis of individual cells stained with anti-N3ECD antibody revealed a cytoplasmic distribution of Notch3, with no evidence of cell surface expression (Fig. 6C). In accordance, individual cells simultaneously stained with anti-N3ECD and anti-N3ICD antibodies showed co-localization of these two domains only in the cytoplasm of E18.5 VSMCs (Fig. 6D). In contrast *Jagged1* was found intracellularly and on the cell surface, and consistent with their physical association (Fig. 4F), co-localized with Notch3 in the interior of E18.5 VSMCs (Fig. 6E).

To rule out the possibility of Notch3 epitope masking or disruption by the enzymatic cell isolation procedure, Notch3 expression in adult lung CD45<sup>+</sup> cells isolated by the same method was determined. We observed that Notch3 was detectable on the surface in this cell population (supplemental Fig. S8), consistent with published work (31) and confirming that this procedure does not affect Notch3 integrity or antibody binding. To demonstrate that the intracellular localization of Notch3 is not due to receptor internalization during cell processing, E18.5 hrGFP<sup>+</sup> cells were fixed and stained at 4 °C. Under

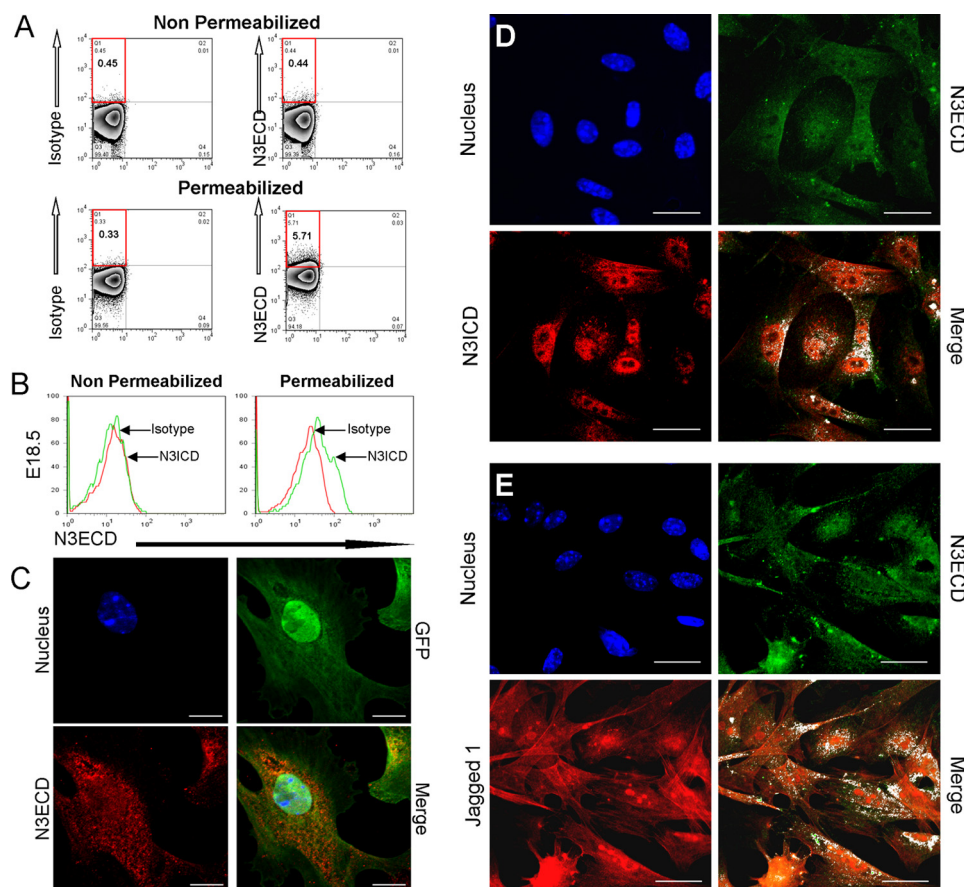


**FIGURE 6. Intracellular localization of Notch3 in VSMCs.** *A*, flow cytometry for the N3ECD in non-permeabilized and permeabilized E18.5 lung cells. *B*, flow cytometry for the N3ECD in non-permeabilized and permeabilized E18.5 hrGFP<sup>+</sup> mouse lung cells. *Red histogram*, isotype; *green histogram*, the N3ECD. *C*, perinuclear distribution of the N3ECD in E18.5 hrGFP<sup>+</sup> mouse lung cells as determined by confocal microscopy. *Upper left panel*, nucleus; *upper right panel*, GFP; *lower left panel*, the N3ECD (*red*); *lower right panel*, merged image. *D*, intracellular co-localization of the N3ECD and N3ICD in isolated E18.5 hrGFP<sup>+</sup> mouse lung cells. *Upper left panel*, nucleus (*blue*); *upper right panel*, the N3ECD (pseudo-colored *green*); *lower left panel*, the N3ICD (*red*); *lower right panel*, merged image. Co-localization is shown in *white*. *E*, intracellular co-localization of the N3ECD and Jagged1 in isolated E18.5 hrGFP<sup>+</sup> mouse lung cells. *Upper left panel*, nucleus; *upper right panel*, the N3ECD (pseudo-colored *green*); *lower left panel*, Jagged1 (*red*); *lower right panel*, merged image. Co-localization is shown in *white*. Scale bars = 20  $\mu$ m.

these conditions, the N3ECD was observed only inside VSMCs, thus ruling out receptor recycling from the cell surface.

To evaluate whether Notch3 cellular localization in RPASMCs is similar to that in mouse VSMCs, confocal microscopy was employed. As in the mouse, Notch3 was not detected on the cell surface of RPASMCs but rather localized to the perinuclear region (Fig. 7, *A* and *B*). To further corroborate these findings, biotinylated proteins from RPASMCs were analyzed. In agreement, we were unable to detect Notch3 in a biotinylated surface protein fraction by Western analysis (*supplemental Fig. 7C*). In contrast, Notch3 was detected in the non-biotinylated fractions and total cell lysates. As expected, Jagged1 was found in biotinylated and non-biotinylated fractions and whole cell lysates. On the other hand, the intracellular protein p53 was markedly enriched in the non-biotinylated internal fraction (Fig. 7C). Additionally, Ponceau S staining revealed approximate equal protein loading (data not shown). Taken together, these results demonstrate Notch3 expression restricted to the interior of pulmonary artery VSMCs.

To determine whether the restricted intracellular Notch3 receptor localization is dependent on cellular context, recombinant GFP, N3ICD-GFP, and Notch3-GFP fusion proteins

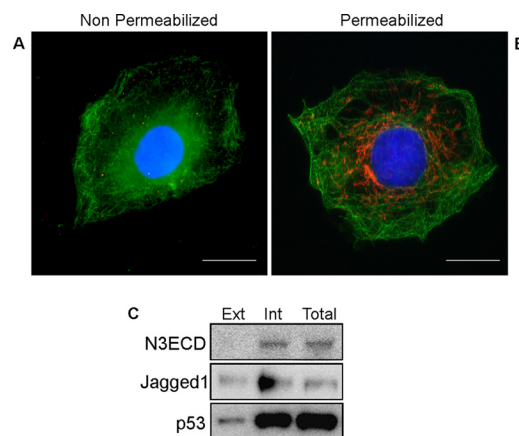


**FIGURE 7. Notch3 localization in neonatal RPASMCs.** *A* and *B*, confocal microscopy of N3ECD staining (*red*) in non-permeabilized (*A*) and permeabilized (*B*) RPASMCs.  $\beta$ -Tubulin staining is shown in *green*. Scale bars = 20  $\mu$ m. *C*, Western blot for the N3ECD, Jagged1, and p53 in the biotinylated extracellular fraction (*Ext*), non-biotinylated intracellular fraction (*Int*), and total cell lysates.

were transfected into RPASMCs and human kidney epithelial 293T cells. Confocal microscopy showed cytoplasmic GFP expression in both cell types with the control plasmid (Fig. 8, *A*

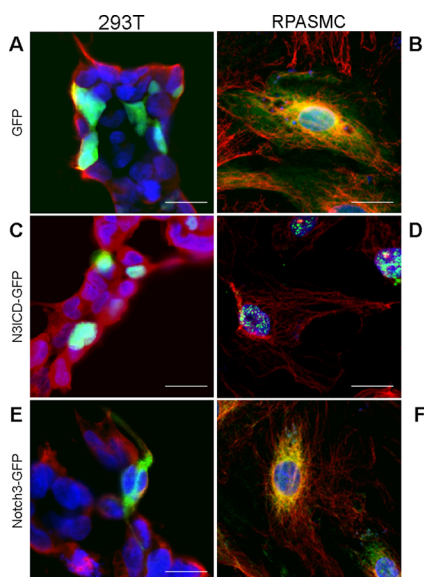


**FIGURE 8. Localization for recombinant Notch3-GFP fusion proteins in transfected RPASMCs and 293T cells as determined by confocal microscopy.** A and B, cytoplasmic GFP distribution in cells transfected with a control plasmid. C and D, nuclear GFP localization in cells transfected with the N3ICD-GFP construct. E, cytoplasmic and cellular membrane GFP distribution in 293T cells transfected with the full-length Notch3-GFP construct. F, perinuclear GFP distribution in RPASMCs cells transfected with the full-length Notch3-GFP construct. Green, GFP; red,  $\beta$ -tubulin; blue, nuclei. Scale bars = 20  $\mu$ m.

and B). GFP was localized in the nuclei of both RPASMCs and 293T cells transfected with N3ICD-GFP (Fig. 8, C and D). Consistent with previous reports (32), GFP was detected on the cell surface and cytoplasm of 293T cells transfected with Notch3-GFP (Fig. 8E). In RPASMCs transfected with Notch3-GFP, however, GFP localized exclusively to the perinuclear region without evidence of surface expression (Fig. 8F). These findings show that, even under conditions of overexpression, Notch3 localizes to the interior of VSMCs.

## DISCUSSION

In this study, we found that Notch3 expression is restricted to pulmonary artery VSMCs in the developing lung. We observed that activation of this receptor occurs during a discrete time period spanning late fetal to early postnatal life and is dependent upon VSMC-derived Jagged1. This time-restricted signal regulates pulmonary artery cell phenotype, as evidenced by alterations in expression of smooth muscle-related genes and VSMC morphology in the *Notch3*<sup>-/-</sup> mouse.

Importantly, we were unable to detect Notch3 cell surface expression in lung VSMCs by a variety of assays. Rather, we demonstrated that this receptor displays an intracellular localization that appears unique to VSMCs. The differential targeting of overexpressed Notch3 to the interior of RPASMCs and to the cell surface of human kidney epithelial 293T cells and macrophages underscores the importance of cellular context in determining the cellular localization of Notch3. The relative basis for how particular structural elements of the Notch3 protein facilitate targeting to an intracellular compartment in VSMCs, as opposed to the surface of macrophages, is not yet evident but is a focus of ongoing investigation. On the basis of our overexpression data, we speculate that differences in asso-

ciated Notch3 targeting molecules underlie these observations. Overall, these data argue for a cell-autonomous signaling mode of Notch3 signaling that involves an engagement with the Jagged1 ligand in the interior of VSMCs.

It is important to emphasize the functional differences between the ligand-dependent intracellular Notch pathway described in *Drosophila* (17) and the pathway we identified in VSMCs. In *Drosophila*, this pathway is active during mitosis and plays a defining role in determining the differential cell fates of the two daughter cells that arise from the asymmetric cell division of sensory organ progenitor cells. This process involves the asymmetric sorting of a subtype of endosomes containing Notch and Delta, which leads to release of the Notch intracellular domain to only one daughter cell (17). In contrast, during active intracellular Notch3 signaling, we found no evidence that VSMCs are proliferating (data not shown). Furthermore, cell-autonomous Notch3 signaling occurs in cells with an already established fate during late gestation.

There are differences in the structure of Notch3 compared with other family members. One speculation is that these structural features mediate selectivity for Jagged1 (33). There are, however, unique functional properties for Notch3. In systemic vessels, Notch3 may serve as a direct regulator of hemodynamic tone (15). One possibility is that Notch3 is a direct regulator of tone in the pulmonary artery during the transition to postnatal life.

Previous work has indicated Notch-ligand interactions occurring in *cis*, resulting in inhibition of Notch signaling (34). Rather, we found in VSMCs that Notch3-Jagged1 interaction in *cis* leads to activation. In ongoing work, we found that Notch3 and Jagged1 reside in the same endosomal compartments, suggesting the possibility of receptor-ligand interaction and proteolytic release of the N3ICD at this site.

In the context of our findings, this leads us to propose two models of cell-autonomous intracellular Notch3 activation in VSMCs. In one model, membrane-bound Jagged1 interacts with membrane-bound Notch3 in the interior of the same endosome, thereby generating the force required to expose the  $\gamma$ -secretase target site in the cytoplasm for cleavage. In the second model, membrane-bound Jagged1 and membrane-bound Notch3 interact on the cytoplasmic side of two contiguous endosomes, thereby exposing the Notch intracellular domain cleavage site in the endosomal interior. Of note, although  $\gamma$ -secretase substrates are processed at or near the cell surface, this enzyme complex also resides in the endoplasmic reticulum, Golgi network, and intermediate compartments (17). Its optimal activity is at low pH, indicating that  $\gamma$ -secretase could function within the acidic milieu of late endosomes (35).

A broader biological question relates to why this alternative mode of Notch activation is operative in pulmonary artery VSMCs. Although unclear at this time, cell-autonomous Notch3 signaling may have involved, in part, to ensure the efficient and homogeneous adaptation of pulmonary artery VSMCs to the sudden and dramatic increase in blood flow and pressure associated with birth and air breathing. The restricted timing of Notch3 activation is consistent with this possibility, thereby pointing to a key role for this pathway in regulating the final stages of VSMC maturation. The emer-



gence of dysmorphic VSMCs early after birth in *Notch3*<sup>-/-</sup> mice, which is highly suggestive of an injury response (36), further underscores a role for Notch3-dependent signals in the adaptation from a fetal to a postnatal pulmonary vasculature. The improved morphological appearance of the adult as opposed to the postnatal day 3 vessels in *Notch3*<sup>-/-</sup> mice suggests the presence of an active repair process.

Finally, we posit that our findings may have relevance to understanding two pathological conditions. Recently, dysregulation of Notch3 activation has been implicated as a key factor in the pathogenesis of adult pulmonary hypertension (27). Whether Jagged1-dependent cell-autonomous Notch activation is involved in this pathological process will need to be clarified, particularly if targeted Notch3-dependent therapies are considered. Furthermore, in view of the late timing of Notch3 activation during development and its effects on VSMC phenotype, we wonder whether relative Notch3 signaling deficiency plays a role in the pathogenesis of the pulmonary vasculopathy associated with prematurity.

**Acknowledgments**—We thank Anne Hinds and Yun Qian for technical support.

## REFERENCES

- Gao, Y., and Raj, J. U. (2010) *Physiol. Rev.* **90**, 1291–1335
- deMello, D. E., Sawyer, D., Galvin, N., and Reid, L. M. (1997) *Am. J. Respir. Cell Mol. Biol.* **16**, 568–581
- Hellström, M., Kalén, M., Lindahl, P., Abramsson, A., and Betsholtz, C. (1999) *Development* **126**, 3047–3055
- Wang, Z., Shu, W., Lu, M. M., and Morrissey, E. E. (2005) *Mol. Cell. Biol.* **25**, 5022–5030
- Tallquist, M. D., French, W. J., and Soriano, P. (2003) *PLoS Biol.* **1**, E52
- Artavanis-Tsakonas, S., Rand, M. D., and Lake, R. J. (1999) *Science* **284**, 770–776
- Nichols, J. T., Miyamoto, A., and Weinmaster, G. (2007) *Traffic* **8**, 959–969
- Nakagawa, O., McFadden, D. G., Nakagawa, M., Yanagisawa, H., Hu, T., Srivastava, D., and Olson, E. N. (2000) *Proc. Natl. Acad. Sci. U.S.A.* **97**, 13655–13660
- Schroeter, E. H., Kisslinger, J. A., and Kopan, R. (1998) *Nature* **393**, 382–386
- Clément, N., Gueguen, M., Glorian, M., Blaise, R., Andréani, M., Brou, C., Bausero, P., and Limon, I. (2007) *J. Cell Sci.* **120**, 3352–3361
- Sweeney, C., Morrow, D., Birney, Y. A., Coyle, S., Hennessy, C., Scheller, A., Cummins, P. M., Walls, D., Redmond, E. M., and Cahill, P. A. (2004) *FASEB J.* **18**, 1421–1423
- Domenga, V., Fardoux, P., Lacombe, P., Monet, M., Maciazek, J., Krebs, L. T., Klonjowski, B., Berrou, E., Mericskay, M., Li, Z., Tournier-Lasserre, E., Gridley, T., and Joutel, A. (2004) *Genes Dev.* **18**, 2730–2735
- Liu, H., Zhang, W., Kennard, S., Caldwell, R. B., and Lilly, B. (2010) *Circulation Res.* **107**, 860–870
- Morrow, D., Sweeney, C., Birney, Y. A., Cummins, P. M., Walls, D., Redmond, E. M., and Cahill, P. A. (2005) *Circ. Res.* **96**, 567–575
- Belin de Chantemèle, E. J., Retailliau, K., Pinaud, F., Vessièrès, E., Bocquet, A., Guihot, A. L., Lemaire, B., Domenga, V., Baufréon, C., Loufrani, L., Joutel, A., and Henrion, D. (2008) *Arterioscler. Thromb. Vasc. Biol.* **28**, 2216–2224
- Lin, L., Mernaugh, R., Yi, F., Blum, D., Carbone, D. P., and Dang, T. P. (2010) *Cancer Res.* **70**, 632–638
- Coumilleau, F., Fürthauer, M., Knoblich, J. A., and González-Gaitán, M. (2009) *Nature* **458**, 1051–1055
- Wilkin, M., Tongngok, P., Gensch, N., Clemence, S., Motoki, M., Yamada, K., Hori, K., Taniguchi-Kanai, M., Franklin, E., Matsuno, K., and Baron, M. (2008) *Dev. Cell* **15**, 762–772
- Tsao, P. N., Chen, F., Izvolzky, K. I., Walker, J., Kukuruzinska, M. A., Lu, J., and Cardoso, W. V. (2008) *J. Biol. Chem.* **283**, 29532–29544
- Woodsome, T. P., Polzin, A., Kitazawa, K., Eto, M., and Kitazawa, T. (2006) *J. Cell Sci.* **119**, 1769–1780
- Feng, X., Krebs, L. T., and Gridley, T. (2010) *Development* **137**, 4191–4199
- Choi, J. H., Park, J. T., Davidson, B., Morin, P. J., Shih, I. M., and Wang, T. L. (2008) *Cancer Res.* **68**, 5716–5723
- Wiznerowicz, M., and Trono, D. (2003) *J. Virol.* **77**, 8957–8961
- Murphy, G. J., Mostoslavsky, G., Kotton, D. N., and Mulligan, R. C. (2006) *Nat. Med.* **12**, 1093–1099
- Arboleda-Velasquez, J. F., Rampal, R., Fung, E., Darland, D. C., Liu, M., Martinez, M. C., Donahue, C. P., Navarro-Gonzalez, M. F., Libby, P., D'Amore, P. A., Aikawa, M., Haltiwanger, R. S., and Kosik, K. S. (2005) *Human Mol. Genet.* **14**, 1631–1639
- Zhu, J. H., Chen, C. L., Flavahan, S., Harr, J., Su, B., and Flavahan, N. A. (2010) *Am. J. Physiol. Heart Circ. Physiol.* **300**, 1762–1769
- Li, X., Zhang, X., Leathers, R., Makino, A., Huang, C., Parsa, P., Macias, J., Yuan, J. X., Jamieson, S. W., and Thistlethwaite, P. A. (2009) *Nat. Med.* **15**, 1289–1297
- Wang, W., Campos, A. H., Prince, C. Z., Mou, Y., and Pollman, M. J. (2002) *J. Biol. Chem.* **277**, 23165–23171
- Liu, H., Kennard, S., and Lilly, B. (2009) *Circ. Res.* **104**, 466–475
- Holtwick, R., Gotthardt, M., Skryabin, B., Steinmetz, M., Potthast, R., Zetsche, B., Hammer, R. E., Herz, J., and Kuhn, M. (2002) *Proc. Natl. Acad. Sci. U.S.A.* **99**, 7142–7147
- Fung, E., Tang, S. M., Canner, J. P., Morishige, K., Arboleda-Velasquez, J. F., Cardoso, A. A., Carlesso, N., Aster, J. C., and Aikawa, M. (2007) *Circulation* **115**, 2948–2956
- Rauen, T., Raffetseder, U., Frye, B. C., Djudjaj, S., Mühlenberg, P. J., Eitner, F., Lendahl, U., Bernhagen, J., Dooley, S., and Mertens, P. R. (2009) *J. Biol. Chem.* **284**, 26928–26940
- Bellavia, D., Checquolo, S., Campese, A. F., Felli, M. P., Gulino, A., and Screpanti, I. (2008) *Oncogene* **27**, 5092–5098
- D'Souza, B., Miyamoto, A., and Weinmaster, G. (2008) *Oncogene* **27**, 5148–5167
- Pasternak, S. H., Bagshaw, R. D., Guiral, M., Zhang, S., Ackerley, C. A., Pak, B. J., Callahan, J. W., and Mahuran, D. J. (2003) *J. Biol. Chem.* **278**, 26687–26694
- White, T. A., Witt, T. A., Pan, S., Mueske, C. S., Kleppe, L. S., Holroyd, E. W., Champion, H. C., and Simari, R. D. (2010) *Am. J. Respir. Cell Mol. Biol.* **43**, 35–45



# Modeling the effects of stretch-dependent surfactant secretion on lung recruitment during variable ventilation

Samir D. Amin<sup>1</sup>, Arnab Majumdar<sup>1</sup>, Phil Alkana<sup>2</sup>, Allan J. Walkey<sup>2</sup>, George T. O'Connor<sup>2</sup>, Béla Suki<sup>1\*</sup>

<sup>1</sup>Department of Biomedical Engineering, Boston University, Boston, USA

<sup>2</sup>School of Medicine, Boston University, Boston, USA

Email: [bsuki@bu.edu](mailto:bsuki@bu.edu)

Received 24 October 2013; revised 26 November 2013; accepted 15 December 2013

Copyright © 2013 Samir D. Amin *et al.* This is an open access article distributed under the Creative Commons Attribution License, which permits unrestricted use, distribution, and reproduction in any medium, provided the original work is properly cited.

## ABSTRACT

Variable ventilation (VV) is a novel strategy of ventilatory support that utilizes random variations in the delivered tidal volume ( $V_T$ ) to improve lung function. Since the stretch pattern during VV has been shown to increase surfactant release both in animals and cell culture, we hypothesized that there were combinations of PEEP and  $V_T$  during VV that led to improved alveolar recruitment compared to conventional mechanical ventilation (CV). To test this hypothesis, we developed a computational model of stretch-induced surfactant release combined with abnormal alveolar mechanics of the injured lung under mechanical ventilation. We modeled the lung as a set of distinct acini with independent surfactant secretion and thus pressure-volume relationships. The rate of surfactant secretion was modulated by the stretch magnitude that an alveolus experienced per breath. Mechanical ventilation was simulated by delivering a prescribed  $V_T$  at each breath. The fractional  $V_T$  that each acinus received depended on its local compliance relative to the total system compliance. Regional variability in  $V_T$  thus developed through feedback between stretch and surfactant release and coupling of regional  $V_T$  to ventilator settings. The model allowed us to simulate patient-ventilator interactions over a wide range of PEEPs and  $V_T$ s during CV and VV. Full recruitment was achieved through VV at a lower PEEP than required for CV. During VV, the acini were maintained under non-equilibrium steady-state conditions with breath-by-breath fluctuations of regional  $V_T$ . In CV, alveolar injury was prevented with high-PEEP-low- $V_T$  or low-PEEP-high- $V_T$  combinations. In contrast, one contiguous region of PEEP- $V_T$  combinations al-

lowed for full recruitment without overdistention during VV. We found that maintaining epithelial cell stretch above a critical threshold with either PEEP or  $V_T$  may help stabilize the injured lung. These results demonstrate the significance of patient-ventilator coupling through the influence of cellular stretch-induced surfactant release on the whole lung stability.

**Keywords:** Computational Modeling; Mechanical Ventilation; Variable Ventilation; Surfactant Secretion Dynamics

## 1. INTRODUCTION

Acute lung injury (ALI) and acute respiratory distress syndrome (ARDS) represent a continuum of lung injury that affects over 200,000 patients in the US yearly, with a 30% - 40% mortality rate [1]. The ALI and ARDS arise from either systemic insult (e.g., sepsis, pancreatitis) or local injury (e.g., pneumonia, aspiration injury) and manifest as acute inflammatory edema and diffuse alveolar damage. The inflammatory responses result in severely impaired lung function with reduced compliance and gas exchange, often culminating in respiratory failure and the need for mechanical ventilation. Currently, the only therapy that improves survival in ALI/ARDS is the ARDSNet ventilatory protocol, which decreases ventilator-associated lung injury (VALI) by avoiding alveolar overdistention [2].

In addition to alveolar overdistention injury, VALI can also be induced through the gradient of normal forces acting on epithelial cells during the reopening process of closed units [3,4]. These alveolar collapse-associated causes of VALI are attenuated by the addition of positive end expiratory pressure (PEEP), which is intended to recruit atelectatic lung, prevent alveolar surfactant depletion and end expiratory collapse. Unfortunately, the addi-

\*Corresponding author.

tion of PEEP can lead to further overdistention and injury of healthy, high compliance alveolar units [5]. The success of mechanical ventilation depends on the right balance between overdistention and cyclic collapse-induced injury [6]. Although the ARDSNet strategy was a major advance in critical care, this method of mechanical ventilation did not completely eliminate VALI [7]. Thus, alternative mechanical ventilation strategies that can better balance overdistention and cyclic collapse have been sought.

Variable ventilation (VV) is a relatively novel strategy of ventilatory support that utilizes random variations in the delivered tidal volume ( $V_T$ ) to improve lung function [Much]. Multiple pre-clinical models of acute lung injury have shown VV to be superior to conventional mechanical ventilation in inducing endogenous surfactant secretion [8,9], improving alveolar recruitment [10,11], and reducing cytokine [11,12] and histologic [13] evidence of VALI. Several mechanisms have been proposed to explain the benefit from adding variability to mechanical ventilation including variations along the nonlinear pressure-volume curve of the injured lung [14], time dependent closure and opening [11] and variable stretch-induced surfactant release [8,9].

Single large stretches have been shown to be a potent stimulus for surfactant release [15]. On the other hand, monotonous large amplitude cyclic stretch of epithelial cells in culture down-regulates surfactant release [8]. Thus, different stretch patterns delivered by a mechanical ventilation mode should have a significant impact on surfactant turnover which in turn determines lung compliance and hence patient outcome. To our knowledge, interactions among PEEP and  $V_T$  during mechanical ventilation, surfactant release and lung physiology have not been studied in a systematic way.

Combined with PEEP, VV has been shown to outperform CV in recruitment and reduction of epithelial injury in HCl-injured mice [12]. We thus hypothesized that there were combinations of PEEP and  $V_T$  during VV that led to improved alveolar recruitment through stretch-induced surfactant release compared to conventional mechanical ventilation (CV). To test this hypothesis, we have developed a computational model of stretch-induced surfactant production and release combined with abnormal alveolar mechanics of the injured lung during mechanical ventilation. Using this model, we compared alveolar recruitment-derecruitment behavior over a wide range of PEEP and  $V_T$  during both VV and CV.

## 2. METHODS

We model the lung as a parallel arrangement of  $N_A$  acinar units (**Figure 1(A)**), each with independent surfactant secretion and thus pressure-volume ( $P$ - $V$ ) relationship. Each acinar unit is assumed to consist of many alveoli

which are not modeled separately. Within an acinar unit, surfactant secreted by type II epithelial cells accumulates onto the air-liquid interface to reduce surface tension and thus increase local alveolar compliance (**Figure 1(C)**). Epithelial cells secrete surfactant at a rate determined by the magnitude of stretch their unit experiences over a given breath (**Figure 1(B)**). Units that receive either more or less than average regional  $V_T$  also experience correspondingly more or less stretch; over time this will affect the amount of surfactant accumulated locally at the air-liquid interface and thus each unit consequently softens or stiffens.

The model simulates mechanical ventilation by delivering a prescribed  $V_T$  to the entire parallel set of acinar units each breath. The fractional tidal volume ( $V_{Ti}$ ) that the  $i$ -th unit receives depends on its local compliance relative to the total compliance of the system (**Figure 1(D)**). Regional variability in  $V_T$  can thus develop through 1) the feedback between stretch and surfactant release, and 2) the coupling of regional  $V_T$  to mechanical ventilator settings. We can then compare this coupling behavior during simulated CV and VV of the lung model.

### 2.1. Modulation of Surfactant Release by Periodic Stretch

Alveolar tissue stretches to accommodate the variations in lung volume during ventilation. We define the magnitude of stretch  $\varepsilon$  in a unit over a given breath as the relative change in surface area at end-expiration  $A_{EE}$  to that at end-inspiration  $A_{EI}$ . Thus,  $\varepsilon$  approximately represents the biaxial strain the cells experience during tidal ventilation assuming that surface area of a single cell is much smaller than  $A_{EE}$ .

It is well documented that surfactant release increases with stretch amplitude up to moderate strains [15,16], while large stretch inhibits release [8,16]. It naturally follows that there must be some intermediate stretch level that produces a peak in surfactant release, although the exact relation has yet to be determined.

Thus, to incorporate in the model stretch-induced cellular surfactant release and inhibition (from excessive stretch) in a simple manner, we assume that the rate of surfactant release in a unit increases with stretch magnitude until  $\varepsilon$  surpasses a critical threshold  $\varepsilon^*$ , whereby surfactant release reduces with further stretch magnitude (**Figure 1(B)**). A piecewise linear relation is used for surfactant release rate  $\varphi$  as a function of  $\varepsilon$ :

$$\varphi = \begin{cases} \frac{\varepsilon}{\varepsilon^*} & \varepsilon \leq \varepsilon^* \\ 2 - \frac{\varepsilon}{\varepsilon^*} & \varepsilon^* \leq \varepsilon \leq 2\varepsilon^* \\ 0 & \varepsilon > 2\varepsilon^* \end{cases} \quad (1)$$

Note that in the context of the model, the exact linear shape is not important; it's the existence of a peak that we aim to capture. Furthermore this curve only represents the stretch-dependent fraction of surfactant release, which is in addition to a baseline rate which we assume is constant throughout the simulation. This point is elaborated on in Section 4.2.

## 2.2. Dynamics of Surfactant Secretion and Degradation

We propose a simple first order dynamics description of surfactant secretion (**Figure 1(C)**). Stretch  $\varepsilon$  induces the release of surfactant. At each breath  $n$ , a small amount of surfactant is released from the cells onto the alveolar air-liquid interface. Interfacial surfactant ( $S$ ) is simultaneously removed through degradation, uptake or other processes at a rate  $\lambda$  so that  $S$  at breath  $n + 1$  is given by:

$$S_{n+1} = (1 - \lambda)S_n + \varphi_n \quad (2)$$

## 2.3. Sigmoidal Pressure-Volume Relation

The volume  $V$  of each acinar unit obeys a sigmoid relation with transpulmonary pressure  $P$ :

$$V = \frac{V_{\max}}{1 + e^{-\kappa(P-G)}} \quad (3)$$

The parameter  $\kappa$  corresponds to the compliance of the curve,  $V_{\max}$  is the volume at total lung capacity (TLC) and  $G$  is the inflection point. The  $P$ - $V$  curve of each acinus, which we assume is proportional to the entire volume of the unit, is modulated breath-by-breath by the available interfacial surfactant  $S_n$  as

$$G_n = G_0 e^{\frac{S_n}{S_0}} \quad (4)$$

where  $S_0$  is a scaling parameter, and  $G_0$  corresponds to the inflection point of **Eq.3** arising solely from the equilibrium amount of stretch-independent surfactant release. Thus, an increase in interfacial surfactant shifts the inflection point to the left resulting in a higher volume for a given pressure (**Figure 1(D)**). This form presented by [17] was chosen as it captures lung  $P$ - $V$  curves under a variety of conditions, and is further discussed in Section 4.5.2.

## 2.4. Simulation of Mechanical Ventilation

Ventilation of the model is calculated using a prescribed PEEP and  $V_T$  as follows. We assume that all acinar pressures  $P_i$  reach equilibrium both at end expiration (EE) and end inspiration (EI), and thus tissue and surface film viscoelasticity is immaterial. Thus, at end expiration, the pressure in each unit is equal to the prescribed PEEP

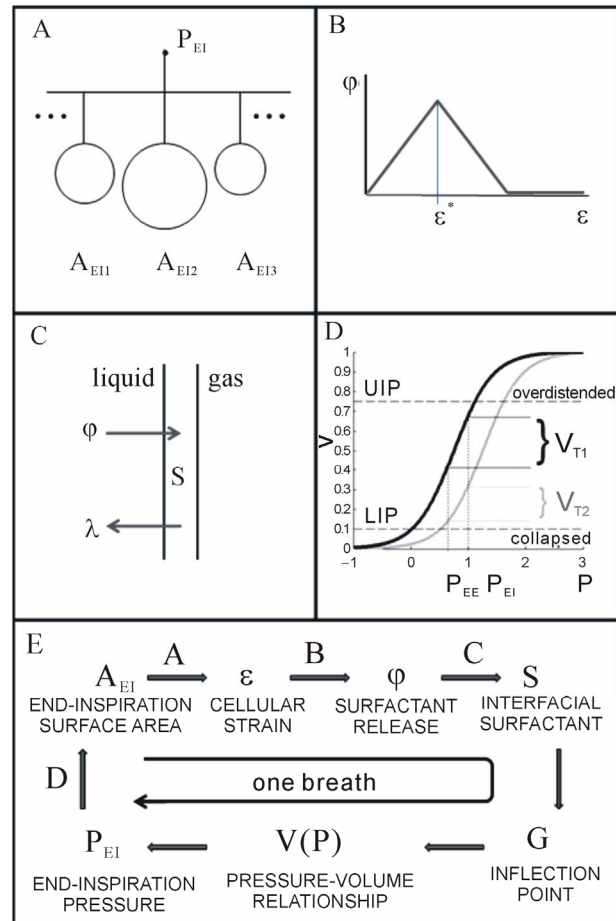


**Figure 1.** Total Surfactant Release and Regional Tidal Volume is Modulated by Periodic Stretch. (A) The lung is divided into parallel alveolar units each defining an acinus, and ventilated with a given tidal volume ( $V_T$ ). Individual tidal volumes, and thus strains, vary with regional compliances. At end-inspiration with airway pressure  $P_{EI}$  each unit can have a different alveolar surface area  $A_{EI}$ . (B) Rate of surfactant secretion  $\varphi$  as a function of stretch amplitude  $\varepsilon$  of a single unit. (C) Schematic of the accumulation of surfactant ( $S$ ) on the gas-liquid interface. Surfactant is also removed from the interface at a rate. (D) Sigmoid pressure-volume ( $P$ - $V$ ) relation of a single alveolar unit is shifted to the left with increasing interfacial surfactant ( $S$ ).  $U_{IP}$  and  $L_{IP}$  denote the upper and lower inflection point, respectively. (E) Strains from previous breaths modulate surfactant levels which alter the  $P$ - $V$  relationship of individual units and thus the strains for the next breath, resulting in a closed feedback loop. See text for further explanation.

with total lung volume  $V_{EE}$ . At the end of inspiration, the total lung volume  $V_{EI}$  increases above  $V_{EE}$  by the prescribed tidal volume  $V_T$  which is distributed among the acinar units labeled with  $i$  according to the stiffness of their individual pressure-volume  $P_i$ - $V_i$  curve. Thus,

$$V_{EE} = \sum_i V_i(P = \text{PEEP}) \quad (5a)$$

$$V_{\text{TARGET}} = V_{EE} + V_T \quad (5b)$$

$$V_{EI} = \sum_i V_i (P = P_{EI}) \quad (5c)$$

where we replaced  $P_i$  with  $P$  both at end-inspiration and end-expiration. Once  $V_{EE}$  is determined from the previous breath according to **Eq.5a**, the target end-inspiratory volume  $V_{TARGET}$  is computed from **Eq.5b**. To ensure that total lung volume is equal to  $V_{EI}$  at end inspiration,  $P$  is increased by a small amount, the corresponding  $V_i$  of each unit is computed using **Eq.3**, and the sum on the right hand side of **Eq.5c** is determined. This process is iterated until the sum of the volumes  $V_i$  equals  $V_{TARGET}$ . The final value of  $P$  defines  $P_{EI}$  of the model, and is calculated with a maximum error tolerance of 0.01%. The surface areas  $A_{EE}$  and  $A_{EI}$  of each unit are then calculated from their respective volumes assuming spherical acini. Note that regardless of the particular shape of each acinus, the area will scale with volume raised to the 2/3 power. The value of  $\varepsilon$  is computed from  $A_{EE}$  and  $A_{EI}$  as described above which is then used to determine surfactant secretion  $\varphi$  (**Eq.1**). Next, the amount of surfactant secreted over the current breath is determined by solving **Eqs.1** and **2**. Finally,  $S$  is substituted into **Eq.4** to determine all regional  $P$ - $V$  curves for the next breath.

We simulate ventilation in discrete, breath by breath steps. Tidal volume  $V_T = V_{T0}$  is fixed for each breath during CV simulations. For VV,  $V_T$  is uniformly distributed within 10% above and below  $V_{T0}$ . We set functional residual capacity (FRC) defined as  $V_{EE}$  in the absence of PEEP, TLC, and minute ventilation (MV) according to values for a standard adult male. Parameter values, found in **Table 1**, were scaled such that the FRC, TLC and MV correspond to those in the healthy human adult lung.

## 2.5. Introduction of Injury

### 2.5.1. Heterogeneity in Intracellular Surfactant Release

Starting at breath  $n = N_{INJ}$ , the efficiency of intracellular surfactant secretion  $\varphi$  is disrupted. This is implemented by multiplying  $\varphi(n \geq N_{INJ})$  for each unit by a factor  $(1 + \eta_i)$ , where  $\eta_i$  is a random variable between  $-0.05$  and  $0.05$ . Note that  $\eta_i$  is selected once at  $N_{INJ}$ , and then each  $\eta_i$  is held constant over time for the duration of the simulation.

### 2.5.2. Heterogeneity in Regional Stiffness

An identical procedure was applied to varying acinar

regional stiffness  $\kappa$  as with surfactant release described above.

## 3. RESULTS

We present two major results. First, our four unit simulation results in **Figure 2** demonstrate how PEEP can both increase long-term recruitment and also delay the eventual collapse of unrecoverable units in CV. In combination with VV, however, this delay can be made much

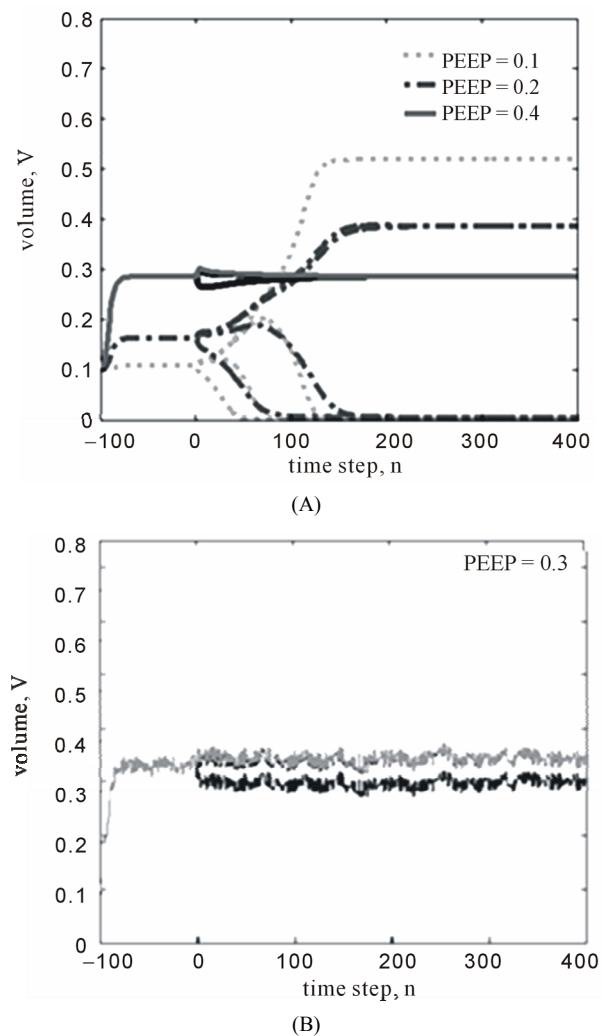


**Figure 2.** Four unit simulations. (A) End-inspiratory volumes  $V_{EI}$  stabilized by the application of PEEP during Conventional Ventilation. Dotted, dashed-dotted and solid lines correspond to PEEP = 0.1, 0.2 and 0.4, respectively. The four curves with each line type correspond to the four compartments. (B) Variable ventilation results in the lung reaching steady equilibrium, reducing the extent of alveolar collapse as compared to conventional ventilation. For clarity, here only the traces of the 4 units corresponding to PEEP = 0.3 are shown where all four units remain open. Notice that 3 units follow essentially the same pattern while the fourth is kept open at a slightly lower  $V_{EI}$ . This is the same unit that collapsed during CV at PEEP < 0.4.

**Table 1.** Parameter values.

| Param | Value | Param     | Value     | Param         | Value | Param | Value |
|-------|-------|-----------|-----------|---------------|-------|-------|-------|
| $N_A$ | 1024  | TLC       | 6.0 L     | T             | 4 s   | L     | 4E-3  |
| FRC   | 2.5 L | MV        | 7.5 L/min | $\varepsilon$ | 0.13  | $G_0$ | 1     |
| $V_T$ | 0.5 L | $V_{MAX}$ | TLC/NA    | $\kappa$      | 2.97  | $S_0$ | 1.72  |



longer as injured units appear to remain at non-equilibrium, fluctuating volumes. Second, during ventilation in the presence of heterogeneous surfactant release or tissue stiffness, we find that VV can maintain higher recruitment while avoiding overdystension for a wider range of PEEP and mean  $V_T$  values, partly through the mechanism described above.

### 3.1. Four Unit Simulations

We first simulated CV or VV of a lung model including only four units, tracing individual  $V_{EI}$  over time in **Figure 2** for PEEP values ranging from 0 to 0.4 (in arbitrary units). The simulations include an initial transient region between  $n = -100$  and 0, where either CV or VV was applied in the absence of any injury. At  $n = 0$ , heterogeneity in intracellular surfactant release was introduced as described in the Methods, while CV or VV was continued for another 400 breaths. The injury was identical in the two cases.

For CV at PEEP = 0.1, three units collapsed following injury. Increasing PEEP to 0.2, there was a reduction to only 2 collapsed units and also an increased transient time for the second compartment to collapse. A full recruitment of all 4 units was still not achieved at PEEP = 0.3, and was qualitatively similar to the PEEP = 0.2 condition (not shown). With PEEP = 0.4, all 4 units are stretched beyond  $\varepsilon^*$ , and thus we observe stable behavior with full recruitment. In contrast to CV, full recruitment was achieved through the use of VV at the lower PEEP of 0.3. Notice that during VV, the acinar compartments were maintained under non-equilibrium steady-state conditions with breath-by-breath fluctuations of  $V_{EI}$ . Thus, the variability in delivered tidal volumes prevented the quick collapse of all injured acini.

### 3.2. Optimization of PEEP and $V_T$ for Maximal Recruitment with Minimal Overdystension

We next simulated mechanical ventilation with a 1024 unit model as described in the Methods. Again, we tracked  $V_{EI}$  of each individual unit after introduction of injury at breath  $n = 0$ . However, we analyze two types of injury—heterogeneity in surfactant release and in acinar stiffness, for 20 values of PEEP and 30 values of  $V_T$  utilizing CV and VV. At the end of the simulation, the fraction of collapsed and overdystended units were determined and plotted as a function of PEEP and  $V_T$ .

**Figure 3** presents the results for CV with heterogeneous injury to surfactant release. On the left panel, we see alveolar collapse with PEEP < 0.5 and  $V_T$  < 0.5. The extent of collapse gradually decreases with increasing  $V_T$ . On the other hand, there appears to be a distinct threshold around PEEP = 0.4 where collapse is completely avoided regardless of  $V_T$ . Overdystension defined as

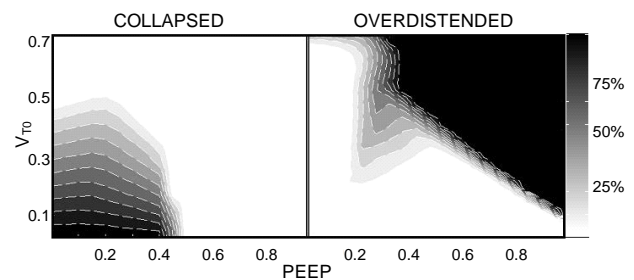


**Figure 3.** Alveolar collapse and overdystension in the presence of surfactant heterogeneity during conventional ventilation. Contour plots describe the fraction of the lung in the specified category when ventilating with a given PEEP and  $V_T$ . Left: Fraction of collapsed alveoli reduces gradually with increasing  $V_T$  and sharply with PEEP. Right: Fraction of overdystended alveoli increases with PEEP at high tidal volumes.

$V_{EI} = V_{EE} + V_T$  reaching 75% of maximum alveolar volume showed an opposing trend, where the highest  $V_T$  which avoids overdystension decreases approximately linearly with increasing PEEP. Simultaneous collapse and overdystension can be observed at midrange values of PEEP and  $V_T$ .

Additional simulations allowed us to compare and contrast the results for applying VV or CV for heterogeneous surfactant release as well as heterogeneous acinar stiffness (**Figure 4**). For a disruption of normal homogeneous surfactant release under CV (top left panel), alveolar collapse occurs at low-PEEP-low- $V_T$  settings, while overdystension occurs for high-PEEP-high- $V_T$  settings resulting in two relatively small disjoint regions (blue) whereby alveolar injury is prevented. When VV is applied (top right panel), one contiguous region of PEEP and  $V_T$  allows for full recruitment without overdystension. Overall, the possible combinations of PEEP and  $V_T$  during VV are much greater than during CV. For the heterogeneous acinar stiffness case under CV (bottom left panel), again alveolar collapse occurs at low-PEEP-low- $V_T$  settings, while overdystension occurs for high-PEEP-high- $V_T$  settings. However, in this case a contiguous band of good PEEP- $V_T$  settings exist. When VV is applied (right panel), the size of this region is significantly larger.

## 4. DISCUSSION

In this study, we developed a model that incorporates stretch-induced surfactant release into the regional pressure-volume curve of a parallel set of acinar units exposed to various ventilator settings. To our knowledge, this is the first attempt to couple surfactant metabolism with stretch and regional lung mechanics. The model allows us to simulate patient-ventilator interactions over a wide range of PEEPs and  $V_T$ s. The primary finding of the study is that the particular ventilator settings have a critical role in surfactant distribution, regional lung compliance and hence predicted ventilation outcome.

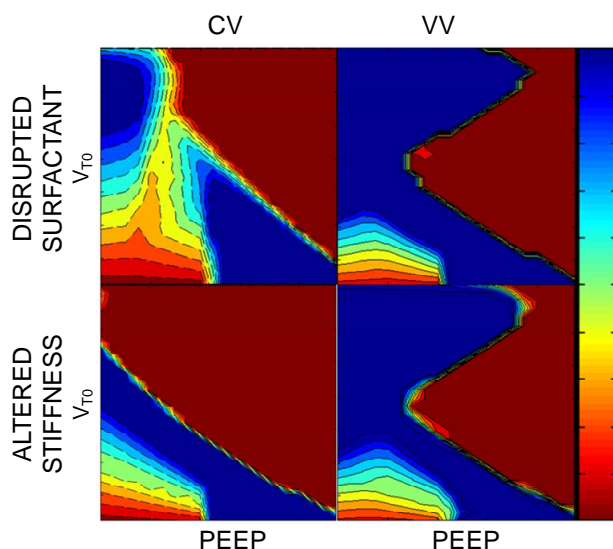


**Figure 4.** Comparison of best PEEP- $V_T$  settings for CV vs. VV for two different pathologies. Contour plots describe the fraction of the lung which are neither collapsed nor overdistended when ventilating with a given PEEP and  $V_T$  for CV and VV. For instance, the top left panel shows the superimposed view of **Figures 3(A)** and **(B)**, presenting the PEEP and  $V_T$  settings which resulted in the best outcomes (number of units recruited but not overdistended) in blue and injury due to collapse or overdistention marked by red. Top left: Heterogeneous surfactant release under CV. Top right: Heterogeneous surfactant release under VV. Bottom left: Heterogeneous alveolar stiffness under CV. Bottom right: Heterogeneous alveolar stiffness under VV.

Specifically, VV provides a much wider range of possible ventilator settings that result in maximum lung recruitment and minimal overdistention when compared to CV.

#### 4.1. Optimal PEEP- $V_T$ Values for CV and VV

In this model, alveolar collapse is prevented by stretching the acinar units above  $\varepsilon^*$ . This can be accomplished through either large tidal stretches alone, by providing a sufficiently high PEEP such that  $\varepsilon > \varepsilon^*$  at end expiration, or by a combination of both ventilator settings. This is reflected in the lower left-hand corner of each panel in **Figure 4**: low PEEP and small  $V_T$  leads to collapse whereas large  $V_T$  values provide adequate stretch and surfactant release. With increasing PEEP, a lower  $V_T$  is sufficient to produce the necessary stretch. At around PEEP = 0.4, the end-expiratory pressure alone is sufficient to maintain alveolar recruitment. Naturally, there is an inverse relationship between the  $V_T$  and PEEP required to reach the absolute volume beyond which overdistention of the alveoli occurs. The reason for this is that PEEP effectively increases  $V_{EE}$ . These characteristics are common to each simulation case.

The difference between VV and CV are illustrated in

the presence of heterogeneous surfactant release in the top panels of **Figure 4**. As some acinar units collapse, their volume is diverted into the remaining units triggering simultaneous collapse and overdistention as seen in the top left panel of **Figure 4**. However, we observe that VV allows for full recruitment at a lower  $V_T$  than CV. In fact, the overlapping region of collapse and overdistention is completely removed. Overall, a larger range of PEEP and  $V_T$  can provide optimal acinar recruitment (area of the blue regions) in VV than for CV.

We also note here a qualitative difference between the results for the two injury cases during CV. In the presence of heterogeneous stiffness, we no longer observe an area of simultaneous collapse and overdistention. The model also predicts a larger area of overdistention, and low-PEEP-high- $V_T$  settings no longer produce a positive outcome (defined as full recruitment). In contrast, the acceptable combinations of PEEP and  $V_T$  during VV seem to be insensitive to the simulated injuries. Additional sensitivity analysis, in which model parameters were varied between 50% and 200% of their baseline values, indicated that the advantage of VV over CV is robust and does not depend on particular model settings.

In both cases of injury during VV, there exists an unexpected region at intermediate PEEPs where increasing tidal volume first causes and then prevents overdistention. We note that these PEEP- $V_T$  combinations are well above physiologic values, and discuss this further in the section on model limitations.

#### 4.2. Stability of the Alveolus through Stretch-Surfactant Relation

The shape of the stretch-surfactant relationship (**Figure 1(B)**), in particular its peak, has two consequences on model behavior. First, there appears to be an optimal stretch magnitude for surfactant secretion, and thus reduction of mechanical injury induced by ventilation. The second, seemingly counterintuitive, consequence is that optimal lung function actually requires the majority of the lung to be stretched beyond this threshold. Consider an alveolus ventilated at or below the stretch threshold  $\varepsilon^*$ . A minor reduction in stretch attenuates surfactant production, increasing stiffness which in turn further reduces stretch, eventually leading to full collapse. This is in agreement with recent data that ventilating normal mice at a PEEP of 3 cm H<sub>2</sub>O for 30 min, a reduction in  $V_T$  from 8 to 6 ml/kg significantly reduced the level of surfactant protein B, a key component of surfactant that contributes to normal surface tension [18]. In contrast, in the regime above the stretch threshold, reduced/increased alveolar stretch increases/reduces surfactant production, and thus deviations from the initial stretch magnitude are countered by the stretch modulated surfactant secretion.

In other words, an inverse relation between stretch and surfactant secretion beyond the critical value  $\varepsilon^*$ , in combination with the nonlinear pressure-volume relationship, guarantees the stability of acinar units.

### 4.3. Coupling of Local Surfactant Secretion and Compliance to Regional Ventilation

Next, we consider several connected acinar units ventilated at a fixed global tidal volume such that the alveolar stretch magnitudes are beyond  $\varepsilon^*$ . If one alveolus is injured and thus stretched below the threshold, it would tend to collapse according to the mechanism described in Section 4.2, diverting its tidal volume into the remaining normal alveoli. This extra volume causes the normal alveoli to be stretched further above the threshold, reducing their surfactant thus increasing their stiffness. This redirects flow back into the injured unit, increasing its surfactant production possibly preventing collapse. This protective mechanism no longer holds, however, when the entirety of units are also stretched below the threshold. After a large fraction of the units collapse, the diverted tidal volume is forced into the small remaining open fraction of the units resulting in their overdistention. Consequently, a heterogeneous distribution of severe injury through surfactant interference or local trauma can result in neighboring regions of collapsed and overdistended acinar units. Images of subpleural alveoli of normal and ventilator-injured lungs are consistent with this notion (10). Thus, maintaining above-threshold stretch with either PEEP or tidal volume may help stabilize the injured lung.

### 4.4. Non-Equilibrium Steady State during Variable Ventilation

Through the proposed mechanisms, progressive alveolar collapse and ventilation redistribution occurred due to the instability of the system when stretch is below  $\varepsilon^*$ . During CV, the final outcome (e.g. whether an acinus collapses) was a function of the stretch magnitude of each acinus relative to the threshold. The time scale of collapse depended primarily on surfactant dynamics ( $\phi$  and  $\lambda$ ) and tidal volume, and in many cases a long transient period preceded equilibrium. During VV, the cycle-by-cycle variations of regional tidal volumes disrupted the stretch-surfactant coupling, prolonging this transient period indefinitely. Indeed, such dynamic equilibrium has been found experimentally in mice during ventilation with VV [19]. In our model, this steady state maintains on average a larger number of recruited acinar units than CV. We can speculate that in real patients, if such steady state exists, it may allow time for the injury to heal and thus faster return to normal function upon release from the ventilator. We also note that experimen-

tally it was found that VV stimulates surfactant release as well as production [20]. Our simulations are consistent with this since on average a higher lung volume in the model is due to more surfactant. Thus, the non-equilibrium steady state seen in the model offers a mechanistic explanation for such experimental findings.

### 4.5. Model Limitations

Several assumptions in our model were implemented to simplify the dynamics and study regional surfactant metabolism coupled with regional alveolar stretch. Additionally, several important phenomena have also been neglected. These are discussed next.

#### 4.5.1. Modeling Stretch-Induced Surfactant Release

Little is known about the stretch-induced dynamics of surfactant release and production in vivo. In vitro studies suggest that increasing the amplitude of a single biaxial stretch applied to cells in culture, increases the amount of surfactant released in a quasi-exponentially increasing manner while the time course of the release showed an asymptotic approach to a constant [15]. During cyclic stretch; however, large amplitudes down-regulated surfactant release [8]. The shape of the surfactant release-stretch curve in our model (**Figure 1(B)**) incorporated these observations. As described in Section 4.2, it is the slope of the stretch-surfactant curve below and above the peak that drives the stability of the overall system. In light of this, our choice of a linear relation as opposed to another would not qualitatively affect our results. This feature of the model together with how surfactant affects the pressure-volume curve (**Figure 1(D)**) led to the prediction of reversal of overdistention with unphysiologically large  $V_T$  values superimposed on medium PEEP levels. Nevertheless, VV still outperformed CV even if we did not include this region in the comparison.

#### 4.5.2. Pressure-Volume Relation

We selected the empirical pressure-volume relation presented by [17] as it is able to capture the convex  $P$ - $V$  relation at low volumes resulting from recruitment and the plateau at high pressures due to tissue stiffening. Our implicit assumption is that the  $P$ - $V$  relation on the scale of individual acinar units is similar to that of the whole lung. In this manner, we are able to parameterize individual acinar units based on published values corresponding to whole lung data [17]. The disadvantage of an empirical curve is that it does not account for the contribution of tissue and surface forces separately.

Although the relation presented by Bachofen and Wilson [21] and subsequent modifications [22,23] explicitly includes the micromechanical response of fiber stretch and surface tension within individual acini, it is unsuitable to our needs as its applicability is limited be-

tween 40% and 80% of TLC, whereas our model necessarily contains acini outside of this range. The model presented by Denny and Shroter [24] contain surface and tissue forces similar to that of [21] at the level of individual acini, showing a sigmoidal relation qualitatively similar to [17] for the full range of volumes, but lacks an analytic  $P$ - $V$  relation. We note that similar to the stretch-surfactant relation, the exact  $P$ - $V$  relation does not qualitatively affect our results, but rather the second derivative of this curve (how stiffness varies with volume). Any sufficiently similar  $P$ - $V$  curve would deliver similar results.

#### 4.5.3. Parameter Selection

The exact values of many of our model parameters are difficult to quantify *in vivo*, and thus remain unknown. For instance,  $\phi_{\max}$  corresponds to the peak surfactant release rate per cell at a given stretch amplitude and frequency, while  $\lambda$  is the collective rate of several processes of surfactant depletion (re-uptake, enzymatic reuptake, de-activation, etc.). The exact shape of the  $\phi$  versus  $\varepsilon$  relation is also unknown, and the effect of surfactant on the static  $P$ - $V$  relationship of a single alveolus was only estimated as shifting the curve along the pressure-axis. To justify our parameter selection, we note that changing  $\phi_{\max}$  in our model amounts to multiplying  $\phi$  by a constant proportionality factor for all units, and would not change the overall system's qualitative behavior. The degradation parameter  $\lambda$  effectively "smoothens out" the changes in surfactant from each breath:  $\lambda = 1$  corresponds to immediate degradation of surfactant after each breath. Thus, adjusting  $\lambda$  affects the time course of collapse which is not systematically analyzed in this study, and does not alter the end result of the number of stable and collapsed acini. For the normal uninjured lung, we chose the values of  $\phi_{\max}$ ,  $\lambda$ ,  $G_0$ , and  $\varepsilon^*$  to correspond to a lung with FRC = 2.5 L and TLC = 6 L while ventilated with  $V_T = 0.5$  L and PEEP = 0.

#### 4.5.4. Breath-by-Breath Dynamics

Assuming full equilibrium of pressures both at end-expiration and end-inspiration neglected the presence intra-breath dynamics and discounted the effects of tissue and surface film viscoelasticity. As a result, the model is unable to reproduce hyperinflation, and the time dependence of the opening and closing processes has been neglected [25] that would likely further complicate the process of gradual collapse in the model. The surface area-surface tension loop depends on the constituents of the surfactant at the air-liquid interface and exhibits hysteresis during a breath cycle in overinflated but otherwise normal regions [26] which is not taken into account.

#### 4.5.5. Parallel Compartment Model

Another simplification was that we modeled a parallel

set of units; hence, any effects due to airway structure are absent. One important aspect of this may be that repeated airway opening and closing can produce shear and/or normal stresses [27] that would amplify epithelial injury. A further limitation is that due to the previous assumption of pressure equilibrium, applying a different pathway resistance for each parallel compartment would not introduce heterogeneous regional flow delivery and pressure fluctuations [28]. Additionally, inter-regional airflows causing heterogeneous emptying of the lung are not possible in our model.

#### 4.5.6. Independent Lung Regions

In the current model, the coupling between regions is attributed to the redirection of tidal volume from stiffer to softer compartments in the presence of a fixed total tidal volume. The effects of fluid accumulation and the corresponding effects of gravity were not taken into account. Both of these phenomena have been shown to play a role in VALI (8) and future extensions of the model should explicitly incorporate them. Additionally, mechanical coupling through parenchymal interactions likely promotes regional interdependence.

#### 4.5.7. Limited Injury Mechanisms

Finally, our models of lung injury at the alveolar and cellular levels are non-specific. For example, fluid leakage from the vasculature alters the composition and hence the surface-tension surface area relation of the surfactant [26]. Fluid accumulation in the alveoli changes the shape of the local  $P$ - $V$  curve with a significant decrease in compliance [29]. These mechanisms of lung injuries should be explored since it is possible that the best PEEP- $V_T$  combination is injury specific. For instance, atelectatic opening and closing may cause more lung injury than sustained collapse, as could high strain magnitudes without overdistention leading cell membrane rupture [30].

Despite the limitations discussed above, the novel features of the model allowed us to explore patient-ventilator coupling and optimization of best PEEP- $V_T$  combination in the presence of collapse and overdistention injury. The main result was that the coupling between surfactant secretion and regional lung mechanics during ventilation has a significant impact on the outcome of patient ventilation. While this was possible only using an appropriate computational model due to the difficulties associated with the breath-by-breath experimental assessment of surfactant pool and regional lung mechanics, the long-term predictions of the model could be tested in clinical settings.

## 5. CONCLUSION

It is now well-acknowledged that protecting epithelial



cells from injury is the most important goal of any ventilation strategy. The model developed in this study demonstrates the significance of the cellular stretch-induced surfactant release relationship with respect to the whole lung stability. Maintaining epithelial cell stretch above a critical threshold with either PEEP or  $V_T$  may help stabilize the injured lung. Moreover, the injured lung can see additional benefit from breath-by-breath variation of tidal volumes which maintains the lung periphery open under a dynamic equilibrium with a better outcome than the corresponding conventional ventilation strategy. Thus, irrespective of the particular model used in this study, our results point to the clinical significance of ventilator-patient coupling.

## 6. ACKNOWLEDGEMENTS

Funded by HL-098976, HL-111745, DoD W81XWH-08-1-0148 and the Coulter Foundation.

## REFERENCES

- [1] Rubenfeld, G.D., Caldwell, E., Peabody, E., Weaver, J., Martin, D.P., Neff, M., Stern, E.J. and Hudson, L.D. (2005) Incidence and outcomes of acute lung injury. *The New England Journal of Medicine*, **353**, 1685-1693. <http://dx.doi.org/10.1056/NEJMoa050333>
- [2] The Acute Respiratory Distress Syndrome Network (2000) Ventilation with lower tidal volumes as compared with traditional tidal volumes for acute lung injury and the acute respiratory distress syndrome. *The New England Journal of Medicine*, **342**, 1301-1308. <http://dx.doi.org/10.1056/NEJM200005043421801>
- [3] Bilek, A.M., Dee, K.C. and Gaver 3rd., D.P. (2003) Mechanisms of surface-tension-induced epithelial cell damage in a model of pulmonary airway reopening. *Journal of Applied Physiology*, **94**, 770-783.
- [4] Kay, S.S., Bilek, A.M., Dee, K.C. and Gaver 3rd., D.P. (2004) Pressure gradient, not exposure duration, determines the extent of epithelial cell damage in a model of pulmonary airway reopening. *Journal of Applied Physiology*, **97**, 269-276. <http://dx.doi.org/10.1152/japplphysiol.01288.2003>
- [5] Puybasset, L., Gusman, P., Muller, J.C., Cluzel, P., Coriat, P. and Rouby, J.J. (2000) Regional distribution of gas and tissue in acute respiratory distress syndrome. III. Consequences for the effects of positive end-expiratory pressure. CT Scan ARDS Study Group. Adult Respiratory Distress Syndrome. *Intensive Care Medicine*, **26**, 1215-1227. <http://dx.doi.org/10.1007/s001340051340>
- [6] Rouby, J.J. and Brochard, L. (2007) Tidal recruitment and overinflation in acute respiratory distress syndrome: Yin and yang. *American Journal of Respiratory and Critical Care Medicine*, **175**, 104-106. <http://dx.doi.org/10.1164/rccm.200610-1564ED>
- [7] Terragni, P.P., Rosboch, G., Tealdi, A., Corno, E., Menaldo E, Davini, O., Gandini, G., Herrmann, P., Maschia, L., Quintel, M., Slutsky, A.S., Gattinoni, L. and Ranieri, V.M. (2007) Tidal hyperinflation during low tidal volume ventilation in acute respiratory distress syndrome. *American Journal of Respiratory and Critical Care Medicine*, **175**, 160-166. <http://dx.doi.org/10.1164/rccm.200607-915OC>
- [8] Arold, S.P., Bartolak-Suki, E. and Suki, B. (2009) Variable stretch pattern enhances surfactant secretion in alveolar type II cells in culture. *American Journal of Physiology: Lung Cellular and Molecular Physiology*, **296**, L574-L581. <http://dx.doi.org/10.1152/ajplung.90454.2008>
- [9] Arold, S.P., Suki, B., Alencar, A.M., Lutchen, K.R. and Ingenito, E.P. (2003) Variable ventilation induces endogenous surfactant release in normal guinea pigs. *American Journal of Physiology: Lung Cellular and Molecular Physiology*, **285**, L370-L375.
- [10] Arold, S.P., Mora, R., Lutchen, K.R., Ingenito, E.P. and Suki, B. (2002) Variable tidal volume ventilation improves lung mechanics and gas exchange in a rodent model of acute lung injury. *American Journal of Respiratory and Critical Care Medicine*, **165**, 366-371. <http://dx.doi.org/10.1164/ajrcm.165.3.2010155>
- [11] Bellardine, C.L., Hoffman, A.M., Tsai, L., Ingenito, E.P., Arold, S.P., Lutchen, K.R. and Suki, B. (2006) Comparison of variable and conventional ventilation in a sheep saline lavage lung injury model. *Critical Care Medicine*, **34**, 439-445. <http://dx.doi.org/10.1097/01.CCM.0000196208.01682.87>
- [12] Thammanomai, A., Hueser, L.E., Majumdar, A., Bartolak-Suki, E. and Suki, B. (2008) Design of a new variable-ventilation method optimized for lung recruitment in mice. *Journal of Applied Physiology*, **104**, 1329-1340. <http://dx.doi.org/10.1152/japplphysiol.01002.2007>
- [13] Spieth, P.M., Carvalho, A.R., Pelosi, P., Hoehn, C., Meissner C., Kasper, M., Hubler, M., von Neindorff, M., Dassow, C., Barrenschee, M., Uhlig, S., Koch, T. and de Abreu, M.G. (2009) Variable tidal volumes improve lung protective ventilation strategies in experimental lung injury. *American Journal of Respiratory and Critical Care Medicine*, **179**, 684-693. <http://dx.doi.org/10.1164/rccm.200806-975OC>
- [14] Suki, B., Alencar, A.M., Sujeer, M.K., Lutchen, K.R., Collins, J.J., Andrade Jr., J.S., Ingenito, E.P., Zapperi, S. and Stanley, H.E. (1998) Life-support system benefits from noise. *Nature*, **393**, 127-128. <http://dx.doi.org/10.1038/30127>
- [15] Wirtz, H.R. and Dobbs, L.G. (1990) Calcium mobilization and exocytosis after one mechanical stretch of lung epithelial cells. *Science*, **250**, 1266-1269. <http://dx.doi.org/10.1126/science.2173861>
- [16] Arold, S.P. (2006) Effects of cyclic stretch on surfactant secretion and cell viability in alveolar epithelial cells grown in culture Diss. ProQuest, Boston University, UMI Dissertations Publishing, Boston.
- [17] Venegas, J.G., Harris, R.S. and Simon, B.A. (1998) A comprehensive equation for the pulmonary pressure-volume curve. *Journal of Applied Physiology*, **84**, 389-395.
- [18] Thammanomai, A., Majumdar, A., Bartolak-Suki, E. and

- Suki, B. (2007) Effects of reduced tidal volume ventilation on pulmonary function in mice before and after acute lung injury. *Journal of Applied Physiology*, **103**, 1551-1559.  
<http://dx.doi.org/10.1152/japplphysiol.00006.2007>
- [19] Hubmayr, R.D. (2002) Perspective on lung injury and recruitment: A skeptical look at the opening and collapse story. *American Journal of Respiratory and Critical Care Medicine*, **165**, 1647-1653.  
<http://dx.doi.org/10.1164/rccm.2001080-01CP>
- [20] Thammanomai, A., Hamakawa, H., Bartolák-Suki, E. and Suki, B. (2013) Combined effects of ventilation mode and positive end-expiratory pressure on mechanics, gas exchange and the epithelium in mice with acute lung injury. *PLoS One*, **8**, Article ID: e53934.  
<http://dx.doi.org/10.1371/journal.pone.0053934>
- [21] Wilson, T.A. and Bachofen, H. (1982) A model for mechanical structure of the alveolar duct. *Journal of Applied Physiology*, **52**, 1064-1070.
- [22] Stamenovic, D. and Wilson, T.A. (1985) A strain energy function for lung parenchyma. *Journal of Biomechanical Engineering*, **107**, 81-86.  
<http://dx.doi.org/10.1115/1.3138525>
- [23] Ingenito, E.P., Tsai, L.W., Majumdar, A. and Suki, B. (2005) On the role of surface tension in the pathophysiology of emphysema. *American Journal of Respiratory and Critical Care Medicine*, **171**, 300-304.  
<http://dx.doi.org/10.1164/rccm.200406-770PP>
- [24] Denny, E. and Schroter, R.C. (1997) Relationships between alveolar size and fibre distribution in a mammalian lung alveolar duct model. *Journal of Biomechanical Engineering*, **119**, 289-297.  
<http://dx.doi.org/10.1115/1.2796093>
- [25] Massa, C.B., Allen, G.B. and Bates, J.H. (2008) Modeling the dynamics of recruitment and derecruitment in mice with acute lung injury. *Journal of Applied Physiology*, **105**, 1813-1821.  
<http://dx.doi.org/10.1152/japplphysiol.90806.2008>
- [26] Ingenito, E.P., Mark, L., Morris, J., Espinosa, F.F., Kamm, R.D. and Johnson, M. (1999) Biophysical characterization and modeling of lung surfactant components. *Journal of Applied Physiology*, **86**, 1702-1714.
- [27] Ghadiali, S.N. and Gaver, D.P. (2008) Biomechanics of liquid-epithelium interactions in pulmonary airways. *Respiratory Physiology & Neurobiology*, **163**, 232-243.  
<http://dx.doi.org/10.1016/j.resp.2008.04.008>
- [28] Amin, S.D., Majumdar, A., Frey, U. and Suki, B. (2009) Modeling the dynamics of airway constriction: Effects of agonist transport and binding. *Journal of Applied Physiology*, **109**, 553-563.  
<http://dx.doi.org/10.1152/japplphysiol.01111.2009>
- [29] Wilson, T.A., Anafi, R.C. and Hubmayr, R.D. (2001) Mechanics of edematous lungs. *Journal of Applied Physiology*, **90**, 2088-2093.
- [30] Vlahakis, N.E., Schroeder, M.A., Pagano, R.E. and Hubmayr, R.D. (2002) Role of deformation-induced lipid trafficking in the prevention of plasma membrane stress failure. *American Journal of Respiratory and Critical Care Medicine*, **166**, 1282-1289.  
<http://dx.doi.org/10.1164/rccm.200203-207OC>